KOCAELI JOURNAL OF SCIENCE AND ENGINEERING

Kocaeli University

Kocaeli Journal of Science and Engineering

http://dergipark.org.tr/kojose

Quasi-Primary Spectrum of a Commutative Ring and a Sheaf of Rings

Neslihan Ayşen ÖZBAY [1], * (iD) , Zehra BİLGİN [2] (iD)

[1] *Department of Information Systems Engineering, Ankara Science University, Ankara, 06570, Turkey,* **ORCID:** *0000-0002-7403-8701*
[2] *History of Science Department, Istanbul Medeniyet University, Istanbul, 34700, Turkey,* **ORCID:** *0000-0002-6147-3018*

Abstract

In this work, the set of quasi-primary ideals of a commutative ring with identity is equipped with a topology and is called the quasi-primary spectrum. Some topological properties of this space are examined. Further, a sheaf of rings on the quasi-primary spectrum is constructed and it is shown that this sheaf is the direct image sheaf with respect to the inclusion map from the prime spectrum of a ring to the quasi-primary spectrum of the same ring.

1. Introduction

The set of all prime ideals of a commutative ring R, called the *prime spectrum* of R, denoted by $Spec(R)$, is a well-known concept in commutative algebra. This set is equipped with the famous Zariski topology, where closed sets are defined as

$$V(I) = \{P \in Spec(R) : I \subseteq P\}$$

for any ideal, I of R. Topological properties of $Spec(R)$ are widely examined throughout the years and can be found in many of the standard commutative algebra and algebraic geometry references. Besides, there is a famous sheaf construction, named *the structure sheaf*, on $Spec(R)$ which is a very useful tool to connect algebraic geometry and commutative algebra. For details of the structure sheaf, the reader may consult [1-3].

In [4], the authors generalized the Zariski topology on $Spec(R)$ to the set of primary ideals of a commutative ring R, denoted by $Prim(R)$, and they called it the *primary spectrum* of R. They defined the closed sets as

$$V_{rad}(I) = \{Q \in Prim(R) : I \subseteq \sqrt{Q}\}$$

for any ideal I of R where $\sqrt{Q}$ denotes the radical of Q. They showed that these closed sets satisfy axioms of a topology on $Prim(R)$. They investigated some topological properties of this space and compared them with the well-known properties of $Spec(R)$. We note that, since any prime ideal is primary and equal to its radical, the space $Spec(R)$ is in fact a subspace of $Prim(R)$.

When [4] is examined in detail, it can be realized that the given topological construction depends only on the fact that the radical of a primary ideal is prime. So, this topology is in fact valid on a much larger set, the set of ideals whose radicals are prime. These types of ideals are first introduced by L. Fuchs in [5]. He named them *quasi-primary* ideals. We aim to investigate the set of quasi-primary ideals of a commutative ring R equipped with a topology similar to the one defined in [4] and to construct a sheaf of rings on this topological space.

In Section 2, after observing certain general topological aspects of the quasi-primary spectrum, we deal with irreducibility and irreducible components of this space. Moreover, we examine the disconnectedness of the space and finally prove that the dimension of the quasi-primary spectrum of a Noetherian local ring is finite. In

* Corresponding Author: aysen.ozbay@ankarabilim.edu.tr

Section 3, we construct a sheaf of rings on the quasi-primary spectrum of and prove that this sheaf is actually the direct image sheaf under the inclusion map from the prime spectrum to the quasi-primary spectrum.

2. The Quasi-Primary Spectrum of a Ring

Throughout this paper, all rings are commutative with identity. In this section, we define a topology on the set of all quasi-primary ideals of a ring and examine some properties of this topological space.

First, we present some (known) properties of quasi-primary ideals we need in the rest of the paper. Let R be a ring. Following [5], an ideal I of R is called *quasi-primary* if the radical of I, denoted by $\sqrt{I}$ is prime.

Lemma 2.1 *Let I be an ideal of a ring R and S a multiplicative subset of R. Denote the localization of R with respect to S by R_S.*
  i. *If I is primary, then I is quasi-primary.*
  ii. *If I is a quasi-primary ideal, the I has only one minimal prime ideal.*
  iii. *If IR_S is a quasi-primary ideal of R_S, then $IR_S \cap R$ is a quasi-primary ideal of R.*
  iv. *If I is a quasi-primary ideal of R such that $\sqrt{I} \cap S = \emptyset$, then IR_S is a quasi-primary ideal of R_S.*

Proof. (i) and (ii) is obvious. For (iii) and (iv) it is enough to observe that $\sqrt{IR_S} = \sqrt{I}R_S$. $\square$

Let
$$QPrim(R) = \{I \subseteq R : I \text{ is a quasi-primary ideal}\}.$$
For any subset S of R, let us define the set
$$V_q(S) = \{Q \in QPrim(R) : S \subseteq \sqrt{Q}\}.$$
Observe that, for any subset S of R, if $I = (S)$ we have $V_q(S) = V_q(I)$. If $S = \{a\}$ for $a \in R$, we write $V_q(S) = V_q(a)$.

In [4], the authors defined a topology on the set $Prim(R)$ of primary ideals of a commutative ring using the sets $V_{rad}(I) = \{Q \in Prim(R) : I \subseteq \sqrt{Q}\}$ as the closed sets. In this construction, they only used the property that a primary ideal has a prime radical. So, we realized that the topology axioms for closed sets are in fact satisfied by the sets
$$V_q(I) = \{Q \in QPrim(R) : I \subseteq \sqrt{Q}\}$$
where I any ideal of R. Thus, $QPrim(R)$ is a topological space with closed sets $V_q(I)$ where I is an ideal of R. Since any primary ideal is quasi-primary, we have $Prim(R)$ as a subspace of $QPrim(R)$.

For the sake of completeness, we note some properties (from Proposition 2.2 to Corollary 2.6) of $V_q(I)$ without proofs. For details, see [4].

Proposition 2.2 *Let I, J be ideals of R and $\{I_\lambda\}_{\lambda \in \Lambda}$ a family of ideals of R. Then the followings hold:*
  i. *If $I \subseteq J$, then $V_q(J) \subseteq V_q(I)$.*
  ii. *$V_q(0) = QPrim(R)$ and $V_q(R) = \emptyset$.*
  iii. *$V_q(I \cap J) = V_q(IJ) = V_q(I) \cup V_q(J)$.*
  iv. *$V_q(\sum_{\lambda \in \Lambda} I_\lambda) = \bigcap_{\lambda \in \Lambda} V_q(I_\lambda)$.*
  v. *$V_q(I) = V_q(\sqrt{I})$.*

Proof. Similar to [4, Remark 2.1] and [4, Proposition 2.3]. $\square$

Corollary 2.3 *The family $\{V_q(I) : I \text{ is an ideal of } R\}$ satisfies the axioms of closed sets of a topology on $QPrim(R)$.*

This topology is called *Zariski topology* on $QPrim(R)$ and the space $QPrim(R)$ is named as the *quasi-primary spectrum* of R. We note that any open set in $QPrim(R)$ is of the form $QPrim(R) \backslash V_q(S)$ for some subset S of R.

Consider the set $U_a = QPrim(R) \backslash V_q(a)$ for any $a \in R$.

Theorem 2.4 *Let R be a ring. The family $\{U_a\}_{a \in R}$ is a base for the Zariski topology on $QPrim(R)$.*

Proof. Similar to [4, Theorem 3.1]. $\square$

Note that $U_0 = \emptyset$ and $U_r = QPrim(R)$ for every unit $r \in R$.

Theorem 2.5 *Let R be a ring and $a, b \in R$. The followings hold:*
  i. *$\sqrt{(a)} = \sqrt{(b)}$ if and only if $U_a = U_b$.*
  ii. *$U_{ab} = U_a \cap U_b$.*
  iii. *$U_a = \emptyset$ if and only if a is nilpotent.*
  iv. *U_a is quasi-compact.*

Proof. Similar to [4, Theorem 3.2]. $\square$

Corollary 2.6 *Let R be a ring. The space $QPrim(R)$ is quasi-compact.*

Quasi-primary ideals were firstly introduced and examined thoroughly in [5]. It is generally studied on rings satisfying maximal conditions; in other words, every ascending chain of ideals is finite. It is also noted that the

quasi-primary ideals in rings satisfying maximal conditions can be characterized as follows: A quasi-primary ideal is either a power of a prime ideal or an intermediate ideal between two powers of one and the same prime ideal. In view of this fact, the following theorem is given for rings satisfying maximal condition.

Theorem 2.7 *[5, Theorem 4] If Q_1 and Q_2 are quasi-primary ideals having the radicals P_1 and P_2 respectively, and $P_1 \subseteq P_2$. Then $Q_1 Q_2$ is also quasi-primary having the radical P_1.*

Theorem 2.8 *Let R be a ring satisfying maximal condition and Q_1 and Q_2 be quasi-primary ideals of R such that $Q_1 \subseteq Q_2$. If $Q_1 \in V_q(I)$, then $Q_1 Q_2 \in V_q(I)$ for any ideal I of R.*

Proof. Let I be an ideal and Q_1, Q_2 two quasi-primary ideals such that $Q_1 \subseteq Q_2$ in a ring R satisfying maximal condition. Suppose $Q_1 \in V_q(I)$. Then $I \subseteq \sqrt{Q_1} \subseteq \sqrt{Q_2}$ by the assumption. So, we obtain $I \subseteq \sqrt{Q_1 Q_2}$ by Theorem 2.7, which yields $Q_1 Q_2 \in V_q(I)$. □

It is known that Theorem 2.7 has no analogue in primary ideal theory. Similarly, Theorem 2.8 does not valid for the primary spectrum as can be seen in the following example.

Example 1 *Consider the residue class ring $R = K[X_1, X_2, X_3]/(X_1 X_3 - X_2^2)$ where K is a field. It is clear that R satisfies the maximal condition. Let x_i denote the natural image of X_i in R for each $i \in \{1,2,3\}$. Then, the ideal $P = (x_1, x_2)$ is a prime ideal of R but P^2 is not primary [6, Example 4.12]. It is trivial that P^2 is a quasi-primary ideal of R. Now take $Q_1 = Q_2 = P$. Then, we see that $P \in V_q(P) \cap V_{rad}(P)$, however, $P^2 \in V_q(P) \backslash V_{rad}(P)$.*

Now, let us determine the closure of a point $Q \in QPrim(R)$. The closure $Cl(Q)$ of Q is

$$Cl(Q) = \bigcap_{Q \in V_q(S)} V_q(S) = \bigcap_{S \subseteq \sqrt{Q}} V_q(S) = V_q(Q).$$

Definition 2.9 *A topological space X is irreducible if X is nonempty and X cannot be written as a union of two proper closed subsets, or equivalently, any two nonempty open subsets of X intersect.*

Theorem 2.10 *Let R be a ring. Then $QPrim(R)$ is an irreducible space if and only if the nilradical of R, $\mathcal{N}(R)$, is quasi-primary.*

Proof. Let $\mathcal{N}(R)$ be a quasi-primary ideal and U, V be two non-empty open subsets of $QPrim(R)$. Suppose that $Q_1 \in U \backslash V$. Then there exists a subset S of R such that $U = X \backslash V_q(S)$. This implies $Q_1 \notin V_q(S)$, that is, $S \nsubseteq \sqrt{Q_1}$. Then we get $S \nsubseteq \sqrt{\mathcal{N}(R)}$ since $\mathcal{N}(R) \subseteq \sqrt{Q_1}$. Hence, $\mathcal{N}(R) \notin V_q(S)$. Then, we obtain $\mathcal{N}(R) \in U$. In a similar way, we get $\mathcal{N}(R) \in V$ which yields $U \cap V \neq \emptyset$. For the converse part, let $QPrim(R)$ be an irreducible space and assume that $\mathcal{N}(R)$ is not quasi-primary. Then $\sqrt{\mathcal{N}(R)}$ is not prime. Then there exist $a, b \in R$ such that $a, b \notin \sqrt{\mathcal{N}(R)}$ but $ab \in \mathcal{N}(R)$. Since $a \in \sqrt{\mathcal{N}(R)}$, $V_q(a) \neq QPrim(R)$, that is, $U_a \neq \emptyset$. Similarly, we get $U_b \neq \emptyset$. In addition, $U_{ab} = \emptyset$ since $ab \in \mathcal{N}(R)$. As a result, $U_a \cap U_b = U_{ab} = \emptyset$ for two non-empty open subsets U_a and U_b which means $QPrim(R)$ is not irreducible. □

There is a one-to-one correspondence between points of $QPrim(R)$ and irreducible closed subsets of $QPrim(R)$. The next theorem gives that correspondence.

Theorem 2.11 *Let Y be a subset of $QPrim(R)$. Then Y is an irreducible closed subset of $QPrim(R)$ if and only if $Y = V_q(Q)$ for some $Q \in QPrim(R)$.*

Proof. Let $Y = V_q(Q)$ for any $Q \in QPrim(R)$. Since $V_q(Q) = Cl(Q)$ and $Cl(Q)$ is irreducible, Y is an irreducible closed subset of $QPrim(R)$. Conversely, let Y be an irreducible closed subset of $QPrim(R)$. Then $Y = V_q(I)$ for some ideal I of R. Now suppose that $I \notin QPrim(R)$. Then $\sqrt{I}$ is not prime. Then there are elements $a, b \in R$ such that $ab \in I$ but $a, b \notin \sqrt{I}$. Thus, $Y = V_q(I) \subseteq V_q(ab) = V_q(a) \cup V_q(b)$. Also, $V_q(a) \neq V_q(I)$ and $V_q(b) \neq V_q(I)$ due to $a, b \notin \sqrt{I}$. Therefore, we conclude that Y is reducible, which contradicts our assumption. □

Let I be an ideal of a ring satisfying maximal condition. Then, by [5, Theorem 5], the ideal I is an intersection of a finite number of quasi-primary ideals, say $Q_1, \dots, Q_n$ with radicals $P_1, \dots, P_n$, respectively. Hence, $\sqrt{I} = \cap_{i=1}^n \sqrt{Q_i} = \cap_{i=1}^n P_i$, that is, there is no prime ideal containing I other than P_i's where $i = 1, \dots, n$. Then, for any ideal I in a ring satisfying maximal condition, every closed subset $V_q(I)$ can be written as the finite union of irreducible closed sets, that is,

$$V_q(I) = V_q(P_1) \cup \dots \cup V_q(P_n)$$

by Proposition 2.2 (iii) and (v).

Let V be a closed subset of a topological space X. Recall that a dense point of V is called a *generic point*. By the above theorem, we conclude that every irreducible closed subset of $QPrim(R)$ has a generic point.

The maximal irreducible subsets of a topological space X are called *irreducible components*.

Theorem 2.12 *Irreducible components of $QPrim(R)$ are the closed sets $V_q(Q)$ where $\sqrt{Q}$ is a minimal prime ideal of R.*

Proof. By Theorem 2.11, any irreducible closed subset of $QPrim(R)$ can be written of the form $V_q(Q)$ for some quasi-primary ideal Q of R. Assume that $V_q(Q)$ is not maximal. Then $V_q(Q) \subset V_q(Q')$ for some quasi-primary ideal Q' of R. Since $V_q(Q') = V_q(\sqrt{Q'})$ we have $\sqrt{Q'} \subset \sqrt{Q}$. Hence, $\sqrt{Q}$ is not minimal. Conversely, assume that $\sqrt{Q}$ is not a minimal prime ideal. Then there is a prime ideal P of R such that $P \subset \sqrt{Q}$. Then we get $V_q(Q) \subset V_q(P)$. Therefore, $V_q(Q)$ is not a maximal irreducible set. □

Theorem 2.13 *Let R be a ring. The following are equivalent:*
  i. $QPrim(R)$ is disconnected.
  ii. $R \cong R_2 \times R_2$ where R_1 and R_2 are nonzero rings.
  iii. R contains an idempotent.

Proof. (i)$\Longrightarrow$(ii) Assume that $QPrim(R)$ is disconnected. Then $QPrim(R) = V_q(I) \cap V_q(J)$ for some ideals I and J of R where $V_q(I) \cap V_q(J) = \emptyset$. Then we have $I + J = R$ and $I \cap J = IJ$. So, we get $R = R/I \times R/J$.
(ii) $\Longrightarrow$ (iii) Assume that $R \cong R_2 \times R_2$ where R_1 and R_2 are nonzero rings via an isomorphism ϕ. Then $\phi^{-1}(1,0)$ is a nontrivial idempotent of R.
(iii) $\Longrightarrow$ (i) Assume that $e \in R$ is an idempotent. Then $QPrim(R) = X_1 \cup X_2$ where $X_1 = \{Q \in QPrim(R): e \in \sqrt{Q}\}$ and $X_1 = \{Q \in QPrim(R): 1 - e \in \sqrt{Q}\}$. Observe that $X_1 \cap X_2 = \emptyset$. Thus, $QPrim(R)$ is disconnected. □

The *dimension* of a topological space X is the number n such that X has a chain of irreducible closed sets
$$V_1 \subset V_2 \subset \cdots \subset V_n$$
and no such chain more that n terms.

Theorem 2.14 *Let R be a Noetherian local ring. Then the dimension of $QPrim(R)$ is finite.*

Proof. Let
$$X_1 \subset X_2 \subset \cdots \subset X_n \subset \cdots$$

be a chain of irreducible subsets. This chain can be written as
$$V_q(Q_1) \subset V_q(Q_2) \subset \cdots \subset V_q(Q_n) \subset \cdots$$
where $Q_i \in QPrim(R)$. Let $P_i = \sqrt{Q_i}$ for each i. Then we have
$$\cdots \subset P_n \subset \cdots \subset P_2 \subset P_1.$$
By [7, Corollary 11.11], the dimension of R is finite. So, the above chain of prime ideals must terminate. Therefore, the dimension of $QPrim(R)$ is finite, and in fact equal to the dimension of R. □

3. A Sheaf of Rings on the Quasi-Primary Spectrum

In this section we define a sheaf of rings on the quasi-primary spectrum. Let $\phi: R \to R'$ be a ring homomorphism. For any $Q \in QPrim(R')$, it is easy to show that $f^{-1}(Q) \in QPrim(R)$. So, f induces the map
$$\phi^a: QPrim(R') \to QPrim(R)$$
which is called the *associated map* of ϕ.

For any $A \subseteq R$ we have $(\phi^a)^{-1}(V(A)) = V(\phi(A))$. So, the map ϕ^a is continuous.

Let $S \subseteq R$ be a multiplicative subset of R. Let $\phi: R \to R_S$ be the canonical homomorphism. Since $\sqrt{IR_S} = \sqrt{I}R_S$ for any ideal I of R, the map ϕ^a is an inclusion. The set $U_S = \phi^a(QPrim(R_S))$ is equal to the set of quasi-primary ideals of R whose radicals are disjoint from S. There is a one-to-one correspondence between quasi-primary ideals of R_S and quasi-primary ideals of R whose radicals are disjoint from S. So, the space $QPrim(R_S)$ is homeomorphic to the subspace U_S of $QPrim(R)$.

In particular, if $S = \{f^i: i \in \mathbb{N}\}$ then $U_S = QPrim(R) \backslash V_q(f) = U_f$. So, basis sets U_f are homeomorphic to $QPrim(R_f)$ where R_f is the localization of R with respect to the multiplicative subset $S = \{f^i: i \in \mathbb{N}\}$.

Lemma 3.1 $U_a \subseteq U_b$ *if and only if $a \in \sqrt{(b)}$ for any $a, b \in R$.*

Proof. Assume that $U_a \subseteq U_b$ for some $a, b \in R$. Then, for any $Q \in QPrim(R)$, we have $a \notin \sqrt{Q}$ implies $b \notin \sqrt{Q}$. That means $b \in \sqrt{Q}$ implies $a \in \sqrt{Q}$. Since $QPrim(R)$ contains prime ideals, this observation yields that $a \in \sqrt{(b)}$. Conversely, assume that $a \in \sqrt{(b)}$ for some $a, b \in R$. Let $q \in U_a$. Then $a \notin \sqrt{Q}$. Since a is contained in the intersection of all prime ideals that contain b, we obtain that $b \notin \sqrt{Q}$. Therefore, we have $Q \in U_b$. □

Our aim is to construct a sheaf of rings on $QPrim(R)$. We assign to each open set U_a the ring $\mathcal{F}(U_a) := R_a$, ring of quotients with respect to the multiplicative subset $\{1, a, a^2, \dots\}$, and define the restriction maps

$$res_{U_b,U_a} : R_b \to R_a, \quad r/b^m \mapsto t^m r/a^{nm}.$$

Since, by Lemma 3.1, we have $U_a \subseteq U_b$ if and only if $a^n = tb$ for some positive integer n and $t \in R$, the map res_{U_b,U_a} is well-defined.

For an arbitrary open set U of $QPrim(R)$ let

$$\mathcal{F}(U) = \varprojlim \mathcal{F}(U_a)$$

where the projective limit is taken over all $U_a \subseteq U$ relative to the system of homomorphisms res_{U_b,U_a} for $U_a \subseteq U_b$.

For $U \subseteq V$, each family $\{v_i\} \in \mathcal{F}(V)$ consisting of $v_i \in R_{a_i}$ with $U_{a_i} \subseteq V$ defines a subfamily $\{a_j\}$ consisting of the a_j for those indexes j with $U_{a_j} \subseteq U$. Then $\{v_j\} \in \mathcal{F}(U)$. Define

$$res_{V,U} : \mathcal{F}(V) \to \mathcal{F}(U), \quad \{v_i\} \mapsto \{v_j\} .$$

With this construction, $\mathcal{F}$ turns to be a sheaf of rings on $QPrim(R)$. In fact, this sheaf is the direct image sheaf under the inclusion map from $Spec(R)$ into $QPrim(R)$:

Theorem 3.2 *The sheaf $\mathcal{F}$ on $QPrim(R)$ is equal to the direct image sheaf ι_* under the inclusion map $\iota : Spec(R) \to QPrim(R)$.*

Proof. The inclusion map ι is continuous. For any open set U of $QPrim(R)$, direct image sheaf ι_* is defined as follows:

$$\iota_*(U) = \mathcal{O}(\iota^{-1}(U))$$

where $\mathcal{O}$ denotes the structure sheaf on $Spec(R)$. For $a \in R$, we have

$$
\begin{aligned}
\iota^{-1}(U_a) &= \{P \in SpecR : \iota(P) \in U_a\} \\
&= \{P \in SpecR : P \in U_a\} \\
&= \{P \in SpecR : a \notin \sqrt{P} = P\}
\end{aligned}
$$

The final set is a principal open set for $Spec(R)$ and the corresponding ring for this set is R_a. So, we get $\iota_*(U_a) = R_a = \mathcal{F}(U_a)$.

For $U_a \subseteq U_b$, we have $res_{U_b,U_a} = \rho_{X_a}^{X_b}$ where $\rho_{X_a}^{X_b}$ is the restriction map from principal open set X_b to X_a of $Spec(R)$ with respect to the structure sheaf $\mathcal{O}$. Thus, the sheafs $\mathcal{F}$ and $\iota_* \mathcal{F}$ are the same. $\square$

Similar to the structure sheaf $\mathcal{O}$ on $Spec(R)$, the stalk $\mathcal{F}_Q$ of $\mathcal{F}$ at a point $Q \in QPrim(R)$ is $R_{\sqrt{Q}}$. Therefore, we conclude that $(QPrim(R), \mathcal{F})$ is a locally ringed space.

Declaration of Ethical Standards

The authors of this article declare that the materials and methods used in this study do not require ethical committee permission and/or legal-special permission.

Conflict of Interest

The authors declare that they have no known competing financial interests or personal relationships that could have appeared to influence the work reported in this paper.

References

[1] Shafarevich I. R., 2013. Basic Algebraic Geometry 2: Schemes and Complex Manifolds, Third Edition, Springer-Verlag, Berlin.

[2] Ueno K., 1999. Algebraic Geometry 1: From Algebraic Varieties to Schemes, Translations of Mathematical Monographs, Vol. 185, American Mathematical Society.

[3] Hartshorne R., 2000. Algebraic Geometry, Springer Science+Business Media, LLC, New York.

[4] Özkirişci N. A., Kılıç Z., Koç S., 2018. A Note on Primary Spectrum over Commutative Rings, An. Stiint. Univ. Al. I. Cuza Iasi. Mat. (N.S.), **64**, pp. 111-120.

[5] Fuchs L., 1947. On Quasi-primary Ideals, Acta Sci. Math. (Szeged), **11**(3), pp. 174-183.

[6] Sharp R. Y., 2001. Steps in Commutative Algebra, Second Edition, Cambridge University Press.

[7] Atiyah M. F., MacDonald I. G., 1969. Introduction to Commutative Algebra, Addison-Wesley Publishing Company, Inc., London.
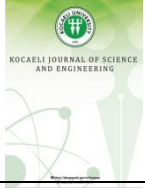
Linear Parameters Causing Landslides: A Case Study of Distance to the Road, Fault, Drainage

Seda ÇELLEK [1], * iD

[1] Department of Geology, Kırşehir Ahi Evran University, Kırşehir, 40100, Turkey, **ORCID:** 0000-0001-9675-5691

Abstract

Choosing the right parameters for the study area is a compelling process. Parameters provide different results when applied to different areas, and some of these parameters can be evaluated generally, while others reflect the characteristics and properties of the areas. A comprehensive literature study was conducted for this purpose. By conducting this study, only the studies in which the distance to the road, drainage and fault were effective in the formation of landslides were evaluated. 64 landslide areas in Turkey were selected for samplings used in the study. Literature research and case studies were compared, and the effects of the distance from the road, fault and drainage on landslides were investigated. Landslide-prone areas were determined according to the classification ranges for the parameters. The classification ranges were selected according to the literature. This study, which is different from the examples in the literature, was carried out in the form of comprehensive literature research and a comparison of analyzes.

1. Introduction

The distance to the linear parameters is an important factor in a landslide. The distance to road, fault and drainage is frequently preferred for these parameters. In the literature, while some researchers were using all 3 parameters in the same study, some researchers evaluated only 2 of them. In most studies, only one of the three was preferred.

Wang and Li [1], Kornejady et al. [2], Chen et al. [3], Hong et al. [4], Jaafari et al. [5], Panchal and Shrivastava [6], Rozos et al. [7], Kumtepe et al. [8] used all three parameters in their studies. Pourghasemi and Rossi [9] determined that landslides were reduced when moving away from drainage, roads and faults, according to expert opinion. Tanoli et al. [10], Zhang et al. [11], Kamp et al. [12], Blesius and Weirich [13], and Van Westen et al. [14] emphasized that it is very important for landslide susceptibility analysis to use distance to river and highway. According to Hong et al. [4], Poudyal et al. [15], Preuth et al. [16], and Lee and Chi [17], geological faults and roads are accepted as factors that can affect landslides. Bai et al. [18], Özdemir [19], and

Barredo et al. [20] evaluated the distance of the river and fault as a landslide susceptibility factor.

One of the factors that destroys the natural topography and affects the stability in slopes is the situation of the existing road networks [21-25]. The construction of infrastructural elements like roads is accepted as human construction activity that affects slope instability. Slopes are shears for road construction, vegetation is altered, and highway tourism increases because of the economic activity near the roads [26]. The general concept is that the horizontal and natural sections around a road are more susceptible to landslides [7]. For this reason, landslides can occur on roads and around the edges of slopes that are affected by roads [27-30]. In other words, landslides can occur in slopes where roads intersect [31]. Many researchers claim that the existence of roads in mountainous areas increases the change that landslides will form [32-38]. Because of the reasons these explanations reveal, the road proximity parameter is used in landslide susceptibility map studies [2, 39-41]. The construction of infrastructure elements like roads is accepted as human construction

activity that affects slope instability.

One of the parameters chosen in the preparation of landslide susceptibility maps is the structural elements. In particular, faults represent suitable conditions for landslides [42]. Faults create a weak line or region of heavily crushed rocks [40]. Generally, the distance or proximity to faults parameter is used. There may be a significant relationship between the landslide settlement areas' proximity to the fault [43]. Tectonic activities can play an important role in large-scale landslides [44]. Zhang et al. [11] stated that the landslide hazard is closely related to the distance from the faults. In the literature, other studies are prepared to measure the effects of the distance from the faults on landslides [45-51]. Pourghasemi and Rossi [9] defend that there is a direct relationship between the distance from the faults and the frequency of landslides. Çevik and Topal [52] stated an inverse relationship exists between the landslide distribution and the distance to the fault. In the literature, most researchers stated that landslides are frequently seen in areas in proximity to the fault [53-56], and landslide susceptibility/hazard/risk will increase in said areas [57, 58]. Likewise, landslides decrease as they move away from fault lines [9, 59-61]. Therefore, the parameter is considered one of the main causes of landslides [62] and it is recommended to use it as a parameter [63]. Çellek et al. [64] searched nearly 300 studies about landslide susceptibility and listed the most used parameters. They stated that distance to the fault is ranked 9th among the literature's top 10 most preferred parameters. This parameter was used in 120 studies. Gökçeoğlu and Aksoy [65] field observations have shown that most of the landslides occurred very close to faults in their study area. Mathew et al. [66] observed that faults are one of the most important factors affecting the stability of slopes in the study area. Thus, they selected the fault buffer as one of the independent variables. Özşahin [67] conducted a study in an area with active faults. As a result, he stated that the distance from the faults effectively affected the landslide. Likewise, Korkmaz [68] noted that the faults in the study area affect the landslide. Xu et al. [6], Regmi et al. [69] and Wang et al. [63] stated that landslides occur along the fault line in the study area, and landslides decrease sharply as they move away from them. Ahmed et al. [2014] stated that the most likely triggering factor for large rock mass move in the study areas is proximity to the fault [30].

In contrast, some studies argue that proximity to the fault isn't the main parameter in the landslide susceptibility study. Kayastha et al [71] stated that they expect landslides to occur near the faults and decrease as the distance increases. However, they found that most landslides in their area occurred more than 100 meters away from faults. In this case, they concluded that faults and folds aren't the main factors for landslides. Likewise, Zhang et al. [72] stated in

the literature that many studies had associated landslides with proximity to the fault, but the data in their study area don't reflect this.

There are more studies that argue that proximity to the fault isn't the main parameter in the landslide susceptibility study. Kayastha et al [71] stated that they expect landslides to occur near the faults and decrease as the distance increases. However, they found that the majority of landslides in their area also occurred more than 100 meters away from faults. In this particular case, they concluded that faults and folds aren't the main factors for landslides to occur. Likewise, Zhang et al. [72] stated in the literature that many studies have associated the occurrence of landslides with proximity to the fault, but the data in their study area don't reflect this.

In many parts of the world, drainage plays an important role in landslides [73, 74]. Because a soil close to the drainage may have higher water content than any other soil far from the drainage [75].

In many studies on the preparation of landslide susceptibility maps, researchers have used the proximity of the drainage as a parameter in landslide evaluations by making use of field observations [1-3, 10, 38, 49, 50, 56, 58, 76-78]. More than half of the landslides in Turkey are observed in the generation of active faults around 60 km wide [79]. This study examined landslide studies conducted in various regions of the world. Landslides that had occurred in areas near faults in Turkey have been analyzed. As a result of the study, the faults in landslide areas were selected and compared with the literature in Turkey.

The effects of proximity to the drainage on landslide susceptibility can be evaluated in two ways. Firstly, it is seen that the discontinuity surfaces on the unstable slope can't resist the pull of gravity, and the collapse facilitates ground movements [80].

Latter relates to the degree of saturation of the material on the slope. The effects of groundwater and surface water also increase with the proximity to the drainage network. The drainages can negatively affect stability by eroding the slopes or saturating the bottom of the material until the water level rises. Therefore, the proximity of drainage is an important factor in stability [3, 49, 50].

A comprehensive field survey should be conducted to determine the effects of drainage on the slope. Statistical analysis shows that a strong relationship can be observed between landslide distribution and distance to drainage [18]. However, in determining the impact on landslides, it is uncertain how to use the main drainages or tributaries that make up the drainage network, and in which distances [81].

Hasekioğulları [82] states that 37 of its studies were used as a distance to the river. The usage rate of this parameter, which is evaluated among topographic parameters and called drainage, is expressed as 72.73% in

the studies examined by Süzen and Kaya [83]. Çellek et al. [64], found that distance to drainage was the 6th most preferred parameter with 153 studies in 300 studies that they examined.

2. Effects on Parameters of Landslides

The parameter of distance to road, fault and drainage disrupts the landslide susceptibility. Parameters separately or together create this effect. The effects on landslides are investigated by using many methods and techniques. The literature for the preparation of linear parameter maps utilizes field studies, topographic maps for studied areas, prepared data sets or linear parameter maps, aerial photographs, and various satellite data from low-resolution images such as Google Earth to high-resolution images such as the multispectral LISS-4 satellite, Aster, and QuickBird. Apart from this, there are those that gather current data with road, fault, drainage networks, GPS, and navigation devices. The researchers digitized these maps using certain ArcGIS programs [66, 82].

2.1. The Effect of the Road Distance Parameter on Landslides

Based on its position on the slope, a previously or newly constructed road could cause landslides [84], but the rate of landslide decreases as the age of the road increases [85]. Road construction alters vegetation [22, 28, 57, 86]. This increases human activity with economic activity conducted in areas close to the roads [26, 87]. High slope changes the stress status and slope balance [32, 88]. It causes the application of static and dynamic loads [11, 54, 55]. The traffic frequent vibrations that vehicles cause [23, 46, 57, 64, 89, 90] trigger the fragmenting-loosening [38, 50] of rocks with bursts in an uncontrolled manner.

Road construction works and over vibration frequency generated by these works are effective in the occurrence of landslides [1-3, 9, 10] because it causes the loss of toe support based on the places where the roads pass the slope and because it would bring additional loads to the slope. On slopes that were balanced before road construction, cracks occur due to increased tension in the back of the slope after the construction [90]. Cracks that form trigger landslide events, as they are being subjected to negative effects such as water input that can come from outside [11, 58, 90]. Gravel materials on roads were designed and compressed to endure heavy loads to make surfaces flat and impermeable. During severe rainfall, they make road surfaces impermeable and provide rapid land flow and surface flow [23, 58].

Despite this, a certain section of the road can function

as a barrier, a network resource, a network pool, or a corridor for water flow [91-93]. It can indirectly cause landslides by increasing the water concentration in the slope, including saturated slopes [11, 30]. Another crucial point is the change of natural hydraulic roads that may water to concentrate in the imbalanced sections of the slope [27]. In addition to these effects, roads cause the emergence of ground waters on the surface, because the roads interrupt the continuity of the slope, and the waters are collected by road drainage systems. Since inadequately or incorrectly projected drainage facilities are unable to securely evacuate these waters with precipitation after severe rainfall, they stand out as an element that triggers landslides [94].

In the literature there are researchers who have identified landslides originating from road construction work in their study areas [95]. Tangestanı [96] reported that development activity in the Kakan region caused the increase of road density. Field observations demonstrate that the possibility increases for slides in places where roads pass by worn, excessively worn, or semicircular rock units or by loosened soil in steep slopes. Dahal [97] reported that roads constructed without taking precautions negatively affected slopes and that many landslides were identified along newly constructed roads. Abedini et al. [76] used this parameter because landslides occurred during reconstruction and road expansion in their study area. Ataol and Yeşilyurt [98] determined that many new landslides and mudslides materialized during road construction work.

Sidle [99] revealed in their study that mass movements were between 30 and 340 times greater in slopes that passed through roads than those that didn't. Piehl et al. [100], reported in a study they conducted in Oregon that landslides that occur based on roads constitute 72% of all landslides. Çellek [95] reported that many landslides occurred during the work for a newly constructed road and that the construction work triggered mass movements, even though the study area wasn't a landslide region. Demir [101] and Regmi et al. [69] reported that landslides occurred in their study area due to construction work on the road. Alexakis et al. [102] accepts the expansion of highway networks as a key factor for the separation of mudslide hazard zones.

2.1.1. The Effect of Distance to Faults with Other Parameters on Landslide

The road parameter is an anthropological factor that causes landslides. It is evaluated together with its effect on landslides, rock bursts, vibration frequency of vehicles passing by on the road, slope change, adding of load to the toe, presence of touristic activity along the road [restaurants and businesses], the change in vegetation, and the effects of precipitation and drainage water.

2.1.1.1. Relationship with Anthropology

The road parameter effect originates from human activity in the area of landslides. They increase human activity with economic activity conducted in areas close to the roads [103]. According to the research, the frequency vibrations caused by cars on highways in turn cause landslides [104]. Many researchers have reported that roads along slope imbalance in study areas are the most influential anthropogenic factor [31, 40, 57, 63, 74, 75, 92, 105-110]

2.1.1.2. Relationship with Hydrogeology

Water can become concentrated in the imbalanced sections of the slope because of change on hydraulic roads during road construction [27]. Roads cause the emergence of ground waters on the surface because the roads interrupt the continuity of the slope, and the waters are collected by road drainage systems. Since inadequately or incorrectly projected drainage facilities are unable to securely evacuate these waters with precipitation after severe rainfall, they stand out as an element that triggers the landslides [94]. Indeed, Ataol and Yeşilyurt [98] observed in the sections in which there was slope imbalance in their study area that landslides with the water satiating the ground in rainy periods. Dahal et al. [111] encountered landslides that happened due to water that was unable to drain in the roads in their study area.

2.1.1.3. Relationship with Vegetation

Transportation lines that cause destruction in vegetation have a clear influence over landslides [22, 57, 112]. Some researchers reported that deforestation performed during road work caused landslides. For example, Petley et al. [113] correlated increasing landslide activity to road construction that caused changes in land use in their study in the rugged regions of Nepal. Dahal [97] said that highway access was established after deforestation in the study area but that the deforestation caused the deterioration of the side slope stability.

2.1.1.4. Relationship with Slope

Comprehensive excavations, the implementation of static and dynamic loads, water drainage, the removal of toe support, and vegetation are some of the most common acts that occur in road network slopes during construction. These load changes are also responsible for triggering landslides [3, 22, 24, 57, 87, 109, 113, 114].

2.1.1.5. Relationship with Load Change

During road construction in areas in which there are lithological units suitable for the landslides, slopes must be made to lean further to one side, slope loads must be decreased, and barriers must be made [98]. Generally, interrupting the lower slope during the construction of roads damages the natural condition of the slope. In this manner, the slope change causes landslides [2, 40, 69]. Zeng et al. [110] reported that landslides in the Enshi region occurred at slopes whose slope changed during road construction.

2.2. Effect of Distance to Faults on Landslide

Faults weaken rock masses and soil material. This makes them more susceptible to landslides [50]. Rocks and soils are made due to breaking and unbalancing by proximity to faults. Therefore it is considered as a potential factor contributing to landslide [88]. The effect of faults to landslides can be evaluated in two ways. Firstly, it increases the probability of a landslide with energy output. Secondly, due to increasing shear resistance to occur landslides [115]. Faults have a strong effect on the strength of the rock [93]. Faults generally reduce the strength of the surrounding rock mass by shear, seismic shake and other mechanisms [40, 74, 116]. Faults generate weakness zones in rocks [117]. Faults divide the rock mass into blocks or pieces, causing joints and breaks [47, 90]. In addition, they increase pore pressure and permeability by negatively affecting the zones of discontinuity, fracture and joints preexisting in rocks. This causes deep weathering zones [62, 118, 119]. In landslide susceptibility studies, the effect of faults is related to the constitutive of fracture and discontinuities of slope [120]. By reducing the shear strength due to intensive shearing [1, 56], it speeds up the weathering process [66] and increases the fracture ratio [121]. This causes rock slides [91]. It also produces discontinuities in rocks [120]. This results in sudden breaks [90] and fragmentation [45] in the rocks. According to Ruff and Czurda [122], the bedrock close to the structural elements is tectonically under tension. So they are highly unstable. Due to the faults, the soil becomes a resistless condition that can cause landslides [112].

2.2.1. The Effect of Distance to Faults with other Parameters on Landslide

Parameters make the area more sensitive to landslides. The lithology of the area is the first parameter that should be evaluated with the distance to fault parameter. It becomes a trigger by making weak zones in the rock weaker or creating new weak zones. Water condition is another parameter that should be evaluated together with the fault.

Of course, erosion and weathering must also be evaluated. Groundwater flow varies along these planes as weathering zones are formed. Groundwater zones can change because of the fault plane. As a result weathering zones comprise. Climate condition is one of the parameters that should be evaluated with this parameter. In addition, weather conditions make the environment prepared by the fault even more insensitive, especially in heavy rains. Also, slope and elevation are parameters that can be evaluated together with the distance to fault parameter. Relatively higher slopes and higher areas are more affected by faulting.

2.2.1.1. Relationship with Lithology

It has been observed that geological parameters, distance to the fault and lithology trigger landslides together under appropriate conditions [44].

Ercanoğlu [123] states that the main reason for approaching proximity to structural elements is that lithological units may become weaker due to the high tension and deformation characteristics of being close to these elements. Proximity to the fault, in general, not only affects the surface material structures, but also contributes to the permeability of the land causing slope instability [11, 31, 62, 92, 124-126].

Conforti et al. [62] stated that in metamorphic rocks in the study areas, as the distance to the fault lines decreases, the degree of rock breakage and weathering increases and therefore the area is prone to landslides. Kritikos and Davies [116] stated that the main fault, schist-origin mylonite and cataclasite, which passed through the study areas, are eroded and cause landslides. Aghdam et al. [24] determined that igneous rocks were broken and crushed by faults in the study area.

2.2.1.2. Relationship with Hydrology

The presence of a fault increases landslide susceptibility because faults can be related to abnormal groundwater conditions [127]. Selective erosion and the movement of water along the fault planes increase the possibility of landslides [57], [89-90]. Fault planes are suitable for improving infiltration and hydrostatic pressure on slope forming material [128]. Strong weather conditions in the faulting zone provide favorable conditions for landslides to occur due to the weakness it creates in the rock structure [58]. Petley et al. [113] stated that proximity to the fault directly triggered mass movements as well as mobilizing the material with subsequent precipitation after faulting.

2.2.1.3. Relationship with Slope and Elevation

Özşahin [46] states that in areas with a high slope in the study area, the proximity parameter to the fault triggers the landslides. Ahmed et al. [70] and Daneshvar [129] stated that the fault movements increase the sensitivity more with the height of the terrain.

2.3. Effects of Distance to Drainage Parameters on Landslide

Statistical analysis shows that there is a strong relationship between landslide distribution and distance to drainage [18]. However, the issue of which distances and how to use the main drainage or tributaries that form the drainage network on landslide formation is uncertain [81]. According to the literature, the general acceptance is that as the distance from the drainage line increases, the landslide frequency gradually decreases [1, 3, 4, 9, 10, 23, 130]. In other words, closer to the drainage, landslides are more likely to happen [7, 11, 58, 131-134]. Dai and Lee [135] and Mossa et al. [136] found a linear decrease between the distance to drainage and the landslide frequency.

The presence of water has an inverse relationship with the shear strength of a substance. Since the leakage of water near the drainage network is much more than these, the shear strength decreases near the drainage network.

Because as the percentage of water increases, the shear strength of the material tends to drop by half as much with an exponential behavior. According to this fact, high accumulation of drainage channels will lead to higher water penetration and consequently reduced shear strength of the formation [22, 128].

It is effective on landslides as they destroy the toe support over time due to the erosion caused by the weathering of the slopes. It increases the possibility of landslides to occur again [22, 125].

With the increase of the proximity value to the drainage network in any area, the effects of groundwater and surface waters will increase and therefore the surface will weather, making it more susceptible to landslides [137].

It moistens the stability of the slopes by moistening the part of the material that forms the slope below the drainage level or by saturating the part up to the drainage level with water [10, 76]. With the effect of water, plasticity and liquidity limits are reached and mass movements occur. Water increases the weight by reducing the angle of balance, reducing friction against it and facilitating movements [138].

Drainage networks form valleys in areas of steep slopes and create sensitive areas for mass movements. As water passes through an area, it washes the rough material

on the surface. Besides the lateral pressure, water wants to penetrate fine-grained material. This influence can cause the entire substance to collapse as a result of the following process [22]. Hydrographic axes constantly change the slopes of the drainage and therefore can be considered as one of the main parameters in landslide manifestation [139].

There is maximum leakage along the slopes adjacent to the currents where materials have maximum permeability [140, 141]. It changes the surface geomorphology and controls the flow of water in landslide prone areas.

Due to the weathering effect of the drainage, it drags the materials from the toe point and eventually causes stepped landslides that trigger movements from the toe to the top elevation with lateral spreading [131]. Pore water pressure is affected, which affects susceptibility [30]. Timilsina et al. [44], in his works, considers the closeness to certain drainages as it applies. Because smaller drainages are less effective in large-scale landslides.

2.3.1. The Effect of Distance to Drainage with other Parameters on Landslide

Considering that landslides are frequently seen in river valleys, it is revealed that distance to drainage in the basin is an important factor along with slope and lithology in landslides [47]. Flow and area lithology affect erosion and weathering processes of drainage [142]. Groundwater exchanges surface water directly by protecting the drainage base, groundwater also provides moisture for riverside vegetation, affects surface water and controls the shear strength of slope materials, thereby affecting slope stability and erosion processes [143]. Groundwater in smaller, low-grade streams also provides most of the increased discharge during and immediately after storms [53].

2.3.1.1. Relationship with Erosion

There are landslides caused by erosion associated with drainage channels [57, 58, 62, 71, 77, 129, 133, 142]. In addition, the relationship between drainage and average erosion rate is a landslide-triggering relationship [144].

2.3.1.2. Relationship with Groundwater

The relationship between streams and groundwater is also important [22, 44, 53, 58, 77, 92]. Distance to drainage can affect the stability of the area as it affects underground flow [126]. With the increase of the proximity to the drainage network in any area, the effects of groundwater and surface waters will increase and therefore the surface will become more susceptible to landslides [137]. It also shows that groundwater tends to occur as a result of the flow of

groundwater into drainages and drainages along the edges of the valleys and, as a result, affects shearing operations [78, 145, 146]. Groundwater basically provides base flow for all drainages and has a major impact on the amount of water and the chemical composition of the drainages [53].

2.3.1.3. Relationship with Vegetation

Drainage networks often affect vegetation by providing moisture for coastal vegetation [53]. The water supplied by the networks affect plant growth. The vegetation capillarity affect the mass movements, as the water in the ground takes up and evaporates with its roots, so that the leaked water holds a soil [138]. Proximity to drainages controls its impact on landscape evolution [116].

2.3.1.4. Relationship with Lithology

A drainage system developing on a surface is controlled by the surface's slope and the underlying rocks' types and attitudes [147]. Likewise, drainage channels significantly affect bedrock incisions [70]. Kritikos and Davies [116] argue that the riverbed reacts to the cut of the bedrock and that they have observed increased landslide erosion rates as the hill slope angles approach and exceed the threshold angle. Matebie et al. [148] determined that drainage plays an important role in changing the landscape by carving different rocks and cutting volcanic rocks and limestones at a depth of 1.5 km in the study areas. Pareek et al. [142] found that the density of landslides in the study areas is higher in the river basin than in quartzites and filites, which are more susceptible to weathering and erosion.

2.3.1.5. Relationship with Seismic

Xu et al. [6] argued that the landslides that were triggered by the Wenchuan earthquake mostly occurred along the drainage lines and as these areas were more susceptible to landslides due to drainage erosion.

2.3.1.6. Relationship with Slope

The proximity of the slope to the drainage structures is an important factor for stability. Considering that landslides are frequently seen in river valleys, it can be deduced that distance to drainages in the basin is an important factor along with lithology in landslides. Currents can adversely affect stability by eroding slopes or saturating the bottom of the material until it causes the water level to rise [52, 135, 149]. Pham et al. [150] determined that landslides occur in areas with 0-40 m distance from the drainage and slope angles greater than 15 degrees.

2.3.1.6. Relationship with Climate

The drainage flow is low when there isn't rain or an inflow of melted snow. Streams immediately provide more discharge during and after rain, snow or storms. The effect of rivers on landslides increases in all of these events [53, 57, 77].

2. Materials and Methods

The classification of linear parameters is created using buffers. There are important points to be considered in classification. First of all, the action distance must be selected. It is another important issue to determine the intervals. Metric system is used in measurements of distance. Mostly, meters are preferred rather than kilometers. Distances range from 50 meters to 1 kilometer. Class numbers can also vary between 3 and 15.

The effects of the linear parameters on landslides are evaluated in two manners according to the literature. The first classification notes the density of linear parameters, and the second classification calculates the distance between the linear parameter and the landslide. The literature mostly prefers the second method, landslide distance/proximity. Kumtepe et al. [8], in their study, they made buffer zoning for 2 km for roads and 1 km for drainages.

3.1. The Classification of the Road Parameter

Conducted classifications are over creating buffer zones. It is essential that different buffer zones are created along the lines through which roads pass to determine the effect of the road on the stability of the slope. The road proximity map determines the landslide areas and percentage distributions according to the degrees of road proximity through a comparison with the landslide inventory map. In the literature, studies that use equal distance for the general area are encountered. It was seen that some researchers performed classifications based on previously conducted classifications. For example, Özşahin [46] assigned the factor of distance to the road, considering the distinction that Yalçın et al. [143] made. Kouli et al. [87] noted landslide-triggering activity and data layers in road network buffer zones in the design of landslide susceptibility maps.

Differently, some researchers applied changes to their buffer distances according to the places they passed by. For example, Ayalew and Yamagishi [105] reported on various buffer thresholds in their study. The researchers' field observations found that the frequency of landslides was highest within 40 m of roads in mountains, within 100 m of coastal highways, and within 150 m in areas in which there

are tunnels. For this reason, buffers were made at a length of 50 m along the edges of mountain roads, 100 m on coastal highways, and 150 m around tunnels. This showed that it is not possible to generalize a buffer application. Pourghasemi and Rossi [9] determined that the distance at which the effect of the road would be significantly reduced was 170 m. Despite this, some studies accept the effective distance from 40 m to 200 m [13, 105, 151].

It is necessary to randomly create different buffer thresholds within the study area. This also demonstrates the importance of field surveys for landslide susceptibility studies. Indeed, Champati Ray et al. [152] created buffer zones by conducting field studies to support the data they received from satellite images.

Researchers working in the local scale classify distances to highways in tens and hundreds of meters while mapping the typical landslide susceptibility [13, 69, 105, 111, 153, 154]. Considering the effect of roads on landslides, they create buffers around the roads [151, 155]. Kamp et al. [12] reported that 50% of landslides that occurred in their study area occurred because of building and road construction excavations.

An evaluation of the literature data sought to determine the range values and classifications used according to the selected studies. The review first sought to identify how many classification ranges researchers had identified. The percentage distribution graphs were created from the studies selected (Figure 1).

Figure 1. The percentage distributions for the buffer ranges created for the distance to the road according to the literature

When studying Figure 1, it was generally determined that researchers used 5 and 6 classification ranges. It is thought that the reason for this is that few classification ranges cannot adequately represent the area and that many classification ranges lead to confusion in calculations.

The range values used in the studies were sought to be identified. Some studies selected randomly were used for this. The range number percentage distributions were attempted to be identified (Figure 2).

It is seen from Figure 2 that the general preference in studies is 100 m ranges and that 50 m and 200 m ranges

follow that. It is thought that larger ranges remove susceptibility and that smaller ranges are not meaningful or that there are much fewer landslides that fall in the ranges.

Finally, it was studied at what kind of approximate distance landslides occur and provide the results of the selected studies. The largest distances according to the literature are greater than 1000 m. The smallest distance is between 0 and 50 m. The effect of the road on landslides varies according to its role in the study area. Some researchers encountered landslides in areas up to 300 m, while other researchers found the most landslides occurred between 40 and 80 m.

Figure 2. The percentage distribution values for the buffer ranges created for the distance to the road according to the literature

3.2. The Classification of the Fault Parameter

When using the proximity parameter for the structural features, more than one buffer zone is created by considering the different proximities. Taking this issue into consideration, many researchers have created different buffer zones. Researchers used meter and kilometer measurements in their studies. 50, 60, 100, 200, 250, 300, 500, 1000 m and 1 km are class ranges that are frequently used in the literature. Usually there are those who use equal class ranges as well as those who use unequal ranges. There are those who use different methods when determining the classification. It is available to those using previously specified class ranges.

Özşahin [67] used the classification prepared by Vahidnia et al. [156]. Dağ et al. [81] proposed a classification based on distances greater than m for sensitivity if it was determined as a result of land observations that the majority of landslides occurred in areas very close to the faults. Again, Gökçeoğlu and Aksoy [65] suggested a classification based on 0, 50, 100, 150, 200 and on distances greater than 200 m for sensitivity, as a result of area research, that the majority of landslides occurred in areas very close to faults. Rozos et al. [139], the classes of the buffer zones "1" nearest [0-50 m], "2" very close [51-100 m], "3" close [101-150 m], "4" middle far

[151- 200 m] and "5" named far [> 200 m]. Likewise, Kayastha et al. [71] created 3 classes as [<100 m] very close, [100-500 m] close, [> 500 m] far. Özşahin and Kaymaz [112] classified the area as very highly sensitive [<100], moderately sensitive [100-1000], very lowly sensitive [> 1000] according to distance.

Alexakis et al. [2014] suggested a buffer distance of 500 m and Mathew et al. [2007] suggested a buffer distance of 300 m for main faults. Alexakis et al. [102] suggested a buffer distance of 250 m and Mathew et al. [66] suggested a buffer distance of 100 m for minor faults. Ramakrishnan et al. [118] created buffers for 3 types of faults in the area consisting of major and minor faults at 100, 50 and 5 m distances.

Some other buffer ranges used according to the literature are as follows;

There are those who restrict the buffers of the faults at a certain distance as well as those who don't set an upper limit. Mathew et al. [66] limited> 2 km for main faults and <2 km for minor faults. Ramakrishnan et al. [118] limited> 1 km for main faults and <1 km for minor faults. Saha et al. [157] prepared a 0.5 km wide buffer zone to represent the area of influence of structural tectonic properties on the landslides. Kumtepe et al. [8] used 2 km buffer zoning to create distance maps for the fault and these zones constituted the basis for classification. Özdemir [19] and Sujatha et al. [140] created scans in the study areas with a distance of 500 meters. Pareek et al. [142], 158] limited the buffer to 5 km. Apart from these, there are those who use disorderly and irregular class ranges [41, 44, 45, 57, 159, 160].

In the studies examined, it was observed that the researchers used a minimum of 3 and a maximum of 15 classes. The classification varies according to the study area. Some class numbers used according to the literature are as follows; It can be seen from here that 5 and 6 classes are the most preferred. This is followed by classes 3 and 4. In the studies examined, no researchers preferred 9, 12, 13 and 14 classes (Figure 3).
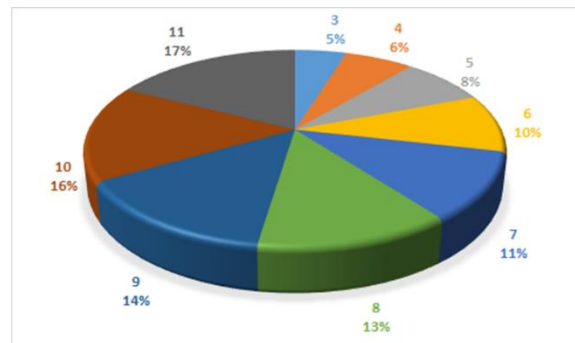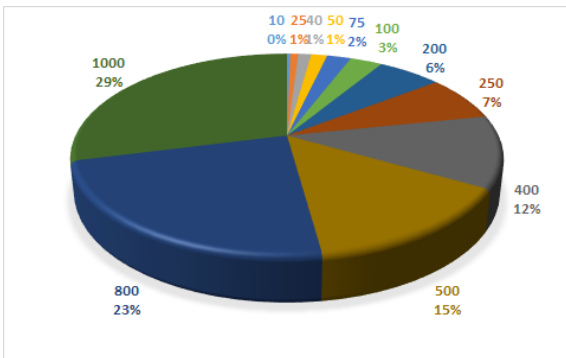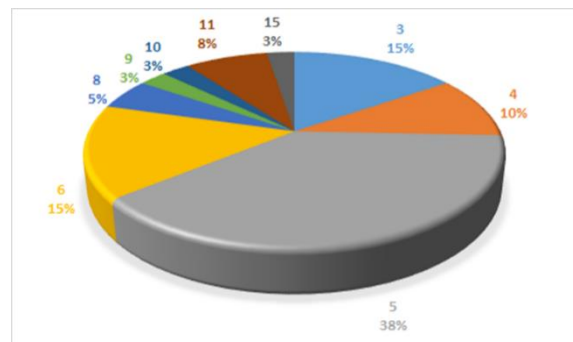

Figure 3. The percentage distributions for the buffer ranges created for the distance to the fault according to the literature

Uromeihy and Mahdavifar [161], Çevik and Topal [52], Özşahin and Kaymaz [112] stated that they expect landslides in areas below that 50 m by giving a lower limit while others no expect a landslide. Some class values that aren't observed in any landslides in the studies are as follows, Özşahin [46] encountered the lowest landslide frequency values in areas close to the fault line. The range values used in the studies were wished to be identified. Some studies selected randomly were used for this. The range number percentage distributions were attempted to be identified (Figure 4).

Figure 4. The percentage distribution values for the buffer ranges created for the distance to the fault according to the literature

It is seen from Figure 4 that the general preference in studies is 50 m ranges and that 1000 m and 100 m ranges follow that.

3.3. The Classification of the Drainage Parameter

The issue of which distances to pick and how to use the main streams or tributaries that form the drainage network on the landslide is uncertain [81]. In research, it is observed that landslides are concentrated after 150 m in general. In Akgün and Türk, [162], it is seen that more than 50% of the landslides are within 0-200 m. He et al. [163] determined that 85.99% of the landslides occurred in the study areas at 749.53 m distance from the drainage. They emphasized the high incidence of landslides in areas close to the river. Dai and Lee [135] found in their study that landslides gradually decrease as they move away from the stream.

Blesius and Weirich [13] and Dai ve Lee [135], on the other hand, determined the maximum distance as 300 m by calculating the effect of distance to the landslide with an equation. Özdemir [19] prepared a buffer showing the width of 250 m from all drainage lines. Sujatha et al. [140], Wang et al. [63], Gandhi [147] determined in their research that landslides occur within 500 meters of drainages. Aghdam et al. [24] stated that distances of more than 1000 meters have the lowest potential of landslides.

Some researchers have created a classification system and assigned values to the classification as follows; Özşahin and Kaymaz [112]; <100 m [very susceptibility], 100-250 m [highly susceptibility], 250-500 m [medium susceptibility], 500-1000 m [low susceptibility] and farther than 1000 m > [very low susceptibility]. Rozos et al. [7], [139]; nearest [0–50 m], nearest [51–100 m], near [101-150 m], middle far [151-200m] and far [200 m].

The most landslide distances in the studied areas; 0-20 m [164], 0 - 50 m [31], [71], [80], [160], [165], 0-75 [22],[62] 0-100 m [11], [38], [47], [57], [112], 0-150 m [53], [67], [166], 50-150 m [19], 0-200 m [1], [7], [147], [162], [167] 100-200 m [24], 100-250 m [59], 0-250 m [131], 0-300 m [52], 200-300 m [134], 500-1000 m [67],< 1km [124].

An evaluation of the literature data search determines the range values and classifications used according to the selected studies. The review was the first research to identify how many classification ranges researchers had identified. The percentage distribution graphs were created from the studies selected (Figure 5).
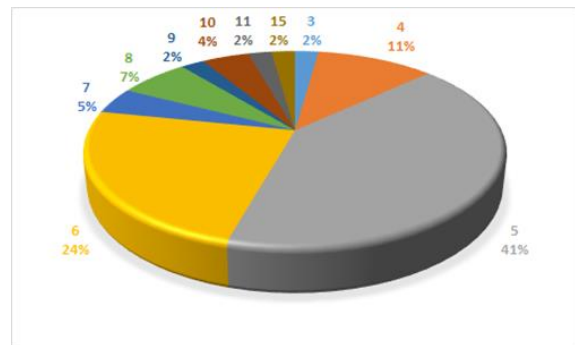
Figure 5. The percentage distributions for the buffer ranges created for the distance to the drainage according to the literature

The range values used in the studies were sought to be identified. Some studies selected randomly were used for this. The range number percentage distributions were attempted to be identified (Figure 6).
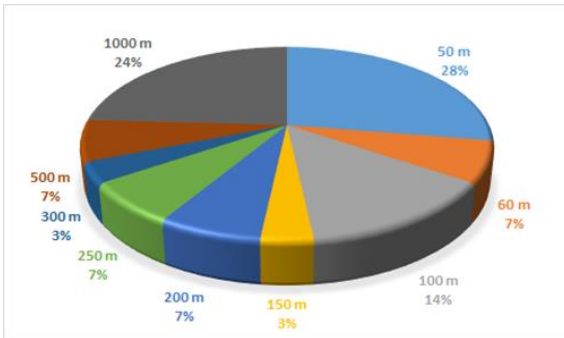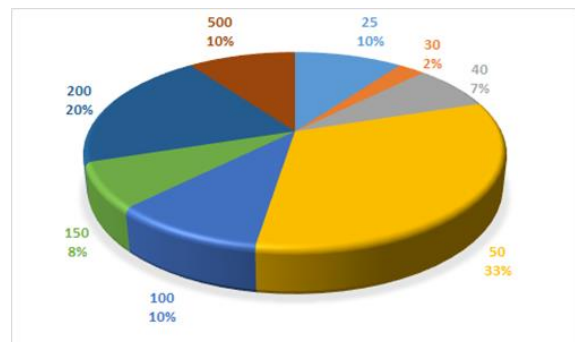

Figure 6. The percentage distribution values for the buffer ranges created for the distance to the drainage according to the literature

It is seen from Figure 6 that the general preference in studies is 50 m ranges and that 200 m and 25 m, 100 m, and 500 m ranges follow that.

4. Linear Parameters Case Study of Turkey

In this study, how the linear parameters were used in the literature, which class intervals were selected, in which class intervals landslide occurred, were determined. In that part of the chosen landslides in Turkey this study has tried to investigate the effect of these parameters. Primarily, for the study, 1: 25.000 scale landslide 64 sheets with 1: 25.000 scale were acquired from the General Directorate of Mineral Research and Exploration [MTA]. Later, road, fault and drainage maps of the areas were taken from the address of the institution "http://yerbilimler.mta.gov.tr/anasayfa.aspx". All maps are digitized. Table 1 was prepared as a result of analysis of distance to road, fault and drainage parameters.

Table 1. Areal distribution of landslides according to class ranges (m²)

Distance	Fault	Road	Drainage	Total
0-50	15	45	11	71
50-100	15	60	11	87
100-150	17	57	12	86
150-250	33	87	26	146
250-500	74	165	70	309
500-750	64	135	68	267
750-1000	63	100	67	230
1000-1500	108	136	127	370
1500-2000	98	91.83	109	299
2000>	677	289	643	1608
Total	1163	1166	1144	3473

While calculating the class values, the three parameters were accepted simultaneously. Thirty-eight maps provided this requirement. Total landslide areas according to class ranges are given in Figure 7.
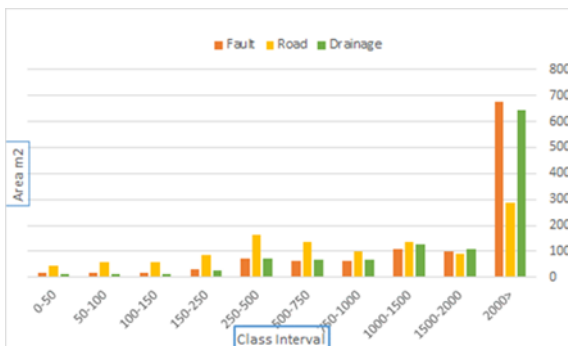
Figure 7. Class range distribution of 3 parameters according to total landslide areas

It is determined that landslides occur in areas close to the road, mostly in areas up to <1500 meters. The % percentage distribution of landslide areas by parameters is given in Figure 8.
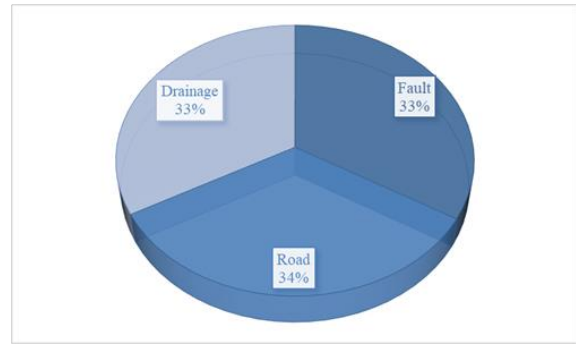
Figure 8. Distribution of landslide areas in% by parameters

Finally, the distribution of all parameters according to each class is given separately in Figure 9. Each graph was created with 50 m intervals, and the value ranges are provided in the chart titles.
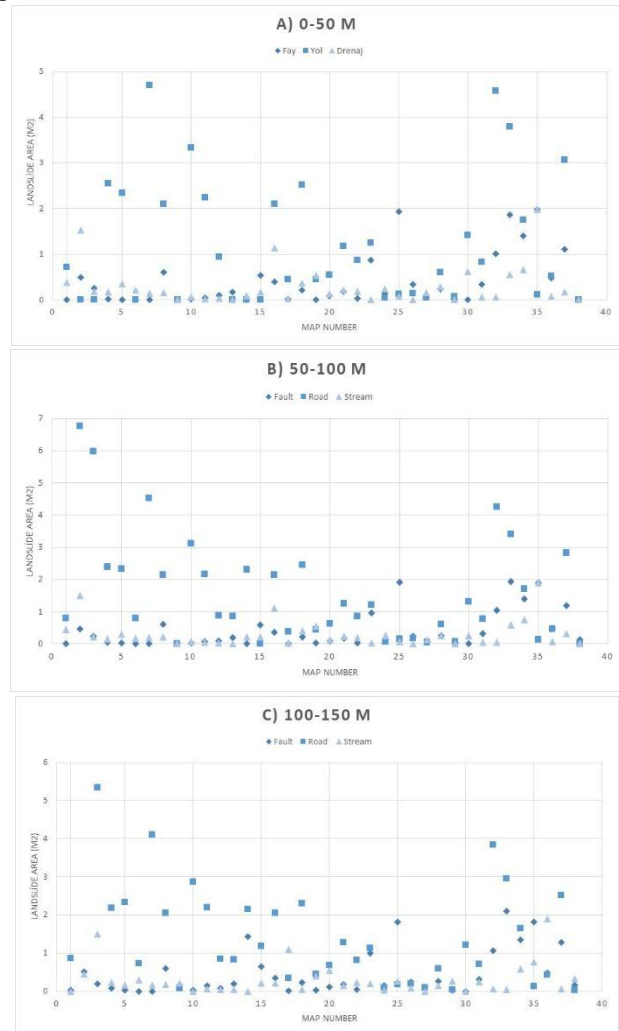
Figure 9. Landslide distribution graphs according to the class ranges of the parameters, According to the intermediate value, the variation of the distance to the road, fault and drainage in the areas according to the landslides, a) 0-50 m; b) 50-100 m, c) 100-150 m, d) 150-250 m, e) 250-500 m, f) 500-750 m, g) 750-1000 m, h) 1000-1500 m, i) 1500-2000 m, j) >2000 m

Figure 9. (Continued) Landslide distribution graphs according to the class ranges of the parameters, According to the intermediate value, the variation of the distance to the road, fault and drainage in the areas according to the landslides, a) 0-50 m; b) 50-100 m, c) 100-150 m, d) 150-250 m, e) 250-500 m, f) 500-750 m, g) 750-1000 m, h) 1000-1500 m, i) 1500-2000 m, j) >2000 m

5. Results

According to the literature, classes ranging from 3 to 15 were selected. In this study, 10 class ranges were preferred for each area. It was observed that different equal class ranges from 50 m to 1000 m [1 km] were used. Apart from that, scattered class ranges were also preferred. In this study, a scattered class range was preferred [0-50, 50-100, 100-150, 150-250, 250-500, 500-750, 750-1000, 1000-1500, 1500-2000 and> 2000 m].

As can be seen from here, the range of classes' susceptibility to one area may be unfavourable for another area. While landslide frequency values close to the fault are high for one area, it can give the lowest landslide frequency values for another area.

It was seen that positive results were obtained for certain areas. It was seen that it was useful to use the

classification range values previously used, based on the character of the study area. For example, 50 m, 100 m, 250 m, 500 m range classification, classification range value used in previous studies, was evaluated. It was seen that it was useful in half of the selected map section. This demonstrates that classification ranges must be selected through test bias in future studies. It is emphasized that field surveys are a useful method for research that cannot be conducted. When all map sections were evaluated, it was seen that more than 80% of landslides occurred in a distance of less than 2 km. It is seen that 55% of landslides occurred in a 1 km area. As a result, a limited number of studies were tested with a certain number of map sections. However, by creating options for the classification ranges and classifications that can be selected, a study was sought to provide ideas for future studies.

Out of 64 layouts, 5 of them don't have 3 parameters. There was no fault in 59, 9 in 7, road in 7 and no drainage in 9. In the study, the class ranges with the most landslides are listed as follows: <2000, 1000-1500, 250-500, 1500-2000, 500-750, 750-1000, 150-250, 50-100, 100-150, 0 -50 meters. Landslides are the most in order; the road can be seen in areas close to drainage and fault.

6. Conclusions

Landslide susceptibility studies, which have been going on for years, still continue today with the application of different methods and parameters. In the studies, performed methods are held in high importance, meanwhile parameter selection is ignored. Each field has a unique structure, and the parameters of that field should be selected accordingly. Parameter usage is not standard. should be selected according to the area. The same rule applies to subparameter class selection. This study is very different from a standard susceptibility study. Weight values are not given to the parameters; only the class ranges of the parameters are evaluated. Instead of comparing with other parameters, linear parameters are evaluated within themselves. This study shows that the selected class range is as important as the selected parameter. And this constitutes a more important issue than the method used. The distances given here also shed light on what kind of changes may occur in the studies. The point that should be evaluated before coming to the weights of the parameters is the distances of their values with class intervals. The ratio of the application of large values to small values should be considered. The distances given in this study will shed light on the future researchers who will use these parameters, and the researcher will consider the application distances of these parameters in the field.

Parameter selection is particularly important in the preparation of landslides susceptibility maps. A literature review constitutes the first step of these types of studies. While there are general classifications for almost no parameters, techniques performed previously in similar studies are implemented. This study sought to determine and implement the distance to road, fault, drainage classifications and range values used in the literature.

Therefore regarding the answer to the question "how effective is the distance to linear parameters in a landslide" these are the parameters that vary according to the study area and are very effective according to their location.

Declaration of Ethical Standards

The author of this article declares that the materials and methods used in this study do not require ethical committee permission and/or legal-special permission.

Conflict of Interest

The author declares that they have no known competing financial interests or personal relationships that could have appeared to influence the work reported in this paper.

Acknowledgements

References

[1] Dağ, S., Akgün, A., Kaya, A., Alemdağ S., Bostancı H. T., 2020. Medium scale earthflow susceptibility modelling by remote sensing and geographical information systems based multivariate statistics approach: an example from Northeastern Turkey. Environ Earth Sci., **79**, pp. 468.

[2] Kornejady A., Ownegh M., Bahremand A., 2017. Landslide susceptibility assessment using maximum entropy model with two different data sampling methods. Catena, **152**, pp. 144–162.

[3] Chen W., Pourghasemi H. R., Kornejady A., Zhang N., 2017. Landslide spatial modeling: Introducing new ensembles of ANN, MaxEnt, and SVM machine learning techniques". Geoderma, **305**, pp. 314–327.

[4] Hong H., Naghibi S. A., Pourghasemi, H. R., Pradhan, B., 2016. GIS-based landslide spatial modeling in Ganzhou city, China. Arab J Geosci., **9**, pp. 1-26.

[5] Jaafari A, Najafi A, Rezaeian J, Sattarian A., 2015. Modeling erosion and sediment delivery from unpaved roads in the north mountainous forest of Iran. International Journal on Geomathematics, **6,** pp. 343

[6] Pancha S, Shrivastava A. Kr., 2022. Landslide hazard assessment using analytic hierarchy process (AHP): A case study of National Highway 5 in India. Ain Shams Engineering Journal, **13**, pp. 101626.

[7] Xu C., Xu X. W., 2012. Spatial prediction models for seismic landslides based on support vector machine and varied kernel functions: A case study of the 14 April 2010 Yushu earthquake in China. Chin J Geophys, pp. 666–679.

[8] Rozos D., Bathrellos G. D., Skilodimou H. D., 2010. Landslide susceptibility mapping of the northeastern part of Achaia Prefecture using Analytical Hierarchical Process and GIS techniques. Paper presented at the Proceeding of the12th International Congress, Patras, Greece, XLIII May, **3**, pp. 1637-1646.

[9] Kumtepe P., Nurlu Y, Cengiz T., Sütçü E., 2009. Bolu çevresinin heyelan duyarlılık analizi [Bildiri]. TMMOB Coğrafi Bilgi Sistemleri Kongresi, 02-06 Kasım, İzmir: TMMOB Yayınları, pp 1-8.

[10] Pourghasemi H. R., Rossi M., 2017. Landslide susceptibility modeling in a landslide prone area in Mazandarn Province, north of Iran: A comparison between GLM, GAM, MARS, and M-AHP methods. Theor Appl Climatol, **130**, pp. 609–633.

[11] Tanoli J. I., Ningsheng C, Regmi A. D., Jun L., 2017. Spatial distribution analysis and susceptibility mapping of landslides triggered before and after Mw7.8 Gorkha earthquake along Upper Bhote Koshi, Nepal. Arabian Journal of Geosciences, **10**, pp. 13.

[12] Zhang J. Q., Liu R. K., Deng W., Khanal N. R., Gurung D. R., Sri Ramachandra Murthy M., Wahid S. 2016. Characteristics of landslide in Koshi River Basin, Central Himalaya. Journal of Mountain Science, pp. 1711–1722.

[13] Kamp U., Growley B. J., Khattak G. A., Owen L. A. 2008. GIS-based landslide susceptibility mapping for the 2005 Kashmir earthquake region. Geomorphology, **101**, pp. 631–642.

[14] Blesius L., Weirich F. 2010. Shallow landslide susceptibility mapping using stereo air photos and thematic maps. Cartography and Geographic Information Science, **37**.

[15] Van Westen C. J., Rengers N., Soeters R., 2003. Use of geomorphological information in indirect landslide susceptibility assessment. Natural Hazards, **30**, pp. 399-419.

[16] Poudyal C. P., Chang C., Oh H. J., Lee S. 2010. Landslide susceptibility maps comparing frequency ratio and artificial neural networks: A case study from the Nepal Himalaya. Environmental Earth Sciences, **61** pp. 1049-1064.

[17] Preuth T., Glade T., Demoulin A., 2010. Stability analysis of a human-influenced landslide in eastern Belgium. Geomorphology, **120**, pp. 38-47.

[18] Lee Y. F., Chi Y. Y., 2011. Rainfall-induced landslide risk at Lushan, Taiwan. Engineering Geology, **123**, pp. 113-121.

[19] Bai S. B., Wang J., Thiebes B., Cheng C., Chang Z. Y. 2014. Susceptibility assessments of the Wenchuan earthquake-triggered landslides in Longnan using logistic regression. Environmental Earth Sciences, pp. 731–743.

[20] Özdemir A., 2009. Landslide susceptibility mapping of vicinity of Yaka Landslide [Gelendost, Turkey] using conditional probability approach in GIS. Environ Geol., **57**, pp. 1675–1686

[21] Barredo J. I., Hervas J., Lomoschitz A., Benavides A., Van W. C. 2000. Landslide hazard assessment using GIS and multi-criteria evaluation techniques in the Tirajana Basin, Gran Canaria Island. 5th EC GIS Workshop.

[22] Kavzoğlu T., Şahin E. K., Çölkesen İ. 2014. Factor Selection based on Chi-Square Test in Landslide Sensitivity Analysis. V. Remote Sensing and Geographical Information Systems Symposium [UZAL-GIS], 14-17 Oct., İstanbul.

[23] Saadatkhahi N., Kassimi A., Lee M. L., 2014. Qualitative and quantitative landslide susceptibility assessments in Hulu Kelang area, Malaysia. EJGE, **19**, pp. 545-563.

[24] Dragicevi C. S., Lai, T., Balram S., 2015. GIS-based multicriteria evaluation with multiscale analysis to characterize urban landslide susceptibility in data-scarce environment. Habitat International, pp.114–125.

[25] Aghdam I. N., Varzandeh M. H. M., Pradhan B., 2016. Landslide susceptibility mapping using an Ensemble Statistical İndex [Wi] and adaptive Neuro-Fuzzy İnference System [ANFIS] Model at Alborz Mountains [Iran]. Environ Earth Sci., **75**, pp. 1-20.

[26] Stanley T., Kirschbaum D. K., 2017. A heuristic approach to global landslide susceptibility mapping. Natural Hazards, **87**, pp. 145, 164.

[27] Yılmaz Ç., Topal T., Süzen M. L., 2012. GIS-based landslide susceptibility mapping using bivariate statistical analysis in Devrek [Zonguldak-Turkey]. Environmental Earth Sciences, **65**, pp. 2161-2178,

[28] Alemdağ S., Kaya A., Karadağ, M., Gurocak, Z., Bulut, F. (2015). Utilization of the limit equilibrium and finite element methods for the stability analysis of the slope debris An example of the Kalebasi District NE Turkey. Journal of African Earth Sciences, **106**, pp. 134-146.

[29] Akıncı H., Kılıçoğlu C., 2015. Production of landslide susceptibility map of Atakum [Samsun] district. MÜHJEO'2015: National Engineering Geology Symposium, 3-5 September, Trabzon.

[30] Kaya A., Alemdağ S., Dağ S., Gürocak Z. 2016. Stability assessment of high steep cut slope debris on a landslide Gumushane NE Turkey. Bulletin of Engineering Geology and the Environment, **75**, pp. 89-99.

[31] Meinhardt M., Fink M., Tünschel H., 2015. Landslide susceptibility analysis in central Vietnam based on an incomplete landslide inventory: Comparison of a new method to calculate weighting factors by means of bivariate statistics. Geomorphology, **234**, pp. 80-97.

[32] Tazik E., Jahantab Z., Bakhtiari M., Rezae A., Alavipanah S. K., 2014. Landslide susceptibility mapping by combining the three methods Fuzzy Logic, Frequency Ratio and Analytical Hierarchy Process in Dozain Basin. International Conference on Geospatial Information Research [GI Research]. pp 15-17 November, Tehran, Iran.

[33] Pourghasemi H. R., Pradhan B., Gökçeoğlu C. 2012. Remote sensing data derived parameters and its use in landslide susceptibility assessment using Shannon's entropy and GIS. AEROTECH IV, Appl Mech Mater, **225**, pp. 486–491.

[34] Mashari S., Solaimani K., Omidvar E., 2012. Landslide susceptibility mapping using multiple regression and GIS tools in Tajan Basin, north of Iran. Environment and Natural Resources Research, **2**, pp. 43-51.

[35] Mohammady M., Pourghasem H. R., Pradhan B. 2012. Landslide susceptibility mapping at Golestan Province Iran: A comparison between frequency ratio, Dempster-Shafer, andweights of evidence models. J Asian Earth Sci., 61, 221.

[36] Pourghasemi H. R., Moradi H. R., Aghda S. F., 2013. Landslide susceptibility mapping by binary logistic regression, analytical hierarchy process, and statistical index models and assessment of their performances. Nat Hazards, **69**, pp. 749–779.

[37] Feizizadeh B., Blaschke T., Nazmfar H., 2014. GIS-based ordered weighted averaging and Dempster-Shafer methods for landslide susceptibility mapping in the Urmia Lake Basin, Iran. International Journal of Digital Earth, **7**, pp. 688-708.

[38] Jebur M. N., Pradhan B., Tehrany M. S. 2015. Manifestation of LiDAR derived parameters in spatial prediction of landslides using a novel ensemble evidential belief functions and support vector machine models in GIS. IEEE J Sel Top Appl Earth Obs Remote Sens., **8**, pp. 674-689.

[39] Pawluszek K., Borkowski A., 2017. Impact of DEM-derived factors and analytical hierarchy process on landslide susceptibility mapping in the region of Rożnów Lake, Poland. Natural Hazards, **86**, pp. 919–952.

[40] Dehnavi A., Aghdam I. N., Pradhan B., Varzandeh M. H. M., 2015. A new hybrid model using step-wise weight assessment ratio analysis [SWARA] technique and adaptive neuro-fuzzy ınference system [ANFIS] for regional landslide hazard assessment in Iran. Catena, **135**, pp. 122–148.

[41] Chen W., Wang J., Xie X., Hong H., Trung Van N., Bui D. T., Wang G., Li X., 2016. Spatial prediction of landslide susceptibility using integrated frequency ratio with entropy and support vector machines by different kernel functions. Environ, Earth Sci., **75**, pp. 1344.

[42] Sangchini E. K., Emami S. N., Tahmasebipour N., Pourghasemi H. R., Naghibi S. A., Arami S. A., Pradhan B., 2016. Assessment and comparison of combined bivariate and AHP models with logistic regression for landslide susceptibility mapping in the Chaharmahal-e-Bakhtiari Province, Iran. Arabian Journal of Geosciences, **9**, pp. 201.

[43] Wang J.-J., Liang Y., Zhang H.-P., Wu Y., Lin X., 2014. A loess landslide induced by excavation and rainfall. Landslides, **11**, pp. 141-152.

[44] Gökçe O., Özden Ş., Demir A., 2008. Spatial and Statistical Distribution of Disasters in Turkey Inventory of Disaster Information. Ministr of Public Works and Settlement General Directorate of Disaster Affairs, Department of Disaster Survey and Damage Assessment, Ankara [In Turkish].

[45] Timilsina M., Bhandary N. P., Dahal R. K., Yatabe R., 2014. Distribution probability of large-scale landslides in central Nepal. **226**, pp. 236-248.

[46] Avcı V., Günek H., 2014. The distribution of active landslides in Karlıova Basin and surrounding [Bingöl] according to lithology, elevation, slope, inspection and NDVI Parts. International Journal of Social Science, pp. 445-464.

[47] Özşahin E., 2015. Landslide susceptibility analysis by geographical information systems: the case of Ganos Mount [Tekirdağ] [in Turkish]. Electronic Journal of Map Technologies, **7**, pp. 47-63.

[48] Avcı V., 2016a. Analysis of landslide succeptibility of Manav Stream Basin [Bingöl], The Journal of International Social Research., **9**, pp. 42-9.

[49] Laldintluanga Er H., Lalbiakmawia F., Lalbiaknungi Er R., 2016. Landslide hazard zonation along state highway between Aizawl City and Aibawk Town, Mizoram, India Using Geospatial Techniques. International Journal of Engineering Sciences and Research Technology, **5**.

[50] Correa-Muñoz N. A., Higidio-Castro J. F., 2017. Determination of landslide susceptibility in linear infrastructure. Case: Aqueduct network in Palacé, Popayan [Colombia]. Ingeniería e Invest, **37**, pp. 17–24.

[51] Pham B. T., Bui D. T., Prakash I., Dholakia M. B., 2017. Hybrid integration of multilayer perceptron neural networks and machine learning ensembles for landslide susceptibility assessment at Himalayan area [India] using GIS. Catena, **149**, pp. 52–63.

[52] Sarkar S., Kanungo D. P., 2017. GIS Application in Landslide Susceptibility Mapping of Indian Himalayas, GIS. Landslide, pp. 211-219.

[53] Çevik E., Topal T., 2003. GIS-based landslide susceptibility mapping for a problematic segment of the natural gas pipeline, Hendek [Turkey]. Environmental Geology, pp. 949-962.

[54] Moradi S., Rezaei M. A. 2014. GIS-based comparative study of the analytic hierarchy process, bivariate statistics and frequency ratio methods for landslide susceptibility mapping in part of the Tehran metropolis, Iran. J Geope., **4**, pp. 45-61.

[55] Meng X., Pei X., Liu Q., Zhang X., Hu Y., 2016. GIS-based environmental assessment from three aspects of geology, ecology and society along the road from Dujiangyan to Wenchuan. Mt. Res., **34**, pp. 110–120.

[56] Komac M., 2006. A landslide susceptibility model using the analytical hierarchy process method and multivariate statistics in perialpine Slovenia. Geomorphology, **74**, pp. 17-28.

[57] Achour Y., Boumezbeur A., Hadji R., Chouabbi A., Cavaleiro V., Bendaoud E. A., 2017. Landslide susceptibility mapping using analytic hierarchy process and information value methods along a highway road section in Constantine, Algeria. Arabian J. Geosci., **10** pp. 194.

[58] Bourenane H., Bouhadad Y., Guettouche M. S., Braham M., 2015. "GIS-based landslide susceptibility zonation using bivariate statistical and expert approaches in the city of Constantine [Northeast Algeria]". Bulletin of Engineering Geology and the Environment, **74**, pp. 337-355.

[59] Dou J., Yamagishi H., Xu Y., Zhu Z., Yunus A. P., 2017. Characteristics of the torrential rainfall-ınduced shallow landslides by typhoon bilis, in July 2006, using remote sensing and GIS". In book: GIS Landslide Publisher: Springer Japan.

[60] Avcı V., 2016b. Analysis of landslide succeptibility of Manav Stream Basin [Bingöl]. The Journal of International Social Research, **9**, pp. 42-9.

[61] Avcı V., 2016c. Landslide susceptibility analysis of Esence Stream Basin [Bingöl] by weight- of- evidence method. International Journal of Social Science, **44**, pp. 287-310.

[62] Simon N. de Róiste M., Crozier M., Rafek A. G., 2017. Representing Landslides as Polygon [Areal] or Points? How Different Data Types Influence the Accuracy of Landslide Susceptibility Maps. Sains Malaysiana, pp. 27-34.

[63] Conforti M., Pascale S., Robustelli G., Sdao F., 2014. Evaluation of prediction capability of the artificial neural networks for mapping landslide susceptibility in the Turbolo River catchment [northern Calabria Italy]. Catena, pp. 236-250.

[64] Wang H. Q., He J., Liu Y., Sun S., 2016. Application of analytic hierarchy process model for landslide susceptibility mapping in the Gangu County, Gansu Province, China. Environ Earth Sci., **75**, pp. 422.

[65] Çellek S., Bulut F., Ersoy H., 2015. Utilization and Application of AHP Method in Landslide Susceptibility Mapping Production [Sinop and its Surroundings]. Journal of Geological Engineering, **39** pp. 59-90.

[66] Bostanci H. T., Alemdağ, S., Gürocak Z., Gökçeoğlu 2018. Combination of discontinuity characteristics and GIS for regional assessment of natural rock slopes in a mountainous area (NE Turkey). Catena, **165**, pp. 487-502.

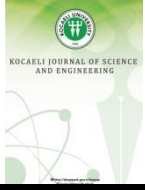[67] Mathew J., Jha V. K., Rawat G. S. 2007. Weights of evidence modelling for landslide hazard zonation

mapping in part of Bhagirathi valley, Uttarakhand. Current science, **92**, pp. 628-638.

[68] Özşahin E., 2014. The mass movement vulnerability evaluation of Antakya [Hatay] city through Geographic Information Systems [GIS] and Analytic Hierarchy Process [AHP]. Ege Coğrafya Dergisi, **23**, pp. 19-35.

[69] Korkmaz H., 2006. Antakya'da zemin özellikleri ve deprem etkisi arasındaki ilişki. Ankara Üniversitesi, Türkiye Coğrafya Araştırma ve Uygulama Merkezi, Coğrafi Bilimler Dergisi, **4**, pp. 47- 63.

[70] Regmi N. R., Giardino J. R., McDonald E. V., Vitek J.D., 2014. A comparison of logistic regression-based models of susceptibility to landslides in western Colorado, USA. Landslides, **11**, pp. 247-262.

[71] Ahmed M.F., Androgersj D., 2014. Creating reliable, first-approximation landslide inventory maps using ASTERDEM data and geomorphic indicators, an example from theupper Indus River in northern Pakistan. Environmental Engi-neering Geoscience, **20**, pp. 67–83.

[72] Kayastha P., Bijukchhen S.M., Dhital M.R., De Smedt F., 2013. GIS based landslide susceptibility mapping using a fuzzy logic approach: A case study from Ghurmi-Dhad Khola area, Eastern Nepal. Journal of the Geological Society of India, **82**, pp. 249–261.

[73] Zhang M.S., Dong Y., Sun P.P., 2012. Impact of reservoir impoundment-caused groundwater level changes on regional slope stability: A case study in the Loess Plateau of Western China. Environ Earth Sci., pp. 1715–1725.

[74] Pareek N., Pal S., Sharma M.L., Arora M., K., 2013. Study of effect of seismic displacements on landslide susceptibility zonation [LSZ] in Garhwal Himalayan region of India using GIS and remote sensing techniques. Computers & Geosciences, **61**, pp. 50-63.

[75] Wu Y., Li W., Liu P., Bai H., Wang Q., He J., Liu Y., Sun S., 2016. Application of analytic hierarchy process model for landslide susceptibility mapping in the Gangu County, Gansu Province, China. Environ Earth Sci, **75**, pp. 422.

[76] Wan S., 2013. Entropy-based particle swarm optimization with clustering analysis on landslide susceptibility mapping. Environmental Earth Sciences, **68**, pp. 1349-1366.

[77] Abedini M., Ghasemyan B., Mogaddam M.H. 2017. Landslide susceptibility mapping in Bijar City, Kurdistan Province, Iran: A comparative study by logistic regression and AHP models. Environ Earth Sci., **76**, pp. 308.

[78] Acharya S., Pathak D., 2017. Landslide hazard assessment between Besi Sahar and Tal area in Marsyangdi River Basin, West Nepal". Int. Journal of Advances in Remote Sensing and GIS, **5**, pp. 29-38.

[79] Raja N.B., Çiçek I., Türkoğlu N., Aydin O., Kawasaki A., 2017. Landslide susceptibility mapping of the Sera River Basin using logistic regression model. Natural Hazards, **85**, pp. 1323-1346.

[80] Çan T., Duman T.Y., Olgun Ş., Çörekçioğlu Ş., Gülmez-Karakaya F., Elmacı H., Hamzaçebi S., Emre Ö., 2013. Türkiye Heyelan Veri Tabanı. TMMOB Coğrafi Bilgi Sistemleri Kongresi, 11-13 Kasım, Ankara.

[81] Dağ S., Bulut F., 2012. Preparation of GIS-based landslide susceptibility maps: Çayeli [Rize, NE Türkey]. Journal of Geological Engineering, pp. 35-62.

[82] Gurocak, Z., Alemdag, S., Bostanci, H.T. and Gokceoglu, C. (2017). Discontinuity controlled slope failure zoning for a granitoid complex: A fuzzy approach. Rock Mechanics and Engineering, **5**, pp. 1–25.

[83] Hasekioğulları G.D., 2011. Assessment of parameter effects in producing landslide susceptibility maps. Master Thesis [in Turkish], Hacettepe University, Turkey.

[84] Süzen M.L., Kaya B.Ş., 2011. Evaluation of environmental parameters in logistic regression models for landslide susceptibility mapping. Int J Digit Earth, **5**, pp. 1–18.

[85] Harr R.D., Nichols R., 1993. A Stabilizing Forest Roads to Help Restore Fish Habitats: A Northwest Washington Example. Environmental Science, **18**.

[86] Fransen P.J., Phillips B., Chris J., Fahey Barry D., 200. Forest road erosion in New Zealand: overview. Earth Surface Processes and Landforms, **1**.

[87] Ekinci D., 2014. Zonguldak-Hisarönü Arasındaki Karadeniz Akaçlama Havzasının Kütle Hareketleri Duyarlılık Analizi. Titiz Yayınları, İstanbul.

[88] Kouli M., Loupasakis C., Soupios P., Rozos D., Vallianatos F., 2014. Landslide susceptibility mapping by comparing the WLC and WofE mutli-criteria methods in the West Crete Island, Greece. Environ Earth Sci., **72**, pp. 1-25.

[89] Che V.B., Kervyn M., Suh C.E., Fontijn K., Ernst G.G.J., del Marmol M.A., Trefois P., Jacobs P., 2012. Landslide susceptibility assessment in Limbe [SW

Cameroon]: A field calibrated seed cell and information value method. Catena, **92**, 83-98.

[90] Guri P.K., Champati ray P.K., Patel R.C., 2015. Spatial prediction of landslide susceptibility in parts of Garhwal Himalaya, India, using the weight of evidence modelling. Environmental Monitoring and Assessment, **187**, pp. 324.

[91] Youssef A.M., Al-Kathery M., Pradhan B., 2015. Landslide susceptibility mapping at Al-Hasher Area, Jizan [Saudi Arabia] using GIS-based frequency ratio and index of entropy models. Geosci J., **19**, pp. 113–134.

[92] Devkota K.C., Regmi A.D., Pourghasemi H.R., Yoshida K., Pradhan B., Ryu I.C., 2013. Landslide susceptibility mapping using certainty factor, index of entropy and logistic regression models in GIS and their comparison at Mugling–Narayanghat road section in Nepal Himalaya. Nat. Hazards., **65**, pp. 135-165.

[93] Tsangaratos P., Benardos A., 2014. Estimating landslide susceptibility through A artificial neural network classifier. Natural Hazards, **74**, pp. 3.

[94] Liu C-N., Wu C-C. 2007. Mapping susceptibility of rainfall-triggered shallow landslides using a probabilistic approach. Environmental Geology, **55**, pp. 907-915.

[95] Çellek S., 2013. Landslide susceptibility analysis of Sinop-Gerze region. Doctora Thesis [in Turkish], KTU, Turkey.

[96] Tangestani M.H., 2004. Landslide susceptibility mapping using the fuzzy gamma approach in a GIS, Kakan catchment area, southwest Iran. Australian Journal of Earth Sciences, **51**, pp. 439–450.

[97] Dahal R.K., 2014. Regional-scale landslide activity and landslide susceptibility zonation in the Nepal Himalaya. Environmental Earth Sciences, **71**, pp. 5145-5164.

[98] Ataol M., Yeşilyurt S., 2014. Identification of landslide risk zones along the Çankırı-Ankara [between Akyurt and Çankırı] state road. Journal of Geography, **29**, pp. 51-69.

[99] Sidle R.C., 1985. Influence of Forest Harvesting Activities on Debris Avalanches and Flows. Debris-flow Hazards and Related Phenomena, book.

[100] Piehl B.T., Beschta R.L. Pyles M.R., 1988 .Ditch-relief culverts and low-volume forest roads in the Oregon Coast Range. Northwest Sci., **62**, pp. 91-98.

[101] Demir G., 2011. GIS based landslide susceptibility analysis of an area [Niksar-Suşehri] on North Anatolian fault zone. Karadeniz Teknik Üniversitesi, Doctorate Thesis, Trabzon, Turkey.

[102] Alexakis D.D., Agapiou A., Tzouvaras M., Themistocleous K., Neocleous K., Michaelides S., Hadjimitsis D.G., 2014. Integrated use of GIS and remote sensing for monitoring landslides in transportation pavements: the case study of Paphos area in Cyprus. Natural Hazards, **72**, pp. 119-141.

[103] Alemdağ S., Akgun A., Kaya A., Candan G., 2014. A large and rapid planar failure causes mechanism and consequences Mordut Gumushane Turkey. Arabian Journal of Geosciences, **7**, pp. 1205-1221.

[104] Mittal S.K., Singh M., Kapur P., Sharma B.K., Shamshi M.A., 2008. Design and development of instrument network for landslide monitoring, an issue an early warning. Journal of Scientific &Industrial research, **67**, pp. 361-365.

[105] Ayalew L., Yamagishi H., 2005. The application of GIS-based logistic regression for landslide susceptibility mapping in the Kakuda-Yahiko Mountains, Central Japan. Geomorphology, **65**, pp. 15-31.

[106] Pradhan B., 2010a. Landslide susceptibility mapping of a catchment area using frequency ratio, fuzzy logic and multivariate logistic regression approaches. J Ind Soc Rem Sens, **38**, pp. 301-320.

[107] Pradhan B., 2010b. Remote sensing and GIS based landslide hazard analysis and cross validation using multivariate logistic regression model on three test areas in Malaysia. Advncs Space Res, **45**, pp. 1244-1256.

[108] Demir G., Aytekin M., Akgün A., İkizler S.B., Tatar O., 2013. A comparison of landslide susceptibility mapping of the eastern part of the North Anatolian Fault Zone [Turkey] by likelihood-frequency ratio and analytic hierarchy process methods. Natural Hazards, **65**, pp. 1481-1506.

[109] Jacobs L., Dewitte O., Poesen J., Maes J., Mertens K., Sekajugo J., Kervyn M., 2017. Landslide characteristics and spatial distribution in the Rwenzori Mountains, Uganda. Journal of African Earth Sciences, **134**, pp. 917-930.

[110] Zeng B., Xiang W., Rohn J., Ehret D., Chen X. 2017. Assessment of shallow landslide susceptibility using an artificial neural network in Enshi region, China. Nat. Hazards Earth Syst. Sci., Discuss, **176**.

[111] Dahal R.K., Hasegawa S., Nonomura A., Yamanaka M., Dhakal S., Paudyal P., 2008. Predictive modeling of rainfall-induced landslide hazard in the Lesser

Himalaya of Nepal based on weights-of-evidence. Geomorphology, **102**, pp. 496–510.

[112] Özşahin E., Kaymaz Ç.K., 2013. Landslide susceptibility analysis of Camili [Macahel] Biosphere Reserve Area [Artvin, NE Turkey]. Turkish Studies - International Periodical For The Languages, Literature and History of Turkish or Turkic, Turkey, **8**, pp. 471-493.

[113] Petley D.N., Hearn G.J., Hart A., Rosser N.J., Dunning S.A., Oven K., Mitchell W.A., 2007. Trends in landslide occurrence in Nepal. Natural Hazards, **43**, 23-44.

[114] Kuşku İ, Dalgıç S., 2020. Modeling of support system for preventing retrogressive slide of Ambarlı landslide in Avcılar district, Istanbul. Pamukkale Univ Muh Bilim Derg, **26**, pp. 1401-1407.

[115] Mirsanei R., Mahdifar M., 2006. Methods and optimal criteria for preparing Landslide hazard zonation maps, Center for Natural Disasters, Iran. Conference Paper.

[116] Kritikos T., Davies T., 2014. Assessment of rainfall-generated shallow landslide/debris-flow susceptibility and runout using a GIS-based approach: Application to western Southern Alps of New Zealand. Landslides, **12**, pp. 1051–1075.

[117] Saponaro A., Pilz M., Wieland M., Bindi D., Moldobekov B., Parolai B., 2015. Landslide susceptibility analysis in data-scarce regions: The case of Kyrgyzstan. Bulletin of Engineering Geology and the Environment, **74**, pp. 1117–1136.

[118] Ramakrishnan D., Singh T.N., Verma A.K., Gulati A., Tiwari K.C., 2013. Soft computing and GIS for landslide susceptibility assessment in Tawaghat area, Kumaon Himalaya, India. Natural Hazards, **65**, pp. 315–330.

[119] Chen C.W., Saito H., Oguchi T., 2015. Rainfall intensity–duration conditions for mass movements in Taiwan, Progress in. Earth and Planetary Science, **2**, pp. 1–13.

[120] Li C., Xu W., Wu J., Gao M., 2016. Using new models to assess probabilistic seismic hazard of the North–South Seismic Zone in China. Nat Hazards, **82** pp. 659–681.

[121] Hessami K., Jamali F., 2006. Explanatory notes to the map of major active faults of Iran. JSeismol Earthq Eng., **8**, pp. 1–11.

[122] Ruff M., Czurda K., 2008. Landslide susceptibility analysis with a heuristic approach in the Eastern Alps

(Vorarlberg, Austria). Geomorphology, **94**, pp. 314-324.

[123] Ercanoğlu M., 2005. Landslide susceptibility assessment of SE Bartin (West Black Sea region, Turkey) by artificial neural networks. Natural Hazards Earth System Science, pp. 979–992.

[124] Roodposhti M.S., Rahimi S., Beglou M.J., 2014. PROMETHEE II and fuzzy AHP: an enhanced GIS-based landslide susceptibility mapping. Nat. Hazards, **73**, pp. 77–95.

[125] Sadr M.P., Abbas M., Bashir S.S., 2014. Landslide susceptibility mapping of Komroud sub-basin using fuzzy logic approach. Geodyn Res Int Bull., **2**, pp. 14–27.

[126] Ilia, Tsangaratos P., 2016. Applying weight of evidence method and sensitivity analysis to produce a landslide susceptibility map. Landslides, pp. 379–397.

[127] Kayastha P., Dhital M.R. De Smedt F., 2012. Landslide susceptibility mapping using the weight of evidence method in the Tinau watershed, Nepal. Natural Hazards, **63**.

[128] Rajakumar P., Sanjeevi S., Jayaseelan S., Isakkipandian G., Edwin M., Balaji P., Ehanthalingam G., 2007. Landslide susceptibility mapping in a hilly terrain using remote sensing and GIS. Journal of the Indian Society of Remote Sensing, **35**, pp. 31–42.

[129] Daneshvar M.R.M., 2014. Landslide susceptibility zonation using analytical hierarchy process and GIS for the Bojnurd region, northeast of Iran. Landslides, **11**, pp. 1079–1091.

[130] Çoruk Ö, Kavak A., 2020. Causes of Bursa Yıldırım district Mollaarap landslide and its improvement studiesl. Pamukkale Univ Muh Bilim Dergisi, **26**, pp. 1408–1412.

[131] Taşoğlu İ.K., Keskin Çıtıroğlu H., Mekik Ç., 2016. GIS-based landslide susceptibility assessment: A case study in Kelemen Valley (Yenice—Karabuk, NW Turkey). Environmental Earth Sciences, **75**, pp. 1295.

[132] Ercanoğlu M., Gökceoğlu C., Van Asch Th. W.J., 2004. Landslide susceptibility zoning north of Yenice [NW Turkey] by multivariate statistical techniques. Natural Hazards, **32**, pp. 1–23.

[133] Yusof N.M., Pradhan B., 2014. Landslide susceptibility mapping along PLUS expressways in Malaysia using probabilistic based model in GIS. 7th

IGRSM International Remote Sensing & GIS Conference and Exhibition.

[134] Guo D., Hamada M., He C., Wang Y., Zou Y., 2014. An empirical model for landslide travel distance prediction in Wenchuan earthquake area. Landslides, **11**, pp. 281-291.

[135] Dai F.C., Lee C.F., 2001. Terrain-based mapping of landslide susceptibility using a geographical information system: A case study. Can. Geotech. J., pp. 911–923.

[136] Mossa S., Capolongo D., Pennetta L., Wasowski J., 2005. A GIS-based assessment of landsliding in the Daunia Apennines, Southern Italy, in Proceedings of the conference Mass movementhazard in various environments. Polish Geological Institute special papers, **20**, pp. 86–91.

[137] Komac M., 2012. Regional landslide susceptibility model using the Monte Carlo approach - The case of Slovenia. Geological Quarterly, **56**, pp. 41-54.

[138] Ekinci D., 2005. Karadeniz Ereğlisi'nin Zemin Hareketleri Duyarlılık Sahalarının Sınıflandırılması ve Yüksek Riskli Yerleşmelerin Zemin Stabilite Analizi. İstanbul Üniversitesi Edebiyat Fakültesi Coğrafya Bölümü Coğrafya Dergisi, **13**, pp. 121-137.

[139] Rozos D., Bathrellos G.D., Skilodimou H.D., 2011. Comparison of the implementation of rock engineering system and analytic hierarchy process methods, upon landslide susceptibility mapping, using GIS: A case study from the Eastern Achaia County of Peloponnesus Greece. Environ Earth Sci., pp. 49–63.

[140] Sujatha R., Rajamanickam G.V., Pichaimani K., 2012. Landslide susceptibility analysis using Probabilistic Certainty Factor Approach: A case study on Tevankarai stream watershed, India. Journal of Earth System Science, **121**, pp. 5.

[141] Sujatha R., Rajamanickam G.V., Pichaimani K., 2012. Landslide susceptibility analysis using Probabilistic Certainty Factor Approach: A case study on Tevankarai stream watershed, India., Journal of Earth System Science, **121**, pp. 5.

[142] Poudel D.D., Midmore D.J., West L.T., 1999. Erosion and productivity of vegetable systems on sloping volcanic ash-derived Philippine soils. Soil Sci.Soc. Am. J., **63**, pp. 1366–1376.

[143] Yalçın A., Reis S., Aydınoğlu A.C., Yomralıoğlu T.A., 2011. GIS-based comparative study of frequency ratio, analytical hierarchy process, bivariate statistics and logistics regression methods

for landslide susceptibility mapping in Trabzon, NE Turkey. Catena, **85**, pp. 274-287.

[144] Shit P.K. Bhunia G.S., Maiti R., 2016. Potential landslide susceptibility mapping using weighted overlay model [WOM], Modeling. Earth Systems and Environment, **2**, pp. 21.

[145] Korup O., Strom A.L., Weidinger J.T., 2006. Fluvial response to large rock-slope failures-examples from the Himalayas, the Tien Shan, and the New Zealand Southern Alps. Geomorphology, **78**, pp. 3–21.

[146] Tang C., Zhu J., Qi X., Ding J., 2011. Landslides induced by the Wenchuan earthquake and the subsequent strong rainfall event: A case study in the Beichuan area of China. Eng Geol., **122**, pp. 22–33.

[147] Gandhi M.S., 2016. Distribution of Heavy Minerals and its Provenance Studies of Mahabalipuram Beach, South East Coast of Chennai, Tamil Nadu. Acta Pharmaceutica Sciencia, **7**, pp. 1-28.

[148] Matebie M., Netra P.B.R.Y., 2015. Effect of landslide factor combinations on the prediction accuracy of landslide susceptibility maps in the Blue Nile Gorge of Central Ethiopia. Geoenvironmental Disasters, **2**.

[149] Saha A.K., Gupt R.P., Arora M.K., 2002. GIS-based landslide hazard zonation in the Bhagirathi [Ganga] valley, Himalaya. Int J Remote Sens, **23**, pp. 357–369.

[150] Pham B.T., Tien Bui D., Indra P., Dholakia M., 2015. Landslide susceptibility assessment at a part of Uttarakhand Himalaya, India using GIS-based statistical approach of frequency ratio method. Int J Eng Res Technol., **4**, pp. 338–344.

[151] Larsen M.C., Parks J.E., 1997. How wide is a road? The association of roads and mass-wasting in a forested montane environment. Earth Surface Processes and Landforms, **22**, pp. 835-848.

[152] Champati ray P.K., 2004. GIS based landslide modelling, In: Nagarajan R [ed], Landslide disaster: Assessment and monitoring. Anmol Publications, New Delhi, pp. 81–96.

[153] Bhatt B., Awasthi K., Heyojoo B., Silwal T., Kafle G., 2013. Using geographic ınformation system and analytical hierarchy process in landslide hazard zonation. Applied Ecology and Environmental Sciences, **1**, pp. 14-22.

[154] Ahmed B., Rubel Y.A., 2013. Understanding the issues involved in urban landslide vulnerability in Chittagong metropolitan area, Bangladesh. Association of American Geographers (AAG),

Washington DC, Book Section. DOI: 10.13140/RG.2.1.4624.8003/1.

[155] Shaban A., Khawlie M., Bou Kheir R., Abdallah C., 2001. Assessment of road instability along a typicalmountainous road using GIS and aerial photos, Lebanon, Eastern Mediterranean. Bulletin of Engineering Geology and Environment, **60**, pp. 93-101.

[156] Vahidnia M.H., Ale Sheykh A.A., Ali Mohammadi A., Hosseinali F., 2009. Landslide hazard zonation using quantitative methods in GIS. International Journal of Civil Engineering, **7**, pp. 176-189.

[157] Saha A.K., Gupta R.P., Sarkar I., Arora M.K., Csaplovics E., 2005. An approach for GIS-based statistical landslide susceptibility zonation—with a case study in the Himalayas. Landslides, **2**, pp. 61–69.

[158] Pareek N., Sharma M.L., Arora M.K., 2010. Impact of seismic factors on landslide susceptibility zonation: a case study in part of Indian Himalayas. Landslides, **7**, pp. 191–201.

[159] Khanlari G.R., Abdi Y., Babazadeh R., 2014. Landslide hazards zonation using GIS in Khoramabad, Iran. Journal of Geotechnical Geology, Winter, **9**, pp. 343-352.

[160] Akıncı H., Özalp-Yavuz A., Özalp M., Temuçin-Kılıçer S., Kılıçoğlu C., Everan E., 2014. Production of landslide susceptibility maps using bayesian probability theorem. 5. Remote Sensing-GIS Symposium [Uzal-GIS], 14-17 Oct., İstanbul.

[161] Uromeihy A., Mahdavifar M.R., 2000. Landslide hazard zonation of the Khorshrostam area, Iran. Bulletin of Engineering Geology and the Environment, **58**, pp. 207–213.

[162] Akgün A., Türk N., 2010. Landslide susceptibility mapping for Ayvalik [Western Turkey] and its vicinity by multicriteria decision analysis. Environmental Earth Sciences, **61**, pp. 595–611.

[163] He S., Li D., Wu Luo Y., 2011. Study on the rainfall and aftershock threshold for debris flow of post-earthquak. J. Mountain Sci., pp. 750–756.

[164] Erener A., Lacasse S., 2007. Landslide susceptibility mapping using GIS. TMMOB Chamber of Survey and Cadastre Engineers National Geographic Information Systems Congress, KTU, Turkey.

[165] Yalçın A., Bulut F., 2007. Landslide susceptibility mapping using GIS and digital photogrametric techniques; a case study from Ardeşen [NETurkey]. Natural Hazard, **41**, pp. 201-226.

[166] Yalçın A., 2008. GIS-based landslide susceptibility mapping using analytical hierarchy process and bivariate statistics in Ardesen [Turkey]: Comparisons of results and confirmations. Catena, 72 (1) 1, 12.

[167] Chen S.C., Chang C.C., Chan H.C., Huang L.M., Lin L.L., 2013. Modeling typhoon event-induced landslides using GIS-based logistic regression: A case study of Alishan Forestry Railway, Taiwan. Math. Prob. Eng. URL: https://www.hindawi.com/journals/mpe/2013/72830.

Kocaeli University

Kocaeli Journal of Science and Engineering

Privacy-Preserving Wireless Indoor Localization Systems

Beyhan ADANUR DEDETURK [1, *] iD , Burak KOLUKISA [2] iD , Samet TONYALI [3] iD

[1] *Department of Computer Engineering, Abdullah Gul University, Kayseri, 38080, Turkey, **ORCID:** 0000-0003-4983-2417*
[2] *Department of Computer Engineering, Abdullah Gul University, Kayseri, 38080, Turkey, **ORCID:** 0000-0003-0423-4595*
[3] *Department of Software Engineering, Gumushane University, Gümüşhane, 29100, Turkey, **ORCID:** 0000-0001-7799-2771*

Abstract

Recently the number of buildings and interior spaces has increased, and many systems have been proposed to locate people or objects in these environments. At present, several technologies, such as GPS, Bluetooth, Wi-Fi, Ultrasound, and RFID, are used for positioning problems. Some of these technologies provide good results for positioning outdoors whereas some others are effective for indoor environments. While GPS is used for outdoor localization systems, Wi-Fi, Bluetooth, Ultra WideBand, and RFID are used for indoor localization systems (ILSs). Today, due to the proliferation and extensive usage of Wi-Fi access points, wireless-based technologies in indoor localization are preferred more than others. However, even though the abovementioned technologies make life easier for their users, ILSs can pose some privacy risks in case the confidentiality of the location data cannot be ensured. Such an incident is highly likely to result in the disclosure of users' identities and behavior patterns. In this paper, we aim to investigate existing privacy-preserving wireless ILSs and discuss them.

1. Introduction

The number of studies on location-based systems has increased with the evolution of technology in recent years. Positioning techniques are, in general terms, a set of methods used to assess the position of an object or an animal. Many methods have been developed to establish an entity or creature's location, but there are some important points to be considered to determine the correct location [1]. The first of these is to determine the system requirements in detail and to choose the most appropriate method for them. The second is to minimize the external factors that cause errors and make measurements with the least error rate.

Separating the areas where localization is used as indoor and outdoor spaces provides an advantage to classify both the space-specific applications and the preferred technologies according to the space features. There are many different technologies used for localization problems. Some of these are GPS, Bluetooth, Wi-Fi, ultrasound and RFID [2]. While GPS is used for outdoor

positioning systems, it is ineffective due to the signal-weakening effect of interior walls [1]. In an indoor positioning system, the type of signal used, and the type of measurement significantly affect performance. For this reason, global positioning systems do not perform adequately in confined spaces. The necessity of indoor positioning systems has emerged to overcome this problem. Today, with the increase in the number of interior spaces such as airports, shopping centers, business centers, hospitals, universities, courthouses and parking lots, it has become much more important to find the location of people or an object in these places. The general working principle of indoor positioning technologies can be summarized as finding a user's relative position to a transmitter using radio signal characteristics [3]. The main technologies used for indoor localization systems (ILSs) are Wi-Fi, Bluetooth, ultra-broadband, and RFID.

While the increase in the use of the mentioned technologies provides very convenience in people's lives, conversely, if the data obtained as a result of the methods cannot be secured, it can harm individuals by allowing identification and behavior determination of individuals [4]. This study mainly aims that present a review of the

---

* Corresponding Author: beyhan.adanur@agu.edu.tr

latest technology and privacy-preserving ILSs. The remainder of this paper is organized as follows. Similar survey works are summarized in Section 2. In Section 3, we describe indoor localization technologies and techniques. Section 4 illustrates the challenges of indoor localization systems. In Section 5, we examine and evaluate existing privacy-preserving wireless indoor localization systems. The study is concluded in Section 6.

2. Related Survey Works

In Table 1 we have determined 36 major survey papers that have been published between 2015 and 2022 on indoor localization [1-28, 54-61]. The 9 papers have shown a general examination of indoor localization systems [1-4, 17, 21, 22, 25, 55]. They examine technologies and techniques used in indoor localization, comparison of systems according to some metrics, related challenges and proposed solutions. The other 7 of them have focused on Wi-Fi-based indoor localization systems [13, 14, 19, 20, 26, 27, 61]. They classify and compare Wi-Fi based indoor localization systems, and some of them propose a solution for a specific challenge on related topic. The other 2 of the papers show wireless and general indoor localization systems which are based on crowdsourcing [15, 24]. Although these two papers contain general information about the wireless indoor localization, they mainly focus on crowdsourcing technique [29] and their applications in the literature. For this reason, they can help researchers who want to work on crowdsourcing. In the remaining 18 papers, the following topics are covered, respectively:

i.   WSN-based indoor localization [12]
ii.   Localization privacy and indoor localization systems for mobile networks [16, 23]
iii.   Indoor localization systems based on visible light [5], computer vision [6], acoustic [7], spatial models [10], industry 4.0 [11], Bluetooth & Fingerprinting [18] and pedestrian dead reckoning [28]
iv.   Simultaneous localization and mapping (SLAM) systems [8]
v.   Image-based indoor localization [9]
vi.   Indoor vehicle localization based on RFID [54]
vii.   Machine-learning based indoor localization [56-58]
viii. Magnetic-field based indoor localization [59]
ix.   Indoor localization for IoT-based applications [60]

As can be understood from the topics covered by these 18 studies, while the other 18 studies give a general review of indoor localization, they focus on more specific topics. Studies with such a special focus will help those who want to work on the same sub-topic. But even though each of them is focused on a particular subject, the overall subject is the difference in technologies used for indoor localization. As a result of the examination of the relevant survey studies, we assume, as far as we know, that no survey paper classifies and compares systems that only contain the challenges of wireless indoor positioning solutions.

The purpose of this work is to give a comprehensive examination of wireless indoor positioning systems that maintain privacy. This study provides the reader with some of the latest privacy-preserving wireless indoor localization systems and gives hints about solutions for privacy problems. Because the security and privacy of indoor localization systems that include the position of users and objects is one of the most important requirements of relevant systems and is still waiting to be solved. With this paper, we aim to attract other researchers' attention to further privacy-preserving wireless indoor localization research.

3. Indoor Localization Technologies and Techniques

In this section, we present the technologies and techniques used in indoor localization.

3.1. Indoor Localization Technologies

The technologies used for indoor localization systems are shown in Figure 1. Bluetooth technology is designed as a wireless alternative technology that requires low energy and low cost to be used in short-range data exchange. Bluetooth modules, Bluetooth tags or sensors, a server, and a WLAN compose the Bluetooth positioning system. Bluetooth devices in the range of Bluetooth sensors in the environment can be connected to the sensors. This leads to the sensor communicating the ID of the device to the server through WLAN. The server determines the computer's location and provides the information to the device's application [21].

ZigBee is a common protocol for communication using IEEE 802.15.4 and is also a radio device deployed in a WSN as a sensor node that communicates via WLAN to the network [30]. Lastly, in a positioning system using ZigBee technology, the location of a person or object is calculated utilizing sensor data from measurements made by fixed sensor nodes and connected to the network at known locations. It should be remembered here that sensor nodes' costs vary according to energy consumption, calculation speed, bandwidth and memory.

Table 1. General information of current indoor localization studies

2022	2021
• [59] Magnetic Field Based Indoor Localization • [60] Indoor Positioning Systems for IoT-Based Applications • [61] WiFi-based Indoor Localization Systems • for Smartphone	• [54] Indoor Vehicle Localization Based on RFID • [55] General Examination of Indoor Localization Techniques and Wireless Technologies • [56-58] Machine Learning Based Indoor Localization

2020	2019	2018
• [5] Indoor Localization Systems Based on Visible Light • [6] Indoor Localization Methods Based on Computer Vision • [7] Indoor Localization Systems Based on Acoustic • [8] Indoor Location and Mapping (SLAM) Systems	• [1] General Examination of Indoor and Outdoor Location Systems • [3] General Examination of Indoor Location Systems • [9] Image Based Indoor Localization • [10] Indoor Localization Methods Based on Spatial Models • [11] Indoor Localization Systems Based on Industry 4.0	• [12] Indoor Localization Algorithms Based on Wireless Sensor Networks (WSN) • [13,14] Indoor Localization Systems Based on Wi-Fi • [15] Wireless Indoor Localization System Based on Crowdsourcing • [16] Localization Privacy For Mobile Networks

2017	2016	2015
• [2, 17] General Examination of Indoor Location Systems • [18] Indoor Localization Systems Based on Bluetooth and Fingerprinting	• [19, 20] Wireless Indoor Localization System • [23] Indoor Localization System for Mobile Networks • [24] Indoor Localization System Based on Crowdsourcing • [4, 21, 22, 25] General Examination of Indoor Location Systems	• [26, 27] Indoor Localization Systems Based on Wi-Fi • [28] Indoor Localization Systems Based on Pedestrian Dead Reckoning

The Radio Frequency Identification System (RFID) is an automated identification mechanism that uses electromagnetic transmission-based RF wireless technologies between RFID readers and RFID tags for monitoring purposes. In a positioning system using RFID technology, a tag is attached to the living or object whose position needs to be known. Radio frequency signals are then sent by the reader for identification. The label, which has entered the radio frequency field of the reader, takes the energy needed for data transfer from this field. It then modulates the carrier signal based on the data preloaded on it. The modulated carrier is sent to the reader from the label. The reader detects and demodulates the modulated signal, then read the data [31].

With its susceptibility to non-line-of-sight propagation (NLOS) and multipath effects, Ultra WideBand (UWB) is a wireless communication technology that uses a short-range, high-speed radio. Owing to its high bandwidth, it is preferred by various applications and positioning systems. In a positioning system, three or more ultra-broadband readers transmit a very broad pulse over the GHz spectrum using UWB technology. Then readers listen to chirps from tags that are ultra-broadband. Such labels have a trigger of the spark-gap type that produces a tiny blast inside them, producing a short, coded, very large, almost instantaneous explosion. Then readers report the measurements back to the central server or cloud from the tags [32].
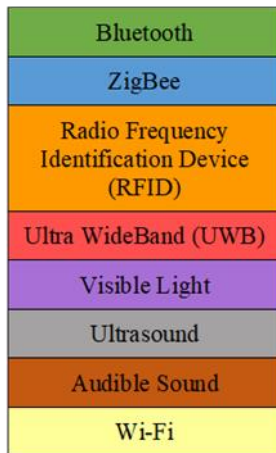
Figure 1. The technologies used in indoor localization

The Visible Light (VL) positioning systems use visible lights to locate an object for tracking and navigation. The positioning system for the VL consists of a transmitter or light source, a handheld terminal or receiver, and a contact path for the LOS. Light sources are positioned on the ceiling of a room or the side wall as base stations in this system to broadcast their known location information. The information is received from a location unknown by a mobile terminal or an image sensor and demodulated. The unbeknown location is then calculated using this information [33].

Positioning mechanisms for ultrasound require the ultrasonic markers' utilization or nodes which are on users and objects. The above-mentioned labels or nodes work qua receivers or transmitters; the other will be in motion while one is fixed. Active Bat, Cricket Device and Dolphin [2] are widely recognized ultrasound positioning systems. Audible Sound based localization is a system where standard device sound cards determine a person's or an object's position in a building by using audible sound waves. Audible sound-based localization systems generally use both software and hardware infrastructures [34].

The Internet can be accessed wirelessly via tablets, phones, smart watches and similar devices in the Wi-Fi signal area. In a positioning system using Wi-Fi technology, which is the main focus of our work, easy packets are transmitted by Wi-Fi transmitters to a range of Wi-Fi connection points in a facility [27]. These access points provide the time and intensity of their readings to a server, which calculates position using algorithms. The location information is then transferred to a cloud or server. The difficulty with privacy begins at the moment that location data is exchanged with the cloud or server.

The advantages and disadvantages of indoor localization technologies are given in Table 2. When deciding which technology should be used in an indoor localization system, the most important thing is to determine the system requirements thoroughly and select the most suitable one considering these advantages and disadvantage of technologies. For this reason, it would be wrong to say for any technology has the best performance and features. However, it can be said that wireless-based technologies are preferred more than other technologies in indoor location systems due to the increase in Wi-Fi usage all over the world.

3.2. Indoor Localization Techniques

The techniques used in indoor localization systems can be categorized as signal properties and algorithms. Although signal properties are utilized to determine and approximate the position of sensor nodes to increase the precision of localization, algorithms are used to transform the properties of the registered signal in distances and angles and after to measure the target object's real position.

Signal properties used for indoor localization systems are shown in Figure 2. The angle of arrival (AOA) is the measured angle and distance dependent on the intersection of path lines between reference points in relation to two or more reference points. The angle and distance calculation is used for estimating and determining a transmitter's position, and the information is used for purposes of tracking or navigation [3]. With AOA few sensors can be used to determine a position.
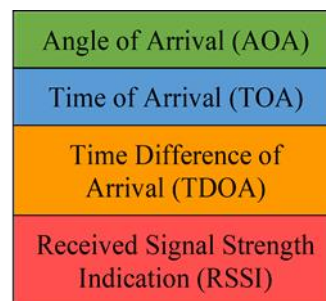
Figure 2. Signal properties for indoor localization

Time of Arrival (TOA) is the time taken from a fixed transmitter to arrive at a receiver through a signal, with the transmitter qua a reference point. In addition, instead of using the time difference determined between departure from a transmitter and arrival at the receiver, TOA uses the absolute time of arrival at the receiver. Therefore, it is possible to precisely calculate the distance between the transmitter and the receiver from the TOA, and the position can be calculated using this information [2]. Time Difference of Arrival (TDOA) determines a mobile transmitter's relative location based on the difference between the time of transmission of the transmitter and the different reference points or sensors. With this information, when the location of the mobile transmitter is identified,

monitoring may be impaired.

Received Signal Strength Indication (RSSI) is a calculation of the received signal strength (RSS) power level present in a radio infrastructure compared to angular and distance-dependent metrics. RSSI may be utilized to determine how far apart handheld computers are. Also known, to measure signal intensity reduction or loss due to transmission, the RSSI mechanism determines how much broadcast signals are attenuated. As a result, the distance among handheld computers can be calculated. Location information can be acquired through estimation [35].

Briefly, in position determination, the signal property is an integral element as it will be important in position calculation and estimation. In determining the positioning technique's potency, the signal property used with a positioning algorithm goes a long way. Thus, to use the most acceptable property, it is necessary to understand the positioning algorithms.

Table 2. Advantages and disadvantages of indoor localization technologies

Technology	Advantages	Disadvantages
Bluetooth	• High security, throughput and reception rate • Low cost and power • Small size	• Low localization accuracy • Has not resistance to noise • High cost to ensure privacy
ZigBee	• Uses for WSN • Cost-effective	• Not readily available on majority of the user devices • Difficult to find suitable position for non-anchor nodes • Low localization accuracy
RFID	• Needs low power • Has wide range	• Low localization accuracy
UWB	• Has resistance to interference • Provides high accuracy	• Shorter range • Needs extra hardware • High cost
Visible Light	• Widely available • High accuracy • Multipath-free	• Needs high power and LoS • Obstacles affect range
Ultrasound	• Less absorption	• High dependence on sensor placement
Audible Sound	• Uses in proprietary applications • Provides high accuracy	• Has not resistance to sound pollution • Needs extra hardware
Wi-Fi	• Eliminates LoS issues • Widely available • Provides high accuracy • No need complex extra hardware	• Inclined to noise • Uses complex processing algorithms • Low speed

The algorithms used for indoor localization systems are shown in Figure 3, and their advantages and disadvantages are shown in Table 3.

To approximate the location of a target object, triangulation uses triangular geometric properties by calculating angular measurements based on two supplied

reference points. Another saying, the intersection of two sets of angle directions is used to determine the target object's position, a technique acknowledged qua direction finding. To locate an item, AOA calculates the distance between direction lines or fixed points. The position of the transmitter is calculated based on the angle and distance between the reference points to estimate the object's location [36].

| Triangulation |
| Trilateration |
| Proximity |
| Fingerprinting |

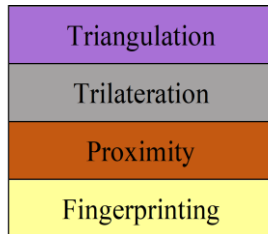**Figure 3.** Algorithms used in indoor localization

The target object's location is calculated using TOA to calculate the time a signal takes to get from a transmitter to a receiver. In certain cases, TDOA, which is an upgrade on TOA, is also used. Trilateration also uses triangular geometry to estimate a target object's location. Nonetheless, in this situation, distance measurements are used to assess the location by calculating the attenuation relative to the three given reference points of the transmitted signal [36].

As in triangulation and trilateration, proximity does not provide an absolute or relative position estimate, because it merely offers location knowledge. To decide the position to supply the data, a grid of antennas with specified locations is used. If a mobile device is detected in motion, it uses the nearest antenna to determine its position. Yet, if a mobile device is detected by more than one antenna, the strongest signal antenna is used to measure its location [37]. The location of the mobile device is calculated using RSSI, which is typically used close to measure the distance between mobile devices to gain knowledge about the location of the device.

In fingerprinting, which is also called Scene Analysis, the location calculation is performed independently of the angle or the distance. Fingerprinting collects data or features from a scene or observation and then calculates the location of an object by matching or comparing the information collected in an existing database with that. It is an algorithm based on the RSS in wireless or RF networks. The fingerprinting system uses an RSS-value database to assess a Wi-Fi device's location within a Wi-Fi coverage area. Location fingerprinting refers to the fingerprint of any feature of a position-based signal. It can be performed in two stages, in other words offline and online. The area

inside a building is surveyed in the offline process, and grid points are measured at different locations in the building [38].

For the locations with visible access points, each grid point has a list of RSSI values. Furthermore, for position estimation purposes, the respective position information and signal strengths are collected from the different locations. The precision accuracy obtained by this method is greater than the RF-based indoor positioning technique. In the online process, the object's most feasible location is computed by gathered grid points and localization information.

Fingerprinting is an RSS-based technology and is also widely utilized as an interior localization method. Fingerprinting is an RSS-based technology and is also widely utilized as an interior localization method.

The main idea of this approach is to estimate the user location using the pre-built database. One of the first studies is Radar, which is an RF-based system and obtained accuracies of 2 to 3 meters (The median error distance is 2 to 3 meters). Furthermore, today, many studies and applications are available in the fingerprinting approach. Fingerprinting consists of 2 stages. The offline part is known as the first stage. Designated interior spaces are divided into grids, and in each grid, the RSS values emitted by the Wi-Fi and Access Point devices are collected, and Radiomap is generated. As can be seen in Equation (1), while creating the database, "i" indicates the index, x and y hold the coordinate point of the index "i," and "V_i" is an array of the signal strength of all Wi-Fi and Access Points at that point, and "n" represents the number of devices overall. It should be noted here that when a grid is smaller the performance is lower. The second phase is called the online part. According to the RSS values received by the user, $V' = <V_1, V_2, V_3, ..., V_n>$, the (x_i, y_i) point is determined by using the k-Nearest Neighbor (KNN) algorithm.

$$<i, (x_i, y_i), V_i>$$
$$V_i = <V_1, V_2, V_3, ..., V_n> \qquad (1)$$

Machine learning (ML) is characterized by an algorithm that can automatically recognize and understand data patterns. Based on this learning, an algorithm can recognize patterns or conduct various decision-making tasks for unknown incoming data. ML is often divided into three basic categories: supervised learning, unsupervised learning, and reinforcement learning. In supervised learning, all training samples have labels available.

Table 3. Advantages and disadvantages of indoor localization algorithms

Localization Algorithm	Signal Property	Advantages	Disadvantages
Triangulation	Angle of Arrival	Easy of its application Low cost and high accuracy at room level	Complex, expensive and low accuracy at wide coverage
Trilateration	Time of Arrival / Time Difference of Arrival	High accuracy	Complex and expensive due to hardware complexity
Proximity	Received Signal Strength Indication	High accuracy	Complex and expensive
Fingerprinting	Received Signal Strength Indication	High performance and easy to use	Complex, expensive, low medium accuracy and time consuming

In unsupervised learning, none of the training samples have labels. In reinforcement learning, an agent learns how to function or conduct actions in a potentially unpredictable and complicated environment in exchange for incentives. Another subtype of ML is semisupervised learning, in which some training samples are labeled but the remainder is not. On a variety of tasks, ML approaches can achieve human-level performance. Therefore, researchers have utilized ML in indoor localization to achieve high performance and compensate for or alleviate different difficulties encountered during data collecting, such as missing RSSIs, redundant RSSIs, and abnormalities (or mistakes) in RSSI fingerprints [56-58].

In indoor localization applications, the ML algorithms used for data preprocessing and dimensionality reduction are as follows [62-69]:

i.   Singular value decomposition (SVD)
ii. Principal component analysis (PCA)
iii. Kernel PCA (KPCA)
iv. Locally linear embedding (LLE)
v.   Linear discriminant analysis (LDA)
vi. t-distributed stochastic neighbor embedding (t-SNE)
vii. Autoencoders

Data that has been preprocessed is utilized to train machine learning prediction models for indoor localisation. The hyperparameters of the models are optimized for high accuracy and to minimize under- and/or overfitting. The authors of [70] provide a guideline for selecting the optimal hyperparameters of many ML models, including k-nearest neighbors (kNN), support vector machine (SVM), decision tree (DT), artificial neural networks (ANN), evolutionary algorithms, and federated computing. Each of these ML models has distinct underlying results based on their respective prediction methods. Typically, the performance of prediction models is assessed using a validation/test subset of database/radio maps. Additionally, the aforementioned prediction models may be used in a supervised, unsupervised, or semisupervised (partial labels for data) manner for the indoor localization problem.

Postprocessing [71] is an extra operation that enhances the performance of the ML model output. Post-processing methods include various pruning systems, quality processing standards, sorting rules, etc. These approaches apply different example filters on information generated by an algorithm that is noisy, imprecise, or unwanted. Similarly, post-processing is required for an indoor localization output, since it may wrongly forecast the location of the user owing to insufficient signal strength of the APs, hardware problems, etc., resulting in faulty positioning models. When constructing ML models, frequent retraining is required to account for data changes and the dynamic nature of the environment. This retraining of the model may increase the system's downtime, expense, and complexity. To prevent these challenges, researchers have begun employing a transfer learning (TL) approach. TL is an ML approach for storing the

information obtained during problem-solving and applying it to the solution of other related issues [72].

4. Challenges of Indoor Localization Sytems

In this section, some of the major challenges of indoor localization and its adoption are presented. Using a technology that is readily accessible to the user and does not require special hardware at the user end, availability is supported in indoor localization. The accuracy of UWB-based systems, for example, is high, but there are no UWB chips for most current user devices. So, it is necessary to obtain localization systems that will operate seamlessly with commonly available devices such as smartphones [3]. Wi-Fi, which is ready for use on almost all user computers, is the most widely used technology nowadays.

Cost is the key element in a market's acceptance of localization systems. It is a complex factor that is not confined to hardware alone. In the development and installation of a product, time and human resources are essential aspects that must be addressed. So the cost of the indoor localization systems should be low. Generally, as the hardware number used increases, system accuracy and cost increase. In this regard, the aim of today's indoor localization studies is to develop systems with high accuracy despite the minimum number of equipment and low cost [20].

It is optimal for an industrial localization system to cover vast areas with the fewest number of nodes, resulting in a cost-effective solution. However, if the ranges are expanded, the performance may suffer. Tx-power is the primary element for altering the system's coverage according to the use case. The capacity of a system to withstand interruptions and signal losses that might impair its functionality. A strong positioning system must account for environmental cues that are inaccurate. This measure is essential for the constant operation of all systems, especially on industrial sites and in emergency situations [60].

Another fundamental requirement of indoor localization is energy efficiency due to systems that consume a great deal of energy, drains battery from consumer devices cannot be commonly used [4]. Periodicity, transmission capacity and computational complexity are possible variables that could have an impact on any localization system's energy consumption. They can be done by using less energy-using technologies or by discharging the localization algorithm's computational portion to a server or any organization that has access to the uninterrupted power supply and high processing ability.

One of the most critical aspects of the localization method [21] is the accuracy. Accuracy is the proximity between the measured or predicted position and the actual position [39]. It depends on many factors, such as noise, LoS, signal propagation, and so on. The presence of obstacles and multi-path impacts make indoor localization more difficult to work on. Hence, to achieve highly accurate systems, it is necessary for the device to minimize the impact of multipath effects and other noises from the environment. This could include comprehensive signal processing and noise reduction, which is a very difficult job. A positioning approach should have the ability to locate the occupant or object within 10 cm of accuracy, preferably.

An indoor localization model is expected to be capable of recording occupant locations and coordinates without apparent delay. For this to happen, user location should be reported with a small number of reference signals, and complex operations are performed in milliseconds granularity [3]. However, this process will have some delay. To reduce delay, optimized signal processing is required which should remove noise and provide a visible delay to the user position.

Numerous heterogeneous devices supporting diverse communication technologies and protocols are included in location-based systems. Consequently, the interaction between many components is one of the greatest obstacles in this field. Developing n interoperable middleware for interaction between diverse components and standardized equipment and protocols may be a viable solution for this issue. Consequently, the establishment of a complete central platform or hub outfitted with all communication technologies might be a viable solution.

The security and privacy of indoor localization systems including the position of users and objects is the focus of this study and among the most critical needs for relevant structures. An occupant position can now be correlated with several device locations and show much more personal details such as people's health, mood, and behavior [16]. Even if the consumer does not have a mobile device, several IoT sensors can deduce its location and actions by processing a sequence of data collected in an immediate indoor environment. In the WLAN-IPS environment, traditional indoor positioning services (IPS) are endangered. Because a mobile device collects measurements from all AP devices and personal information, the RSS-based positioning system poses a security risk. The IPS server, for example, receives the AP ID. Privacy in IPSs may also be improved by regulating access to information dissemination and location information. From a software and system architectural standpoint, IPS security and privacy may also be improved. When calculating the position of the target device, for example, position system design dealing with

self-location will ensure consumers a high level of privacy and safety. Therefore, no one in Personal Networks can access the location information if an entity does not obtain it from the target device [40, 41].

5. Evaluation of Existing Privacy-Preserving Wireless Indoor Localization Systems

We have found 15 studies [42-51, 73-77] in the literature on privacy-preserving Wi-Fi-based indoor localization published between 2018 and 2022. In Table 4, related papers are classified according to their publication year, used technologies, algorithms, signal properties and methods for providing localization privacy. Below, we summarized the relevant studies briefly.

The study [73] proposes a Bloom filter-based preserving anonymity localization approach that creates a partial radio map during the localization process. Anonymizers hide user identities from Location Service Providers. The suggested approach is simpler than encryption or clustering methods and offers a strategy that increases the radio map by verified users without sacrificing privacy to reduce complexity and boost accuracy. Using the Hilbert curve to preserve user location uncertainty improves this strategy, and Location Service Providers provide verified user certificates. This certificate boosts users' Location Based Services queries. Simulations and observations reveal that the suggested strategy increases localization accuracy compared to location privacy methods.

Wang et al. [74] design a privacy-preserving IPS using a time difference of arrival (TDOA) positioning algorithm applied in an environment backed by a resourceful cloud system. Inner product encryption is used to protect users' privacy against attackers. Moreover, k-anonymity is used to ensure the security of data stored on cloud systems that can be modeled as semi-honest. Thus, the proposed scheme does not disclose private anchor information and users' location. In the proposed scheme, the least-squares estimation method used in the TDOA algorithm is decomposed into the basic form of inner products. This computation is performed on the ciphertext that holds distance difference and anchor information. Hence, the attackers cannot extract any useful information but the inner product from which they cannot determine users' location. Additionally, the client device adds some fake distance difference information in the location request sent to the cloud server, so it cannot distinguish users' real location from the fake data. Experimental results show that the proposed scheme both provides user privacy and meets efficiency and computational expectations for real-time indoor localization.

Beets et al. [75] design and implement a fingerprint-based privacy-preserving indoor localization scheme using a secure two-party computation protocol on RSS data obtained from a Wi-Fi access point. The proposed scheme provides privacy not only to users but also to service providers. The localization protocol is divided into vector-matrix multiplication with secret arithmetic shares and the k-nearest neighbor algorithm. With the proposed techniques, it is possible to make the online localization phase work 16 times faster. Finally, the paper presents an implementation of an indoor localization scheme based fully on Yao's Garbled Circuits. Although it cannot achieve the same level of localization accuracy when compared to the proposed scheme it can be employed in some scenarios where accuracy objectives are relaxed.

Zhang et al. [76] combine Wi-Fi and BLE fingerprints to develop a semi-supervised machine-learning model for indoor positioning. They take advantage of the computational capabilities of edge and cloud servers in the localization process. To prevent attackers and third-party cloud positioning servers from accessing users' real-time location data, they utilize the ε-differential privacy technique. According to the results obtained from experiments conducted in real indoor environments, the proposed model both reduces human intervention for calibration and outperforms five semi-supervised learning methods and six localization methods in terms of location accuracy and time consumption, respectively.

Hu et al. [77] extend an IPS named Horus which is based on maximum likelihood estimation and introduces PriHorus which provides privacy both for users' location and the IPS operator. To this end, PriHorus employs Paillier's cryptosystem, and experimental results show that it can achieve the same level of accuracy as Horus with an acceptable level of the computational burden.

Nieminen R. et al. [42] propose an indoor localization method that protects privacy based on measurements of signal intensity obtained from WiFi access points. Using secure two-party computing with Paillier encryption and garbled circuits, this technique tries to preserve the privacy of both the client's location and the service provider's database. It describes several optimizations that reduce the scheme's overheads in computation and present those overheads' theoretical assessments. They further illustrate the scheme's practicality by constructing a proof-of-concept implementation for Android devices and commodity servers. Hereby, it has been shown that the scheme is not eligible for real-world indoor localization applications, or that some applications require at least some additional measures to suit it. The downside is that there is more processing and communication overhead, which leads to slower response times, greater power consumption, and higher per-query data use.

Zhang G. et al. [43] propose a low-cost, lightweight privacy-preserving scheme (LWP2) that preserves the privacy of both the location and data. The fundamental idea is to first describe the problem of privacy-preserving localization as reducing the least squared error for an overdetermined linear formulation, and then to build a lightweight method exploiting the overdetermined linear formulation's particular structure in ciphertext space. Cost analysis, privacy, average time cost, bandwidth cost, and localization error metrics are used to demonstrate the study's performance.

To maintain anonymity for localization, The Encrypted Indoor Positioning Service (EIPS) approach proposed by Wang W. et al. [44] protects user privacy from a centralized server while maintaining localization accuracy. Their EIPS approach allows customers to encrypt and decrypt their requests bi-directionally utilizing an EDS (Encryption and Decryption Server) in a commutative manner, ensuring that both EIPS and EDS remain anonymous. To prevent Known Plaintext Attacks, they frequently offer Query Split, Artificial Dimensions, and Columns. The performance of the study is shown with the accuracy and time efficiency of EIPS, and energy consumption metrics. This scheme works without loss of quality, for both snapshot and continuous queries.

Eshun S.N. Et al. [45] offer an indoor privacy-preserving protocol that allows a service provider (SP) to query the location of a user without compromising their users' privacy. The protocol preserves the privacy of both the user and the SP while also delivering the service based on the user's location. They claim that most of the user-side computational overhead is delegated to the server using Paillier's cryptosystem during keeping the server's precise location hidden.

Järvinen K. et al. [46] introduced Practical Privacy-Preserving Indoor Localization Using OuTsourcing (PILOT), which safeguards the privacy of user locations and protects the database of the server. To save electricity and network bandwidth for mobile end devices in privacy-preserving indoor localization, PILOT safely outsources the computations to two non-colluding semi-honest parties (PPIL). After evaluating system performance, they claim that PILOT is the first PPIL system with realistic run-times of less than 1 s online and is quicker than previous works by many orders of magnitude.

Zhang X. et al. [47] proposed a lightweight, indoor privacy-conserving mechanism called EC-DPELM (a lightweight differential privacy-based indoor localization privacy-preserving mechanism) for a complex and dynamic Edge Computing environment. The RSSI dataset, which is utilized to train the model for indoor localization,

will be adequately insulated within EC-DPELM. EC-DPELM also uses an edge-computing architecture, which means that the training cycle is distributed throughout the network's edges, reducing the load on cloud servers. Their tests revealed that the model is capable of ensuring both privacy and indoor localization accuracy while consuming less time.

Yang Z. et al. [48] introduce the privacy model for PPIL-based Wi-Fi fingerprint systems, where both client and server privacy is built to cover current active attacks in a unilateral malicious environment. Client privacy is defined based on the classic notion of distinguishability, and server privacy is defined computationally.

Zhao P. et al. [49] presented a Privacy-Preserving Paradigm-driven framework for indoor Localization (P3-LOC), a system for indoor localization privacy. P3-LOC takes advantage of the fact that most indoor localization systems follow a growing two-stage localization paradigm: measuring information and estimating locations. On this basis, P3-LOC perturbs and cloaks the transmitted data in these two stages and utilizes k-anonymity and differential privacy to provide privacy. The main benefit is that it does not rely on any previous knowledge of the underlying localization algorithms, and it guarantees the anonymity of the position of both users and the data of the server.

Alikhani N. et al. [50] suggested a framework for protecting user privacy in both the training and position estimation stages of data fingerprinting. In the training process, by using the Hilbert curve, when users are active in the crowdsourcing network, their privacy is maintained. Then, the privacy of users is protected in the location estimation stage by using both the double encryption technique and the Hilbert curve. The proposed method includes an anonymizer that is unaware of the real user's position and a server that is unaware of the user's identity.

Wang Y. et al. [51] suggest a Differential Privacy (DP)-based indoor localization system DP3, composed of four different stages: client-side access point (AP) fuzzification and position retrieval, and server-side DP finger clustering and finger permutation. The localization server then divides the fingerprints related to the AP sequence into k clusters using DP-enabled clustering, permutes these reference points in each cluster using an exponential mechanism to mask the true positions of these fingerprints, and sends the modified data set to the to-be-localized (TBL) client. The location retrieval step on the client side calculates the client's location. Theoretical and experimental findings reveal that DP3 can safeguard both the TBL client's location and the localization server's data privacy.

Table 4. Features of privacy-preserving Wi-Fi based indoor localization

Paper	Year	Technology	Signal Property	Algorithm	Used Method for Providing Location Privacy
[77]	2022	Wi-Fi	RSS	Fingerprinting	• Paillier's Homomorphic Encryption
[76]	2022	Wi-Fi and BLE	RSSI	Fingerprinting	• ε-Differential Privacy
[75]	2022	Wi-Fi	RSS	Fingerprinting	• Secure Two-Party Computation • Yao's Garbled Circuits
[74]	2022	Wi-Fi	TDOA	Ranging	• Inner Product Encryption • k-Anonymity
[73]	2021	Wi-Fi	RSSI	Fingerprinting	• Bloom Filter-based Partial Radio Map
[42]	2020	Wi-Fi	RSSI	Fingerprinting	• Secure Two-Party Computation • Paillier's Homomorphic Encryption
[43]	2020	Wi-Fi	RSSI	Fingerprinting	• Paillier's Homomorphic Encryption
[44]	2019	Wi-Fi	RSSI	Fingerprinting	• Asymmetric Scalar-Product • Preserving Encryption kNN Search
[45]	2019	Wi-Fi	RSSI	Fingerprinting	• Paillier's Homomorphic Encryption • Secure Two-Party Computation • Spatial Bloom Filter
[46]	2019	Wi-Fi	RSSI	Fingerprinting	• Secure Two-Party Computation • Depth-Optimized Circuits
[47]	2019	Wi-Fi	RSSI	Fingerprinting	• Differential Privacy Edge Computing
[48]	2019	Wi-Fi	RSSI	Fingerprinting	• Secure Two-Party Computation • Paillier's Homomorphic Encryption
[49]	2018	Wi-Fi	RSSI	Fingerprinting Model Dead-Reckoning	• Differential Privacy k-Anonymity
[50]	2018	Wi-Fi	RSSI	Fingerprinting	• Hilbert curve Double encryption
[51]	2018	Wi-Fi	RSSI	Fingerprinting	• Differential Privacy Based Clustering

5. Conclusions

Today, the number of indoor spaces such as airports, hospitals and universities has increased considerably. Therewithal, locating people or an object in these interiors has become much more important. Although human life has become easier with the widespread use of positioning systems if positioning data cannot be protected, people's actions and information can be easily detected and people can be harmed. Because Wi-Fi access points are so widely used, wireless-based technologies are preferred more than

Bluetooth, ultra-broadband and RFID technologies in indoor localization [52-53]. Based on the importance of indoor localization systems, their data privacy and the widespread use of wireless technology in the field, we wanted to examine the privacy-preserving wireless indoor localization systems in this study.

In the wireless indoor localization systems we have examined, we see that RSSI and fingerprinting techniques are generally chosen. Studies based on RSSI values o Wi-Fi technologies rely on the fact that the devices implementing these devices spread signals to a certain

distance. Our research firstly revealed that Wi-Fi technologies perform better than other technologies when used with RSSI as signal property and fingerprinting as positioning algorithms. Secondly, it revealed that for solving data privacy, the majority of studies have used secure two-party computation and homomorphic encryption methods. With homomorphic encryption, without breaking the encrypted data, different operations can be performed. Also, the client and the server provide complete security. But there is serious energy consumption for operations. For privacy protection, a hybrid approach can be built with Wi-Fi using other technologies, so the performance rate and client-server protection can be improved without the need for high energy consumption.

Declaration of Ethical Standards

The author(s) of this article declare that the materials and methods used in this study do not require ethical committee permission and/or legal-special permission.

Conflict of Interest

The authors declare that they have no known competing financial interests or personal relationships that could have appeared to influence the work reported in this paper.

References

[1] Alinsavath K.N., Nugroho L.E., and Hamamoto K., 2019. The Seamlessness of Outdoor and Indoor Localization Approaches based on a Ubiquitous Computing Environment: A Survey. In Proceedings of the 2019 2nd International Conference on Information Science and Systems, Tokyo, 16-19 March, pp. 316-324.

[2] Sakpere W., Adeyeye-Oshin M., Mlitwa N.B., 2017. A state-of-the-art survey of indoor positioning and navigation systems and technologies. South African Computer Journal, **29(3),** pp. 145-197.

[3] Zafari F., Gkelias A., Leung K.K., 2019. A survey of indoor localization systems and technologies. IEEE Communications Surveys and Tutorials, **21(3)**, pp. 2568-2599.

[4] Yassin A., Nasser Y., Awad M., Al-Dubai A., Liu R., Yuen C., Aboutanios E., 2016. Recent advances in indoor localization: A survey on theoretical approaches and applications. IEEE Communications Surveys and Tutorials, **19(2)**, pp. 1327-1346.

[5] Rahman A. B. M., Li T., Wang, Y., 2020. Recent Advances in Indoor Localization via Visible Lights: A Survey. Sensors, **20(5)**, pp. 1382.

[6] Morar A., Moldoveanu A., Mocanu I., Moldoveanu F., Radoi I. E., Asavei V., Butean, A., 2020. A Comprehensive Survey of Indoor Localization Methods Based on Computer Vision. Sensors, **20(9)**, 2641.

[7] Liu M., Cheng L., Qian K., Wang J., Wang J., and Liu, Y., 2020. Indoor acoustic localization: a survey. Human-Centric Computing and Information Sciences, **10(1)**, pp. 1-24.

[8] Gaber H., Marey M., Amin S., Tolba M.F., 2020. Localization and Mapping for Indoor Navigation: Survey. In Robotic Systems: Concepts, Methodologies, Tools, and Applications, **1**, pp.930-954.

[9] Bai X., Huang M., Prasad N. R., Mihovska A.D., 2019. A Survey of Image-Based Indoor Localization using Deep Learning. In 2019 22nd International Symposium on Wireless Personal Multimedia Communications, Lisbon, 24-27 November, pp. 1-6.

[10] Gu F., Hu X., Ramezani M., Acharya D., Khoshelham K., Valaee S., Shang J., 2019. Indoor localization improved by spatial context—A survey. ACM Computing surveys (CSUR), **52(3)**, pp. 1-35.

[11] Mieth C., Humbeck P., Herzwurm G., 2019. A Survey on the Potentials of Indoor Localization Systems in Production. In Interdisciplinary Conference on Production, Logistics and Traffic, Dortmund, pp. 42-154.

[12] Sumitra I. D., Supatmi S., Hou R., 2018. Enhancement of Indoor Localization Algorithms in Wireless Sensor Networks: A Survey. In IOP Conference Series: Materials Science and Engineering, **407(1)**, pp. 1-8.

[13] Liu Y., Liu W., Luo, X., 2018. Survey on the Indoor Localization Technique of Wi-Fi Access Points. International Journal of Digital Crime and Forensics (IJDCF), **10(3)**, pp. 27-42.

[14] Zhou M., Bulgantamir O., Wang, Y., 2018. Highly Available Localization Techniques in Indoor Wi-Fi Environment: A Comprehensive Survey. In International Conference on Machine Learning and Intelligent Communications, Hangzhou, pp. 460-469.

[15] Zhou X., Chen T., Guo D., Teng X., Yuan B., 2018. From one to crowd: A survey on crowdsourcing-based wireless indoor localization. Frontiers of Computer Science, **12(3)**, pp. 423-450.

[16] Zakhary S., Benslimane A., 2018. On location-privacy in opportunistic mobile networks, a survey.

Journal of Network and Computer Applications, **103**, pp. 157-170.

[17] Brena R. F., García-Vázquez J. P., Galván-Tejada C. E., Muñoz-Rodriguez D., Vargas-Rosales C., and Fangmeyer J., 2017. Evolution of indoor positioning technologies: A survey. Journal of Sensors, **2017**.

[18] Samu G. W., Kadam P., 2017. Survey on Indoor Localization: Evaluation Performance of Bluetooth Low Energy and Fingerprinting Based Indoor Localization System. International Journal of Computer Engineering & Technology (IJCET), **8(6)**, pp. 23-35.

[19] Basri C., El Khadimi A., 2016. Survey on indoor localization system and recent advances of Wi-Fi fingerprinting technique. In 2016 5th International Conference on Multimedia Computing and Systems (ICMCS), Marrakesh, pp. 253-259.

[20] Xiao J., Zhou Z., Yi Y., Ni L. M., 2016. A survey on wireless indoor localization from the device perspective. ACM Computing surveys (CSUR), **49(2),** pp. 1-31.

[21] Khudhair A. A., Jabbar S. Q., Sulttan M. Q., Wang, D., 2016. Wireless indoor localization systems and techniques: survey and comparative study. Indonesian Journal of Electrical Engineering and Computer Science, **3(2)**, pp. 392-409.

[22] Kim C. M., Jang B., 2016. "Indoor Localization Technology Survey", Journal of The Korea Society of Computer and Information, **21(1)**, pp. 17-24.

[23] Stojkoska B. R., Kosovic I. N., Jagust T., 2016. "A Survey of Indoor Localization Techniques for Smartphones. Web Proceedings of ICT Innovations, Ohrid, pp. 11-22.

[24] Pei L., Zhang M., Zou D., Chen R., Chen Y., 2016. A survey of crowd sensing opportunistic signals for indoor localization. Mobile Information Systems, **2016**, pp. 1-16.

[25] Xi R., Li Y. J., Hou M. S., 2016. Survey on indoor localization. Computer Science, **43(4),** pp. 1-6.

[26] Yang Z., Wu C., Zhou Z., Zhang X., Wang X., Liu Y., 2015. Mobility increases localizability: A on wireless indoor localization using inertial sensors. ACM Computing Surveys (Csur), **47(3)**, pp. 1-34.

[27] Shandilya S., Idate S. R., 2015. Survey on Localization of Smartphone User in an Indoor Environment Using Wi-Fi and Navigation through Layout of the Floor Plans. International Journal of Innovative Research in Computer and Communication Engineering, **3(5)**, pp. 3784-3789.

[28] Minmin C., 2015. A survey of indoor localization using Pedestrian Dead Reckoning. Microcomputer & Its Applications, **13**, pp. 9-11.

[29] Ji H., Xie L., Wang C., Yin Y., Lu S., 2015. CrowdSensing: A crowd-sourcing based indoor navigation using RFID-based delay tolerant network. Journal of Network and Computer Applications, **52**, pp. 79-89.

[30] Luo C., Hong H., Cheng L., Chan M. C., Li J., Ming Z., 2016. Accuracy-aware wireless indoor localization: Feasibility and applications. Journal of Network and Computer Applications, **62**, pp. 128-136.

[31] Bianchi V., Ciampolini P., De Munari I., 2018. RSSI-based indoor localization and identification for ZigBee wireless sensor networks in smart homes. IEEE Transactions on Instrumentation and Measurement, **68(2)**, pp. 566-575.

[32] Ni L. M., Zhang D., Souryal M.R., 2011. RFID-based localization and tracking technologies. IEEE Wireless Communications, **18(2)**, pp. 45-51.

[33] García E., Poudereux P., Hernández Á., Ureña J., Gualda D., 2015. A robust UWB indoor positioning system for highly complex environments. In 2015 IEEE International Conference on Industrial Technology (ICIT), Seville, pp. 3386-3391.

[34] Hassan N. U., Naeem A., Pasha M. A., Jadoon T., and Yuen C., 2015. Indoor positioning using visible led lights: A survey. ACM Computing Surveys (CSUR), **48(2)**, pp. 1-32.

[35] Moutinho J. N., Araújo R. E., Freitas D., "Indoor localization with audible sound—Towards practical implementation. Pervasive and Mobile Computing, **29**, pp. 1-16.

[36] Luo X., O'Brien W. J., Julien C.L., 2011. Comparative evaluation of Received Signal-Strength Index (RSSI) based indoor localization techniques for construction jobsites. Advanced Engineering Informatics, **25(2)**, pp. 355-363.

[37] Kulshrestha T., Saxena D., Niyogi R., Raychoudhury V., Misra M., 2017. SmartITS: Smartphone-based identification and tracking using seamless indoor-outdoor localization. Journal of Network and Computer Applications, **98**, pp. 97-113.

[38] Al-Ammar M. A., Alhadhrami S., Al-Salman A., Alarifi A., Al-Khalifa H. S., Alnafessah A., Alsaleh, M., 2014. Comparative survey of indoor positioning technologies, techniques, and algorithms. In 2014 International Conference on Cyberworlds, Cantabria, pp. 45-252.

[39] Zegeye W. K., Amsalu S. B., Astatke Y., Moazzami, F., 2016. WiFi RSS fingerprinting indoor localization for mobile devices". In 2016 IEEE 7th Annual Ubiquitous Computing, Electronics and Mobile Communication Conference (UEMCON), New York, pp. 1-6.

[40] Li H., Sun L., Zhu H., Lu X., Cheng, X., 2014. Achieving privacy preservation in WiFi fingerprint-based localization. In IEEE INFOCOM 2014-IEEE Conference on Computer Communications, Toronto, pp. 2337-2345.

[41] Ziegeldorf J. H., Viol N., Henze M., Wehrle K., 2014. Poster: Privacy-preserving indoor localization. 7th ACM Conference on Security & Privacy in Wireless and Mobile Networks (WiSec'14), Oxford, pp. 1-2.

[42] Nieminen R., Järvinen K., 2020. Practical Privacy-Preserving Indoor Localization based on Secure Two-Party Computation. IEEE Transactions on Mobile Computing, **20**, pp. 2877-2890.

[43] Zhang G., Zhang A., Zhao P., Sun, J., 2020. Lightweight Privacy-Preserving Scheme in Wi-Fi Fingerprint-Based Indoor Localization. IEEE Systems Journal, **14(3)**, pp. 4638-4647.

[44] Wang W., Gong Z., Zhang J., Lu H., Ku W. S., 2019. On Location Privacy in Fingerprinting-based Indoor Positioning System: An Encryption Approach. In Proceedings of the 27th ACM SIGSPATIAL International Conference on Advances in Geographic Information Systems, Chicago, pp. 289-298.

[45] Eshun S. N., Palmieri P., 2019. A privacy- preserving protocol for indoor Wi-Fi localization. In Proceedings of the 16th ACM International Conference on Computing Frontiers, Alghero, pp. 380-385.

[46] Järvinen K., Leppäkoski H., Lohan E. S., Richter P., Schneider T., Tkachenko O., Yang Z., 2019. PILOT: practical privacy-preserving indoor localization using outsourcing. In 2019 IEEE European Symposium on Security and Privacy (EuroSandP), Stockholm, pp. 448-463.

[47] Zhang X., Chen Q., Peng X., Jiang X., 2019. Differential Privacy-Based Indoor Localization Privacy Protection in Edge Computing. In 2019 IEEE (SmartWorld/SCALCOM/UIC/ATC/CBDCom/IOP/S CI), Leicester, pp. 491-496.

[48] Yang Z., Järvinen K., 2019. Towards Modeling Privacy in WiFi Fingerprinting Indoor Localization and its Application. Journal of Wireless Mobile Networks, Ubiquitous Computing, and Dependable Applications (JoWUA), **10(1),** pp. 4-22.

[49] Zhao P., Jiang H., Lui J. C., Wang C., Zeng F., Xiao F., Li Z., 2018. P3-LOC: A privacy-preserving paradigm-driven framework for indoor localization. IEEE/ACM Transactions on Networking, **26(6)**, pp. 2856-2869.

[50] Alikhani N., Moghtadaiee V., Sazdar A. M., Ghorashi S. A., 2018. A Privacy Preserving Method for Crowdsourcing in Indoor Fingerprinting Localization. In 2018 8th International Conference on Computer and Knowledge Engineering (ICCKE), Iran, pp. 58-62.

[51] Wang Y., Huang M., Jin Q., Ma J., 2018. DP3: A differential privacy-based privacy-preserving indoor localization mechanism. IEEE Communications Letters, **22(12)**, pp. 2547-2550.

[52] Altintas B., Tacha, S., 2011. Improving RSS-based indoor positioning algorithm via k-means clustering. 17th European Wireless 2011-Sustainable Wireless Technologies. VDE, Vienna, pp. 1-5.

[53] Halder S., Ghosal A., 2016. A survey on mobility-assisted localization techniques in wireless sensor networks. Journal of Network and Computer Applications, **60**, pp. 82-94.

[54] Motroni A., Buffi A., Nepa P., 2021. A survey on indoor vehicle localization through RFID technology. IEEE Access, **9**, pp. 17921-17942.

[55] Obeidat H., Shuaieb W., Obeidat O., Abd-Alhameed R., 2021. A review of indoor localization techniques and wireless technologies. Wireless Personal Communications, **119(1)**, pp. 289-327.

[56] Roy P., Chowdhury C., 2021. A survey of machine learning techniques for indoor localization and navigation systems. Journal of Intelligent & Robotic Systems, **101(3)**, pp. 1-34.

[57] Singh N., Choe S., Punmiya R., 2021. Machine learning based indoor localization using Wi-Fi RSSI fingerprints: an overview. IEEE Access, **9**, pp. 127150 – 127174.

[58] Yang T., Cabani A., Chafouk H., 2021. A Survey of Recent Indoor Localization Scenarios and Methodologies. Sensors, **21(23)**, 8086.

[59] Ouyang G., Abed-Meraim K., 2022. Survey of Magnetic-Field-Based Indoor Localization. Electronics, **11(6)**, 864.

[60] Farahsari P. S., Farahzadi A., Rezazadeh J., Bagheri A., 2022. A Survey on Indoor Positioning Systems for IoT-based Applications. IEEE Internet of Things Journal, **9(10)**, pp. 7680-7699.

[61] Roy P., Chowdhury C., 2022. A survey on ubiquitous

WiFi-based indoor localization system for smartphone users from implementation perspectives. CCF Transactions on Pervasive Computing and Interaction, pp. 1-21.

[62] Sorour S., Lostanlen Y., Valaee S., Majeed K., 2015. Joint indoor localization and radio map construction with limited deployment load. IEEE Trans. Mobile Comput., **14(5)**, pp. 1031-1043.

[63] Gu Z., Chen Z., Zhang Y., Zhu Y., Lu M., Chen A., 2016. Reducing fingerprint collection for indoor localization. Comput. Commun., **83**, pp. 56-63.

[64] Lee W. H., Ozger M., Challita U., Sung K.W., 2021. Noise learning based denoising autoencoder. In IEEE Communications Letters, **25(9),** pp. 2983-2987.

[65] Jia B., Huang B., Gao H., Li W., 2018. Dimension reduction in radio maps based on the supervised kernel principal component analysis. Soft Comput., **22(23)**, pp. 7697-7703.

[66] Lian L., Xia S., Zhang S., Wu Q., Jing C., 2019. Improved indoor positioning algorithm using KPCA and ELM. In Proc. 11th Int. Conf. Wireless Commun. Signal Process. (WCSP), 23-25 October, pp. 1-5.

[67] Imran S., Ko Y. B., 2018. A novel indoor positioning system using kernel local discriminant analysis in Internet-of-Things. Wireless Commun. Mobile Comput., **2018**, pp. 1-9.

[68] Adege A., Lin H. P., Tarekegn G., Jeng S. S., 2018. Applying deep neural network (DNN) for robust indoor localization in multi-building environment. Appl. Sci., **8(7)**, 1062.

[69] Lopez-de-Teruel P., Canovas O., Garcia F. J., 2017. Using dimensionality reduction techniques for refining passive indoor positioning systems based on radio fingerprinting," Sensors, **17(4)**, 871.

[70] Bengio Y., 2012. Practical recommendations for gradient-based training of deep architectures. In Neural Networks: Tricks Trade. Berlin, Germany: Springer, 2012, pp. 437-478.

[71] Bruha I., Famili A., 2000. Postprocessing in machine learning and data mining. ACM SIGKDD Explor. Newslett., **2(2)**, pp. 110-114.

[72] Zhuang F., Qi Z., Duan K., Xi D., Zhu Y., Zhu H., Xiong H., He Q., 2021. A comprehensive survey on transfer learning. Proc. IEEE, **109(1)**, pp. 43-76.

[73] Sazdar A. M., Alikhani N., Ghorashi S. A., Khonsari A., 2021. Privacy preserving in indoor fingerprint localization and radio map expansion. Peer-to-Peer Networking and Applications, **14(1)**, pp. 121-134.

[74] Wang Z., Xu Y., Yan Y., Zhang Y., Rao Z., Ouyang X, 2022. Privacy-preserving indoor localization based on inner product encryption in a cloud environment. Knowledge-Based Systems, **239**, 108005.

[75] van der Beets C., Nieminen R., Schneider T., 2022. FAPRIL: Towards Faster Privacy-Preserving Fingerprint-Based Localization. In: *SECRYPT*. 2022.

[76] Zhang X., He F., Chen Q., Jiang X., Bao J., Ren T., Du X., 2022. A differentially private indoor localization scheme with fusion of WiFi and bluetooth fingerprints in edge computing. Neural Computing and Applications, **34**, pp. 4111–4132.

[77] Hu Z., Li Y., Jiang G., Zhang R., Xie M., 2022. PriHorus: Privacy-Preserving RSS-Based Indoor Positioning. In ICC 2022-IEEE International Conference on Communications, pp. 5627-5632.

Kocaeli University

Kocaeli Journal of Science and Engineering

http://dergipark.org.tr/kojose
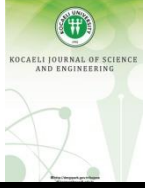
Ensemble Learning Approach to Chatbot Design Based on Paraphrase Detection

H. Toprak KESGİN [1, *] (iD) , Onur ÖZTUNÇ [2] (iD) , Banu DİRİ [3] (iD)

[1] *Department of Computer Engineering, Yildiz Technical University, İstanbul, Turkey,* **ORCID:** *0000-0001-7554-1387*
[2] *Department of Computer Engineering, Yildiz Technical University, İstanbul, Turkey,* **ORCID:** *0000-0001-8597-2770*
[3] *Department of Computer Engineering, Yildiz Technical University, İstanbul, Turkey,* **ORCID:** *0000-0002-6652-4339*

Abstract

In this paper, we present a design for an ensemble chatbot based on paraphrase detection. Our proposed chatbot is intended to assist companies in reducing the need for costly call center operations by providing a 24-hour service to customers seeking information about products or services. Our algorithm is designed to work effectively on small data sets, such as an existing FAQ, and does not require a large number of instances. We evaluated the performance of our chatbot using publicly available data from the websites of major telecommunication companies and found that the ensemble model improved success rates by 6% compared to the single best model, with a top 3 accuracy of 84.54% and a top 1 accuracy of 70.10%.

1. Introduction

In recent years, many companies have established call centers to improve customer satisfaction by providing 24-hour service. However, this can be a significant financial burden for the companies. To address this issue, companies have turned to chatbots as a means of reducing the need for call centers. Chatbots can increase self-service engagement and handle a significant number of customer requests, reducing the time that customers spend while waiting for the information. Domain-specific chatbots tend to be more successful than general-purpose chatbots.

In this study, we focus on the telecommunications field and develop a chatbot designed as a question-answering system. We create a dataset of question-and-answer pairs specific to the telecommunications field to do this. While the study is conducted within this particular domain, the chatbot design could be applied to any field with a similar dataset.

The chatbot operates by taking in a customer's question and measuring its similarity to the questions stored in the system. The answer to the most similar question is then returned to the customer as a response to their inquiry. To measure the similarity of the questions, we employ four different methods: cosine similarity of average sentence vectors, cosine similarity of weighted average sentence vectors, n-gram similarity of sentences, and word mover's distance. By combining all of these methods, we create an ensemble similarity measurement that outperforms any individual method. The proposed method is not limited to use in chatbot applications but can be utilized for any system requiring paraphrase detection.

The main contributions of this article to the literature are; the development of a novel ensemble chatbot for the telecommunications field that effectively reduces the need for costly call center operations by providing a 24-hour service to customers seeking information about products or services, the introduction of an ensemble model approach for measuring the similarity between questions, which demonstrates superior performance compared to individual methods and has the potential to be applied to a wide range of fields and systems requiring paraphrase detection, the design and evaluation of a chatbot that is able to achieve high accuracy and effectiveness with small datasets,

* Corresponding Author: tkesgin@yildiz.edu.tr

without the need for a large number of instances. This approach has the potential to significantly reduce the burden of data collection and annotation in chatbot development.

2. Literature Review

In this section, common techniques used in the design of chatbot models are presented. Many different techniques can be used to create a chatbot.

Template-based chatbots use pattern matching to answer user questions [1]. These systems are relatively easy to build and are a popular choice for small-scale applications [2]. Eslam et al. used BERT [3] vectors for chatbot design [4], training and testing their system on the SQuAD dataset [5]. Their workflow achieved 98% training and 96% test set accuracy. In a separate study, BERT was also used to develop a chatbot text classification system that aimed to reduce memory and storage needs by using a single model for multiple chatbots with multiple languages [6]. The proposed model demonstrated high accuracy and reduced system resources compared to individually trained models.

Transfer learning is widely used in the task of text classification, including in the context of chatbot intention classification. BERT and ERNIE (Enhanced Representation through Knowledge Integration) have been particularly effective in this regard, but their computational performance can be an issue in high QPS (queries per second) intelligent dialogue systems [7]. The authors propose using the knowledge of the ERNIE model to distil a FastText model, with the ERNIE model serving as a teacher model to predict massive online unlabeled data for data enhancement and guiding the training of the FastText student model. This approach not only maintains the FastText model's strong computational performance but also significantly improves its intention classification accuracy.

Recurrent Neural Networks (RNN) [8] have also been used in chatbot design, with one study proposing a system that actively interacts with the user to maximize their knowledge gain [9]. The proposed DeepProbe framework used a sequence-to-sequence (seq2seq) RNN and was evaluated using computer-based BLEU and AUC methods and human judge evaluation. Another study developed an ensemble-based dialogue system for the Amazon Alexa Prize competition, incorporating deep learning and reinforcement learning techniques, including seq2seq models and latent variable models for natural language processing [10].

Word embedding techniques, such as Word2vec and FastText, have also been applied to chatbot design.

Word2vec is an unsupervised and predictive method for representing words as vectors [11], with two deep learning algorithms: Continuous Bag of Words (CBOW) and Skip-gram. FastText, an improved version of Word2vec, also considers subword information while calculating word vectors [12].

Seq2seq is a technique that transforms an input sequence into an output sequence with a tag and attention value [13]. It consists of two RNNs: an encoder and a decoder. The encoder processes the input data and passes the last state of its recurrent layers to the decoder's first recurrent layers. The decoder then uses this initial state to generate the output sequence. Seq2seq has been used to analyze user input and generate a thought vector, which is then used to generate a response to the user. Martin Boyanov and Ivan Koychev proposed a system of answering questions in their work [14]. For this, they used the data collected from forums instead of dialogue question-and-answer datasets. The questions in the forums and the answers given to them were trained by using the seq2seq model. They used data collected from forums rather than dialogue question-and-answer datasets. The proposed system can answer correctly 49.5 % of the questions. In the questions asked in a completely new way, the accuracy rate decreases to 47.3%.

Chatbots can be used for many different applications. For example, a chatbot design consisting of 3 layers that analyzes and corrects Syntax errors in the Turkish language has been proposed [15]. In another study, a chatbot was proposed to be used in customer service management using the BERT model [16]. Another usage area of chatbots is recommendation systems. In another study, the seq2seq chatbot model was used in the Turkish venue recommendation system [17].

The reliance on large, labeled datasets and correspondingly large models is a common feature of effective chatbot systems. However, the acquisition and annotation of such data can be resource-intensive, and the cost of training large models can be high. In contrast, template-based or rule-based approaches that do not rely on extensive data may be less effective.

The use of chatbots in business marketing strategies has increased in recent years due to advances in artificial intelligence and the widespread acceptance of Internet and messaging platforms [18]. Also, it was found that the attitude of Turkish consumers toward chatbots has a positive effect on the intention to use chatbots [19]. In addition, the results of the research showed that the perceived usefulness and perceived ease of use of chatbots have a positive effect on the attitude toward chatbots.

We aim to advance the field of chatbot design and provide practical solutions for real-world applications, specifically addressing the need for cost-effective and

efficient customer service in the telecommunications industry. One of the key contributions of our research is the development of a novel ensemble model for measuring the similarity between questions, which not only outperforms individual methods for paraphrase detection in the context of our chatbot but has the potential to be widely applicable in any system that requires paraphrase detection. Additionally, we demonstrate the success of our chatbot using a small data set, which has the potential to significantly reduce the burden of data collection and annotation in chatbot development. Our research also differs from previous literature on chatbot design in that it focuses on a specific industry rather than general-purpose, and utilizes a domain-specific dataset of question-answer pairs. Overall, these contributions make our research a valuable addition to the field of chatbot design, particularly for applications that require paraphrase detection.

3. Materials and Methods

To develop our chatbot, we used a dataset of question-answer pairs obtained from frequently asked question sections of major telecommunication companies. We preprocessed the collected dataset to improve the performance of machine learning algorithms and used the FastText method to create word vectors for the words in the dataset. We measured the similarities between the questions using various methods and combined the similarity ratios of these methods to form the final ensemble similarity measurement.

3.1. Telecommunication FAQ Dataset

To evaluate the performance of our chatbot, we constructed a dataset of question-answer pairs using publicly available data from the websites of major telecommunication companies. We collected frequently asked questions from the websites across all categories and organized them into a dataset containing 1887 question-answer pairs, each consisting of a question, an answer, and the company it pertains to. We did not include categories of questions in the dataset to allow users to communicate with the chatbot without selecting a specific category. To receive service, the user simply needs to select the company they wish to receive service from and write their question or problem. To evaluate the effectiveness of the system, test questions were created by independent users that are semantically equivalent to the existing questions but are worded differently and were not used in the training of the model.

3.2. Preprocessing

The dataset underwent preprocessing to improve the machine's performance. To achieve this, we converted all characters in the sentences to lowercase, removed URLs and numbers, punctuation marks, and special characters, stemmed all words in the sentences, removed stop words, and detected and merged multi-word expressions (phrases). These techniques were applied to the dataset in order to enhance its overall performance.

3.3. Creating Word Embeddings

After preprocessing, word embedding was used to represent each word as a vector in space. In this study, FastText was used to create word vectors using the questions-and-answers dataset as input. FastText does not require a labeled dataset and can be trained in an unsupervised manner. It has been shown to be particularly effective at capturing semantic similarity. The CBOW and Skip-gram algorithms, window size, and word embedding size for the FastText method were compared as hyperparameters.

3.4. Creating Sentence Vector

The dataset consists of questions and answers. In order to find the most similar question to the user's question in the dataset, the user's question is compared to all questions in the dataset. Sentence vectors are created to measure the similarity between sentences. FastText vectors were used to create the sentence vectors. The goal of the sentence vector is to have sentences that contain similar words close to each other in the vector space. Two different methods were used to construct the sentence vectors: the average method and the weight average method.

In the average method, the vectors of the words comprising a sentence are summed and divided by the number of words in the sentence. The weight average method, on the other hand, gives more weight to words that contribute more meaning to the sentence. To calculate this effect, the term frequency-inverse document frequency (TF-IDF) measure was used to determine the importance of a word in a collection or corpus [20, 21]. The TF-IDF values of the same word in each sentence were averaged to create a fixed TF-IDF value for each word. A summary of the process for creating sentence vectors is shown in Figure 1.
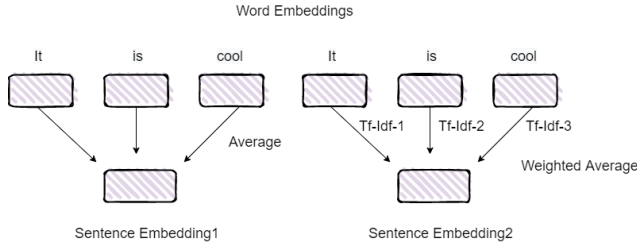
Figure 1. Creating Sentence Embedding

3.5. Sentence Similarity Methods

We calculated the similarity between the user-entered sentence and the questions in the dataset using the n-gram similarity method, the cosine similarity between sentence vectors for both average and weighted average sentence embeddings, and the reversed Word Mover's Distance method.

3.5.1. Sentence Similarity Methods

The cosine similarity between the sentence vector of the user-entered question and the vector of each question in the dataset was calculated. The similarity is defined as the scalar product of two vectors divided by the product of the lengths of the two vectors, as shown in Equation 1, where t is the sentence vector of the user's question and e is the sentence vector of a question in the dataset.

$$\cos(t, e) = \frac{t \cdot e}{|t||e|} = \frac{\sum_{i=1}^{n} t_i e_i}{\sqrt{\sum_{i=1}^{n}(t_i)^2}\sqrt{\sum_{i=1}^{n}(e_i)^2}} \qquad (1)$$

The similarity between the two sentences ranges from -1 to +1, with a value closer to +1 indicating a greater similarity.

3.5.2. N-gram Similarity

The n-gram similarity method is a character-based string comparison technique. In this method, a string is divided into n-grams based on the specified value of n. The n-gram similarity is calculated by dividing the number of common n-grams in the two sequences by the total number of n-grams in both sequences. This is formally defined in Equation 2, where s1 and s2 are the n-gram sequences in sentence 1 and sentence 2, respectively.

$$sim(s1, s2) = \frac{2 * |pairs(s1) \cap pairs(s2)|}{|pairs(s1)| + |pairs(s2)|} \qquad (2)$$

3.5.3. Word Mover's Distance

The Word Mover's Distance method calculates the distance between two sentences based on the word embeddings of the sentences. It has been shown to outperform many other methods in k-nearest neighbors' classification [22]. The method matches the two sentences using words or phrases that are closely related, even if they have no common words. The similarity is measured using word embeddings, and a word in one sentence may be expressed as a phrase in the other sentence. The Word Mover's Distance method handles this by merging words into phrases when necessary and calculating the distance by summing the distances of the nearest words.

For example, the distance between the sentences "Obama speaks to the media in Illinois" and "The President greets the press in Chicago" is 1.07, while the distance between "The band gave a concert in Japan" and the same first sentence is 1.63. This is because, after stop words are removed, the total distance of the matching closest words is higher in the second example.

3.6. Ensemble Method

Ensemble learning, which involves combining the predictions of multiple models, is a powerful technique for improving the performance of machine learning algorithms. Ensemble models are most effective when the individual models are both successful and diverse. In previous sections, we proposed four different methods for calculating sentence similarity: average sentence vector cosine similarity, TF-IDF weighted average sentence vector cosine similarity, n-gram similarity, and Word Mover's Distance. These methods approach the paraphrase detection problem in different ways.

The average sentence vector cosine similarity method is based on the assumption that the mean of the words in a sentence represents its meaning. The weighted average method takes a different approach by assigning higher weights to the most important words in the vector. The n-gram similarity method compares only n-grams and measures spelling differences between sentences, using a completely different approach from word embeddings. The Word Mover's Distance method, on the other hand, measures distance instead of similarity by matching the closest words or phrases in each sentence and adding the distances between them. This method is also distinct from the other approaches. The distance calculated by the Word Mover's Distance method is converted to similarity by taking its inverse.

Since our proposed method utilizes algorithms that make different assumptions and employ different techniques, combining the predictions of these algorithms significantly increases the success of the ensemble model.

4. Experiments

In this section, we describe our experiments, evaluation methodology, and results. We used the FAQ dataset described in Section 3.1 to evaluate the performance of our chatbot.

4.1. Measuring Performance

Measuring the model's performance requires questions that are not included in the training data. Therefore, we used questions that differ from the ones in the training dataset, but have the same meaning as one of them. The test questions were created by independent users. The accuracy of a question in a test dataset is calculated by computing similarities with each sentence in the training dataset. For the model to be successful, the sentence with the highest similarity value must be an equivalent sentence that has the same meaning as the sentence with the highest similarity value. After completion this process for all test sentences, the Top 1 accuracy of the model is determined.

In this measure, there is no difference between predicting the correct question in the second or third position and predicting the correct question in the last position. However, the Top n accuracy can also be important in chatbot-style applications. Therefore, we calculated the Top 1, Top 3, and weighted accuracy of the model in our experiments. Top 1 accuracy is whether the model answered the question correctly on its first prediction. The Top 3 accuracy is considered correct if the correct answer is among the first 3 answers of the model. In the weighted accuracy, if the model is correct on the first prediction, it scores 1; if it is correct on the second prediction, it scores 1/2, and so on until the 3rd prediction, that is, if it is correct on the third prediction, it scores 1/3. However, if the correct answer is not among the first 3 predictions, it is evaluated as 0. The mean of these scores is used as the weighted accuracy.

In this study, we propose a method for paraphrase detection that utilizes unsupervised techniques and does not require a labeled dataset containing examples of paraphrased and non-paraphrased sentences. Specifically, we use FastText and TF-IDF to generate sentence vectors, and then calculate the cosine similarity between these vectors and the distance of word carriers, and also use n-gram similarity to determine similarity between texts. All four of these methods are trained in an unsupervised manner, without the use of any label information. During testing, the most similar question to the query is identified and the answer to that question is provided to the user, eliminating the need for a dataset containing labeled instances of paraphrased and non-paraphrased sentences. This approach allows for the identification of paraphrases without relying on supervised learning algorithms, which typically require a large number of labeled examples. Overall, our method offers a practical solution for paraphrase detection in real-world applications.

4.2. Experimental Results

In this section, we present an analysis of the chatbot's performance. The system has been tested using questions provided by independent users. Only one answer is allowed for each question in order to produce reliable test results. We searched only for the questions related to the company.

We optimized the parameters of the algorithms. The FastText algorithm used to generate word vectors has three hyperparameters. For the optimization of the FastText model parameters, we used vector size (50, 100, 200), training algorithm (Skip-gram, CBOW), and Window Size (2, 3, 4). In the n-gram similarity method, we tested different values of n (1, 2, 3, 4, 5).

4.2.1. Stemming Parameter

Stemming is performed in the preprocessing step. Stemming is basically removing the suffix from a word and reducing it to its root word. In the preprocess stage, stemming is one of the parameters that most affect the success of the system. Tests were conducted to determine whether stemming was applied in parameter optimization.

In the optimization of the stemming parameter, skip-gram is used as the training algorithm with default parameters. Tests were performed for vector lengths 50, 100 and 200. The accuracy of the models created in cases where the stemming process is applied and not applied is shown in Table 1.

Table 1. Effect of Stemming

Stemming	Vector Size	Top 1 Acc	Top 3 Acc	Weighted Acc
Yes	50	62.89	80.41	72.44
Yes	100	**68.04**	83.51	**76.31**
Yes	200	67.01	**84.54**	76.07
No	50	59.79	79.38	70.23
No	100	60.82	78.35	71.76
No	200	61.86	80.41	72.72

Based on the accuracy values shown in Table 1, it appears that the stemming process improves performance. Therefore, stemming is applied in preprocessing step.

4.2.2. Selection of Training Algorithm

FastText has 2 training algorithms, CBOW and Skip-gram. Choosing the training algorithm as CBOW or Skip-gram is a hyperparameter that directly affects the success of the training. In order to measure the performance of the CBOW and Skip-gram algorithms, experiments were performed with default hyperparameters and for vector sizes of 50, 100, 200. Stemming was also applied for training and test set. Table 2 shows the accuracy of the models created with the CBOW algorithm and the Skip-gram algorithm. Experiments show that Skip-gram algorithm performed better than CBOW algorithm. It is also shown that the Skip-gram algorithm gives better results when using a small dataset. For these reasons, we chose our algorithm as a Skip-gram.

Table 2. Selection of Training Algorithm

Training Algorithm	Vector Size	Top 1 Acc	Top 3 Acc	Weighted Acc
Skip-gram	50	62.89	80.41	72.44
Skip-gram	100	**68.04**	83.51	**76.31**
Skip-gram	200	67.01	**84.54**	76.07
CBOW	50	62.89	82.47	73.66
CBOW	100	63.92	81.44	73.61
CBOW	200	**68.04**	80.41	75.53

4.2.3. Selection Window and Vector Size

The window size is another hyperparameter for FastText. One of the FastText assumptions is that the words around a word are the words associated with that word. This hyperparameter specifies the number of words to associate with the left and right sides of the word. For these experiments, the windows size selected as 2, 3, 4 tested for vector sizes of 50, 100, 200. The results are shown in Table 3. While window size 2 and vector size 100 gave the best results for top 1 accuracy, vector size 200 gave the best results for Top 3 and Weighted Accuracy.

Table 3. Selection Window and Vector Size

Window Size	Vector Size	Top 1 Acc	Top 3 Acc	Weighted Acc
2	50	62.89	77.32	72.19
2	100	**70.10**	82.47	77.01
2	200	69.07	**84.54**	**77.29**
3	50	62.89	80.41	72.44
3	100	68.04	83.51	76.31
3	200	67.01	**84.54**	76.07
4	50	63.92	80.41	72.83
4	100	62.89	81.44	73.41
4	200	64.95	**84.54**	75.05

4.2.4. Selection Window and Vector Size

The results obtained from the experiments were used to determine the optimal parameters for the model. The model was retrained using the optimal parameters obtained from the experiments. The model was tested using the test set again. The results obtained from the tests are shown in Table 4.

Table 4. Test Results for Optimal Parameters

Model	Top 1 Acc.	Top 3 Acc.	Weighted Acc.
Ensemble	**70.10**	**84.54**	**77.29**
Cos Sim Av. SV	54.64	77.32	65.81
Cos Sim Wt. Av. SV	53.61	64.95	59.71
N-Gram Sim.	63.92	80.41	72.59
WMD	59.79	76.29	68.81

The abbreviations in Table 4 are explained as follows: "Cos Sim Av. SV" stands for "Cosine Similarity of Average Sentence Vectors," "Cos Sim Wt. Av. SV" stands for "Cosine Similarity of Average Weighted Sentence Vectors," "N-Gram Similarity" refers to the similarity between n-grams in the text, and "WMD" stands for "Word Movers Distance." "Ensemble" refers to the combination of four models and the final model. The performance of the ensemble model was compared to the performance of the individual models. The results of the tests show that the ensemble model has the best performance among the models. The Top 1 accuracy of the ensemble model is 70.10%, the Top 3 accuracy is 84.54%, and the weighted accuracy is 72.32%. The Top 1 accuracy of the individual models ranges from 53.61% to 63.92%. The Top 3 accuracy of the individual models ranges from 64.95% to 80.41%. The weighted accuracy of the individual models ranges from 59.71% to 72.59%.

As a result, it can be concluded that the ensemble model has a better performance compared to the individual models. The ensemble model has improved the success rate by 6% compared to the individual model with the highest accuracy.

5. Application

The user interface has been created for the chatbot model created and a demo of the chatbot is shown in this section. Chatbot application works with a web server. Question received from the user is transferred to the application via the web server. The answer that the application finds is transmitted to the user through the web interface. The overall architecture of the system can be seen in Figure 5.

In the Operators section, the user can select the company they want to ask the questions about. On the left side there are chatbot answers with a blue background, on the right side there are user questions with a green background. The user can ask the question they want to ask in the" message" section and click the button on the right to send his message. The web user interface of the chatbot application is shown in Figure 2.
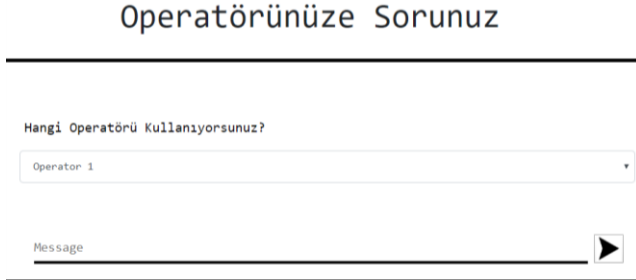
Figure 2. Web User Interface

The example in Figure 3 shows a successful example of how the system works. The user's question is shown on the right. Chatbot's answer is shown on the left. Likewise, if the user asks another similar question after the first, thinking that the user's problem cannot be solved, the system returns the second-best answer. An example of this is shown in Figure 4.
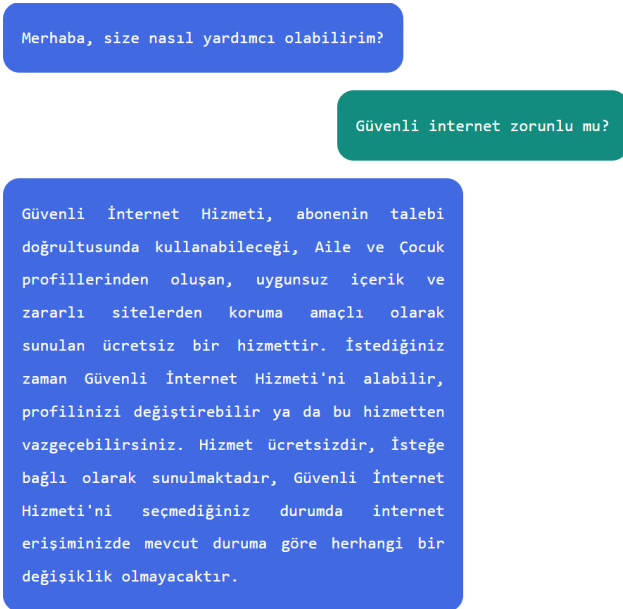
Figure 3. Web User Interface: Successful working example
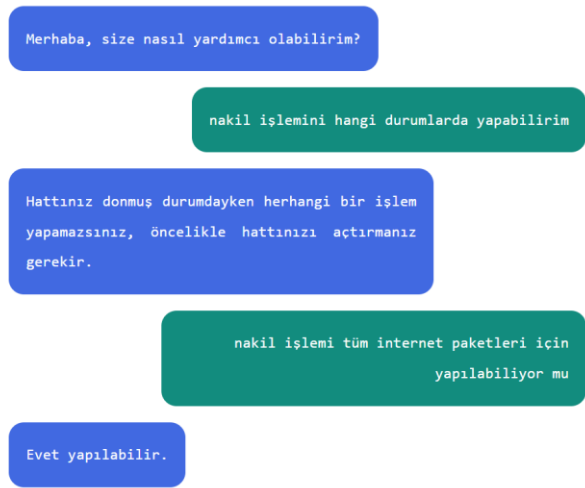
Figure 4. Web User Interface: Second best answer example

Furthermore, questions that are in the flow of conversation, such as greetings, are not in our database, these questions are kept separately and used as needed. Additionally, questions whose similarity to all sentences in the dataset is below a certain threshold will return an error message by the chatbot.
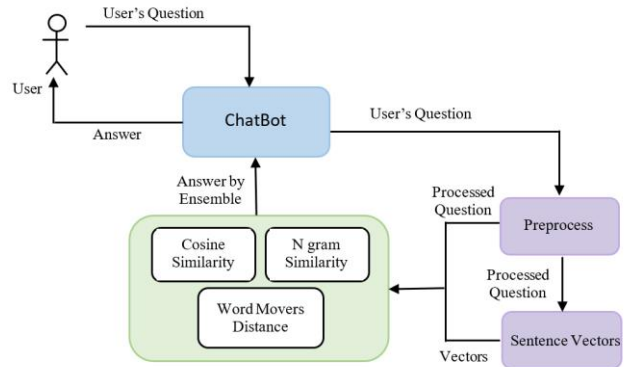
Figure 5. System Architecture

6. Conclusions

In this study, we aimed to show the answer to the user by measuring the similarity of the questions asked by the users to the questions in the system. To do this, we applied a detailed preprocessing on the dataset and the questions asked by the user.

We then used n-gram similarity and vectors created with the FastText model to measure these similarities. Sentence vectors were created using two different methods. With these sentence vectors, we calculated the cosine similarity of the user's question. In addition, we calculated the Word Mover's Distance using these vectors. Finally, we calculated n-gram similarities. The final similarity was measured using the results of these four methods together.

The proposed algorithm was tested with the prepared test questions for different parameters. According to two different accuracy measurement methods, the Top 3 accuracy was measured as 84.54% and the Top 1 accuracy was measured as 70.10% with the best parameters. These test results can be further improved by using a larger corpus with more texts and optimizing the parameters of the ensemble model.

It may take a long time to compare the user's question to all questions in a large dataset. In these cases, the category of the question can be determined with another model and the question can only be compared with questions within that category. The success of the ensemble model can be further improved by including the BERT vectors of the sentences in future studies.

Declaration of Ethical Standards

The author(s) of this article declare that the materials and methods used in this study do not require ethical committee permission and/or legal-special permission.

Conflict of Interest

The authors declare that they have no known competing financial interests or personal relationships that could have appeared to influence the work reported in this paper.

References

[1] AbuShawar B., Atwell E., 2015. ALICE chatbot: Trials and outputs. Computación y Sistemas, 19(4), pp. 625–632. Instituto Politécnico Nacional, Centro de Investigación en Computación.

[2] Luo B., Lau R.Y.K., Li C., Si Y.W., 2022. A critical review of state-of-the-art chatbot designs and applications. Wiley Interdisciplinary Reviews: Data Mining and Knowledge Discovery, 12(1), pp. e1434. Wiley Online Library.

[3] Devlin J., Chang M.W., Lee K., Toutanova K., 2019. BERT: Pre-training of Deep Bidirectional Transformers for Language Understanding. Paper presented at the North American Chapter of the Association for Computational Linguistics.

[4] Amer E., Hazem A., Farouk O., Louca A., Mohamed Y., Ashraf M., 2021. A proposed chatbot framework for COVID-19. Paper presented at the 2021 International Mobile, Intelligent, and Ubiquitous Computing Conference (MIUCC), IEEE, pp. 263-268.

[5] Rajpurkar P., Zhang J., Lopyrev K., Liang P., 2016. SQuAD: 100,000+ Questions for Machine Comprehension of Text. Paper presented at the Conference on Empirical Methods in Natural Language Processing.

[6] Taşar D.E., Şükrü O., Kutal S., Ölmez O., Gülüm S., Akca F., Belhan C., 2021. Performance Trade-Off for Bert Based Multi-Domain Multilingual Chatbot Architectures. Journal of Artificial Intelligence and Data Science, 1(2), pp. 144–149. Izmir Katip Celebi University.

[7] Sak H., Senior A.W., Beaufays F., 2014. Long short-term memory recurrent neural network architectures for large scale acoustic modeling. Paper presented at Interspeech.

[8] Yin Z., Chang K.H., Zhang R., 2017. DeepProbe: Information Directed Sequence Understanding and Chatbot Design via Recurrent Neural Networks. Proceedings of the 23rd ACM SIGKDD International Conference on Knowledge Discovery and Data Mining, pp. 2131–2139. ACM.

[9] Serban I., Sankar C., Germain M., Zhang S., Lin Z., Subramanian S., Kim T., Pieper M., Chandar A.P.S., Ke N.R., Mudumba S., de Brébisson A., Sotelo J.M.R., Suhubdy D., Michalski V., Nguyen A., Pineau J., Bengio Y., 2017. A Deep Reinforcement Learning Chatbot. ArXiv, vol. abs/1709.02349.

[10] Mikolov T., Sutskever I., Chen K., Corrado G.S., Dean J., 2013. Distributed Representations of Words and Phrases and their Compositionality. Paper presented at NIPS.

[11] Bojanowski P., Grave E., Joulin A., Mikolov T., 2016. Enriching Word Vectors with Subword Information. Transactions of the Association for Computational Linguistics, 5, pp. 135–146.

[12] Sutskever I., Vinyals O., Le Q.V., 2014. Sequence to Sequence Learning with Neural Networks. ArXiv, vol. abs/1409.3215.

[13] Boyanov M., Nakov P., Moschitti A., Da San Martino G., Koychev I., 2017. Building Chatbots from Forum Data: Model Selection Using Question Answering Metrics. ArXiv, vol. abs/1710.00689.

[14] Bilgin T.T., Yavuz E., 2021. Conceptual design of python ide with embedded turkish spoken chatbot that analyzes and corrects the syntax errors. Avrupa Bilim ve Teknoloji Dergisi, (29), pp. 415–424.

[15] İçseri İ., Aydın Ö., Tutuk K., 2021. Müşteri Hizmetleri Yönetiminde Yapay Zeka Temelli Chatbot Geliştirilmesi. Avrupa Bilim ve Teknoloji Dergisi, (29), pp. 358–365.

[16] Toprak G., Rasheed J., 2022. Machine Learning based Natural Language Processing for Turkish Venue Recommendation Chatbot Application. Avrupa Bilim ve Teknoloji Dergisi, (38), pp. 501–506.

[17] Barış A., 2020. A new business marketing tool: chatbot. GSI Journals Serie B: Advancements in Business and Economics, 3(1), pp. 31–46.

[18] Eroglu-Hall E., Sevim N., Bulut A., 2022. Çevrimiçi tüketici tutumları chatbotlara yönelik. EKEV Akademi Dergisi, (91), pp. 33–53.

[19] Luhn H.P., 1957. A statistical approach to mechanized encoding and searching of literary information. IBM Journal of Research and Development, 1(4), pp. 309–317.

[20] Sparck Jones K., 1972. A statistical interpretation of term specificity and its application in retrieval. Journal of Documentation, 28(1), pp. 11–21.

[21] Kusner M., Sun Y., Kolkin N., Weinberger K., 2015. From word embeddings to document distances. Paper presented at International Conference on Machine Learning, pp. 957–966

[22] Guo S., Wang Q., 2022. Application of knowledge distillation based on transfer learning of ERNIE model in intelligent dialogue intention recognition. Sensors, 22(3), pp. 1270.

Kocaeli University

Kocaeli Journal of Science and Engineering

http://dergipark.org.tr/kojose
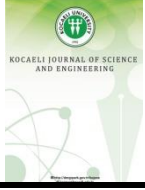
Determination of Groundwater Quality Index in Rural Area: The Case of Bartın City

Gülten GÜNEŞ [1], * (iD) , Burak AKTAŞ [2] (iD) , Mert Buğra BAHAR [3] (iD) , Eftal AVCI [4] (iD)

[1] Department of Environmental Engineering, Bartın University, Bartın, 74110, Turkey, **ORCID:** 0000-0002-1760-2695
[2] Department of Environmental Engineering, Bartın University, Bartın, 74110, Turkey, **ORCID:** 0000-0001-7864-7136
[3] Department of Environmental Engineering, Bartın University, Bartın, 74110, Turkey, **ORCID:** 0000-0001-6844-8416
[4] Department of Environmental Engineering, Bartın University, Bartın, 74110, Turkey, **ORCID:** 0000-0002-3249-1815

Abstract

The aim of the study is to determine the change of groundwater quality in rural areas in rainy and dry periods with respect to physicochemical parameters. pH, total dissolved solids, electrical conductivity, nitrate, sulfate, phosphate hardness, chloride, turbidity and color parameters were investigated. The water quality index (WQI) is widely used for detecting and evaluating water pollution. Water quality index was determined to be 35 and 32 in rainy and dry periods for drinking water. It was also calculated to be 37 for the rainy and dry periods according to the irrigation water limit values. As a result, since WQI<50, groundwater can be used as irrigation water as well as in domestic, industrial use. The difference between the rainy and dry period concentrations of some parameters (color, turbidity, PO_4^{-3}) was significant in the rural area. Color and turbidity were higher in the rainy period unlike TDS, EC and PO_4. In the urban area, significant increases were detected in NO_3^-, SO_4^{-2}, Cl^- concentrations in the rainy period. According to the correlation matrix, groundwater quality in rural areas is affected by multiple sources (aquifer geology, rocks, domestic wastewater, animal waste, river water interference).

1. Introduction

Groundwater is an important water resources used in homes, industrial facilities and agricultural activities [1]. Groundwater is used by approximately 30% of the world's population as drinking water or for various purposes at home [2]. Studies on groundwater quality [3-5] improve processes that manage groundwater quality and ensure effective management of groundwater resources [6]. For this reason, monitoring groundwater quality and determining the factors affecting its quality are important in terms of water quality management. Groundwater chemistry and properties are affected by many sources such as aquifer mineralogy, geochemical processes, excessive land use, source of recharge waters and anthropogenic sources [6-9]. For this reason, the sources that affect the groundwater quality can be categorized in two classes as geological and anthropogenic sources. In recent years, it has been determined that especially anthropogenic activities (urbanization, rapid population growth, industrialization and agricultural activities) negatively affect groundwater quality [10, 11]. Domestic, industrial wastewater discharges and animal wastes are anthropogenic sources that affect groundwater quality. Groundwater flow direction, topographic features, hydrological processes, different rock types are natural sources that affect groundwater metal concentration [10]. Local and regional geology, water/rock interaction, as well as the dilution effect of rainwaters affect groundwater quality [12, 13].

Agricultural activities, animal wastes and septic tanks in rural villages are considered as the most important anthropogenic sources affecting groundwater quality in this study area. Natural and synthetic fertilizers, pesticides, which are generally used during agricultural activities carried out in the gardens of houses or in greenhouses, are considered as other potential pollutants for groundwater. Since there is no sewerage system in the villages, the

---

* Corresponding Author: ggunes@bartin.edu.tr

collection of domestic wastewater in septic tanks is estimated as another source of pollution for groundwater. In addition, it is thought that the leakages that will occur as a result of the storage of animal wastes in the gardens or the use of fertilizers will be effective especially in the rainy period.

For this reason, in this study, it is aimed to: 1) determine the groundwater quality index in rural areas for rainy and dry periods, 2) determine the water quality index according to the limit values reported for irrigation water, and 3) estimate the sources that may be effective in rainy and dry periods using the correlation matrix 4) compare the water quality determined for rural areas and urban areas.

2. Materials and Methods

2.1. Sampling Area

Bartın is a city in the western Black Sea region of Turkey. Due to its geological structure, Bartın City offers a suitable formation environment especially for hard coal and industrial raw material deposits. The geological structure of Bartın province and its surroundings generally consists of formations containing shale, sandstone, limestone, dolomitic limestone, dolomite, claystone and marl. The formation carrying groundwater in the borders of the Central District is alluvial. The Eocene Flysch, which dominates almost the entire area, is alternated with abundant clayey and silty units. The annual rain average is 1049 mm. The average rain amounts for the winter and summer seasons are 112.8 mm and 70 mm. There are significant seasonal variations in monthly precipitation throughout the year in the Bartın region. The rainiest month in the Bartın region is December, with an average precipitation of 85 millimeters. The least rainy month in the Bartın region is May, with an average precipitation of 33 millimeters. The groundwater level in the study area is quite high and varies between 2 and 5 m. There is no regular storage area for solid wastes in the city and wastes are stored irregularly. In addition, the Bartın River, which passes through the city center, is fed by two separate branches as Kocaçay and Kocanaz Stream, and the river it forms is approximately 15 km. It reaches the Black Sea from the Bosphorus location by traveling a long way. Its flow rate is 12 m per minute and it discharges 1,000,000,000 m^3 of water into the sea every year [14].
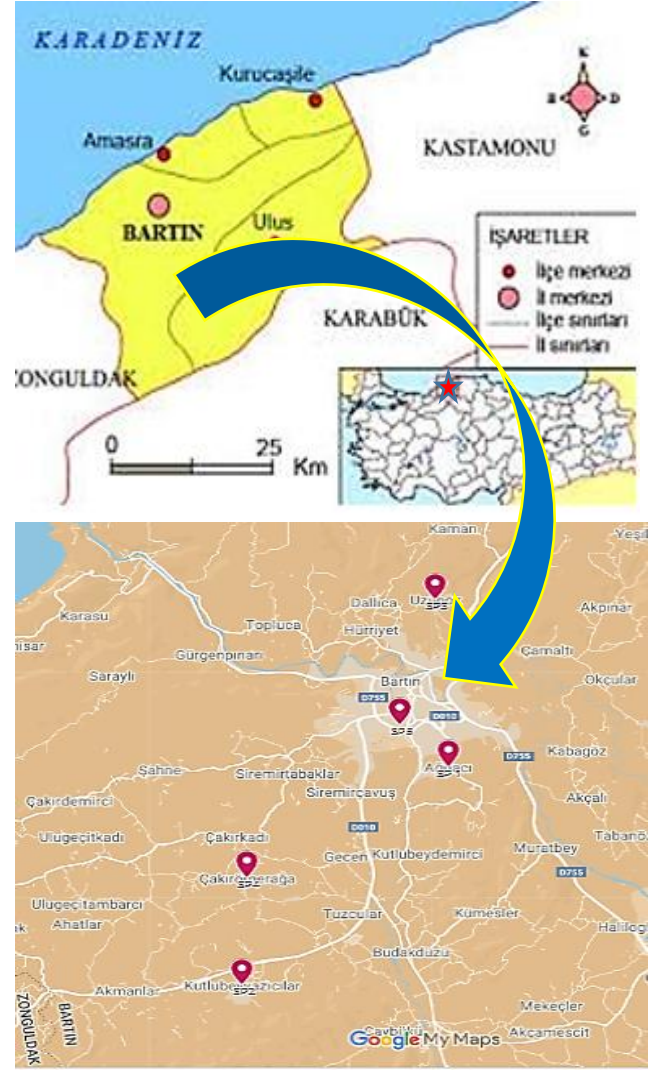
Figure 1. Groundwater sampling points

2.2. Sampling and Analysis

Samples were collected from 5 points in rainy (March and April) and dry (end of may and early october) periods. The reason for choosing the months of March and April is that the water level in the wells is high after rain and snowfall in winter. In May and October, the water level in the wells is low since it is after the dry period. In terms of representing the rural area, water samples were collected from 4 different villages. Water was sampled from only one point in the urban area to compare with the results obtained for the rural area. The shortest distance between sampling points is approximately 2.2 km, while the longest distance is 13 km (Figure 1). Samples for physicochemical analysis were collected with sterile plastic bottles in accordance with method ISO 5667-3:2018 [15]. Total dissolved solids, electrical conductivity, total hardness, turbidity, sulphate, nitrate, phosphate, chloride concentrations were determined. Phosphate, nitrate, sulphate and total hardness (TH) analyzes were made

according to the American Public Health Association Method [16]. Total hardness and chloride concentrations were determined by the titrimetric method. Phosphate, nitrate and sulphate were determined according to the spectrophotometric method by UV-VIS Spectrophotometer (HACH Lange 6000 DR). Turbidity and color were determined by turbidimetric (Hach 2100 Q Portable Turbidimeter) and colorimetric (Hach Lico 620) methods, respectively. pH, electrical conductivity (EC), temperature (T), total dissolved solids (TDS) were measured in situ (Hanna HI 9812-5) according to the electrode method. All calculations for the evaluation of the data were made with Microsoft Excel 2016 program.

2.3. Groundwater Quality Index (GWQI)

The water quality index is a widely used metric for detecting and evaluating water pollution. This index allows the water quality to be summed up with a single value and is calculated according to Eq. (1), Eq. (2), Eq. (3) and Eq. (4) [17]. According to this index, water quality can be categorized in 5 classes: <50: excelllent, 50-100: good water, 100-200: poor water, 200-300: very poor water, > 300: unfit for drinking [17]. The relative weight values (W_i) for each parameter were calculated according to Eq. (1).

$$W_i = \frac{w_i}{\sum_{i=1}^{n} w_i} \tag{1}$$

where W_i is the relative weight, w_i is the weight of each parameter (Table 1) [17, 18] and n is the number of parameters.

$$q_i = \frac{C_i}{S_i} \times 100 \tag{2}$$

where q_i= quality rating, C_i= concentration of each

chemical parameter in each water sample in mg/L, S_i = drinking water standard value for each chemical parameter in mg/L except for conductivity (μS/cm) and pH. S_i^*= Irrigation water standard value for each chemical parameter in mg/L except for conductivity (μS/cm) and pH.

$$SI_i = W_i \times q_i \tag{3}$$

where SI_i is the sub-index of the ith parameter; q_i is the rating based on concentration of ith parameter and n is the number of parameters.

$$GWQI = \sum SI_i \tag{4}$$

3. Results and Discussion

3.1. Evaluation of groundwater quality

The results of the physicochemical parameters are shown in Table 2. pH is an indicator of the acidic-basic interaction of the organic components of water and some minerals [13, 19]. pH was determined to be 8.5 and 8.3 for the dry and rainy periods, respectively, and showed slightly alkaline properties. In other studies, while acidic pH values were generally determined for industrial areas, it has been reported that pH changes from acidic to basic in rural, semi-urban and urban areas [17]. All pH values were in accordance with WHO [20] and TS [21] standards for drinking water (Table 2).

Total dissolved solids in groundwater are mainly related to inorganic salts and dissolved organic matter [22]. Salts can be of geogenic origin (decomposition of rocks) or anthropogenic origin (domestic/industrial wastewater discharge, pipe material feature in the water transport line) [23].

Table 1. Standard values, weightage factors and relative weights of water quality parameters.

	Weightage (w_i)	Relative weight (W_i)	S_i (standard values for drinking water) [20]	S_i^* (standard values for irrigation water) [24]	S_i^* (standard values for irrigation water) [25]
pH	4	0.16	6.5-8.5	8.5	9
TDS	4	0.16	1500	2000	>2100
EC	1	0.04	2500	3000	>3000
TH	2	0.08	500	120	
Phosphate	2	0.08	0.5[a]	6.13	
Sulfate	4	0.16	250	960	>960
Chloride	3	0.12	200	1063	>710
Nitrate	5	0.2	50	44	>50
	Σw_i=25	ΣW_i=1			

a Tirkey et al. [17], All parameters mg/L except pH and EC (μS/cm)

In this study, the TDS values were determined to be 273 mg/L and 504 mg/L for the rainy and dry periods, respectively. These values are suitable for drinking water according to the limit values reported in WHO standards. The higher concentration in the dry period indicates that the TDS is of geogenic origin, especially related to aquifer geology. While the lower groundwater level in this period causes the TDS concentration to increase, the increased amount of water during the rainy period may cause a dilution of TDS concentration.

The electrical conductivity is related to dissolved solids in water. It was determined to be 543 µS/cm and 964 µS/cm for the rainy and dry periods, respectively. According to WHO [20] and TS [21] standards, groundwater is suitable as drinking water in terms of EC. TDS and EC are directly proportional to each other. Therefore, the explanations for TDS also apply to the EC parameter. In a study conducted in Ghana, it was reported that the TDS concentration was higher in the dry period [26]. Mean values for TDS and EC in Arabia (Hail Zone) were reported to be 1119 mg/L and 2239 µS/cm, respectively [13]. For a rural area in India (Ranchi City), TDS and EC have been reported in the ranges of 51.4 -434 mg/L and 101-855 µS/cm, respectively [17]. In another study in Zimbabwe, EC was reported in the range of 169.1-922 µS/cm (452 µS/cm) [27].

The mean NO_3^- concentration (2.2 mg/L) was much lower than the limit values reported in WHO [20] and TS [21] standards. Although the concentration determined for the rainy period (2.24 mg/L) was higher than the concentration for the dry period (2.17 mg/L), the difference between both periods was insignificant. It is known that nitrate compounds in groundwater are related to nitrogen oxides in rain waters, leakage from nitrogen-containing fertilizers, interference from river water contaminated with NO_3^-, bacteriological conversion of NH_4^+ to NO_3^- in an oxygenated environment, and industrial discharges [6, 28]. In this study, the increase in concentration determined during the rainy period can be explained by the high solubility of nitrate in water [13] and the transport of nitrate compounds in the soil to the groundwater together with the rain waters. Since the sampling points are located in rural areas, it is thought that the nitrate compounds found naturally in the soil or those that may have leaked from manure, animal waste and septic tanks were transported to groundwater with rain waters.

In another study, it was determined that the NO_3^- concentrations in the groundwater samples (92 pieces) collected in July in the Amik Plain (Turkey) ranged between 0.38 and 300 (23.16) mg/L and only 2 samples exceeded the limit value (50 mg/L) reported for drinking water [29]. In another study conducted in Batman (Turkey), it was reported that NO_3^- concentrations ranged from 1.9-50.4 mg/L in 30 groundwater samples [30]. Again, in this study, it was determined that the limit value was exceeded in areas with agriculture and livestock activities, and it was reported that the highest concentrations were determined in the city center where anthropogenic sources (fertilizer and pesticide use) were effective [30]. In Ghana, it was reported that the NO_3^- concentration ranged from 0.4 mg/L to 48.4 mg/L (18.7 mg/L) (36 samples) and the limit value (50 mg/L) was not exceeded at any sampling point [31]. In another study conducted in Zimbabwe, the NO_3^- concentration was in the range of 0.032-3.22 mg/L, and the average concentration (1.45 mg/L) was close to that of this study [27].

Phosphate, on the other hand, showed an opposite trend compared to nitrate, and the concentration determined for the dry period (0.51 mg/L) was higher than the concentration of rainy period (0.29 mg/L). Although the average phosphate concentration was lower than the limit value reported in the literature [17], it exceeded the limit value, especially in the urban area during the dry period (Table 2). The concentration difference between the two periods was significant. The high concentration determined during the dry period can be explained by 2 reasons: 1) The low amount of water in the dry period and the longer contact of the water with the aquifer rocks 2) The phosphate compounds that can leak from the septic tanks. In addition, these results indicate that phosphate transport from the soil was not effective during the rainy season. This can be explained by the low solubility of phosphate [32] and its strong adsorbability on soil particles [17]. In Ghana [31] and Arabia [13], the mean phosphate concentrations were reported to be 0.4 mg/L (0.1 -1.2 mg/L) and 0.1 mg/L (0.01-0.43 mg/L), respectively [13].

Since the average sulfate concentration was determined to be 38 mg/L, it complies with the relevant standard values (Table 2). The concentrations were detected to be 40 mg/L and 36 mg/L for the rainy and dry periods, respectively. According to WHO [20] and TS [21] standards, groundwater is suitable as drinking water in terms of sulfate. Although there is no significant difference between the two periods, the high concentration in the rainy period can be explained by the dissolution of sulfate minerals in soil and rocks in rain waters.

In a study conducted in Zimbabwe, the SO_4^{-2} concentration was determined in the range of 0.146 to 12.7 mg/L (5.3 mg/L), which is lower than the concentration in this study [27]. In a study in India (Ranchi City), concentrations were reported in the range of 0-152.82 mg/L [17]. The concentrations determined in Arabia are in the range of 16.8-1242 mg/L (266 mg/L) [13], which is considerably higher than this study and other studies.

The average Cl^- concentration for the rainy period (18

mg/L) was higher than the dry period (13 mg/L) while there was no significant difference between them. The mean values determined for the chloride concentration were considerably lower than the limit values reported in the WHO [20] and TS [21] standards. These results for chloride are consistent with the results for nitrate and sulfate. Chloride mixes with groundwater from many sources, including natural (sea water intrusion, sedimentary rocks, soil minerals) and anthropogenic (domestic waste, animal waste, industrial waste) [17, 33]. As a result, the higher concentration in the rainy season for these 3 compounds can be explained by the contact of the soil or rocks with rainwater or the transfer of leakages from the sewage system or septic tanks to the groundwater with rainwater. It is known that domestic wastewater is one of the anthropogenic sources for NO_3^-, SO_4^{-2}, Cl^- salts dissolved in groundwater [6, 34].

The average TH concentrations were found to be 244 and 259 mg $CaCO_3$/L for the rainy and dry periods, respectively in this study area. According to the limit value (500 mg $CaCO_3$/L) reported in TS [21], groundwater is suitable as drinking water. According to the classification reported by [35], groundwater is in the hard water class since the average concentrations were in the range of 150-300 mg $CaCO_3$/L.

Similar to the phosphate compound, the total hardness was also higher in the dry period. Hardness in

groundwater is related to the rocks with which groundwater interacts and to the soil mineralogy containing Ca^{+2} and Mg^{+2}. Dolomite ($CaCO_3$, $MgCO_3$), which is one of the most important sources of industrial raw materials in Bartın, may be the cause of the total hardness in groundwater.

Turbidity and color were detected to be higher in the rainy season. The average values were detected to be 6.09 NTU and 54 Pt-Co in the rainy period. These values were higher than the limit values reported in the relevant standards (Table 2). Suspended solids such as clay and silt particles, organic matter, microscopic organisms and colloids cause turbidity in natural waters [36]. The dominance of silty and clay units in this study area also supports this idea. Fulvic and humic acids dissolved in water cause color formation in water [36]. Suspended or dissolved substances in water also affect the color of the water. In this study, it is thought that suspended solids and dissolved substances carried by rain waters cause color and turbidity in groundwater. At the sampling points where the color parameter was higher, the yellow color of the water may be related to the presence of fulvic and humic acids dissolved in the water [37].

Although the aim of the study was to determine the groundwater quality in the rural area, one of the sampling point was in the urban area and the results from rural area samples and urban area sample were compared.

Table 2. Summary of measured water quality parameters

	Rural			Urban							
	Dry	Rainy	Mean	Dry	Rainy	Mean	Tirkey et al. [17]	WHO [20]	TS [21]	Irrigation [24]	S_i^*(standard values for irrigation water) [25]
TDS	504	273	388	498	320	409		1000		2000	>2100
EC	964	543	753	990	650	820		2500	2500	3000	>3000
NO_3^-	2.17	2.24	2.20	3.4	4.9	4.2		50	50		>50
NO_3-N	0.49	0.51	0.5	0.77	1.11	0.95				10	
PO_4^{-3}	0.51	0.29	0.40	0.57	0.24	0.403	0.5				
PO_4-P	0.17	0.09	0.13	0.08	0.19	0.13				2	
SO_4^{-2}	36	40	38	37	69	53		250	250	960	>960
Cl^-	13	18	16	18	30	24		200	250	1063	>710
TH	259	244	251	281	295	288		500	500		
pH	8.5	8.3	8.4	7.9	8.4	8.2		6.5-8.5	6.5-9.2	8.5	9
Turbidity	0.87	6.09	3.5	0.33	2	1.0		5.0	1.0		
Color	13	54	33	3	25	14		15	20		

All parameters in mg/L except EC: (µs/cm). Turbidity: NTU. Color: Pt-Co (PCU). T:ºC. TH: Total hardness. TDS: Total dissolved solid. EC: Electrical conductivity

TDS, EC, NO_3^-, SO_4^{-2}, Cl^-, TH were detected higher in urban area unlike pH, turbidity and color. The sampling point in the urban area is located very close to the river (30-40 m). For this reason, it is thought that the river-

groundwater interaction or leakage from the sewer line may be effective at the point in the urban area. The largest concentration difference between rural and urban areas was determined for NO_3^-. In general, the variation of

parameters during rainy and dry periods is similar for both locations. In both settlements, NO_3^-, SO_4^{-2}, Cl^-, pH, color and turbidity parameters were higher in the rainy season. This situation can be explained by the transport from the soil during the rainy period, the interaction of river and groundwater, and the transportation of leakages from the sewage systems with the rain waters. The concentration difference of NO_3^-, SO_4^{-2}, Cl^- between both periods was greater in the urban area. In previous studies, it has been reported that Cl^-, SO_4^{-2}, NH_4^+, and NO_3^- salts dissolved in groundwater are related to landfill leakage, domestic wastewater, agricultural chemicals, industrial chemicals, and recharge waters [6, 34]. Similar to the rural area, the higher phosphate concentration in the urban area in the dry season indicated that phosphate may be related to aquifer geology and wastewater leakage. In the urban area, only PO_4^{-3}, turbidity and color exceeded the limit values reported in the relevant standards. According to the classification reported by [35], groundwater is in the hard water class since the TH concentration is in the range of 150-300 mg $CaCO_3$/L.

3.2. Evaluation of Suitability as Irrigation Water

According to the irrigation water standard values (Table 2), the groundwater was suitable as irrigation water in both periods. In another classification, irrigation water quality is categorized in 5 classes according to EC values [38]: EC<250 (Excellent), 250-750 (Good), 750-2000 (Permissible), 2000-3000 (Doubtful), >3000 (Unsuitable).

In this study, irrigation water quality was determined in the good quality class (EC=250-750 µs/cm) in the rainy period, while detected in the permissible quality class (750-2000 µs/cm) in the dry period.

The suitability of groundwater as irrigation water is categorized in 4 classes according to their total hardness [39]: <60 mg $CaCO_3$/L (soft), 60-120 mg $CaCO_3$/L (medium hard), 120-180 mg $CaCO_3$/L (hard), >180 mg $CaCO_3$/L (very hard). It was determined that the groundwater in the rural area is in the very hard water class as irrigation water in this study. One of the indexes used to determine the quality of irrigation water is the potential salinity, which is determined according to the SO_4^{-2} and Cl^- anions in the water. Potential salinity was calculated according to Eq. (5) [40]. Cl^- and SO_4^{-2} concentrations are taken as meq L^- in the equation.

$$PS = Cl^- + 0.5SO_4^{-2} \qquad (5)$$

Potential salinity values were determined in the range of 0.51-0.92 (0.74) in the dry period and between 0.78-

1.04 (0.93) in the rainy period. Since PS<3 in both periods, groundwater is suitable as irrigation water. It was determined that groundwater could be used as irrigation water according to the water quality parameters determined for the urban area. According to the EC parameter, the groundwater is in the permissible quality class (750-2000 µs/cm) as irrigation water for both periods. Similar to the rural area, the groundwater in the urban area is in the very hard water class as irrigation water.

3.3. Assessment of Water Quality Index

The water quality index was calculated according to the standard values reported for both drinking water and irrigation water for the samples collected from rural areas, and the average values are shown in Figure 2. Since the average WQI was calculated to be 35 and 32 for the rainy and dry periods, the groundwater was determined to be in the good quality class in both periods. According to the reported standard values for irrigation water, average WQI was calculated to be 37 for rainy and dry periods, and it was determined that groundwater was suitable for irrigation water. WQI values determined according to drinking water standard values showed that groundwater at all sampling points can be used in homes and industries as well as irrigation water.
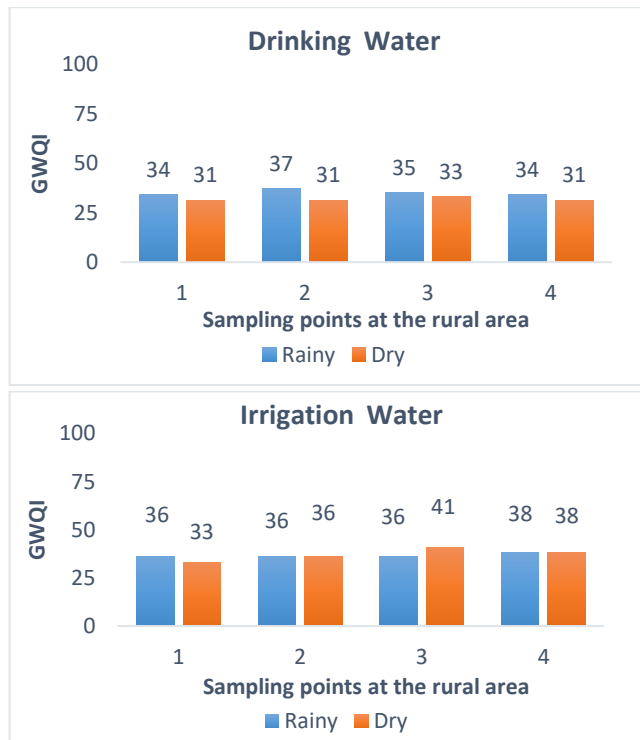

Figure 2. Water quality index values for groundwater

3.4. Correlation Matrix

The relationships between the physicochemical parameters of groundwater can demonstrate the processes that generated the water composition [6, 41]. In this study, the correlation matrix was created only for the rural area and is shown in Table 3. Significant negative correlations were determined between SO_4^{-2} and $TDS/EC/PO_4^{-3}/Cl^-$ during the rainy season. This shows that there is an inversely proportional linear relationship between SO_4^{-2} and these compounds. Inorganic salts can be formed from geogenic sources as well as from anthropogenic sources (domestic and industrial wastewater discharges) [23]. Geogenic sources may be related to soil mineralogy and aquifer geology. $TDS/EC/PO_4^{-3}/Cl^-$ parameters may be related to geogenic sources, especially aquifer geology, as well as leakages from septic tanks. While rain waters cause some minerals in the soil to dissolve and move to groundwater, it may cause dilution of some minerals related to aquifer geology.

Table 3. Correlation matrix for physicochemical parameters.

Parameters	TDS	EC	NO_3^-	PO_4^{-3}	SO_4^{-2}	TH	pH	Turbidity	Color	Cl^-
TDS	1	1.00	0.44	0.26	-0.71	-0.34	-0.93	-0.52	-0.04	-0.18
EC	0.92	1	0.45	0.25	-0.71	-0.32	-0.94	-0.53	-0.05	-0.19
NO_3^-	0.50	0.79	1	-0.38	-0.07	0.40	-0.70	-0.33	-0.55	-0.33
PO_4^{-3}	-0.10	-0.01	0.35	1	-0.85	-0.99	0.05	0.59	0.95	0.85
SO_4^{-2}	-0.26	-0.34	-0.55	-0.93	1	0.87	0.49	-0.20	-0.65	-0.56
TH	0.62	0.56	0.12	-0.83	0.58	1	0.01	-0.50	-0.93	-0.79
pH	-0.77	-0.78	-0.68	-0.55	0.81	0.00	1	0.65	0.35	0.39
Turbidity	0.18	0.24	0.46	0.96	-0.99	-0.65	-0.76	1	0.77	0.92
Color	0.03	0.11	0.40	0.99	-0.97	-0.75	-0.65	0.99	1	0.93
Cl^-	0.25	0.53	0.61	-0.46	0.32	0.64	0.04	-0.42	-0.45	1

Pink: rainy period; blue: dry period.

According to the positive correlation between chloride and phosphate, the sources of these compounds may be similar. Contrary to the positive significant correlation between TH and SO_4^{-2}, detected negative correlation between TH/PO_4^{-3} indicates that SO_4^{-2} and TH may be related to similar geogenic sources or river water intrusion.

Another remarkable point is the positive correlations between color/turbidity/phosphate/chlorine. This indicates that the sources of these parameters are the same. On the other hand, the negative correlation between color/turbidity and TH/SO_4^{-2} indicates that the sources of TH and SO_4^{-2} may differ from color and turbidity. The positive correlation between PO_4^{-3}, Cl^-, turbidity and color indicated that leakage from septic tanks, animal waste, and fertilizers can be effective in the rainy season. Additionally, the compounds in the soil can be dissolved by rain waters and transported to the groundwater.

A significant relationship was found between TDS and $EC/TH/NO_3^-$ in the dry period. Similar to the rainy season, positive correlation coefficients indicate that turbidity, color and PO_4^{-3} are affected by the same sources during the dry period. Unlike the rainy period, a positive correlation was found between Cl^- and NO_3^-/TH in this period. This indicates that different sources such as river water intrusion and irrigation water may be effective as well as geological sources and septic tanks in dry period.

These correlations indicated that SO_4^{-2} and TH could be affected by the same sources (geogenetic structures or river water inflow) in both periods. Color, turbidity and PO_4^{-3} may have been affected by anthropogenic sources, particularly leakage from septic tanks or animal waste. The results showed that the groundwater quality was affected by multiple pollution sources in both periods. In another study, no correlation was found between physicochemical parameters except $EC/Cl^-/Salinity$ [31]. It has been reported that groundwater may be affected by multiple sources, since no direct correlation could be determined between the pollution parameters (NO_3^-, PO_4^{-3}, Cl^-) [31]. In the study conducted in Arabia (Hail Region), a significant correlation was determined between TDS, EC, Cl^-, SO_4^{-2}, but no correlation was found between pollution indicators (NO_3^-, PO_4^{-3}, Cl^-) [13].

4. Conclusions

Groundwater samples collected from rural areas comply with the reported standard values for drinking

water according to WHO [20] and TS [21] standards. TDS, EC, PO_4, TH and pH were higher in the dry period. However, the concentration difference between the two periods of TDS, EC and PO_4^{-3} was greater. According to irrigation water quality standards, groundwater is of suitable quality as irrigation water. While groundwater is suitable as irrigation water according to the potential salinity index (PS<3) determined for SO_4^{-2} and Cl^- anions (except SP4 in the dry period), it is in the very hard water class according to the hardness parameter. TDS, EC, NO_3^-, SO_4^{-2}, Cl^-, TH were detected higher in urban area unlike pH, turbidity and color. The river-groundwater interaction or leakage from the sewer line may be effective at the point in the urban area. NO_3^-, SO_4^{-2}, Cl^-, pH, color and turbidity parameters were higher in the rainy season in both settlements. Concentration difference of nitrate between rural and urban areas was higher than other parameters.

According to the WQI values calculated according to the drinking water and irrigation water quality standard values, groundwater is suitable for both drinking water and irrigation water for both periods (WQI<50). According to the correlation matrix, a significant positive correlation was determined between Cl^-, PO_4^{-3}, turbidity and color during the rainy season. For this reason, it was estimated that the sources of these parameters were the same during the rainy season and they could be related to domestic wastewater or animal waste. The correlation between TH and SO_4^{-2} in the rainy season showed that these compounds may be related to geogenic sources (soil mineralogy, rocks) or river water intrusion. In the dry period, a significant positive correlation was determined between PO_4^{-3}/turbidity/color and SO_4^{-2}/TH as in the rainy period. A significant positive correlation was determined between Cl^-/NO_3^-/TH, different from the rainy period. As a result, it is thought that groundwater quality in rural areas is affected by many sources, including anthropogenic and geogenic sources.

Declaration of Ethical Standards

The author(s) of this article declare that the materials and methods used in this study do not require ethical committee permission and/or legal-special permission.

Conflict of Interest

The authors declare that they have no known competing financial interests or personal relationships that could have appeared to influence the work reported in this paper.

References

[1] Singh R.K. Sengupta B., Bal R., Shukla B.P., Gurunadharao V.S., Srivatstava, R., 2009. Identification and mapping of chromium (VI) plume in groundwater for remediation: a case study at Kanpur, Uttar Pradesh, Journal of the Geological Society of India, 74 (1), pp. 49–57.

[2] Adeyemi A.A., Ojekunle Z.O 2021. Concentrations and health risk assessment of industrial heavy metals pollution in groundwater in Ogun state, Nigeria. Scientific African 11, pp. e00666.

[3] Ledesma-Ruiz R., Pasten-Zapata E., Parra R., Harter T., Mahlknecht J., 2015. Investigation of the geochemical evolution of groundwater under agricultural land: a case study in northeastern Mexico, Journal of Hydrology, 521, pp. 410–423.

[4] Liu F., Song X., Yang L., Han D., Zhang Y., Ma Y., Bu H., 2015a. The role of anthropogenic and natural factors in shaping the geochemical evolution of groundwater in the Subei Lake basin, Ordos energy base, northwestern China. Science of The Total Environment, 538, pp. 327–340.

[5] Martos-Rosillo S., Moral F., 2015. Hydrochemical changes due to intensive use of groundwater in the carbonate aquifers of Sierra de Estepa (Seville, southern Spain), Journal of Hydrology, 528, pp. 249–263.

[6] Niu B., Wang H., Loáiciga H.A., Hong S., Shao W. 2017. Temporal Variations of Groundwater Quality in The Western Jianghan Plain, China. Science of the Total Environment, 578, pp. 542–550.

[7] Kurilić S.M., Ulniković V.P., Marić N., Vasiljević M., 2015. Assessment of typical natural processes and human activities' impact on the quality of drinking water. Environmental Monitoring & Assessment 187, pp. 659.

[8] Sahraei Parizi H., Samani N., 2013. Geochemical evolution and quality assessment of water resources in the Sarcheshmeh copper mine area (Iran) using multivariate statistical techniques. Environmental Earth Sciences, 69, pp. 1699–1718.

[9] Wang X., Ji H., Wang Q., Liu X., Huang D., Yao X., Chen G., 2016. Divisions based on groundwater chemical characteristics and discrimination of water inrush sources in the Pingdingshan coalfield. Environmental Earth Sciences, 75, pp. 1–11.

[10] Adewoyin O.O., Kayode O.T., Omeje O., Odetunmibi O.A., 2019. Risk assessment of heavy metal and trace elements contamination in groundwater in some parts of Ogun state, Cogent Engineering, 6 (1), pp. 1632555.

[11] Abraham M.R., Susan T.B., 2017. Water contamination with heavy metals and trace elements from Kilembe copper mine and tailing sites in Western Uganda; implications for domestic water quality, Chemosphere, 169, pp. 281–287.

[12] Zaidi F.K., Nazzal, Y., Jafri, M.K., Naeem, M., Ahmed, I., 2015. Reverse ion exchange as a major process controlling the groundwater chemistry in an arid environment: a case study from northwestern Saudi Arabia. Environmental Monitoring & Assessment, 187 (10), pp. 607.

[13] Abdel-Satar A.M., Manal H., Waed A.K., Alahmad R., Yousef W.M., Alsomadi H.R., Iqbal T., 2017. Quality assessment of groundwater and agricultural soil in Hail region, Saudi Arabia, Egyptian Journal of Aquatic Research, 43, pp. 55-64.

[14] Gunes G., 2019. The Change of Physicochemical Properties of Bartın River in Rainy and Dry Period. Dokuz Eylul University Faculty of Engineering Journal Of Science And Engineering, 21(63), pp. 761-774.

[15] ISO 5667-3:2018 Water quality Sampling Part 3: Preservation and handling of water samples. [Internet] https://www.iso.org/standard/72370.html.

[16] APHA, 2012. Standard Methods for the Examination of Water and Waste Water. 22nd ed. Washington, American Public Health Association, American Water Works Association, Water Environment Federation. DC: American Public Health Association.

[17] Tirkey P., Bhattacharya T., Chakraborty S., Baraik S. 2017. Assessment of groundwater quality and associated health risks: A case study of Ranchi city, Jharkhand, India. Groundwater for Sustainable Development, 5, pp. 85–100.

[18] Khan S.M., Kumar A.R., 2013. Geogenic assessment of water quality index for the groundwater in Tiruchengode Taluk, Namakkal District, Tamilnadu, India. Chemical Science Transactions, 2 (3), pp. 1021–1027.

[19] Sowrabha J., Narayana J., 2014. Assessment of ground water quality using for drinking purpose in Shivamogga Town, Karnataka, India. International Journal of Current Microbiology and Applied Sciences, 3 (12), pp. 381. 38.

[20] WHO, 2011. Guidelines for Drinking-water Quality, 4th ed. Geneva, Switzerland.

[21] TS 266, 2013. Regulation on Water Intended for Human Consumption. Official Gazette Date/Number: 07.03.2013/28580.

[22] U.S. Environmental Protection Agency, Office of Water, 1986. Quality Criteria for Water (Gold Book). EPA 440/5-86-001. Washington D.C.

[23] Raju N.J., Patel P., Gurung D., Ramb P., Gossel W., Wycisk P., 2015. Geochemical assessment Richardof groundwater quality in the Dun valley of central Nepal using chemometric method and geochemical modelling. Groundwater for Sustainable Development, 1, pp. 135–145.

[24] Ayers, R.S., Westcot, D.W. 1985. Water quality for agriculture. Irrigation and drainage, Food and agriculture organization of the United Nations. Rome, 29, pp. 1-117.

[25] Water Pollution Control Regulation Administrative Procedures Communiqué – Legislation. Published in the Official Gazette dated 7 January 1991 and numbered 20748.

[26] Kulinkina A.V., Kosinski K.C., Plummer J.D., Durant J.L., Bosompem K.M., Adjei M.N., Griffiths J.K., Gute D.M., Naumova E.N., 2017. Indicators of improvedwater access in the context of schistosomiasis transmission in rural Eastern Region, Ghana. Science of The Total Environment, 579, pp. 1745–55.

[27] Masocha M., Dube T., Dube T. 2019. Integrating microbiological and physico-chemical parameters for enhanced spatial prediction of groundwater quality in Harare. Physics and Chemistry of the Earth 112, 125–133.

[28] Umezawa Y., Hosono T., Onodera S.i., Siringan F., Buapeng S., Delinom R., Yoshimizu C., Tayasu I., Nagata T., Taniguchi M., 2009. Erratum to "Sources of nitrate and ammonium contamination in groundwater under developing Asian megacities". Science of The Total Environment 407, pp. 3219–3231.

[29] Ağca N., Karanlık, S., Ödemiş B., 2014. Assessment of ammonium, nitrate, phosphate, and heavy metal pollution in groundwater from Amik Plain, southern Turkey. Environmental Monitoring & Assessment, 186, pp. 5921–5934.

[30] Nalbantcilar M.T., Pinarkara S.Y., 2016. Public health risk assessment of groundwater contamination in Batman, Turkey. Journal of Water and Health, 14 (4), pp. 650-661.

[31] Lutterodt G., Miyittah M.K., Addy B., Ansa E.D.O., Takase M., 2021. Groundwater pollution assessment in a coastal aquifer in Cape Coast, Ghana. Heliyon, 7, pp. e06751.

[32] Elangovan N.S., Lavanya V., Arunthathi S., 2018. Assessment of groundwater contamination in a suburban area of Chennai, Tamil Nadu, India. Environment, Development and Sustainability, 20, pp. 2609–21.

[33] Sarath-Prasanth S.V., Magesh N.S., Jitheshlal K.V., Chandrasekar N., Gangadhar K. 2012. Evaluation of groundwater quality and its suitability for drinking and agricultural use in the coastal stretch of Alappuzha District, Kerala, India. Applied Water Science, 2, pp. 165–175.

[34] McArthur J.M., Sikdar P.K., Hoque M.A., Ghosal U., 2012. Waste-water impacts on groundwater: Cl/Br ratios and implications for arsenic pollution of groundwater in the Bengal Basin and Red River Basin, Vietnam. Science of The Total Environment, 437, pp. 390–402.

[35] Sawyer G.N., McCarthy D.L., 1967. Chemistry of sanitary engineers, 2nd edn. Mc Graw Hill, New York, p 518.

[36] Popek E., 2018. Sampling and Analysis of Environmental Chemical Pollutants, 2 th ed., Walnut Creek, California, USA.

[37] Bennett L.E., and Drikas M., 1993. The evaluation of colour in natural waters. Water Research, 27 (7), pp. 1209-1218.

[38] Richards L.A., 1954. Diagnosis and Improvement of saline and alkali soils. Agric. Handbook 60, USDA & IBH Publishing Company Limited, New Delhi, India. 98- 99.

[39] Dufor C.N., Becker E., 1964. Public water supplies of the100 largestcities in the United States, 1962: U.S. Geological Survey, Water-Supply Paper, pp. 1812.

[40] Doneen, L.D., 1964. Notes on water quality in agriculture, Published as a water science and engineering paper 4001, Department of Water Science and Engineering, University of California, 1964.

[41] Sahraei Parizi H., Samani N., 2013. Geochemical evolution and quality assessment of water resources in the Sarcheshmeh copper mine area (Iran) using multivariate statistical techniques. Environmental Earth Sciences, 69, pp. 1699–1718.

Kocaeli University

Kocaeli Journal of Science and Engineering

http://dergipark.org.tr/kojose
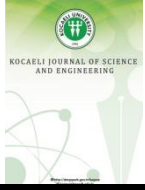
Detection of Fault from Acoustic Signals in Automobile Engines using Deep Learning Techniques

Fatih Alperen ERDOĞAN [1] (iD) , Ayhan KÜÇÜKMANİSA [2] (iD) , Zeynep Hilal KİLİMCİ [3, *] (iD)

[1] Department of Electronics and Communication Engineering, Kocaeli University, Kocaeli, 41001, Turkey, **ORCID:** 0000-0001-9871-6784
[2] Department of Electronics and Communication Engineering, Kocaeli University, Kocaeli, 41001, Turkey, **ORCID:** 0000-0002-1886-1250
[3] Department of Information Systems Engineering, Kocaeli University, Kocaeli, 41001, Turkey, **ORCID:** 0000-0003-1497-305X

Abstract

Detecting faults in automobile engines from sound signals is a challenging task in the production phase of automobiles. That is why it attracts engineers and researchers to handle this issue thereby applying various solutions. In this work, we propose a deep learning-based fault detection mechanism in automobile engines from different sound resources. In the dataset collection phase, various vehicle breakdown sounds are gathered from social media environments by constructing our own customized crawler. Moreover, noise addition is applied to increase the amount of data. Subsequently, raw audio files are processed at the feature extraction step employing mel-frequency cepstral coefficients. To detect the vehicle breakdown sounds, 1-D and 2-D convolutional neural networks, long short-term memory networks, artificial neural networks, and support vector machines are modeled. Experiment results show that the usage of a 1-D convolutional neural network is transcendent with 99% accuracy compared to the other techniques, especially, state-of-the-art studies are considered.

1. Introduction

With the rapid growth of the automobile industry, the detection of possible engine faults both during the production phase and individual use has crucial importance due to ensuring matutinal caution about the engine's situation of operation. There are so many reasons related to engine faults that can be arisen from the different parts of the automobile. For instance, flooded engine failure, ball failure, brake pedal failure, radiator water boiling failure, ripping motor failure, timing belt failure, engine failure due to lack of oil, etc. In this work, we concentrate on detecting automobile engine faults from sound signals.

Fault detection and condition monitoring of such engines using acoustic signals has been the object of many studies and has attracted interest from researchers and engineers. In [1], a visual point model is introduced to diagnose acoustic emission and vibration signals for fault detection in an internal combustion engine and drive axle

shaft. With the help of the template matching method, the proposed system can detect error states. The study concluded that the use of a visual model point model provides effective fault detection in an internal combustion engine and drive axle shaft. In [2], the authors propose to detect faults in an automobile engine by observing the acoustic emission status. Principal component analysis and discrete wavelet transform technique are performed to construct the feature space. Then, a support vector machine was used for classification in 300 sound samples, 150 of which were intact and the rest were faulty motors. The experimental results show that the proposed model can detect engine failures with an accuracy of 72.64%. In [3], a continuous wavelet transform model is proposed for the purpose of detecting faults in internal combustion engines. The authors concentrate on three different categories namely, slightly different form normal, clearly different form normal, and sound signal without fault. They report that the wavelet technique is efficient to diagnose faults in internal combustion engines. In [4], the authors investigate the combination of discrete wavelet transform (DWT) and neural networks in the detection of engine faults. With the

---

help of DWT, time and frequency domain information is also included unlike the other literature studies. In addition to DWT, Parseval's theorem is also utilized in the feature extraction step. After that, the classification task is performed by the neural network. The experimental results show that the proposed framework is capable to categorize different failures of engines.

In [5], the authors introduce a wavelet-based support vector machine for induction machine fault detection. In the first stage, feature space is constructed from a transient current signal with the help of a discrete wavelet transform. To perform the dimension reduction process, principal component analysis (PCA) and kernel PCA are implemented. After that, an SVM classifier is employed for the classification task to detect faults. Experiment results indicate that the utilization of W-SVM with Daubechies and Symlet kernels results in high accuracy. In [6], automobile fault detection is proposed using Fast Fourier Transform (FFT) on acoustic emission thereby distinguishing various operational states of a machine. With the usage of FFT, the fault within the ignition system of the engines can be detected from acoustic signals. Therefore, the frequency differences in the energy of FFT coefficients are the indicator of the resource of the faults that reflects the importance of features called representative attributes for the fault detection system. Then, PCA is carried out to provide for reducing the dimension of feature space. The authors inform that SVM classifier exhibits approximately 80% of accuracy. In [7], authors propose to categorize faulty and healthy sound signals from automobile engines using wavelet transformation at the feature extraction step. The sound signals are gathered from ignition system of four different automobile engines. After performing wavelet transformation at the feature extraction stage, more relevant features are picked up employing correlation-based feature selection (CFS) algorithm. Then, k-Nearest Neighbor (k-NN), Support Vector Machine (SVM), and multi-layer perceptron (MLP) method are utilized for the classification task. Experiment results show that k-NN technique with 5 neighbors outperforms other models for all datasets.

In [8], noise-based engine fault diagnosis is introduced thereby consolidating wavelet packet analysis, artificial neural network, and intensity analysis of sound (WPA-ANN). The noises of the engine-fault-diagnosis system are classified as normal and faulty using an artificial neural network after carrying out the feature extraction step with the discrete wavelet transform technique. Experiment results demonstrate that the proposed WPA-ANN method under nine different states is capable to detect faults in the engine. In [9], authors investigate fault detection in motors of unmanned aerial vehicle (UAV). Because brushless DC (BLDC) motors employed in UAVs operate at high speed bringing about failures, authors mainly focus on the propeller, eccentric and bearing faults in UAV motors by analyzing sound data. The statistical-based feature extraction techniques are applied to the sound data obtaining average, standard deviation, variance, correlation, kurtosis, and skewness scores. After that, decision tree (DT), SVM, and k-NN algorithms are utilized for the purpose of detecting faults. Authors report that SVM and k-NN exhibit similar classification results with nearly 99.75% of accuracy while DT performs approximately 99.16% of accuracy. In [10], the authors concentrate on the detection of failures in diesel engine components by performing classification tasks on the vibration and acoustic signals with the help of machine learning methodology. The signals are analyzed in the frequency-domain, time-domain, and time–frequency domain employing fast Fourier transform (FFT) and short-time Fourier transform (STFT) techniques. To perform the classification task, Artificial Neural Network (ANN) is modeled. Experiment results show that ANN efficaciously categorizes the scuffing faults in the components of diesel engine with 100% of accuracy. In [11], the authors present the vibration-based diagnosis of gear failures in internal combustion (IC) engine gearboxes utilizing the K star technique. At first, features are extracted from the vibration signals utilizing discrete wavelet transform. Furthermore, feature space is extended by more representative features with the aid of the decision tree method. Next, the classification task is considered as driving gear with a healthy state and gradual tooth failure states. K-NN algorithm, K-star algorithm, and locally weighted learning algorithm are assessed for the categorization task. Experimental results indicate that the classification performance of the K-star algorithm outperforms others with 97.5% of accuracy.

Recently, the application of deep learning algorithms in different research areas attracts researchers due to ensuring better results compared to the conventional machine learning models. The main reason behind of it is performing feature extraction process is carried out automatically. Thence, more representative features of the dataset are gathered with the help of deep networks, which strengthens the generalization capability of the system during the training stage.

In recent years, the application of deep learning methodology in a different type of motors for the purpose of detecting failures have become popular. In [12], Autoencoder -based unsupervised machine failure detection is proposed from acoustic signals for noisy domain adaptation. Authors concentrate on the proposed approach because of lacking research on functional adaptation models across different noisy domains and the

necessary bulky computational space. For this purpose, a noisy domain adaptive marginal stacking denoising auto-encoder (NDAmSDA) is proposed to address this problem on acoustic signals. To demonstrate the contribution of the proposed framework, datasets blended with additive white Gaussian noise (AWGN) and binary masking noise (BMN) from the motor tests and gear tests are evaluated. Experiment results show that the inclusion of auto-encoder-based fault detection model cuts across other models. In [13], authors introduce an efficient failure detection model employing convolutional attention neural network (CANN) model and continuous wavelet transform. At the data collection step, vibration signals are gathered and tagged into five classes namely, normal condition, outer ring fault, inner ring fault, misalignment condition, and broken rotor bar for induction motors. After that, vibration signals are converted into scalogram feature images with the aid of continuous wavelet transform. Next, the time-frequency images are constructed. The features of the images are evaluated as input of the proposed CANN model to diagnose the faults of the induction motor. The authors conclude the paper that the usage of the proposed framework exhibits superior performance with 99.43% accuracy compared to the literature studies. In [14], an approach is introduced for failure detection of hydraulic piston pumps with acoustic images, called adaptive convolutional neural network. Firstly, acoustic signals are transformed into time–frequency features by employing continuous wavelet transform. After constructing a base convolutional neural network, the architecture is improved providing parameter tuning with Bayesian optimization. After that, an improved model (CNN-BO) is used for classification purposes for detecting failures. Experiment results show that CNN-BO performs well and ensures better robustness in failure detection for a hydraulic piston pump.

In this work, unlike the studies done so far, we focus on the detection of different faults in automobile engines by using various deep-learning techniques that have not been tried before in the literature. At first, the dataset is constructed by gathering sounds of different faults from online video-sharing platforms. The sounds capture flooded engine failure, ball failure, brake pedal failure, radiator water boiling failure, ripping motor failure, timing belt failure, and engine failure due to lack of oil. Then, sound signals are extracted using mel-frequency cepstral coefficients to feed into the deep learning architectures. To detect the failure, 1-D and 2-D convolutional neural networks, long short-term memory networks, artificial neural networks, and support vector machines are modeled. Experiment results demonstrate that the 1-D convolutional neural network outperforms other models achieving a 98.5% of accuracy score.

This paper is organized as follows: Section 2 gives the methodology and proposed framework. Section 3 presents the experimental setup and results. Section 4 summarizes and discusses results and outlines future research directions.

2. Proposed Method

This work proposes a deep learning-based automobile engine fault detection system. The proposed method uses engine sounds as input data. Input data is preprocessed with the Mel-frequency Cepstrum Coefficient method for feature extraction. Then, features are fed to Convolutional Neural Network (CNN) and Artificial Neural Network (ANN) based approaches to classify engine sounds. Also, the proposed method is implemented on a mobile platform. The block diagram of the proposed method is shown in Figure 1.
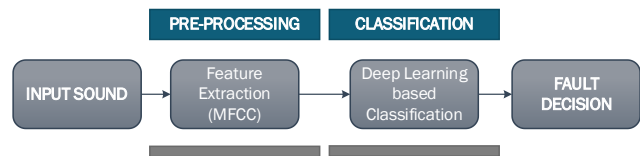

Figure 1. The block diagram of the proposed framework.

2.1. Pre-processing

Deep learning-based approaches have the capacity to perform feature extraction and classification together. However, in general, a large amount of training data is needed to perform these two functions together. In the case of limited training data as in the proposed method, features are extracted from the data with another process and these features are used as input data.

Mel-Frequency Cepstrum Coefficients (MFCC) is one of the well-known and successful feature extraction methods. The MFCC algorithm splits an audio signal into frames by reshaping it into smaller windows using the Hamming window. The spectrum is generated for each frame using the Fast Fourier Transform and each spectrum is weighted using a filter bank. Finally, the MFCC vector is calculated using the Logarithm and the Discrete Cosine Transform [15]. As a result of this processes 39 features are obtained but the first 10 are used as feature vectors, considering that they provided sufficient discrimination. In this study, audio signals are divided into 4 equal parts and 10 coefficients are calculated for each audio segment. therefore, each audio signal has 40 MFCC feature vectors.

2.2. Classification

In the study, ANN and CNN-based architectures are used to classify engine sounds. 1×40 size MFCC features are used as input data with these approaches. Proposed classification architectures are given in Figure 2.

Artificial neural networks are a method inspired by biological neural networks in the human brain. Artificial nerve cells (artificial neurons) form the structure of ANN with the connections they create. There are three or more interconnected layers in an artificial neural network.
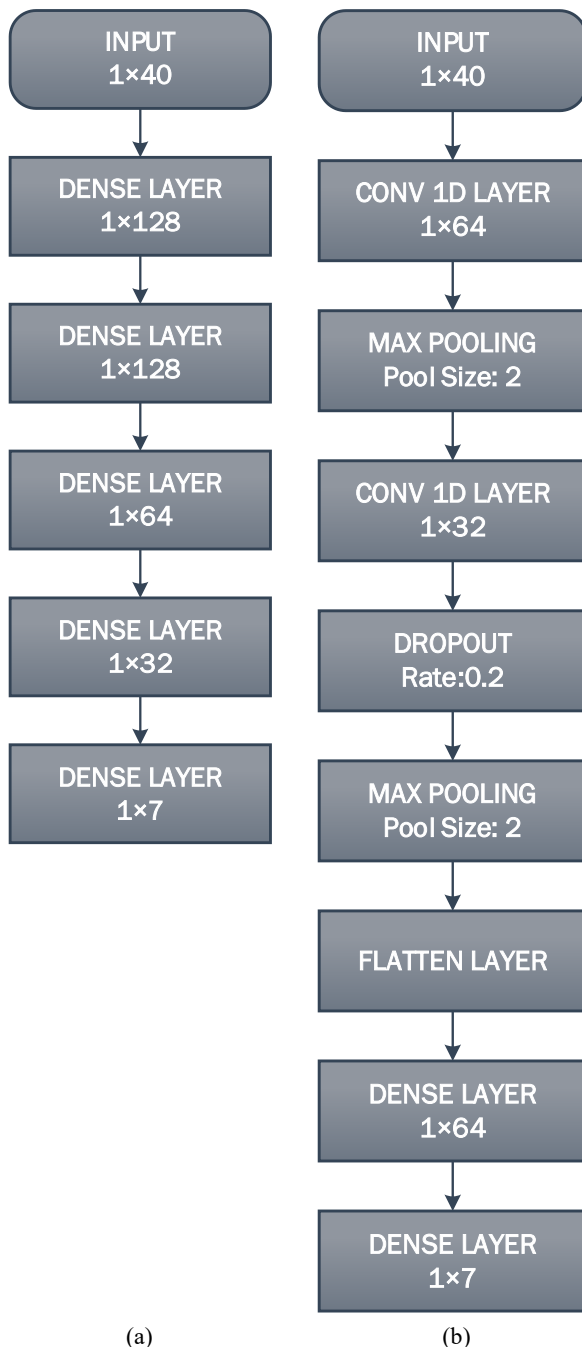
Neurons in the input layer compose the first layer. From the first to the last layer data transmission is carried out. The final layer is usually set up to output the desired result (classification, regression, etc.). The interconnected neural layer units attempt to learn about the information gathered by weighing it. As a result, the error is used to recalculate the weight of the ANN's unit connections to account for the difference between the desired and actual outcomes. Over time, the ANN will "learn" how to reduce this difference. The backpropagation algorithm is preferred to transfer the effect of this error calculated in the last layer to the previous layers and to update the weights depending on the error.

Deep learning approaches, as a continuation of artificial neural networks, have become popular in recent years. The concept of Deep Learning is developed with the aim of increasing the performance and effectiveness of artificial neural networks. Deep learning could be used in many tasks such as classification, object detection or regression. The deep neural network is a type of artificial neural network consisting of many hidden layers. Convolutional neural networks are the most widely used deep neural network. This network consists of one or more convolutional layers, a downsampling layer, a pooling layer and one or more connected layers like a standard multilayer neural network. The main advantage of CNNs is that it requires fewer parameters than a fully connected network with the same number of hidden units.

2.3. Mobile Platform Implementation

Systems created in traditional artificial intelligence studies are implemented in large-scale hardware environments such as computers. This approach has great benefits in the training, testing and analysis phases. However, it is not always possible to have high-capacity processing units when the developed methods are expected to be used in real life.

The deep learning model proposed in this study is implemented on a smartphone. Mobile application is developed on Android Studio using Flutter. The deep learning model trained on the computer is deployed to the mobile application using Tensorflow Lite. In Figure 3, a screenshot of the mobile device screen is shown while the proposed method is running on the mobile device.
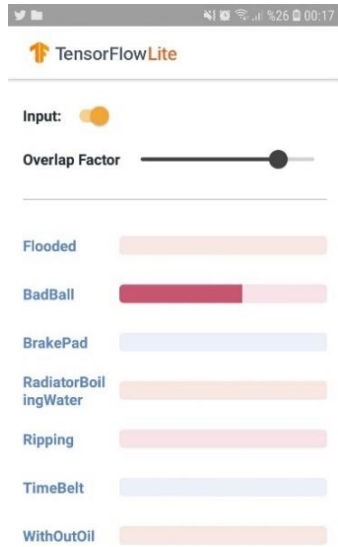

Figure 2. Network architectures used in the proposed model (a) ANN based (b) CNN based

Figure 3. Screenshot of mobile device implementation of the proposed method

3. Experimental Results

The vehicle fault detection sound dataset used in this study is created manually from social media platforms (Instagram, YouTube, etc.). In total, 5000 1 second duration audio recordings are recorded. Recorded vehicle fault types and sample sizes for each type are given in Table 1.

Table 1. Vehicle fault detection sound dataset properties

Fault Type	Sample Size
Flooded Engine Failure	714
Ball Failure	715
Brake Pedal Failure	713
Radiator Water Boiling Failure	715
Ripping Motor Failure	713
Timing Belt Failure	715
Engine Failure Due to Lack of Oil	715

To test the performance of the proposed method more comprehensively, Urban Sound Dataset [16] is also used. The urban sound dataset is a very comprehensive data set consisting of sound samples that are frequently encountered in daily life. It contains sounds belonging to 10 different classes given below.

- Air Conditioning
- Car horn
- Children's playing
- Dog barking
- Drilling
- Vehicle engine
- Gun firing
- Drill
- Siren
- Street music

The performance of the proposed method is evaluated using the formulas given in (1), (2), (3) and (4). These measures are calculated using the confusion matrix shown in Table 2.

$$Accuracy = \frac{TP + TN}{TP + TN + FP + FN} \tag{1}$$

$$Precision = \frac{TP}{TP + FP} \tag{2}$$

$$Recall = \frac{TP}{TP + FN} \tag{3}$$

$$F1 - score = 2 \times \frac{Precision \times Recall}{Precision + Recall} \tag{4}$$

The classification performance of the proposed method on the custom vehicle fault dataset and Urban Sound Dataset is given in Table 3 and Table 4, respectively. There are not many methods in the literature on vehicle fault detection using audio signals. Thus, it was not possible to compare the proposed method with a method working on the same subject. Therefore, sound recognition methods like the proposed method are used for performance evaluation. These methods shared their results on Urban Sound Dataset in their publications. Also, in order to analyze their performance on vehicle fault detection audio datasets, these methods are implemented with respect to their provided information. The performance evaluation of [17], [18] and the proposed method on the Urban Sound Dataset is given in Table 3 and the custom vehicle fault dataset is given in Table 4. In Table 3, their results are shared in their publications, and the results with our implementation and proposed method results are compared. In Table 4, the results obtained with our implementation and proposed method results are compared. In Table 3 and Table 4, those marked with "*" represents our implementations.

Although the main objective of the proposed method is not urban sound classification, it should be noted that the proposed method has decent performance according to Table 3. As seen in Table 4, CNN based proposed method has the best results with all metrics. This shows that the proposed method has superior capabilities for vehicle engine fault detection.

Table 2. Confusion matrix of proposed method

		Actual	
		Positive	**Negative**
Predicted	**Positive**	True Positive	False Positive
	Negative	False Negative	True Negative

Table 3. Performance evaluation on Urban Sound Dataset

Method	Precision	Recall	F1-Score	Accuracy
SVM [17]	0,68	0,72	0,69	0,70
SVM [17]*	0,75	0,80	0,84	0,82
CNN [17]	0,83	0,81	0,82	0,81
CNN [17]*	0,83	0,75	0,79	0,78
LSTM [18]	0,85	0,85	0,85	0,83
LSTM [18]*	0,81	0,76	0,78	0,78
ANN based	0,71	0,66	0,67	0,77
CNN based	0,70	0,65	0,67	0,76

Table 4. Performance evaluation on Vehicle Fault Sound Dataset

Method	Precision	Recall	F1-Score	Accuracy
SVM [17]*	0,98	0,97	0,97	0,96
CNN [17]*	0,98	0,97	0,97	0,97
LSTM [18]*	0,98	0,96	0,98	0,98
ANN based	0,70	0,65	0,67	0,76
CNN based	**0,98**	**0,98**	**0,99**	**0,99**

4. Conclusion

In this study, a deep learning-based fault detection method from audio signals is proposed. Within the scope of the study, a total of 5000 sound data of 1-second engine failures are collected on social media. After the dataset is created, feature extraction is performed using the Mel-Frequency-Cepstrum-Coefficients (MFCC) then 2 different architectures consisting of CNN, ANN are evaluated. In addition to the custom vehicle fault sound dataset, Urban Sound Dataset, which is more popular in sound recognition, is used in the performance evaluation of the proposed method. Experimental results showed that the combination of MFCC and CNN gives the best results with 99 % accuracy when compared to studies in the literature. In the future, it is aimed to make improvements on the proposed method by using long-term dependencies with RNN architectures such as LSTM.

Declaration of Ethical Standards

The authors of this article declares that the materials and methods used in this study do not require ethical committee permission and/or legal-special permission.

Conflict of Interest

The authors declare that they have no known competing financial interests or personal relationships that could have appeared to influence the work reported in this paper.

References

[1] Wu J. D., Chuang, C. Q., 2005. Fault diagnosis of internal combustion engines using visual dot patterns of acoustic and vibration signals, NDT & e International, **38**(8), pp. 605-614.

[2] Kabiri P., Makinejad A., 2011. Using PCA in acoustic emission condition monitoring to detect faults in an automobile engine, In 29th European Conference on Acoustic Emission Testing (EWGAE2010), 8-10 September, pp. 8-10.

[3] Wu J. D., Chen J. C., 2006. Continuous wavelet transform technique for fault signal diagnosis of internal combustion engines, NDT & e International, **39**(4), 304-311.

[4] Wu J. D., Liu C. H., 2008. Investigation of engine fault diagnosis using discrete wavelet transform and neural network, Expert Systems with Applications, **35**(3), pp. 1200-1213.

[5] Widodo A., Yang B. S., 2008. Wavelet support vector machine for induction machine fault diagnosis based on transient current signal, Expert Systems with Applications, **35**(1-2), pp. 307-316.

[6] Ghaderi H., Kabiri P., 2011. Automobile independent fault detection based on acoustic emission using FFT, In Singapore International NDT Conference & Exhibition (SINCE 2011), 3-4 November.

[7] Ghaderi H., Kabiri P., 2017. Automobile engine condition monitoring using sound emission, Turkish Journal of Electrical Engineering and Computer Sciences, **25**(3), pp. 1807-1826.

[8] Wang Y. S., Liu N. N., Guo H., Wang X. L., 2020. An engine-fault-diagnosis system based on sound intensity analysis and wavelet packet pre-processing neural network, Engineering applications of artificial intelligence, **94**, 103765.

[9] Altinors A., Yol F., Yaman O., 2021. A sound-based method for fault detection with statistical feature extraction in UAV motors, Applied Acoustics, **183**, 108325.

[10] Ramteke S. M., Chelladurai H., Amarnath M., 2022. Diagnosis and classification of diesel engine components faults using time–frequency and machine

learning approach, Journal of Vibration Engineering & Technologies, **10(**1), pp. 175-192.

[11] Ravikumar K. N., Madhusudana C. K., Kumar H., Gangadharan K. V., 2022. Classification of gear faults in internal combustion (IC) engine gearbox using discrete wavelet transform features and K star algorithm, Engineering Science and Technology, an International Journal, **30**, 101048.

[12] Xiao D., Qin C., Yu H., Huang Y., Liu C., Zhang J., 2021. Unsupervised machine fault diagnosis for noisy domain adaptation using marginal denoising autoencoder based on acoustic signals, Measurement, **176**, 109186.

[13] Tran M. Q., Liu M. K., Tran Q. V., Nguyen T. K., 2021. Effective Fault Diagnosis Based on Wavelet and Convolutional Attention Neural Network for Induction Motors, IEEE Transactions on Instrumentation and Measurement, **71**, pp. 1-13.

[14] Tang S., Zhu Y., Yuan, S., 2022. A novel adaptive convolutional neural network for fault diagnosis of hydraulic piston pump with acoustic images, Advanced Engineering Informatics, **52**, 101554.

[15] Yıldırım M., 2022. MFCC Yöntemi ve önerilen derin model ile çevresel Seslerin Otomatik olarak sınıflandırılması, Fırat Üniversitesi Mühendislik Bilimleri Dergisi, **34**, 449-457.

[16] Salamon J., Jacoby C., Bello J. P., 2014. A dataset and taxonomy for Urban Sound Research, Proceedings of the 22nd ACM International Conference on Multimedia, 3-7 November.

[17] Salamon J., Bello J. P., 2015. Unsupervised feature learning for Urban Sound Classification, 2015 IEEE International Conference on Acoustics, Speech and Signal Processing (ICASSP), 19-24 April.

[18] Lezhenin I., Bogach N., Pyshkin, E., 2019. Urban sound classification using long short-term memory neural network, Proceedings of the 2019 Federated Conference on Computer Science and Information Systems, 1-4 September.

Kocaeli University

Kocaeli Journal of Science and Engineering
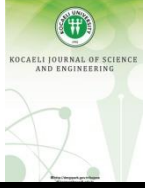
Evaluation of Noise Levels in Flour Factories in Terms of Occupational Health and Safety

Sirer ALBAYRAK [1, *] (iD) , Mustafa ÖZDEMİR [2] (iD) , Melike YAĞCI [3] (iD)

[1] *Program of Occupational Health and Safety, Ağrı İbrahim Çeçen University, Ağrı, Turkey,* **ORCID:** *0000-0002-3201-1789*
[2] *Department of Emergency Aid and Disaster Management, Bayburt University, Bayburt, Turkey,* **ORCID:** *0000-0002-6067-2007*
[3] *Department of Physical Therapy and Rehabilitation, Recep Tayyip Erdoğan University, Rize, Turkey,* **ORCID:** *0000-0001-7250-1750*

Abstract

This study aims to determine the daily noise exposure levels in flour mills and evaluate the effects on the health and safety of workers. The study measured the equivalent sound pressure levels of workers exposed in two flour mills operating in Konya province in dBA. The factories include machines with high noise levels, such as sifters, sieves, and rollers. A Type-2 class sound pressure level meter was used in the measurements taken in accordance with ISO 9612: 2009 standard. Based on the measured values, the A-weighted equivalent sound pressure levels were determined, and the daily personal noise exposure levels were calculated taking into account the working hours. It was determined that the equivalent sound pressure levels and the daily individual noise exposure levels of the workers were in the range of 88.2-97.7 dBA and 87.9-97.4 dBA, respectively, and above the minimum daily personal exposure limit (80 dBA) specified in the legislation. As a result of the study, it was evaluated that the noise in flour mills can negatively affect the health and safety of workers as well as their job performance.

1. Introduction

With the Industrial Revolution that began in Europe and America in the 18th century, there were significant changes in production methods and technology, and the era of machinery, which is synonymous with the Industrial Revolution for industrial production, began. Machinery made it possible to use machine power instead of human power and to produce based on machines, thereby increasing production speed, reducing costs, and improving product quality. The first mechanization occurred in the weaving, mining, manufacturing, transportation, and energy sectors, and soon thereafter, it was seen in all other sectors. Many countries worldwide aimed to replace human power with machine power and achieve this through shorter processing times and lower labor costs with the Industrial Revolution [1]. Machinery has made significant progress in production methods and technology, but along with these progressions, some problems have arisen. One of the most important of these

problems is noise. Noise is a natural result of mechanization and is a frequent problem in production facilities, factories, industrial areas, vehicles, and other industrial areas. The level of noise in these areas is high, and this high noise can create some health risks for workers.

Noise, one of the machine factors negatively affecting worker health caused by technological advancements, is generally defined as an unwanted, disturbing, and annoying sound. However, according to the International Labor Organization (ILO) 148 agreement on noise and vibration published in 1977, noise is defined as "all sounds that can cause hearing impairment or be harmful or dangerous in any other way" [2]. The effects of noise on human health can be grouped into physiological and psychological effects. The most obvious example of a physiological effect is temporary or permanent hearing loss. In addition, some effects such as increased blood pressure, cardiovascular system disorders, increased heart rate, and sleep disorders can also occur. Research has shown that the psychological effects of noise are more widespread than physiological effects. It has been found that noise can lead to changes in character depression and

* Corresponding Author: sireralbayrak@gmail.com

prolong the time it takes for the body to return to its normal state after being ill [3].

According to the Ministry of Labor and Social Security, it has been determined that hearing loss due to exposure to noise constitutes 10% of occupational diseases. However, while many occupational diseases can be treated, some hearing losses cannot be treated [4].

Flour factories are one of the most important work environments where workers are exposed to noise. Flour factories are industrial facilities that produce flour. In these facilities, grains such as wheat, barley, and oats are cleaned, ground into different sizes, and finally turned into flour. In this section, grinding, sifting, rolling, and other operations are carried out. The grinding machine separates the grain into pieces and opens up the surfaces of the particles. The sifting machine separates the small particles, cores, and other waste inside the flour using air currents after grinding. The rolling machine improves the size and shape of the particles inside the flour. The production process of wheat flour generally consists of the stages of raw material procurement, storage, cleaning, washing and rolling, grinding, screening, and storage. The cylinders called rollers in which the grinding process is carried out, the screw conveyors that perform product transfer between processes, the cleaning screens, and the distribution and washing sections are the regions that contribute heavily to noise exposure during this process [5].

Turkey is one of the most suitable countries for grain production in terms of climate and geography [6]. According to TUIK data, approximately 17.7 million tons of wheat were produced in Turkey's 160,615,720 hectares of grain production area in 2021 [7].

Today, there are approximately 621 factories with a production capacity of 24.5 million tons actively producing in Turkey, and these workplaces have a total of 13,710 employees, including 2,899 technical personnel [8]. In 2021, the flour sector had exports of $1.14 billion and imports of $2.67 billion, and the industry, which has a trade deficit of $1.53 billion and imports more than twice its exports, is a net importer. In 2021, the most exported products in the flour sector were wheat flour exports of 3,002,557 tons, wheat bran exports of 123,924 tons, and wheat exports of 3,946 tons, while the most imported products in 2021 were wheat imports of 7,819,217 tons, wheat bran imports of 1,490,419 tons, and wheat flour imports of 12,936 tons. The flour sector, which has a significant trade volume, imports a large amount. In 2021, of the $17.18 billion in food and agriculture imports, $2.67 billion, or 15.5%, was made with wheat, wheat bran, and wheat flour [9].

It can be seen from these statistics that the sector's importance to the country's economy is obvious. However, high production volumes bring high levels of automation.

If necessary occupational health and safety measures are not taken, severe physical risk factors to workers' health may arise.

Machines used in flour production facilities are high-level noise sources. Workers who work near these machines can experience hearing problems due to exposure to high noise levels. Long-term exposure to noisy areas can result in Noise-Induced Hearing Loss (NIHL) in workers. The noise levels of flour mills can also cause damage to workers at similarly hazardous levels [10, 11]. The dynamic nature of the food industry and its high employment opportunities in Turkey show that occupational health and safety are of utmost importance for the food industry in Turkey. When investigating the hazards related to occupational health and safety in flour factories, one of the factors that we need to pay attention to is noise.

It is necessary first to determine the noise levels emitted by the machines used in flour factories, which contribute significantly to the country's economy and are continuously updated with technological developments, in order to examine the adverse effects on human health and work efficiency. Only a few studies examine the noise levels in flour factories from an occupational health and safety perspective. Some of these studies are described below.

In a study conducted by Narasimhan et al., 2022, it was found that 107 workers in rice and flour factories in the state of Tamil Nadu, South India, were exposed to high levels of noise due to machinery in the workplace and experienced hearing loss [12]. In another study conducted by Nimgde et al., 2018 to evaluate occupational noise exposure of 65 flour mill workers in the city of Chandrapur, India, it was found that approximately 70% of the workers had hearing problems, and around 23% experienced constant headaches at work [13]. In a study conducted by Mohammadizadeh et al., 2015 on noise exposure for workers in various sections of a flour factory in Lamerd, Iran, values above the legal limits were detected, and it was reported that there was a relationship between the workers' age and the occurrence of hearing loss [14]. In this study, noise level measurements were taken in various sections of two flour factories in Konya, and the effects on the factory workers were analyzed.

2. Materials and Methods

The noise measurements were conducted in two flour mills operating in Konya province. After obtaining the necessary permissions from the authorities of the flour mills, the environmental measurements taken in the operations were included in the evaluation. The noise

measurements in the study were performed in the pneumatic, electric, sorter, and milling units, which were reported to have the highest noise levels in the flour mills.

The measurement of noise and sound is a broad subject and includes specific techniques. The sound types, spectral forms, time-dependent variables, and many other elements, along with the characteristics of the noise and the sounds planned for measurement, can greatly vary. Therefore, if the equipment used for the measurement is not selected according to the conditions and the purpose, there may be incorrect or misleading results [15].

Therefore, all measurements were carried out on January 4, 2022, by the rules under the "Regulations on the Protection of Workers from the Risks of Noise," which was published in the Official Gazette No. 28721 and became effective. During the measurements, the wind speed, humidity rate, temperature, and pressure of the working environment were taken into consideration. According to the TS EN ISO 9612 standard, task-based measurements were carried out by taking at least three measurements for each different task of the personnel carrying out the measurement. In work-based measurements, the total measurement time described by the standard is taken according to the number of personnel exposed to homogeneous noise. In full-day measurements, measurements are taken with a dosimeter for three full days (8 hours) and reported by calculating the results. In task-based measurements, the SPL meter, a type of hand-held sound level measurement device, is generally used, while in work-based and full-day measurement strategies, a dosimetric sound level measurement device, the Dosimeter, is used [16].

The noise measurement in this study was conducted based on the TS EN ISO 9612 standard, with job-based measurements being carried out and both stable short-term and unstable full-day measurements being conducted based on the TS 2607 ISO 1999 standard. In order to determine the noise level that workers in a flour factory are exposed to, EXTECH SL 355 devices, also known as personal dosimeters, which can both measure an individual's exposure level and the noise level of the work environment, were used [17]. Before starting the measurements, the noise measurement device was calibrated by a firm accredited by TÜRKAK with AB-0113-K and according to the TS EN ISO/IEC 17025-2017 standards. The measurements were made by the device attached to the workers and designed for these measurements. Equivalent SPL (LAeq) values were calculated using Equation (1) using the obtained SPL dBA values. The durations (Tm) for each task were determined by observing the occupational activities of workers in the flour factories where measurements were taken and by

conducting face-to-face interviews with them [8].

$$L_{P,AeqT,m} = 10\log\left[\frac{1}{I}\sum_{i=1}^{I} 10^{0,1 x L_{P,AeqT,mi}}\right] \quad (1)$$

$L_{P,AeqT,m}$: LAeq for task m, dBA

i: Task sample number

I: Total number of task samples

m: Task number

$$L_{Ex,8h,m} = L_{p,AeqT,m} + 10\log\left[\frac{\bar{T}_m}{T_0}\right] \quad (2)$$

$L_{Ex,8h,m}$: LAeq for task m contributing to the daily noise exposure level, dB(A)

$\bar{T}_m$: Effective duration of the working day for task m, h

T_0 : Reference duration, 8 h

Daily personal noise exposure levels were calculated with Equation (3).

$$L_{Ex,8h} = 10\log\left[\sum_{m=1}^{M} \frac{\bar{T}_m}{T_0} 10^{0,1 x L_{P,AeqT,m}}\right] \quad (3)$$

$L_{Ex,8h}$: Daily noise exposure level normalized to nominal eight h working day, dBA

M : Total number of tasks

The study made comparisons and evaluations based on the two flour factories and production units, considering the measured and calculated noise parameters. The parameters were summarized with graphs and figures, including standard deviation values. The possible effects of daily noise exposure values on the workers were evaluated and discussed, taking into account the 2003/10/EC directive of the European Parliament and Council (minimum levels of health and safety requirements for workers' exposure to physical agents).

3. Research Outcomes

This study determined that the equivalent weighted sound pressure level (Leq) in the flour factories measured was between 85.9 and 98.3 dBA, and the daily exposure level (LEX) was between 85.7 and 98.0 dBA. Upon examination of the Leq, Lmax, and LEX values determined in both flour factories, it was observed that the values found are similar to each other (Table 1).

Table 1. Leq, Lmax, and LEX values of the sections of the Flour Mills (Task-based)

Units	F1			F2		
	Leq,8h (dBa)	Lmax (dBc)	LEX	Leq,8h (dBa)	LcPeak (dBc)	LEX
Purifier Section	97.5±3.1	138.5±3.1	97.2±3.1	91.1±3,0	133.4±3.0	90.8±3.0
Sieve Section	85.9±2.0	112.4±2.0	85.6±2.0	90.5±2,0	116.4±2.0	90.2±2.0
Pneumatic Section	86.0±2.3	119.0±2.3	85.7±2.3	98.3±3,0	137.8±3.0	98.0±3.0
Waltz Section	97.2±3.3	137.3±3.3	96.9±3.3	98.3±3,1	139.4±3.1	98.0±3.1
Average	91.6±2.6	126.8±2.6	91.3±2.6	94.5±2,7	131.7±2.7	94.2±2.7

In the two flour factories, when the average of each section is considered, it has been determined that the Leq values in the sections of the factories vary between 88.2 dBA and 97.7 dBA, and the LEX values vary between 87.9 dBA and 97.4 dBA (Table 2).

Table 2. Average Leq, Lmax, and LEX values (Task-Based) for sections of Flour Factories

Units	Leq,8h (dBa)	Lmax (dBc)	LEX
Purifier Section	94.3±3.0	135.9±3.0	94.0±3.0
Sieve Section	88.2±2.0	114.4±2.0	87.9±2.0
Pneumatic Section	92.1±2.6	128.4±2.6	91.8±2.6
Waltz Section	97.7±3.2	138.3±3.2	97.4±3.2
Average	91.6±2.6	126.8±2.6	91.3±2.6

While the sifting sections contain the highest average Leq (97.7 dBA) and LEX values (97.4 dBA), the sifting sections contain the lowest Leq (88.2 dBA) and LEX values (87.9 dBA) (Table 1, Figure 1).
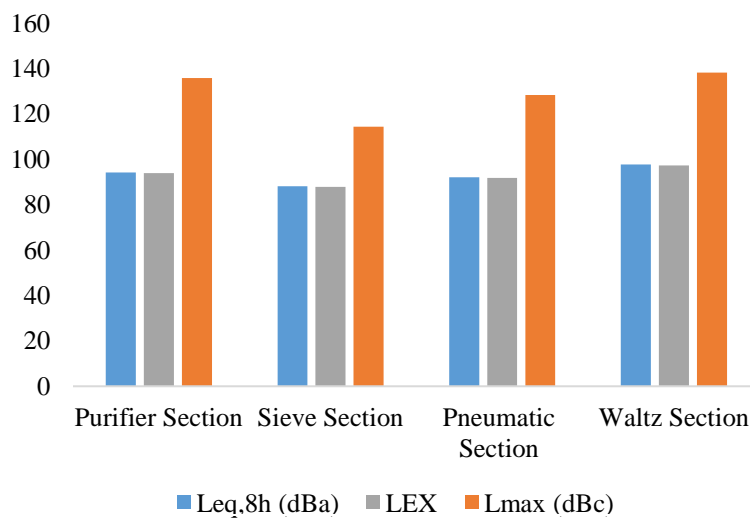
Figure 1. Average Leq, Lmax, and LEX Levels of Flour Factories

According to the 6331 Occupational Health and Safety Law, the obligations that employers and employees must comply with are clearly specified, and the aim is to eliminate the risks that arise from hazards in the working environment [18]. One of the most significant of these risks is noise. According to the Regulation on the Protection of Employees from Noise-Related Risks, published in the Official Gazette No. 28721 on July 28, 2013, and entered into force, Personal Protective Exposure Action Values and Noise Exposure Limit Values are given below.

1) Personal Protective Exposure Action Values and Noise Exposure Limit Values

a) Lowest Protective Exposure Action Values (LEX, 8 hours) = 80 dB(A) or (Ppeak) = 112 Pa [135 dB(C) re. 20µPa] (calculated as 135 dB (C) with reference to 20µPa).

b) Highest Protective Exposure Action Values (LEX, 8 hours) = 85 dB(A) or (Ppeak) = 140 Pa [140 dB(C) re, 20µPa].

c) Exposure Limit Values (LEX, 8 hours) = 87 dB(A) or (Ppeak) = 200 Pa [140 dB(C) re, 20µPa].

2) The protective effect of personal ear protective equipment should be considered when determining exposure to noise.

3) The effect of ear protectors is not considered in Protective Exposure Action Values.

4) In jobs where daily noise exposure shows significant variations from day to day, Weekly Noise Exposure Level can be used instead of Daily Noise Exposure Level in applying Exposure Limit Values and Protective Exposure Action Values. In such jobs:

a) The weekly noise exposure level, determined by sufficient measurement, does not exceed the 87 dB(A) exposure limit value.

b) Appropriate measures are taken to minimize the risks associated with these jobs.

Measurements taken at two flour factories located in Konya have resulted in noise levels exceeding the Personal Exposure Action Values and Exposure Limit Values given above. The values measured, taking into account the expanded measurement uncertainty, are not in line with the values in the aforementioned regulations when evaluated based on the limit values.

The Leq values in the waltz sections of the factories with codes F1 and F2 have been calculated to be 97.2 dBA and 98.3 dBA, respectively. The waltz sections are designed for grinding of grains and contain machines that work with crushing, cutting, and pressing forces to grind the product to the desired size. These machines are referred to as crushing and smooth rolls. The crushing rolls have gears, and the smooth rolls have a flat surface and drums covered with sandpaper, which are high noise sources due to friction. In both flour factories, it has been determined that there were oversights during the periodic maintenance of the roll machines, and the waltz section is the most high-risk section in terms of noise exposure.

The Leq values of the purifier sections in factories with the codes F1ve F2 have been calculated as 97.5 dBA and 91.1 dBA, respectively. The purifier sections are the areas where the grain is separated from straw, ears, and other foreign matter, and they contain large-sized and vibrating metal sieves and machines with engines that are high noise sources. It has been determined that there were shortcomings in the periodic maintenance of the sorter machines in both flour factories, and the purifier sections are the second highest risk areas in terms of noise exposure.

The Leq values of the pneumatic sections in factories with the codes F1ve F2 have been calculated as 86.2 dBA and 92.3 dBA, respectively. The pneumatic sections are the areas that transport grain to be ground to the upper levels, and they contain pneumatic pipes, gravity pipes, elevators, carriers (such as chain, screw, or belt conveyors, etc.). The noises of these carrier elements are high noise sources. It has been determined that there were shortcomings in the periodic maintenance of the pneumatic elements in both flour factories, and the pneumatic sections are the third highest risk areas in terms of noise exposure.

The Leq values in the sieve departments of the five F1ve F2 coded factories have been calculated as 85.9 dBA and 90.5 dBA, respectively. These departments are sections where large-scale screening machines with an oscillating shape are located to ensure that the particle size of the grain is the same after being ground into flour and the flour is homogeneous. These machines are also a high noise source, especially due to vibrations. Neglect of maintenance of the sieve units in both flour factories has been determined, and the sieve departments are the least risky in terms of noise exposure.

Noise, one of the most important harmful factors affecting workers' attention, fatigue, and work capacity, should be reduced in these departments to safety limits. Engineering control, which involves surrounding the noise source and is referred to as engineering control, can be taken as the first measure [19]. The second effective engineering measure is to separate the worker and machine with an acoustically designed cabin or barrier [20]. Management control can also be achieved by regulating break times and work frequency to limit worker exposure [21]. The last measure to be taken should be to provide the worker with personal protective equipment (headphones, earplugs, etc.).

Neither of the noise control methods has been applied in the two flour factories investigated to reduce noise. Without taking the necessary precautions, noise will

continue to have a negative impact on human health from a physiological, physical, and psychological perspective. Many studies have reported that different noise levels have negative effects on workers, such as thought, decision-making, learning, calculation, and hand-eye coordination [22, 23]. Noise can also reduce the productivity of workers. Grandjean (1988) reports that the decrease in productivity starts at 50-60 dB based on laboratory studies [24].

According to the results of the study, workers in all sections of flour factories (8 hours a day) are working in highly noisy conditions. The indoor SPL values of the factories were found to be between 70 and 89 dBA. Based on the Leq values measured, it can be seen that all workers in the flour factories are under health risks. In addition, no measures have been taken regarding the noise in the flour factories studied, and almost no measures have been taken for the health and safety of workers. The workers are untrained and have a very low awareness of work health and safety, so they work with very low-risk perception.

The cost of work accidents and occupational diseases is higher than the cost of preventing them [25, 26]. Taking this into account, efforts should be made to reduce the noise generated by the machine by taking precautions against risks at the source and in the environment in sections where the noise levels are high. In addition, it is also thought that outdated and poorly maintained machines can also be a negative parameter in the high noise levels. When the majority of the working environment poses a threat to the worker's health, instead of eliminating the source, it is preferred to provide the worker with personal protective equipment, which is the last operation that needs to be done instead of the first operation.

Generally speaking, it can be seen that the environmental measurements exceeding acceptable levels that can pose a threat to the health of the workers with regard to noise have been taken in both evaluated factories. Although reducing the source of factors such as noise in the field of occupational health and safety cannot be zeroed, it is accepted as the principle of reducing them. It is necessary to install new generation machines that reduce these factors in production facilities. If technology cannot reduce harmful factors at the source and in the working environment, emphasis should be given to personal protective equipment [27].

4. Conclusion and Suggestions

In this study, the noise levels were determined in one of the most important food industries in Turkey, flour mills, and the following main results were obtained:
• In both of the factories where measurements were

taken, it was observed that the noise exposure in the production sections (sasör, vals, screening, pneumatic) was above the limit values determined in the relevant regulations.
• It is estimated that the noise exposure values of the workers in the regions where the production processes of the factories are carried out are high. This is the main reason that the workers are in a closed environment where machines that continuously and steadily produce noise are located for a large part of their working hours.
• It was observed that no structural measures were taken against noise in the working areas where the measurements were taken. It was also determined that earplugs or other protectors that reduce the impact of noise at the point where it reaches were not widely used in these work environments where noise directly affects human health and work performance.
• Working at high noise levels in flour factories negatively affects both health and reduces work efficiency and safety in the work being done. On the other hand, the worker contracting an occupational disease is a serious cost for both the worker, the employer, and the state.
• In work environments where noise is at a level that can have negative effects on human health and work performance, measures to reduce noise should be taken at the source of the noise, on the transmission path, or at the point where it reaches.
• The general approach to reducing noise exposures is to try to eliminate noise before it occurs, just like reducing other risks. If a solution cannot be found by focusing on applications such as isolation, replacing hazardous with non-hazardous, collective protective measures, engineering solutions, etc., personal protective equipment must be used as a last resort.

Contributions of the Authors

The first author has managed data collection and analysis processes; the second and third authors have made contribution in terms of visualization, original draft, and writing. All the authors have the same rate of contributions for preparing the paper. All of them read and approved the final form.

Declaration of Ethical Standards

The author of this article declares that the materials and methods used in this study do not require ethical committee permission and/or legal-special permission.

Conflict of Interest

The author declares that she has no known competing financial interests or personal relationships that could have appeared to influence the work reported in this paper.

References

[1] Ersoy Z., Barışık T., and Petridis G., 2022. Tekstil Sektöründe Çalışanların Toz ve Gürültü Maruziyetlerinin Değerlendirilmesi. Journal of Medical Sciences, **3**(1), pp. 49-58.

[2] https://www.ilo.org/dyn/normlex/en/f?p=NORMLEXPUB:12100:0::NO::P12100_ILO_CODE:C148.

[3] Özyonar F., and Peker İ., 2008. Sivas Kent Merkezindeki Çevresel Gürültü Kirliliğginin Araştırılması. Ekoloji Dergisi, **17**(69), pp. 75-80.

[4] Soylu M. and Gökkuş Ö., 2016. Endüstriyel kaynaklı gürültü kirliliğinin araştırılması ve bir tekstil fabrikasında uygulama örneği. Erciyes Üniversitesi Fen Bilimleri Enstitüsü Fen Bilimleri Dergisi, **32**(2), pp. 1-7.

[5] Pomeranz Y., Wheat: Chemistry and Technology. AACC Monograph Series (USA), 1988.

[6] http://sanayi.tobb.org.tr/kitap_son3.php?kodu=1061210002.

[7] https://biruni.tuik.gov.tr/medas/?kn=92&locale=tr.

[8] Yağmur R., 2016. Un İmalatinda Çalişanlarin Gürültü ve Titreşim Maruziyetlerinin Değerlendirilmesi. Çalişma ve Sosyal Güvenlik Bakanlığı İş Sağliği ve Güvenliği Genel Müdürlüğü.

[9] https://www.tgdf.org.tr/wp-content/uploads/2022/05/TGDF-2021-Dis-Ticaret-Raporu.pdf.

[10] Akkoyun M., 2013. Gıda Sektöründe Yer Alan İşyerlerinde İş Sağlığı ve Güvenliği Uygulamaları. İş Müfettişi Yardımcılığı Etüdü, Bursa.

[11] Erbaş M., Aslan, S. and Durak, A. 2013. Unlarda Gıda Güvenliği Riskleri Ve Güvenli Un Üretimi İçin Un Fabrikalarında Hijyen ve Sanitasyon. Değirmeci Dergisi. Retrieved from https://www. millermagazine. com/unlarda-gidaguvenligi-riskleri-ve-guvenli-un-uretimi-icin-un-fabrikalarinda-hijyen-vesanitasyon/. html.

[12] Narasimhan S., et al., 2022. Audiometric notch as a sign of noise induced hearing loss (NIHL) among the rice and market flour mill workers in Tamil Nadu, South India. Hearing, Balance and Communication, **20**(1), pp. 21-31.

[13] Nimgade N.R. and Kamble R. 2018. Flour Mill Workers Occupational Noise Exposure in Chandrapur City, Central India. International Journal of Environment, **7**(1), pp. 1-13.

[14] Mohammadizadeh, M., et al. 2015. Noise pollution effect in flour factory on workers' hearing in Lamerd city. Journal of Medicine and Life, **8**(Spec Iss 3): pp. 208.

[15] Özey R., 2009. Çevre Sorunları, Aktif Yayıncılık, 3. Baskı, İstanbul.

[16] https://www.csgb.gov.tr/media/80070/9612-sunumu-haziran2021.pdf.

[17] http://www.extech.com/products/SL355

[18] https://www.mevzuat.gov.tr/mevzuat?MevzuatNo=6331&MevzuatTur=1&MevzuatTertip=5.

[19] Kroemer K.H., 2008. Fitting the human: Introduction to ergonomics. CRC Press.

[20] Sümer S.K., et al. 2006. Noise exposed of the operators of combine harvesters with and without a cab. Applied Ergonomics, **37**(6), pp. 749-756.

[21] Harris, D.A., 1991. Noise control manual. Van Nostrand Reinhold, **3**: pp. 45-53.

[22] Çiçek G. and Sümer S.K., 2021. Noise exposure levels in black tea processing factories and its effects on employees. Tekirdağ Ziraat Fakültesi Dergisi, **18**(2), pp. 282-291.

[23] Thatcher A., and Yeow P., 2018. Ergonomics and Human Factors for a Sustainable Future. Springer.

[24] Grandjean E. and Kroemer K.H., 1997. Fitting the task to the human: a textbook of occupational ergonomics. CRC press.

[25] Muzaffer K. and Akbıyık N., 2011. Türkiye'de İş Kazalarinin Maliyetleri Ve Çözüm Önerileri. Akademik Yaklaşımlar Dergisi, **2**(2), pp. 129-175.

[26] Murlidhar V., Murlidhar V.J. and Kanhere V., 1995 Byssinosis in a Bombay textile mill. National Medical Journal of India, **8**, pp. 204-204.

[27] Adrew Z., Engdaw D., and Tadesse T., 2011. Determinants of Occupational Injury: A Case Control Study among Textile Factory Workers in Amhara Regional State. Ethiopia: Journal of Tropical Medicine, **2011**, Art. No. 657275.

Transcutaneous Nerve Stimulation Current Thresholds Based on Nerve Bending Angle and Nerve Termination Point

Enver SALKIM [1, 2, *] iD

[1] *Department of Electronics and Automation, Muş Alparslan University, Muş, Turkey,* **ORCID:** *0000-0002-7342-8126*
[2] *Department of Electronics and Electrical Engineering, University College London (UCL), London, UK*

Abstract

There is increasing interest in using transcutaneous electrical stimulation to treat or suppress brain-related disorders. Primary headache disorder is a socioeconomic burden whose pharmaceutical and invasive treatment method may have troublesome side effects. There are various transcutaneous electrical nerve stimulation neuromodulation systems that are used for health-related disorders. TMany factors may affect these systems' efficiency, including stimulus current levels. A device for primary headaches showed mixed results. This may be related to the higher stimulus current levels that are applied through the electrodes. A feasible solution to reduce the required current levels is considering the geometrical features of the target nerve bending and nerve termination trajectories. In this study, the impact of the geometrical features of the nerve, such as nerve bending and nerve termination, on the stimulus current thresholds were analyzed based on FEM hybrid models. Twenty nerve models were generated considering statistical variations to assess the effect of the nerve geometrical features on the target neuromodulatory system. Finally, the safety parameters were calculated based on the target neuromodulator settings. The results showed that the geometric features of the target nerve have a significant effect on the required stimulus current thresholds. These results may provide important guidance mainly for transcutaneous nerve stimulation and future electrical nerve stimulation design.

1. Introduction

Transcutaneous electrical nerve stimulation (TENS) is a non-invasive method that is used globally to restore the function of biological disorders. In this technique, the current is applied through the skin via surface electrodes to depolarize the neural tissue underneath. Application of the extracellular stimulation of the peripheral nerve can restore the function of these neurological diseases or injuries by means of generation, inhibition, and modulation of brain activity [1]. The use of TENS as a therapy technique to treat primary headache disorders is growing. The primary headache disorders may be grouped as migraine, cluster headache, and tension-type headache, the most common diseases and leading causes of disability worldwide [2]. Migraine is a disabling neurological disorder (11.6%) [3] characterized by recurrent attacks of moderate to severe head pain associated with nausea, vomiting, photophobia,

and phonophobia [2]. Transcutaneous frontal nerve stimulation (t-FNS) is a peripheral neuromodulation method that has shown some positive results in migraine treatment. This promising non-invasive neurostimulatory therapy with Cefaly (Cefaly, CEFALY Technology, Lige, Belgium) stimulator has been developed to prevent an episodic migraine by stimulating the supraorbital (SON) and supratrochlear (STN) nerves which are the branches of frontal nerve [4]. This neuromodulator generates electrical pulses and transmits them via an electrode to the forehead area to activate the SON and STN nerve branches for alleviating pain, as shown in Figure 1. Studies on the effectiveness of the neuromodulator have shown mixed results [5, 6]. These complications can be associated with the required high current levels [7], due to the variations of the neuroanatomical structures.

It has been shown that the stimulus current levels of the nerve fibers may vary based on the geometric features

---

of the nerve trajectory, including nerve bending and nerve termination [8, 9]. These conditions may also have an impact on the electrical potential distributions along the nerve trajectories, which directly has an impact on the current levels of the stimulation. Also, it has been shown that the target nerve branches have different termination points and follow different angles based on available literature [8, 9]. Thus, analyzing the effect of nerve bending and nerve termination may guide optimizing the neuromodulator design. Investigation of such parameters

may not be possible using the experimental test. It may require massive trail studies which result in costly expenses. Alternatively, the computational models are growingly used in neuromodulation therapy systems to provide important insights into the design, operation, and clinical application [10]. Such models are usually implemented in finite element (FE) models (FEM) involving a volume conductor model representing various anatomical structures, a nerve fiber model, and the electrodes by their respective conductivities and appropriate boundary conditions.
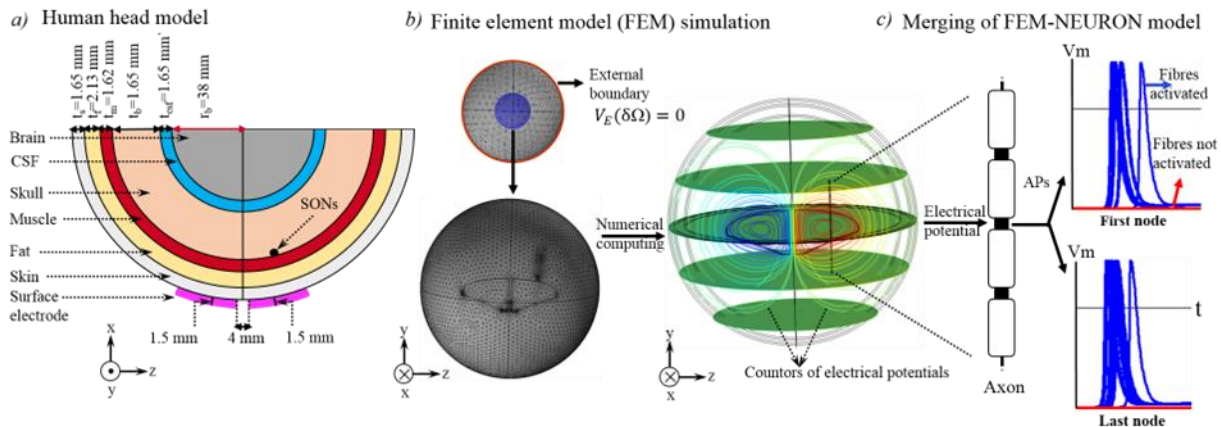

Figure 1. (a) The geometrical human head. Each layer was developed based on average thickness, r_b indicates the radius of the brain. (b.) Volume conductor of the geometrical human head model. The electrical potential distributions based on contours are highlighted. (c) Hybrid model (coupling FEM and neuron models). The extracellular potentials are applied to evaluate the response of the nerve fibers. A sample set of responses (action potentials (AP)) are shown for both the first and last nodes of the nerve fiber trajectory.

In the previous study [11], the realistic human head model was developed based on magnetic resonance imaging (MRI) and the human head was developed based on geometric shapes by mimicking the realistic human head model. It was shown that the geometrical human head could be instead with some error (3%, based on stimulus current thresholds). Also, it was shown that there is no serious effect of the microscopic structures on the stimulus current thresholds [12]. Therefore, in this study, the geometrically realistic human head (as shown in Figure 1a.) is used to evaluate the effect of nerve termination and nerve bending on the stimulus current thresholds for the target neuromodulator.

In this study, twenty different nerve models were generated to analyze the impact of nerve bending and termination on the stimulus current thresholds for given electrode settings. Each model was simulated, and the obtained extracellular potentials were distributed along the nerve trajectory to calculate nerve response to various current levels. Each model was simulated, and the obtained extracellular potentials were distributed along the nerve trajectory to calculate nerve response to various current levels.

2. Materials and Methods

2.1. Volume Conductor Model

TENS human head computational models can be constructed in a range in complexity from concentric sphere models to high-resolution models based on an individual's image data set, depending on the clinical question [13]. The anatomically specific image-based head modeling may require extensive prior work on computational modeling. In the studies [11, 12], it was shown that the geometrical human head (e.g., sphere) could be used instead of MRI a highly detailed human head model, to analyze the effect of model complexity on the stimulus current thresholds and current density with less computation cost but sufficient accuracy. As the clinical question of this study is the same (current thresholds), human head tissue layers and Cefaly patch electrodes were constructed from geometric shapes in COMSOL Multiphysics v5.2a (COMSOL, Ltd., Cambridge, U.K.). The head model consisted of six concentric spheres representing skin, subcutaneous tissue, muscle, skull, Cerebrospinal fluid (CSF), and brain, as detailed in Figure 1(a). The average thickness of each tissue

layer (skin: 1.65 mm [14, 15], fat: 2.13 mm, muscle: 1.62 mm [16], skull: 6.35 mm [17], and CSF: 1.5 mm) was used based on available literature to construct the layers in the geometrical model as indicated in Figure 1(a). As the electrical potential field decays considerably within the skull, the white and gray matter were merged and modeled as a homogeneous volume representing the brain. For this reason, the variations in the trajectory of the were only

considered within the skull to the subcutaneous plane level.

It was assumed that the human head is symmetrical. Therefore, the nerve models were generated only for the left side, as shown in Figure 2. The electrode model was generated separately and merged with the skin. The full list of anatomical tissue layers, electrode patch, and their relative size are shown in Figure 1.
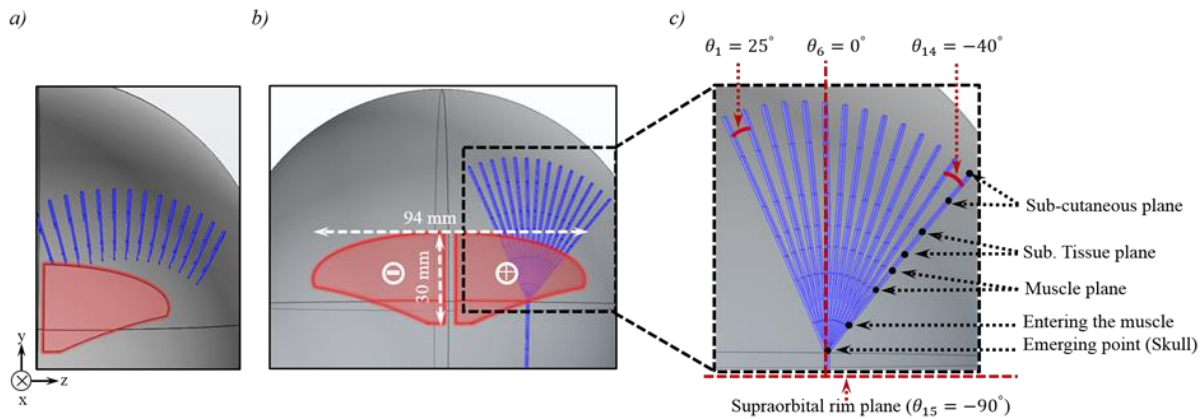

Figure 2. (a) Shows nerve trajectories on the subcutaneous plane. The nerve models are shown in blue, and the electrode patch is shown in red (b) Shows all feasible nerve models based on the statistical variation. The electrode size is highlighted. (c) Shows the generated nerve models in detail. The bending angle and the nerve transition points through the anatomical layers are labelled.

2.2. Nerve Model

The volume conductor of each nerve was constructed from geometric shapes based on the average distribution of anatomical data of SON [18, 19] using fundamental functions (e.g., *Sweep* function) in COMSOL. The SON nerve initially travels from the skull through the muscle plane and generally divides into branches as it runs in this plane. These branches enter the subcutaneous plane with different variations providing sensation to the forehead, as shown in Figure 2(c) [18, 19]. The processes of nerve modeling for nerve bending and nerve termination are detailed in the following subsections, respectively.

2.2.1. Nerve Bending

The nerve-bending models were generated based on their anatomical distributions over the forehead area. They are generated based on an incremental step, as shown in Figure 2(c). It was assured that each nerve model has the same amount of trajectory on each anatomical layer to measure the impact of the nerve bending on the stimulus current thresholds. Since there is no significant variation in the electrical potential variation from the skull layers to through the inner layers (such as the brain), the nerve models were considered from the skull layers to the

superficial layers. These resulted in fourteen models in the z-direction based on assumptions. Each model was generated individually and simulated in COMSOL according to the given neuromodulator settings to simulate electrical potential variations across the nerve trajectory. The stimulus current threshold was recorded in NEURON based on a calculated electrical potential variation on each nerve model.

2.2.2. Nerve Termination

It was recorded that the electrical potential variation decays significantly after a certain distance from the superficial layers toward the inner layers. Thus, the start point of the nerve modeling was assumed to be at the skull layer boundary, as shown in Figure 3. Since the electrical parameters of the anatomical layers vary considerably (as shown in Table 1), the nerve termination point was selected by considering the enter and exit points of the anatomical layers.

It was assumed that the nerve trajectories are modeled based on the same distance from the centerline of the head to obtain a fair comparison. It is noted that the same head model was used to measure the impact of the nerve termination on the stimulus current thresholds for the given electrode and neuromodulator settings.
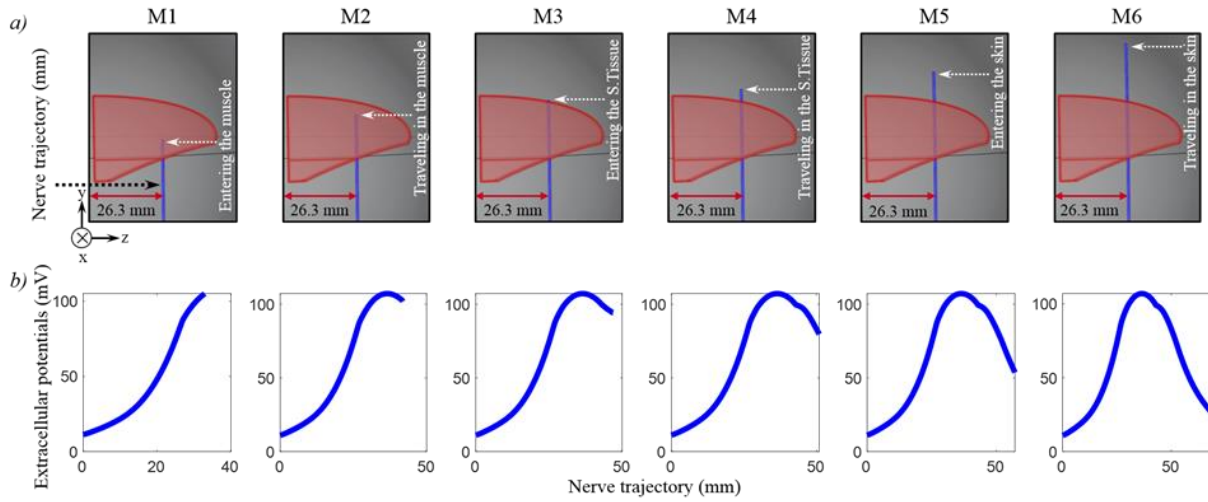
Figure 3. (a) Shows nerve termination models from Model 1(M1) to M6. The average distance of the nerve from the centerline of the forehead is shown. The nerve transition points in the anatomical layers are highlighted. (b) Shows the calculated extracellular electrical potentials along the nerve trajectories.

2.3. Finite Element Method (FEM) Based on the TENS Model

Each completed head model was simulated by dividing the geometry between the model into a mesh of small elements and solving the underlying equation for each element separately but in relation to each other in the COMSOL Multiphysics modeling environment using Cefaly electrode configuration settings.

To determine the distributions of the electrical potentials within the SON nerve in response to various stimulus strategies, the 3D finite element method was used as it provides a unique opportunity to discretize the associated domains in different element sizes during the meshing process, which is the more optimized approach to calculate electric fields in biological tissues.

2.3.1. Applying Boundary Conditions and Discretization Process

A sphere was defined around the model to implement an approximation of ground at infinity by applying the Dirichlet boundary condition ($V_\infty=0$). To obtain the optimum sphere layer, the radius of this layer was parametrized from 150 mm to 500 mm with 50 mm incremental steps, and the electrical potential along the trajectory of the nerve was recorded for each case. There was only 1% difference in the potential value for radius from 250 mm to 500 mm. Thus, the sphere layer was generated based on 250 mm to save computation time. The domains in the volume conductor were discretized using tetrahedral meshing, while the electrode and nerve model were more finely meshed by adjusting the element size parameters. Specifically, the minimum element size for nerve and electrode domains was selected as 1 μm, and the maximum element size was set to 1 mm. The outermost layer was discretized based on the *Normal* default element size in the available software. This resulted in 3.3 M elements (about 4.1 M degrees of freedom). The average tetrahedral mesh quality and average growth rate were 6.82 and 1.3, respectively.

2.3.2. Computational Simulation

Each volume conductor of the nerve model was simulated based on a quasi-static approximation of Maxwell's equations by considering the tissues to be purely resistive. Thus, the free charge source (Q) and any external current density (J_e) in the domain are assumed to be zero. By applying this condition ($Q=0$, $J_e=0$) to equations (2) and (3), Laplace equation (4) is obtained to calculate the electric potential distribution within each FEM domain.

$$E = \nabla V \tag{1}$$

$$J = \sigma E + J_e \tag{2}$$

$$\nabla \cdot J = \nabla \cdot (\sigma \nabla V + J_e) = Q \tag{3}$$

$$\nabla \cdot (\sigma \nabla V) = 0 \tag{4}$$

where diverse operator represents with ∇, the conductivity of the tissue layers is σ, the current density and the electrical field are J and E, respectively.

An electrical current (1 mA) was applied to the anode, and the same current level was injected into the cathode. Anode and cathode electrodes were defined as Terminals in COMSOL. Thus, +1 mA was inserted in Terminal 1, and -1 mA was inserted in Terminal 2. The electrode-tissue

interface contact impedance was not considered, and appropriate continuity conditions were implemented at the boundary of each domain to obtain a unique solution [20].

A non-conductive (σ=1e^{-10} S/m) air layer was defined around the model to obtain accurate results. It is noted that the electrical parameters of each layer were defined based on the low frequencies.

2.3.3. Charge Density

Electrical stimulation may lead to tissue damage either by the flow of current across tissues or by irreversible electrochemical reactions. Thus, following safety criteria to prevent tissue damage and electrode corrosion is essential. Therefore, the charge–balanced biphasic waveform is widely used to avoid damage to electrodes and surrounding tissue. However, in addition to charge balance, the current and charge densities of the stimulation waveforms must be limited to allow charge injection by reversible processes [21, 22]. The safety limits are decided based on the charge density using Shannon safety criteria, as shown in equation (5) for electrical stimulation [23].

$$Q = IT = (A \cdot 10^k)^{0.5} \qquad (5)$$

where I is current amplitude, T is the duration of each phase (250µs) of biphasic neuromodulator pulse, A is surface area, and k is a parameter with an empirical value of 1.0–2.0. For the conservative estimation, k=1 is used. It is noted that the amount of charge per phase in each pulse is important for far-field stimulation (e.g., TENS) rather than charge density [23]. Thus, in this study, the charge density per area per phase on the electrode and along the trajectory of the average SON nerves were calculated for the neuromodulator current range.

2.4. Nerve Fiber Compartmental Model

The nerve fiver was designed based on the cable model of the mammalian McIntyre–Richardson–Grill (MRG) axon model [24]. Each nerve fiber was constructed from multiple compartments representing the nodes of Ranvier, myelin attachment segments, paranodal, and internodal sections. This simple geometric relationship remains valid for the compartments in all models. Also, the same membrane dynamics (i.e., the number of ion channels implemented) were applied in all models.

It is not clear whether fibers convey the sensation over the whole fascicle or only within a limited area, and they have different diameters. To consider these issues, Aβ fibers were designed based on their anatomical statistical distribution (whose diameters followed a Gaussian distribution with a mean of μ_D = 12.5 µm and standard

deviation of σ_D = 2 µm) [7]. The associated parameters were derived by interpolating experimental measurements [24].

2.5. Merging of FEM-NEURON Model

The electrical potentials along the nerve were simulated in COMSOL, interpolated in MATLAB, and distributed along with the fibers' compartments in NEURON V7.4 to evaluate the response of nerve fibers to different amplitudes of currents. 25 µs time steps backward Euler integration was used in all simulations. All threshold values were obtained for 60 Hz and 250 µs current pulses. The percentage of activation of the nerve (PAs) for the initial and last segment of nodes was calculated for different current amplitudes. It is noted that the nerve fiber is activated when activation potentials were observed in both.

3. Results

3.1. Effects of Nerve Bending on the Current Thresholds

The extracellular potential variation along each nerve trajectory and PAs is shown in Figure 4. The results for extracellular potential variation versus the nerve trajectories for models on the left side of the forehead are shown in Figure 4(a), and the PAs of these models are shown in Figure 4(c). The results for extracellular potential variation versus the nerve trajectories for models on the right side of the forehead are shown in Figure 4(b), and the PAs versus the required stimulus current level are shown in Figure 4(d).

Figure 4(a) shows sharp variations at the bending point in extracellular potentials across all the nerve models apart from the average nerve model. It has been shown that these variations may lead to nerve activation with relatively lower stimulus current levels [25, 26]. Figure 4(b) clearly shows that the incremental variations in the bending angle lead to relatively lower stimulus current thresholds. Moreover, the more insufficient stimulus current levels are required after a certain angle (θ_2=20˚) when compared to the average nerve model (θ_6=0˚). This shows the nerve fiber can be activated with a certain level of a sharp change in extracellular potential.

Figure 4(c) indicates relatively lower variations at the bending points in the extracellular potentials for all nerves compared to models θ_1 to θ_5. Importantly, Figure 4(d) shows that all nerve models require higher current thresholds to activate the same amount of nerve fiber compared to the average nerve model current threshold. After a certain angle (θ_8=-10˚), relatively lower current thresholds are required when the bending angle is increased (with respect to the orbital rim). Interestingly, the last nerve model (θ_{14}=40˚)

stimulus current threshold is nearly identical to the average nerve model.

It is noted that the current levels are within the current

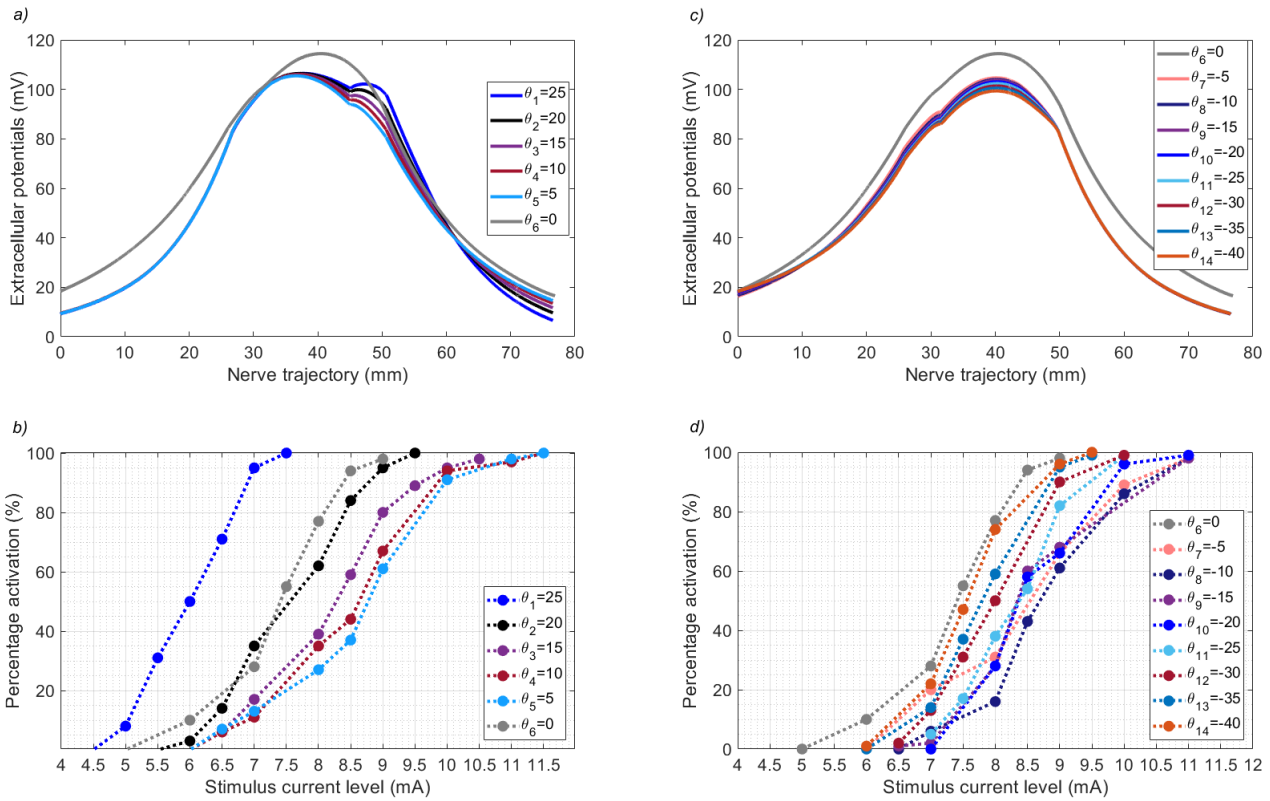range of the neuromodulator for all different angled average nerve models.

Figure 4. (a) Shows the electrical potential variation on the generated nerve bending models in the -z-direction. (b) Shows the required current levels of the nerve bending models based on the percentage activations (PAs) of the nerve fibers. (c) Shows the electrical potential variation on the generated nerve bending models in the +z direction. (d) Shows the required stimulus current levels of the nerve bending models based on the PAs of the nerve fibers in the +z direction.

3.2. Effects of Nerve Termination on the Current Thresholds

The required stimulus current levels versus PAs of the nerve fibers for the nerve termination models are shown in Figure 5.

It is noted that there is a significant effect of the nerve termination on the nerve e activation thresholds. The required stimulation current level can be reduced from 7.5 mA to around 2 mA to activate 50% nerve fiber when compared to the average nerve stimulus current threshold. Relatively more sudden changes in the electrical potentials can be observed in model 5 (M5), which leads to lower stimulus current levels. Thus, if the results in Figure 5 compare to the extracellular potential distributions in Figure 3(a), these relative stimulus current levels can be associated with the second derivative of the potentials along the nerve fiber as sharp changes resulted in lower stimulus current thresholds as also studied in [26].
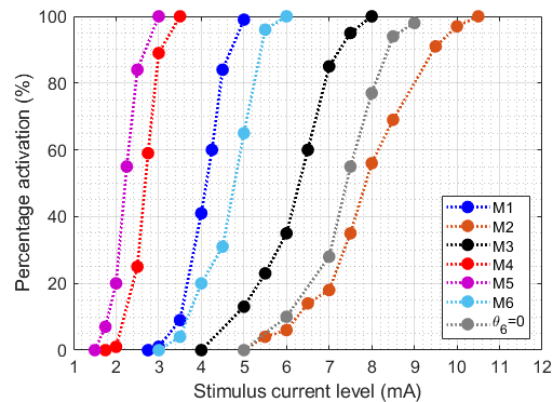

Figure 5. Shows the required stimulus current levels of the nerve fibers based on the PAs for generated nerve termination models. The result for each model is highlighted in different colors.

3.3. Estimating the Safety Limit for the Neuromodulator

The distributions of the charge density based on per

area per phase along the nerve fiber and electrode for the target neuromodulator current range are shown in Figure 6. The results of the figure are significant in safety considerations regarding the neuromodulator.

As is expected, when the current levels are increased, the charge density for both electrode and neural tissue is increased. Also, it is clearly shown that densities at the edges of the electrode are relatively higher. As the surface between two electrodes is a non-conductive medium, the charge density on this is equal to zero, as shown in the first subplot. As previously proposed, the charge density limit for large electrodes has ranged from 15 to 65 $\mu C/cm^2$/phase

[23]. The result shows that the charge density for the electrode of the neuromodulator is within this range.

There is fluctuation in the nerve charge density along the nerve trajectory for all current levels due to traveling through different anatomical layers. As the nerve trajectory travels far from the electrode regarding emerging and termination points, the nerve charge density is considerably reduced in both points. The amount of charge per area per phase along the neural tissue is on the safe side of the limit for a safe charge injection [22].

The charge per area per phase density is far away compared to the safe limit for tissue damage.
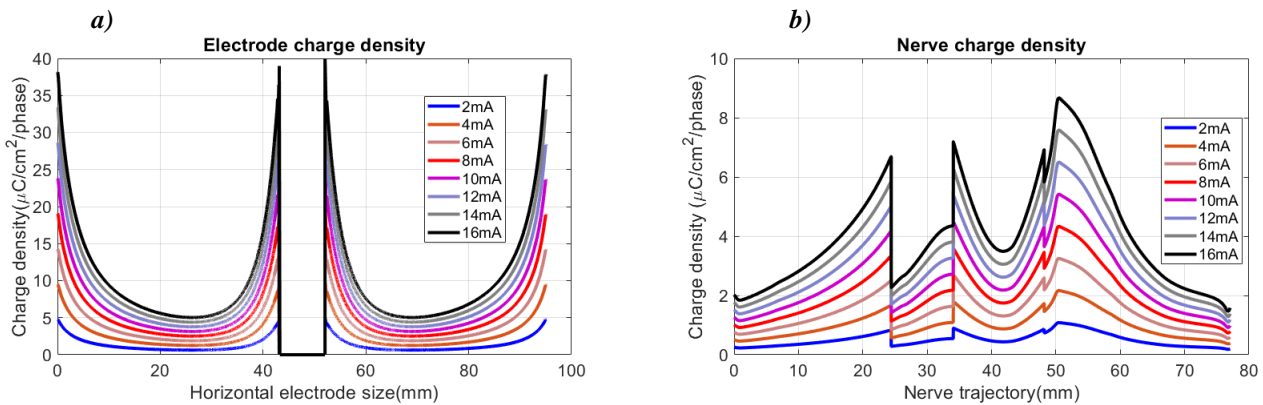

Figure 6. (a) Charge per area per phase along the electrode for a 250 µs pulse of different amplitudes using Cefaly electrode configuration. The current density is considerably higher at the edges of the electrode. The current density between the two electrode zero is due to a conductive layer. (b) Charge per area per phase along the average SON nerve for a 250 µs pulse of different amplitudes of the neuromodulator.

4. Discussing

The development of neuromodulator therapy systems for neurological disorders has accelerated with improved technologies and an expanding understanding of the effect of electrical stimulation on neural tissue. Computational methods are widely used for advancing and optimizing electrode design, stimulation parameters, and understanding the mechanism of action of these neuromodulator devices [27, 28, 29]. The TES neuromodulator procedures have been applied globally [36, 37].

It is known that the nerve termination and nerve bending angle have an impact on the nerve fiber stimulation current levels. The nerve bending point and nerve termination may lead to relatively lower required current thresholds [8, 9]. This study analyzed the effect of the nerve bending and nerve termination on the required stimulus current levels for a neuromodulator using computational hybrid FEM models. It is clearly known that the STN and SON are divided into sub-branches and these branches may terminate and bend with various trajectories and bending points. In this study, the nerve models are constructed based

on the SON anatomical statistical distributions as they travel from the skull through the subcutaneous plane through the subcutaneous plane. The human head models were completed with the fundamental layers using their average statistical anatomical data distributions. Each model was simulated, and the obtained electrical potentials along the neural tissue distributed the compartments of the nerve fibers to calculate the response of different amplitudes to this field. The PAs and the activation current levels of each nerve model were recorded using the neuromodulator parameters (biphasic charge-balanced rectangular 250 µs pulses at 60 Hz) [4]. Also, the charge per area per phase was calculated to examine the safety limit for both electrode and neural tissue using the same neuromodulator parameters.

It was shown that the geometrical features of the neuroanatomical layers (e.g. nerve bending and nerve termination) have a substantial impact on the neuromodulator' current thresholds. The required current level was reduced by about 25 % based on the 50% of nerve fiber activation, comparing the furthest and average nerve models.

Also, the current study's findings suggested that the nerve angle significantly impacts the extracellular potential

distributions. Since the nerve trajectories follow different paths from the subcutaneous through the superficial plane, thus, this can be associated with the second derivative variations of the electrical potentials along the nerve fibers on the neural activation thresholds [25, 26]. It was shown that the required current levels relatively increased for the nerve models that are placed away from the center of the forehead. This can be correlated with the electrode size and shape. It is expected that the induced electrical potential variation in the vicinity of the electrode path is relatively higher. Thus, the electrical potential variations at the bending points are relatively smaller compared to the models towards the midline of the forehead, as shown in Figure 4(a), (c).

The results based on the nerve termination showed that the required current levels were relatively smaller for the nerve models that are closer to the electrode (i.e., M1 and M3) and the models that have superficial trajectories (i.e., M4 and M5). Although M2 is terminated roughly beneath the center of the electrode, the required current levels are comparatively higher. This may be related to the electrical potential variations, as the second derivative is zero at the termination point.

It is noted that the charge density per area per phase was relatively higher at the edge of the electrode due to the equipotential surface of the electrodes but was within the safe zone. The electrode edge effect happens at the metallic surface, which has an interface with the neuromodulator but not the surface that is in immediate contact with the surface of the skin on its other side. Although the charge density per area per phase for neural tissue fluctuated for various current levels, the amount of the charge per phase was far from the neural tissue damage limit.

The effect of nerve bending and nerve termination was investigated based on the average human head model. However, it has been shown that the anatomical layers in the human head have different thicknesses for each individual. Thus, the results may be affected when various human heads are considered. Another limitation of this study is the variations of the STN nerve were not considered.

Overall, the results show that the nerve bending models, which are towards the midline of the forehead, led to lower stimulus current levels after a certain bending angle, while the other resulted in higher current levels. The distance between the termination points and electrode and the superficiality of the nerve trajectory has a serious impact on the nerve trajectory have a serious impact on the nerve termination current thresholds. In most cases, the nerve bending and nerve termination led to different electrical potentials along the nerve fiber, which may result in lower stimulus current thresholds being required and this can be associated with the second derivative of these potentials variations on the activation of the neural tissue.

It noted that only a size of an electrode was considered in the current study. Using different shapes and sizes of the electrodes and targeting different nerves may provide a more insightful outcome. Thus, modeling such parameters may produce more accurate results and detailed conclusions.

5. Conclusion

The FEM models can be used to design and develop neuromodulator settings of the TES therapy systems. This study investigated the effect of nerve termination and nerve bending on the required stimulus current levels for a TES-based neuromodulator using highly realistic human head and mammalian nerve fiber models. The electrical potential along the nerve trajectories was calculated using appropriate boundary and electrical settings.

Results suggest that both nerve bending and nerve termination have a significant effect on the stimulus current thresholds of the neuromodulator, which provides critical guidance for future modeling studies and electrical stimulation design. It was shown that the nerve bending and nerve termination caused non-uniform electrical distributions, and this resulted in lower stimulus current thresholds.

Declaration of Ethical Standards

The author of this article declares that the materials and methods used in this study do not require ethical committee permission and/or legal-special permission.
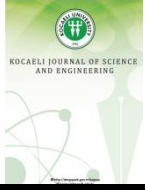
Conflict of Interest

The author declares that he has no known competing financial interests or personal relationships that could have appeared to influence the work reported in this paper.

References

[1] Johnson M. I. and Bjordal J. M., 2011. Transcutaneous electrical nerve stimulation for the management of painful conditions: focus on neuropathic pain, Expert Rev. Neurother., **11**(5), pp. 735–753.

[2] Headache Classification Committee of the International Headache Society (IHS)., 2013. The International Classification of Headache Disorders, 3rd edition (beta version), Cephalalgia, **33**(9), pp. 629–808.

[3] Magis D. *et al.*, 2016. Cerebral metabolism before and after external trigeminal nerve stimulation in episodic migraine, Cephalalgia, **37**(9), pp. 1–11.

[4] Riederer F., Penning S., and Schoenen J., 2015. Transcutaneous Supraorbital Nerve Stimulation (t-SNS) with the Cefaly(®) Device for Migraine Prevention: A Review of the Available Data, Pain Therapy., **4**(2), pp. 135–147.

[5] Magis D., Sava S., d'Elia T. S., Baschi R., and Schoenen J., 2013. Safety and patients' satisfaction of transcutaneous supraorbital neurostimulation (tSNS) with the Cefaly® device in headache treatment: a survey of 2,313 headache sufferers in the general population, J. Headache Pain, **14**, p. 95.

[6] Schoenen J. et al., 2013. Migraine prevention with a supraorbital transcutaneous stimulator: A randomized controlled trial, Neurology, **80**(8), pp. 697–704.

[7] Salkim E., Shiraz A. N., and Demosthenous A., 2017. Effect of Nerve Variations on the Stimulus Current Level in a Wearable Neuromodulator for Migraine: A Modeling Study, in 8th International IEEE EMBS Conference on Neural Engineering, pp. 239–242.

[8] Schiefer M. A. and Grill W. M., 2006. Sites of Neuronal Excitation by Epiretinal Electrical Stimulation, **14**(1), pp. 5–13.

[9] Rubinstein J. T. and Rubinstein J. T., 1193. Axon Termination Conditions for Electrical Stimulation, IEEE Trans. Biomed. Eng., **40**(7), pp. 654–663.

[10] Butson C. R., Computational Models of Neuromodulation, 2012. 1st ed., **107**. Elsevier Inc.

[11] Salkim E., Shiraz A. N., and Demosthenous A., 2017. Effect of Model Complexity on Fiber Activation Estimates in a Wearable Neuromodulator for Migraine, in 2017 IEEE Biomedical Circuits and Systems Conference, pp. 1–4.

[12] Salkim E., Shiraz A., and Demosthenous A., 2018. Influence of cellular structures of skin on fiber activation thresholds and computation cost influence of cellular structures of skin on fiber activation thresholds and computation cost, Biomed. Phys. Eng. Express, **5**(1), p. 015015.

[13] Bikson M., Rahman A., and Datta A., 2012. Computational Models of Transcranial Direct Current Stimulation, Clin. EEG Neurosci., **43**(3), pp. 176–183.

[14] Takema Y., Yorimoto Y., Kawai M., and Imokawa G., 1994. Age-related changes in the elastic properties and thickness of human facial skin, Br. J. Dermatol., **131**(5), pp. 641–648.

[15] Ha R. Y., Nojima K., Adams W. P., and a Brown S., 2005. Analysis of facial skin thickness: defining the relative thickness index, Plast. Reconstr. Surg., **115**(6), pp. 1769–1773.

[16] Pinar Y., Govsa F., Ozer M. A., and Ertam I., 2016. Anatomocosmetic implication rules of the corrugator supercilii muscle for youthful eye appearance, Surg. Radiol. Anat., **38**(9), pp. 1045–1051.

[17] Ruan J. and Prasad P., 2001. The effects of skull thickness variations on human head dynamic impact responses, Stapp Car Crash J., **45**(November), pp. 395–414.

[18] Christensen K. N., Lachman N., Pawlina W., and Baum C. L., 2014. Cutaneous Depth of the Supraorbital Nerve, Dermatologic Surg., **40**(12), pp. 1342–1348.

[19] Gil Y.-C., Shin K.-J., Lee S.-H., Song W.-C., Koh K.-S., and Shin H. J., 2017. Topography of the supraorbital nerve with reference to the lacrimal caruncle: danger zone for direct browplasty, Br. J. Ophthalmol., **101**(7), pp. 940–945.

[20] Raspopovic S., Stanisa and Capogrosso, Marco and Micera, 2011. A computational model for the stimulation of rat sciatic nerve using a transverse intrafascicular multichannel electrode, IEEE Trans. Neural Syst. Rehabil. Eng., **19**(4), pp. 333–344.

[21] Cogan S. F., 2008. Neural Stimulation and Recording Electrodes, Annu. Rev. Biomed. Eng., **10**(1), pp. 275–309.

[22] Salkim E., 2019. Optimization of a Wearable Neuromodulator for Migraine Using Computational Methods, UCL (University College London).

[23] Shannon R. V, 1992. A Model of Save Levels for Electrical Stimulation, IEEE T Bio-Med Eng, **39**(4), pp. 424–426.

[24] McIntyre C. C., Richardson A. G., and Grill W. M., 2002. Modeling the excitability of mammalian nerve fibers: influence of afterpotentials on the recovery cycle., J. Neurophysiol., **87**(2), pp. 995–1006.

[25] McNeal D. R., 1976. Analysis of a model for excitation of myelinated nerve., IEEE Trans. Biomed. Eng., **23**(4), pp. 329–337.

[26] Rattay F., 1989. Analysis of models for extracellular fiber stimulation.pdf., IEEE Trans. Biomed. Eng., **36**(7), pp. 676–682.

[27] Pelot N. A., Behrend C. E., and Grill W. M., 2019. On the parameters used in finite element modeling of compound peripheral nerves, J. Neural Eng., **16**(1).

[28] Howell B., Huynh B., and Grill W. M., 2015. Design and in vivo evaluation of more efficient and selective deep brain stimulation electrodes, J. Neural Eng., **12**(4).

[29] Lempka S. F., McIntyre C. C., Kilgore K. L., and Machado A. G., 2015. Computational Analysis of Kilohertz Frequency Spinal Cord Stimulation for Chronic Pain Management, Anesthesiology, **122**(6), pp. 1362–76.

[30] Yamamoto T. and Yamamoto Y., 1976. Electrical properties of the epidermal stratum corneum, Med. Biol. Eng., **14**(2), pp. 151–158.

[31] Gabriel C. et al., 1996. The dielectric properties of biological tissues: I. Literature survey, Phys. Med. Biol., **41**(11), pp. 2231–2249.

[32] Kuhn A., Keller T., Micera S., and Morari M., 2009. Array electrode design for transcutaneous electrical stimulation: A simulation study, Med. Eng. Phys., **31**(8), pp. 945–951.

[33] Oostendorp T. F., Delbeke J., and Stegeman D. F., 2000. The conductivity of the human skull: Results of in vivo and in vitro measurements, IEEE Trans. Biomed. Eng., **47**(11), pp. 1487–1492.

[34] Baumann S. B., Wozny D. R., Kelly S. K., and Meno F. M., 1997. The electrical conductivity of human cerebrospinal fluid at body temperature, IEEE Trans. Biomed. Eng., **44**(3), pp. 220–225.

[35] "Low Frequency (Conductivity) » IT'IS Foundation." [Online]. Available: https://itis.swiss/virtual-population/tissue-properties/database/low-frequency-conductivity/. [Accessed: 20-December-2022].

[36] Gibson W., Wand B. M., Meads C., Catley M. J., and O'Connell N. E., 2019. Transcutaneous electrical nerve stimulation (TENS) for chronic pain - an overview of Cochrane Reviews doi: 10.1002/14651858.cd011890.pub3.

[37] T Mokhtari., Ren Q., Li N., Wang F., Bi Y., and Hu L., 2020. Transcutaneous Electrical Nerve Stimulation in Relieving Neuropathic Pain: Basic Mechanisms and Clinical Applications, Current Pain and Headache Reports, **24**(4). Springer. doi: 10.1007/s11916-020-0846-1.

Kocaeli University

Kocaeli Journal of Science and Engineering

http://dergipark.org.tr/kojose

First-Principles Study of Titanium and Lithium Adsorption on Perfect and Defective Hexagonal Boron Nitride Monolayer Under Effects of Charging

Bahadır SALMANKURT [1, *] iD

[1] Distance Education Center, Sakarya University of Applied Sciences, Sakarya, 54050, Turkey, **ORCID:** 0000-0001-7611-9647

Abstract

Single Titanium (Ti) and Lithium (Li) atoms adsorption on Pristine and defective hexagonal boron nitride (P-h-BN and BV-h-BN) monolayer were employed using Density Functional Theory (DFT) under effect of charging. Obtained data reveal that Li adsorption on P-h-BN is weak, while Ti adsorption on P-h-BN is strong. When Ti and Li atoms interact with P-h-BN surface, Ti and Li generate 4 μB/cell and 1 μB/cell magnetic moments, respectively. The extraction of an electron from the systems leads to a considerable rise in the adsorption energy, notably in the case of Li-P-h-BN. There is a notable decrease in the band gap of Ti-P-h-BN in both the charged states, especially in the electron-added state. Removing an electron from the Li-P-h-BN system results in a non-magnetic state and a significant increase of the band gap to 4.07 eV. Ti-BV-h-BN system shows significantly stronger adsorption energy due to the d-orbitals of the Ti atom. When an electron is added to the systems, the interaction energy between Ti and BV-h-BN decreases, while the interaction energy between Li and BV-h-BN increases. Moreover, removing an electron from Ti-BN-h-BN increases the band gap to 2.29 eV and the disappearance of the magnetic moment.

1. Introduction

Semiconductors have been regarded as a cornerstone for numerous electronic applications, such as electromedical devices, personal computers, wireless communications, automobiles, and so on. As a result, demand for the most popular semiconductor, silicon, has consistently seen robust growth in recent years [1]. The COVID-19 pandemic has further fueled this momentum, particularly in the automotive and lubricant industries [2]. Hence, the discovery of effective materials for technological applications other than silicon-based electronics is becoming increasingly urgent.

Two-dimensional (2D) materials can support the demand from the silicon-based electronic world. The discovery of Graphene (GR) in 2004 has tremendously aroused interest in the electronic [3]. After this discovery, scientists have been searching for stable and convenient materials in many application areas for years, and they have found materials such as phosphorene, hexagonal boron nitride (h-BN), silicene, stanene, transition metal di-

chalcogenides (TMDCs), etc. [4-7]. Although GR has unique properties, its non-band gap state is an obstacle for most electronic compounds [7]. So, stable and wide band gap 2D material seems to be required from a wide range of industries [7-8].

h-BN monolayer may be exactly what scientists and engineers are looking for in the mentioned fields. Because its band gap theoretically and experimentally was found to be 4.55 and 6.1 eV, respectively [8-9]. Moreover, h-BN is as stable as GR [8]. According to the obtained knowledge, it seems very reasonable to consider h-BN monolayer as potential material for future studies [8-12].

Examining the history of h-BN can provide valuable insight into the material's significance for technological applications. The formation of a highly regular self-assembled BN nanostructure with a periodicity of 3.22 nm on Rh (111) by CVD of borazine ("NanoMesh") was first obtained by *Corso et al.*, and the BN monolayer structure was modeled by *Laskowski et al.* [8-9]. From then until now, many studies related to h-BN monolayer have been performed [10-21].

In recent years, functionalization, or doped h-BN with Lithium (Li), has been explored to enhance its properties and broaden its potential applications [11-12]. Li functionalized or doped h-BN has been shown to exhibit improved electrical conductivity, thermal stability, and catalytic activity compared to pristine h-BN [12,15]. This has made Li functionalized or doped h-BN a promising material for various energy-related applications, such as batteries and supercapacitors [12,15].

Moreover, doping or functionalizing h-BN with transition metals, such as Iron (Fe), Nickel (Ni), and Titanium (Ti), has been shown to introduce localized states into the bandgap and modify its electrical, magnetic, and optical properties [16-21]. Furthermore, the adsorption of Ti at a vacancy site in an h-BN sheet is effortless [16]. Moreover, the incorporation of Ti into h-BN materials leads to the formation of narrow-band semiconductors, which is promising for novel technological devices [18]. This makes h-BN doped or functionalized with transition metals of great interest for the development of new spintronic devices, sensors, and catalysts. Compared to electronic devices, faster reading and writing of data in storage can be achieved through spintronics, which has the potential to replace silicon-based semiconductor devices [22]. Thus, we have also focused on Ti modified h-BN in this work.

Furthermore, modifying the net charge of the systems leads to a significant impact on the binding mechanism. In this way, the charging highly affects the band structures, distance between atoms, and adsorption energies. [23]. A better understanding of these effects can provide valuable insights into the behavior and interactions of charged 2D atoms and can play an important role in advancing our understanding of these systems.

2. Methods

The calculations were performed using the Siesta code, which uses a linear combination of pseudoatomic orbitals (LCAO) as basis functions and implements Density Functional Theory (DFT) [24-26]. The Perdew-Burke-Ernzerhof (PBE) functional within the generalized gradient approximation (GGA) was used as the exchange-correlation potential [27]. The Grimme method was employed to calculate the energetics and interactions of the monolayer and atom systems, which is a correction for Van der Waals (vdW) interactions [28]. A typical vdW effect in the literature is around 3 Å and becomes important for interactions at this distance. However, as the interaction distance decreases, the vdW effect becomes relatively less significant.

The sample was modeled using a 2D periodic 5x5 supercell with a vacuum layer of 20 Å to avoid interactions

between periodic images. A plane wave cutoff energy of 250 Ry was used, and the Brillouin zone (BZ) was sampled using a Monkhorst-Pack grid of 5x5x1 k-points [29]. The geometry optimization was performed using the conjugate gradient (CG) method until the forces on each atom were less than 0.01 eV/Å.

To investigate the electronic properties of the systems, the band structures were calculated. The band structures were calculated along high-symmetry lines in the BZ. The Fermi level was determined by integrating the Density of States (DOS) up to the number of electrons in the system. The adsorption energy (E_{ads}) of a single Li or Ti atom on Pristine h-BN (P-h-BN) or Boron-Vacancy h-BN (BV-h-BN) monolayer is given by the formula:

$$E_{ads} = E_{sys} - E_{BN} - E_X \qquad (1)$$

where E_{sys} is the total energy of P-h-BN or BV-h-BN monolayer with adsorbed single Li or Ti atoms, E_{BN} is the total energy of the P-h-BN or BV-h-BN monolayers, and E_X indicates the energy for isolated single Li or Ti atoms in a vacuum. On the other hand, when the net total charge of the systems changes, the above-mentioned formula is no longer suitable. This is because a change in the net charge of the systems fundamentally affects the binding mechanism. Instead of using the formula, it is a better choice to use the pulling method. In this method, one should gradually pull the atoms out from the layers along a perpendicular direction to the h-BN surface until the interaction energy between the atoms and the layer disappears [23,30]. To carry out this process, it is important to first fix the corner atoms of the monolayer to prevent movement during the pulling process. Also, some parameters should be changed in the Siesta Code. The *tot_charge* tag is used to determine the total charge of the system in the Siesta Code. Its default value is zero, indicating a neutral state. +1 represents the removal of an electron from the corresponding unit cell, while -1 represents the addition of an electron to the cell. After the parameter was modified, the relaxation calculation was performed again. For example, when one electron was added to a 5x5 h-BN cell using *tot_charge=-1* tag, the charge was uniformly distributed on the h-BN surface, leading to an extra 0.12 Coulomb per square meters (-0.12 C/m^2) on h-BN surface.

The total energy difference between the relaxed state and the final step in the pulled state gives the pulling energy value, which can be defined as follows:

$$E_P = E_T[Relaxed] - E_T[Pulled\_final] \qquad (2)$$

where E_P represents the energy required for the adsorption of charged systems. $E_T[Relaxed]$ represents the total

energy of the system that is in the relaxed state, while $E_T[Pulled\_final]$ represents the total energy of the system that is the final step in the pulled state. E_P gives us the same results with E_{ads}.

To draw geometric structures, Vesta software was used [31].

3. Results and Discussion

3.1. The Structural and Electronic Properties of P-h-BN and BV-h-BN

First of all, the lattice constants of 1x1 P-h-BN (a, b) were calculated, and the obtained data reveal that the values of a, b for 1x1 P-h-BN have been found to be 2.51 Å. This value is in good agreement with previous studies [10-20]. Additionally, the bond distance between the N and B atoms was calculated to be 1.45 Å, within the previous data range [10-20].
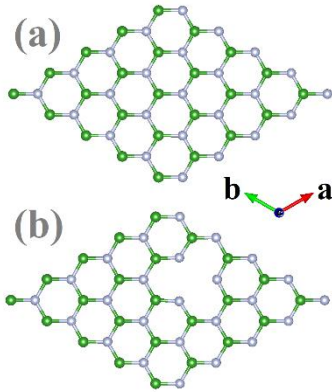

Figure 1. Schematic illustration of a top view of a) P-h-BN and b) BV-h-BN. The green ball stands for the B atom, and the gray one is for the N atom.

Next, the size of 1x1 P-h-BN expanded to 5x5, as shown in Figure 1(a), to investigate electronic and other properties. The first of these is to calculate band structures.

The band gap of P-h-BN has been calculated as 4.55 eV, as seen in Figure 2(a), and is very close to the data in the literature [10-20].

Finding a perfect crystal in nature is quite difficult, and defects always occur. One of the possible defects is caused by atomic vacancy. So, the effect of vacancy defects has been considered.

Due to the more favorable B vacancy on h-BN monolayer (BV-h-BN) compared to regular N vacancy, B vacancies on monolayers have been extensively studied [13,15,32]. The removal of a B atom from the layer does not result in a significant change in the structure after structural relaxation (as seen in Figure 1(b)); however, magnetic moment arises due to the presence of non-bonding atoms. Because of this, a spin-polarized state has been considered.

In this case, there will be three N atoms that cause a missing bond, which leads to 3 μB/cell of magnetic moment, in line with previous study [32]. Naturally, this situation also caused changes in the band structure. The band structures of BV-h-BN are depicted in Figure 2(b). Obtained data reveal that there is no band gap for the spin-down (Blue lines in Figure 2(b)) state. However, spin-up has a band gap of 4.65, which is almost the same as a pristine state. This implies that BV-h-BN is in a semimetallic state, as previously reported in studies. [15,32].
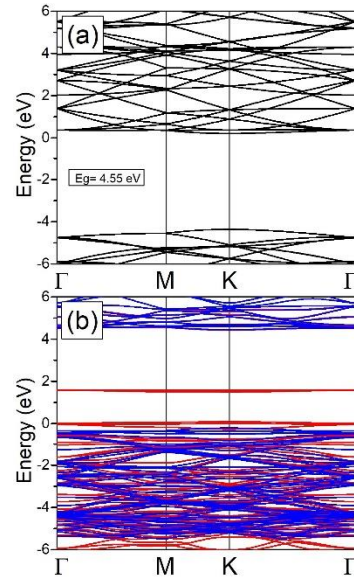

Figure 2. Electronic band structures of a) P-h-BN and b) BV-h-BN. The Fermi level is set to zero. Black lines mean a non-magnetic state. Red lines indicate a spin-down state, while blue lines are a spin up state. Eg indicates band gap value in eV.

The results obtained in this section demonstrate the reliability of the study and can be easily considered in the following sections.

3.2. Binding Mechanism of Li or Ti Functionalized P-h-BN

In this section, the focus is on Li/Ti functionalized P-h-BN (Li/Ti-P-h-BN). The calculation that included spin-polarization was also considered because bare Ti and Li atoms are spin-polarized.

The calculation started with atom-monolayer interaction. The atom was placed at a location that is 3 Å away from the surface of P-h-BN, then the system was relaxed. This was applied to both Ti and Li atoms. As we can see from Figure 3, both atoms preferred the hollow site of P-h-BN. Furthermore, the E_{ads} was calculated using the formula provided in the Methods section, and the results are presented in Table 1. Obtained data reveal that the E_{ads} of

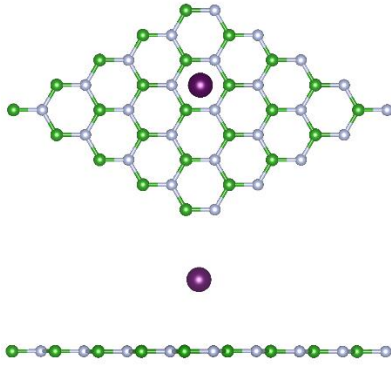Li-P-h-BN is relatively weaker than that of Ti-P-h-BN.

Figure 3. Schematic illustration of top and side view of Li/Ti-P-h-BN. The green ball stands for B atom and the gray one is for N atom. The purple indicates Li or Ti atoms.

This is probably due to the role of d-electrons, which play an important role in the E_{ads} [10]. So, interacting P-h-BN with d-electron atoms can cause stronger E_{ads}, which might be considered in a situation where atoms need to be strongly held on the surface. As we know, typically, an inverse relationship exists between energy and atomic distances, whereby an increase in interaction between the atom and layer results in a corresponding decrease in atomic distances. The minimum distances between the atom and the monolayer were considered to deeply understand interaction mechanism for all calculations. For example, the minimum

atomic distances between Ti and Li atoms with P-h-BN were calculated as 2.25 Å and 3.62 Å, respectively. The results have been calculated as expected.

Table 1. The E_{ads} of Li/Ti-P-h-BN (in eV). N1, Neutral and P1 indicate Q=-1e/cell, Q=0 and Q=+1e/cell case of GGA-vdW.

Cases	Li	Ti
ΣQ=-1 (N1)	-0.06	-1.61
Neutral	-0.19	-0.72
GGA-vdW [11]	-0.02	-
GGA-vdW [10]	-	-1.27
GGA-vdW [12]	-0.16	-
ΣQ=+1 (P1)	-1.55	-2.03

Next, the magnetic moments of the systems have been considered. As can be seen from Table 2, it was found that Ti-P-h-BN has a magnetic moment of 4 μB/cell, while that of the Li-P-h-BN atom is 1 μB/cell. The result for Ti-P-h-BN is consistent with previous studies [10]. On the other hand, the effects of changing the net charge in the supercell were examined. It is known that the net charge of the system can be manipulated by adding or removing an electron to or from the system [23]. This has a significant impact on the E_P and electronic properties [23,30]. Here, N1 refers to adding one electron to the supercell, while P1 represents removing one electron from the supercell.
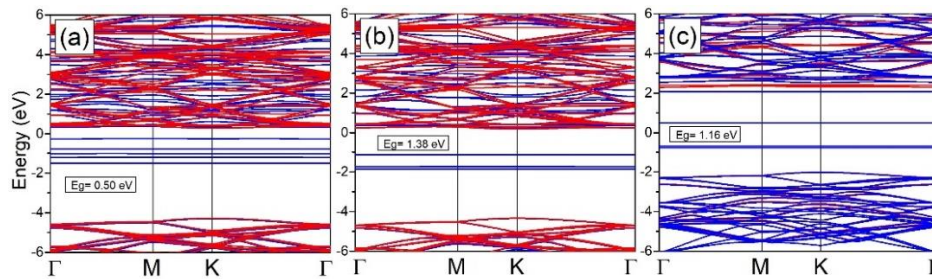

Figure 4. The band structures of (a) Q=-1e/cell, (b) Neutral and (c) Q=+1e/cell case for Ti-P-h-BN. The Fermi level is set to zero. Red lines indicate a spin-down state, while blue lines are a spin-up state. Eg indicates band gap value in eV.
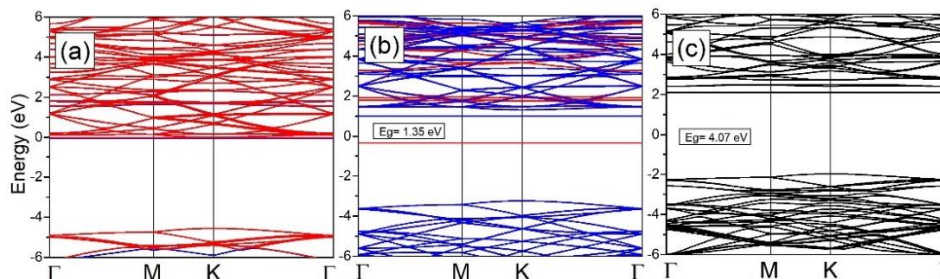

Figure 5. The band structures of (a) Q=-1e/cell, (b) Neutral, and (c) Q=+1e/cell case for Li-P-h-BN. The Fermi level is set to zero. Black lines mean a non-magnetic state. Red lines indicate a spin-down state, while blue lines are a spin-up state. Eg indicates band gap value in eV.

Table 2. The magnetic moment of Li/Ti-P-h-BN (in µB/cell). N1, Neutral, and P1 indicate Q=-1e/cell, Q=0, and Q=+1e/cell case of GGA-vdW.

Cases	Li	Ti
ΣQ=-1 (N1)	0.03	5.00
Neutral	1.00	4.00
GGA-vdW [10]		4.00
ΣQ=+1 (P1)	0.00	3.00

As can be seen from Table 1, removing an electron from the system results in a significant increase in the E_P, especially for Li-P-h-BN. However, when one electron is added to the system, the E_P of Li-P-h-BN becomes very low, compared to P1 state. Therefore, Li atoms can be kept on the P-h-BN layer by removing electrons and released easily by adding electrons. This method may be used in Li-ion based materials.

On the contrary, the change in net charge (N1 or P1) leads to an increase in E_P for the Ti-P-h-BN system. Charging the system also affects the electronic properties. For instance, the band gap of Ti-P-h-BN decreases in both the N1 and P1 states, especially in the N1 state (as seen in Figure 4). Thus, it is possible to manipulate band gap. In the case of Li-P-h-BN, significant events occur. When an electron is removed from the system, a non-magnetic state is created and the band gap significantly increases to 4.07 eV. When an electron is added, a very small magnetic moment is observed and no band gap is observed (Figure 5). Hence, changing the net charge of the system provides the opportunity to use the material in many electronic devices. Furthermore, the calculated magnetic moments are given in Table 2. Obtained daha reveal that magnetic moments of the systems are highly affected by the changing the net charge.

3.3. Binding Mechanism of Li or Ti (Li/Ti) doped BV-h-BN

The most stable configuration of Li/Ti-BV-h-BN is shown in Figure 6. For Ti-BV-h-BN, the minimum distance between Ti-N atoms is found to be 1.87 Å, while for Li-BV-h-BN, the minimum distance of Li-N atoms is 2.00 Å.

Here, the vacancy site of the monolayer has interacted with Ti or Li atoms and then the E_{ads} was calculated. As seen in Table 3, the strong E_{ads} is noticed, which is in good agreement with previous studies [15-21]. However, E_{ads} in Ti-BV-h-BN system is much stronger than in Li-BV-h-BN. Because transition metals with d-orbitals interact more strongly with surfaces [16-21].
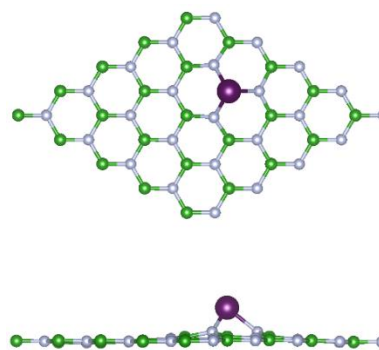

Figure 6. Schematic illustration of top and side view of Li/Ti-BV-h-BN. The green ball stands for B atom and the gray one is for N atom. The purple indicates Li or Ti atoms.

When an electron was added to the systems, the interaction between Ti and BV-h-BN decreased, while the interaction between Li and BV-h-BN increased, vice versa. This is due to the different charge distributions between Ti/Li and BV-h-BN, which can be understood by analyzing the molecular orbitals with magnetism.

Table 3. The E_P of Li/Ti-BV-h-BN (in eV). N1, Neutral and P1 indicate Q=-1e/cell, Q=0 and Q=+1e/cell case of GGA-vdW.

Cases	Li	Ti
ΣQ=-1 (N1)	-5.09	-9.32
Neutral	-4.61	-11.82
GGA-vdW [15]	-5.30	
GGA [16]		-11.39
GGA-vdW [17]		-11.59
GGA-vdW [18]		-11.60
GGA-vdW [19]		-11.48
GGA-vdW [20]		-12.70
GGA-vdW [21]		-12.90
ΣQ=+1 (P1)	-3.01	-13.12

Herein, *Wang. et al.* have used molecular orbital theory (MOT) to show the mechanism of the magnetic properties of Ti-BV-h-BN [22]. In the mentioned study, the magnetic moment of Ti-BV-h-BN was found to be 1 µB/cell because a spin electron was left in the orbital $\pi_{E'}$. Also, there were found to be five orbitals that did not have any electrons.

When we added an electron to the same system, one of the orbitals that did not have an electron was filled. This resulted in two half-filled orbitals, corresponding to a magnetic moment of 2 µB/cell. However, when an electron is removed from the same system, the electron occupying the orbital $\pi_{E'}$ is removed, resulting in a non-magnetic state.

But the same story is not seen for Li-BV-h-BN, where the magnetic moment increased by adding an electron and

decreased by removing an electron. So, changing the net charge gives rise to different results in the magnetic moment for both systems, resulting in different charge distributions.

Afterwards, the band structures of the systems were calculated and described in Figures 7 and Figures 8. For both neutral systems, the band gap was observed. However, the band structures became different by manipulating the net charge. For example, if an electron was removed from Ti-BV-h-BN, the band gap increased to 2.29 eV, and the magnetic moment disappeared. On the other hand, for Li-BV-h-BN, it is possible to eliminate the band gap by changing the net charge of the system.
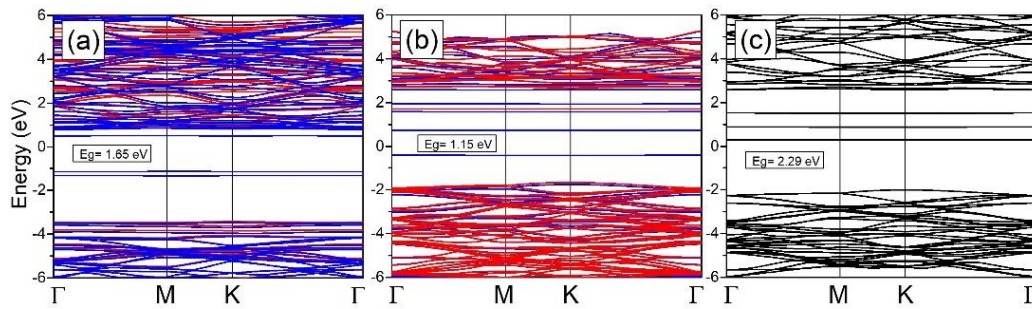
Table 4. The magnetic moment of Li/Ti-BV-h-BN (in μB/cell). N1, Neutral, and P1 indicate Q=-1e/cell, Q=0, and Q=+1e/cell case of GGA-vdW.

Cases	Li	Ti
ΣQ=-1 (N1)	1.00	2.00
Neutral	2.00	1.00
GGA [13]	-	1.00
GGA [14]	-	1.00
ΣQ=+1 (P1)	3.00	0.00

Figure 7. The band structures of (a) Q=-1e/cell, (b) Neutral, and (c) Q=+1e/cell case for Ti-doped h-BN. The Fermi level is set to zero. Black lines mean a non-magnetic state. Red lines indicate a spin-down state, while blue lines are a spin-up state. Eg indicates band gap value in eV.
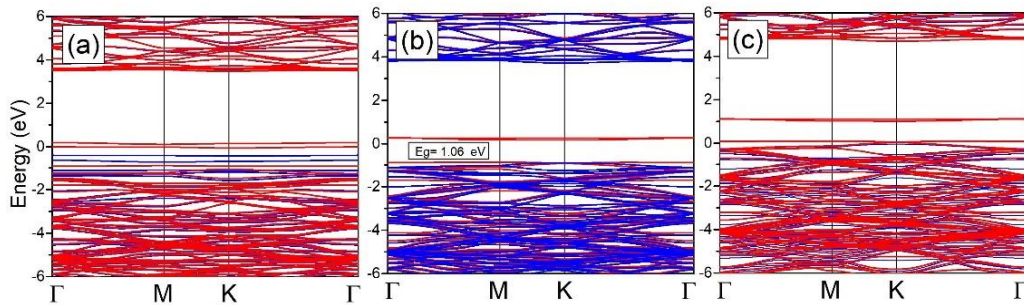

Figure 8. The band structures of (a) Q=-1e/cell, (b) Neutral, and (c) Q=+1e/cell case for Li-doped h-BN. The Fermi level is set to zero. Red lines indicate a spin-down state, while blue lines are spin-upup state. Eg indicates band gap value in eV.
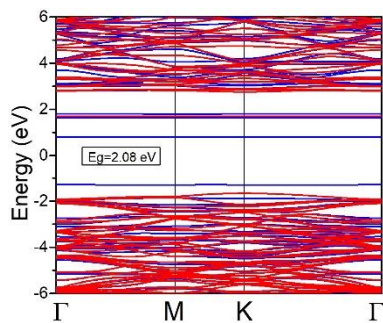

Figure 9. The band structure of Ti-BV-h-BN with DFT+U. The Fermi level is set to zero. Red lines indicate spin down state, while blue lines are spin up state. Eg indicates band gap value in eV.

Further, the effects of the E_{ads} and band structure have been demonstrated using the DFT+U method [33-35], with Ti-BV-h-BN serving as an example. For Ti, U value of 3.3 eV, as indicated in the literature [22], was chosen. The E_{ads} was found to be -7.93 eV, weaker than the GGA results. The impact of the DFT+U method on the band structure was also analyzed. As known, GGA generally underestimates the band gap [33-35]. With the implementation of the DFT+U method, the band structure of Ti-BV-h-BN changed, resulting in an increase in the band gap from 1.15 eV to 2.08 eV, as illustrated in Figure 9. The obtained data is in good agreement with previous findings [22].

The study has been extended to investigate the effect of the N-vacancy defect (NV-h-BN) with Ti/Li atom (Ti/Li-NV-h-BN). N-vacancy in the h-BN monolayer can be

observed, making the investigation of the N-vacancy defect an important matter. Initially, an N atom was removed, and then the system was relaxed. The results indicate that removing an N atom induced 1 μB/cell of magnetic moment. Subsequently, Ti/Li atoms interacted with the vicinity of the N-vacancy site, and after full relaxation, the band structures were obtained and presented in Figure 10. Specifically, Figure 10(a) indicates a band gap of 0.98 eV with up spin to down spin transition, which is different from Figure 7(b). On the other hand, there is no band gap for Li-NV-h-BN, as illustrated in Figure 10(b). These changes are not limited to the band structures only. The E_{ads} values were found to be -4.20 eV and -2.23 eV for the Ti-NV-h-BN and Li-NV-h-BN cases, respectively, while the total magnetic moments were calculated as 5 μB/cell for Ti-NV-h-BN and 2 μB/cell for Li-NV-h-BN.
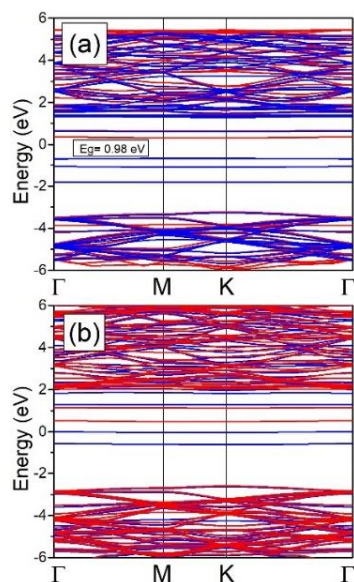

Figure 10. The band structures of (a) Ti-NV-h-BN, (b) Li-NV-h-BN. The Fermi level is set to zero. Red lines indicate a spin-down state, while blue lines are a spin up state. Eg indicates band gap value in eV.

4. Conclusions

The data obtained from the study showed that the adsorption energy of Ti-P-h-BN is stronger than that of Li-P-h-BN, and the Ti-P-h-BN system has a magnetic moment of 4 μB/cell, while that of Li-P-h-BN is 1 μB/cell. The net charge of the system can be manipulated by adding or removing an electron, which results in a significant increase in the interaction, especially for Li-P-h-BN. In the case of Ti-P-h-BN, the band gap decreases in both the N1 and P1 states, particularly in the N1 state. Meanwhile, removing an electron from Li-P-h-BN leads to a non-magnetic state and a significant increase in the band gap to 4.07 eV. The magnetic moments of the systems are highly affected by

changing the net charge. On the other hand, the adsorption energy in the Ti-BV-h-BN system is much stronger than that in the Li-BV-h-BN system, which can be attributed to the strong interaction of transition metals with d-orbitals with surfaces. Adding an electron to the systems decreased the interaction between Ti and BV-h-BN, while it increased the interaction between Li and BV-h-BN. Finally, removing an electron from the Ti-BN-h-BN system increased the band gap to 2.29 eV, and the magnetic moment disappeared. As a result, it is clear that the modified h-BN will be of great benefit to the needs of the silicon-based semiconductor world, and experimental applications of such studies should be developed more.

Conflict of Interest

The author declare that they have no known competing financial interests or personal relationships that could have appeared to influence the work reported in this paper.

References

[1] Knobloch T., Illarionov Y. Y., Ducry F., Schleich C., Wachter S., Watanabe K., Grasser T., 2021. The performance limits of hexagonal boron nitride as an insulator for scaled CMOS devices based on two-dimensional materials. Nature Electronics, **4**(2), pp. 98-108.

[2] Gupta S., 2022. Chip demand pushes automotive and lubricant industry changes. Tribology & Lubrication Technology, **78**(3), pp. 22-24.

[3] Geim A. K., Novoselov K. S., 2007. The rise of graphene. Nature materials, **6**(3), pp. 183-191.

[4] Gürel H. H., Salmankurt B., 2021. Quantum Simulation of the Silicene and Germanene for Sensing and Sequencing of DNA/RNA Nucleobases. Biosensors, **11**(3), pp. 59-62.

[5] Salmankurt B., Gürel, H. H., 2022. Two-Dimensional Nanomaterials Based Biosensors. In Progress in Nanoscale and Low-Dimensional Materials and Devices: Properties, Synthesis, Characterization, Modelling and Applications. 1st ed., Springer, Berlin, Germany, pp. 767-778.

[6] Elias C., Valvin P., Pelini T., Summerfield A., Mellor C. J., Cheng T. S., Cassabois, G., 2019. Direct bandgap crossover in epitaxial monolayer boron nitride. Nature Communications, **10**(1), pp. 2639-2646.

[7] Wang B., Sun Y., Ding H., Zhao X., Zhang L., Bai J., Liu K., 2020. Bioelectronics-related 2D materials beyond graphene: fundamentals, properties, and applications. Advanced Functional Materials, **30**(46), pp. 2003732-2003761.

[8] Corso M., Auwarter W., Muntwiler M., Tamai A., Greber T., Osterwalder J., 2004. Boron nitride nanomesh. Science, **303**(5655), pp. 217-220.

[9] Laskowski R., Blaha P., Gallauner T., Schwarz K., 2007. Single-layer model of the hexagonal boron nitride nanomesh on the Rh (111) surface. Physical Review Letters, **98**(10), pp. 106802-106806.

[10] Li S., Zhou M., Li M., Lu G., Wang X., Zheng F., Zhang P., (2018). Adsorption of 3d, 4d, and 5d transition-metal atoms on single-layer boron nitride. Journal of Applied Physics, **123**(9), pp. 095110-095116.

[11] Hwang Y., Chung Y. C., 2013. Lithium adsorption on hexagonal boron nitride nanosheet using dispersion-corrected density functional theory calculations. Japanese Journal of Applied Physics, **52**(6S), pp. 06GG08-06GG12.

[12] Sarikurt S., 2019. A first-principles investigation of Lithium Adsorption and Diffusion on BN, AlN and GaN monolayers. Eskişehir Technical University Journal of Science and Technology A-Applied Sciences and Engineering, **20**(4), pp. 436-445.

[13] Wang M., Li H., Ren J., Gao L., Feng T., Hao Z., Hou D., 2021. Ab initio study on electronic structure and magnetic properties of AlN and BP monolayers with Ti doping. Superlattices and Microstructures, **158**, pp. 107010-107021.

[14] Zhou Y. G., Yang P., Wang Z. G., Zu X. T., Xiao H. Y., Sun X., Gao F., 2011. Electronic and magnetic properties of substituted BN sheets: A density functional theory study. Physical Chemistry Chemical Physics, **13**(16), pp. 7378-7383.

[15] Wang L. C., Zhang Z. C., Ma L. C., Ma L., Zhang, J. M., 2022. First-principles study of hydrogen storage on Li, Na and K-decorated defective boron nitride

nanosheets. The European Physical Journal B, **95**(3), pp. 50-64.

[16] Ramirez-de-Arellano J. M., Jiménez G A. F., Magaña L. F., 2021. Catalytic Effect of Ti or Pt in a Hexagonal Boron Nitride Surface for Capturing CO_2. Crystals, **11**(6), pp. 662-675.

[17] Sun P. F., Wang W. L., Zhao X., Dang J. S., 2020. Defective h-BN sheet embedded atomic metals as highly active and selective electrocatalysts for NH_3 fabrication via NO reduction. Physical Chemistry Chemical Physics, **22**(39), pp. 22627-22634.

[18] Liu Y., Yang L. M., Ganz E., 2019. First-principles investigations of single metal atoms (Sc, Ti, V, Cr, Mn, and Ni) embedded in hexagonal boron nitride nanosheets for the catalysis of CO oxidation. Condensed Matter, **4**(3), pp. 65-78.

[19] Deng C., He R., Wen D., Shen W., Li M., 2018. Theoretical study on the origin of activity for the oxygen reduction reaction of metal-doped two-dimensional boron nitride materials. Physical Chemistry Chemical Physics, **20**(15), pp. 10240-10246.

[20] Kalwar B. A., Fangzong W., Soomro A. M., Naich M. R., Saeed M. H., Ahmed I., 2022. Highly sensitive work function type room temperature gas sensor based on Ti doped hBN monolayer for sensing CO_2, CO, H_2S, HF and NO. A DFT study. RSC Advances, **12**(53), pp. 34185-34199.

[21] Zhong S. Y., Wu S. Y., Yu X. Y., Shen G. Q., Yan L., Xu K. L., 2022. First-principles studies of the adsorption and catalytic properties for gas molecules on h-BN monolayer doped with various transition metal atoms. Catalysis Surveys from Asia, **26**(2), pp. 69-79.

[22] Wang M., Meng F., Hou D., Han Y., Ren J., Bai C., Zhou T., 2020. Electronic structure and spin properties study on 2D h-BN nanosheet with Ti or Fe doping. Solid State Communications, **307**, pp. 113803-113809.

[23] Gürel H. H., Salmankurt B., 2017. Binding mechanisms of DNA/RNA nucleobases adsorbed on graphene under charging: first-principles van der Waals study. Materials Research Express, **4**(6), pp. 065401-065409.

[24] Soler J. M., Artacho E., Gale J. D., García A., Junquera J., Ordejón P., Sánchez-Portal D. 2002. The SIESTA method for ab initio order-N materials simulation. Journal of Physics: Condensed Matter, **14**(11), pp. 2745–2779.

[25] Hohenberg P., Kohn W., 1964. Inhomogeneous electron gas. Physical Review, **136**(3B), pp. B864-B872.

[26] Kohn W., Sham L. J., 1965. Self-consistent equations including exchange and correlation effects. Physical Review, **140**(4A), pp. A1133- A1139.

[27] Perdew J. P., Burke K., Ernzerhof M., 1996. Generalized gradient approximation made simple. Physical Review Letters, **77**(18), pp. 3865-3868.

[28] Grimme S., 2006. Semiempirical GGA-type density functional constructed with a long-range dispersion correction. Journal of Computational Chemistry, **27**(15), pp. 1787-1799.

[29] Monkhorst H. J., Pack J. D., 1976. Special points for Brillouin-zone integrations. Physical Review B, **13**(12), pp. 5188-5192.

[30] Gürel H. H., Özçelik V. O., Ciraci S., 2013. Effects of charging and perpendicular electric field on the properties of silicene and germanene. Journal of Physics: Condensed Matter, **25**(30), pp. 305007-305013.

[31] Momma K., Izumi F., 2011. VESTA 3 for three-dimensional visualization of crystal, volumetric and morphology data. Journal of Applied Crystallography, **44**(6), pp. 1272-1276.

[32] Karki R., Khatri K., Adhikari K., Adhikari N. P., Pantha N., 2021. First Principles Study of Structural, Electronic and Magnetic Properties of Defected (Monovacant) Hexagonal Boron Nitride Sheet. Journal of Nepal Physical Society, **7**(4), pp. 19-27.

[33] Anisimov, V. I., Zaanen, J., Andersen, O. K. 1991. Band theory and Mott insulators: Hubbard U instead of Stoner I. Physical Review B, **44**(3), pp. 943-954.

[34] Cococcioni, M., De Gironcoli, S. 2005. Linear response approach to the calculation of the effective interaction parameters in the LDA+U method. Physical Review B, **71**(3), pp. 035105-035121.

[35] Anisimov, V. I., Aryasetiawan, F., Lichtenstein, A. I. 1997. First-principles calculations of the electronic structure and spectra of strongly correlated systems: the LDA+U method. Journal of Physics: Condensed Matter, **9**(4), pp. 767-808.
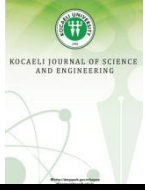
Effect of Using Recycled Colemanite Waste and Cathode Ray Tube Glass in the Cement Mortar on Physical and Mechanical Properties

Salih Taner YILDIRIM [1] (iD) , Arif YILMAZOĞLU [2, *] (iD)

[1] Department of Civil Engineering, Kocaeli University, Kocaeli, 41380, Turkey, **ORCID:** 0000-0003-0021-0625
[2] Department of Civil Engineering, Kocaeli University, Kocaeli, 41380, Turkey, **ORCID:** 0000-0002-3995-3904

Abstract

In this study, the performance of colemanite, which is a valuable boron waste, and recycled cathode ray tube glass (CRT) in the cement mortar was examined by experimentally. Colemanite waste (CW) and CRT were replaced with cement and aggregate and used as mineral additives, and their effect on the physical and mechanical properties (PP and MP) of mortar was investigated. In addition to the reference sample that didn't contain CW or CRT, seven more samples were used. In these samples, cement was used at a rate of 2.5% along with CW, and the aggregate was replaced with CRT at the rates of 10%, 20%, and 30%, and with the combination of CW and CRT. The workability, unit weight, and water absorption, compressive strength (CS), flexural strength (FS), and abrasion resistance properties of the mortars were compared. As a result of this study, it has been observed that the use of waste materials can make positive contributions to some of the PP and MP of the mortar. Thus, the goal of both improving the properties of the mortar and making it affordable by using waste materials were achieved.

1. Introduction

Mortar generally serves as a binder between wall units made of materials such as brick, briquettes, and autoclaved aerated concrete, or as a plastering material to protect the walls against external factors and improve the aesthetic appearance. The mechanical and physical properties expected from a good mortar mixture are resistance to external factors, low permeability, void-free structure and good adhesion to surfaces. In order to provide and develop these desired properties, additives are also occasionally utilized in mortars.

In today's world, where the problem of sustainability has become an increasingly widespread issue with the consumption of natural resources, the needs of the constantly developing construction sector are increasing and varying day by day. It is now an economic need for the construction industry to develop sustainable, eco-friendly mortar and concrete products from non-organic industrial waste products. The number of studies that examine how the using different industrial wastes as alternative materials improve the properties of mortar and concrete, and reduce costs, energy consumption, and environmental pollution with the elimination of these wastes is increasing every day.

Turkey is a boron-rich country, which is an industrial raw material. Thanks to technological developments in recent years, the number of sectors where boron is used has been increasing. Industrial applications for the utilization of boron waste by reusing it in concrete and thus reducing environmental pollution are limited. There are some studies in the literature where the waste of colemanite concentrator, a type of boron mineral, is used as an admixture in cement manufacturing, and PP and MP of that cement, such as the concrete slump test, FS, CS, and shrinkage were investigated. In the study conducted by Sevim [1], the concrete produced by using colemanite waste (CW) at the rates of 3%, 5%, 10%, and 15% was observed in terms of its properties of shrinkage, CS, and splitting tensile strength. As the result, in comparison to the reference sample, the new type of concrete produced by the addition of CW in the

---

mixing ratios of 3% and 5% was observed to have higher 28-day CS and tensile strength, and 37% less drying shrinkage. Mushurov et al. [2] used CW at rates of 5% and 7% and metakaolin at rates of 20% and 30%, it was concluded that the rates of colemanite used in the study significantly reduced the 28-day CS and FS. Gencel et al. [3] used CW in concrete, replacing aggregate with CW at 10%, 20%, 30%, 40%, and 50% aggregated and examined their mechanical and physical properties. It is observed that the best result is provided by 10% colemanite replacement, and which somewhat increases the slump and unit weight value. Conversely, the CS and FS decreased at all respective rates.

Considering the storage, disposal, and transportation costs, as well as the increase in the daily accumulation of waste glass (WG) in recent years, which is the most widespread waste material in the world, an urgent solution to eliminate WG is being sought. In addition to the glasses that can be found in many different colours and textures in different industries, there are many other kinds of glass, such as window glass, bottle glass, LCD screen glass, and cathode ray tube (CRT) glass, etc. [4-10]. While it is necessary in the glass industry to separate and recycle different types of glass and use one kind of glass during production, all kinds of WG can be used in cement-based mortar and concrete without the need to separate [9-10]. There are industrial applications for the utilization of the WG by reusing it in mortar and concrete, thus reducing environmental pollution. Kou and Poon [11] investigated the properties of self-consolidating concrete produced by replacing river sand with10 mm recycled glass aggregate at rates of 5%, 10%, and 15%. Based on the test results, it has been observed that CS, tensile strength, modulus of elasticity, and drying shrinkage decreased with the increase of the WG content in the recycled glass aggregate concrete while the chlorine ion penetration resistance increased. The properties of a new type of concrete produced by replacing fine aggregate with recycled glass at the rates of 10%, 15%, and 20% were investigated through experimental methods by Ismail and Al-Hashmi [12]. After 28 days of experiments in which it was observed that the WG increases the pozzolanic effect, it was concluded that CS value of the samples produced by using 10% and 15% recycled glass aggregate was lower than that of the reference samples, while an increase was seen in the values of FS and CS of the samples produced by using 20% recycled glass aggregate. In the study conducted by Kavas et al. [13], the use of glass wastes that are recycled into fine grains in the manufacturing of cement as an additive was investigated. For this purpose, WG was added to the cement at the rates of 5%, 10%, 15%, 20%, 25%, and 30% in the preparation of mortar. After the experiments, in line with the increasing WG, an average of 9% decrease in the 90-day CS and a 2.4% decrease in FS were observed in all produced cement

groups. Despite these results, it has been observed that even though introducing WG additives into cement up to a rate of 30% causes loss of MP; it is possible to use this type of cement in areas like field concrete, in which strength values do not come to the fore.

When the glass contacts concrete, cement, or mortar, the alkalies in these materials affect the silicates in the glass, causing alkali-silica reactions (ASR), and as a result, expansion and internal stresses occur. Since ASR does not occur when there is no moisture in the environment, it is indicated that glass aggregate concrete should not be used in an environment where it may be exposed to water [10]. Although not all kinds of glass cause ASR, it is necessary to check whether the kind of glass being used triggers an ASR reaction in the mortar before use, and if it occurs, the necessary additives should be used for protection [4, 9, 14, 15]. In the studies conducted by Topçu et al. [14], it was stated that ASR causes expansion increases, and internal stresses in direct proportion to the increase in the amount of WG in the concrete. In order to decrease the expansion and keep it under the critical level, fly ash surpassing 20%, and the chemical additive of Li_2CO_3 at the rate of 2% should be utilized. In addition, it has been observed in various studies that whether the glass is colourless, brown, or green has an effect on expansion, and colourless glasses cause the biggest expansion [4, 14, 15]. In their literature review, Saha et al. [16] stated that the replacement of cement with silica fume, blast furnace slag, and fly ash in order to reduce ASR in active glasses has proven to be effective in many studies. In a study conducted by Yildirim [9], in which cement was replaced with CRT glass at the rates of 5%, 10%, 15%, and 20%, new types of concrete samples with good consistency and increased unit weight, and reduced water absorption capacity were obtained. In the new concrete, a slight decrease in the 28 and 90-day CS and FS, a slight increase in the modulus of elasticity, and a slight decrease in abrasion were obtained due to the increase of the glass content in the concrete. Also, ASR expansion values determined with the ASTM C1260-07 [17] were found to be well below the 0.1% limit value for all samples. One of the problems that arises when glass aggregate is used in concrete because of the cracking of the glass and the spreading of these cracks within the concrete [9, 14, 18, 19]. According to Siddiqui et al. [20], the smooth surface of the glass facilitates crack movement, which negatively affects strength. The FS of mortar samples containing glass aggregate can be 10% less. In addition, when the size of the aggregates is increased from 1 mm to 3 mm, it is seen that the strength and resistance to cracks increase. In the study carried out by Batayneh et al. [21] in which WG, plastic, and broken concrete pieces were added at rates of 5%, 10%, 15% and 20% to the concrete being produced, and CS, FS, and the splitting tensile strength of the concrete were tested. The researchers stated that there is an increase in CS value,

especially in the splitting and FS values of the glass aggregate concrete.

In this study, the performance of CRT glass and CW a valuable boron waste in the mortar was examined. CW and CRT glass were replaced with cement and aggregate, and used as mineral additives, and their effect on the PP and MP of the mortar was investigated. Together with the reference sample, a total of eight samples were used in which cement was replaced with CW at the rate of 2.5%, and aggregate was replaced with CRT glass at the rates of 10%, 20% and 30%, and with the combination of CW and CRT glass. The workability (flow), unit weight, water absorption, CS, FS, and abrasion resistance properties of the mortars were compared. This experimental study intended to improve certain PP and MP of the mortar with the use of waste materials as well as to provide an affordable alternative and environmental protection with the utilization of these materials.

2. Materials and Method

2.1. Materials

The analyses of cement, CW, and CRT properties are given in Table 1. The cement used in this study was supplied from Nuh Cement Factory and was CEM I/42.5 R cement conforming to TS 197-1 [22]. The CW used in the study was obtained from Kütahya Emet Eti Mines. On the other hand, CRT is milled and recycled by a company called Exitcom operating in Kocaeli. River sand in the range of 0-4 mm was used in the mortar. Figure 1 shows CRT and CW materials. CRT was obtained from the company as ground, with the CW sample, it was obtained from the waste piles in the quarry in its current form. Since it was proven that the CRT sample did not cause any problems in terms of ASR in the

study performed by Yildirim (2018), the ASR test was not performed again in this study [9].

As seen in Figure 2, CRT has a fine distribution and sand has a coarser distribution. Here, it is aimed that the curve will approach the more ideal Fuller-Thompson curve since it will pull the curve up a little if CRT is used [23]. For this purpose, CRT10, CRT20, and CRT30 mixtures were made by replacing 10%, 20%, and 30% sand with CRT, and their granulometric compositions were shown. As can be seen, the increase in the CRT ratio brought the curve closer to the Fuller-Thompson curve. The CW material was used here as a mineral cement additive and was added to the mortar at the rate of 2.5% of the cement.

Reference sample, CW (2.5%) sample, three different 10%, 20% and 30% CRT samples, and 3 different CW (2.5%) + 10% CRT, CW (2.5%) + 20% CRT, CW (2.5%) + 30% CRT samples with mix designs seen in Table 2 were used in the study. From the mortars produced from the samples, six samples of 40x40x160 mm in size were used for unit weight, water absorption, FS and CS tests, and three samples of 71x71x71 mm in size for abrasion tests.

2.2. Method

The eight types of samples produced were first subjected to the flow table test according to ASTM C 1437 in the fresh state of the mortar and their spreading diameters were measured as the flow value [24]. Then, six samples of 40x40x160 mm and three pieces of 71x71x71 mm were kept in water until they were 28 days old after they were taken out of the mold. Three 40x40x160 mm samples were dried and weighed after they came out of the water, and their saturated dry surface weights were found. The dry weights were found by weighing the samples
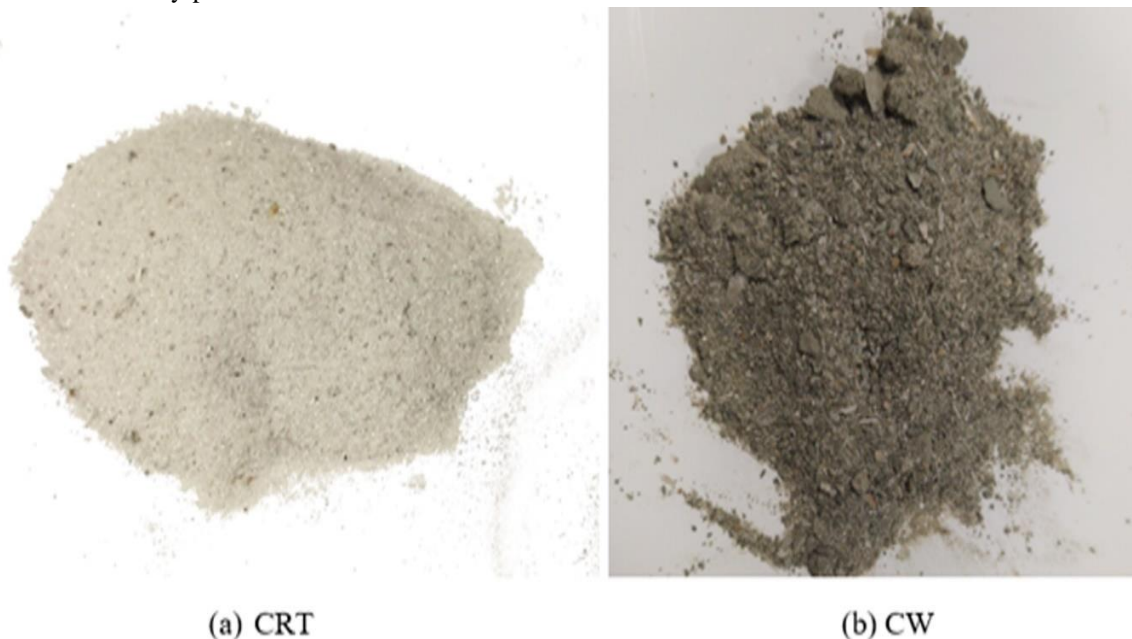

(a) CRT   (b) CW

Figure 1. Physical appearance of the CRT and CW.

Table 1. Properties of cement, CW and CRT.

Chemical properties				PP and MP			
Constituent (%)	Cement	CW	CRT	Properties	Cement	CW	CRT
SiO_2	20.5	18.77	50.9	Specific gravity (g/cm^3)	3.12	2.42	2.70
Al_2O_3	4.65	5.23	2.62	Blaine (m^2/kg)	360	102	-
Fe_2O_3	3.40	1.98	0.12	Mass stability (mm)	2.00	-	-
CaO	62.7	17.59	1.54	Starting setting time (min)	153	-	-
Free CaO	1.09	-	-	Final setting time (min)	188	-	-
MgO	1.02	6.78	0.64	90 μ sieve (%)	0.20	-	-
SO_3	2.21	0.20	-	45 μ sieve (%)	12.8	-	-
Na_2O	0.18	0.08	3.60	2-day strength (MPa)	30.2	-	-
K_2O	0.41	1.40	4.30	7-day strength (MPa)	51.1	-	-
PbO	-	-	0.29	28-day strength (MPa)	62.2	-	-
BaO	-	-	9.10				
Sb_2O_3	-	-	0.31				
ZrO2	-	-	0.91				
SrO	-	-	5.97				
TiO	-	-	0.39				
CeO_2	-	-	0.25				
B_2O_3	-	28.28	-				
Insoluble residue	0.60	-	-				
Ignition loss	2.15	0.54	-				
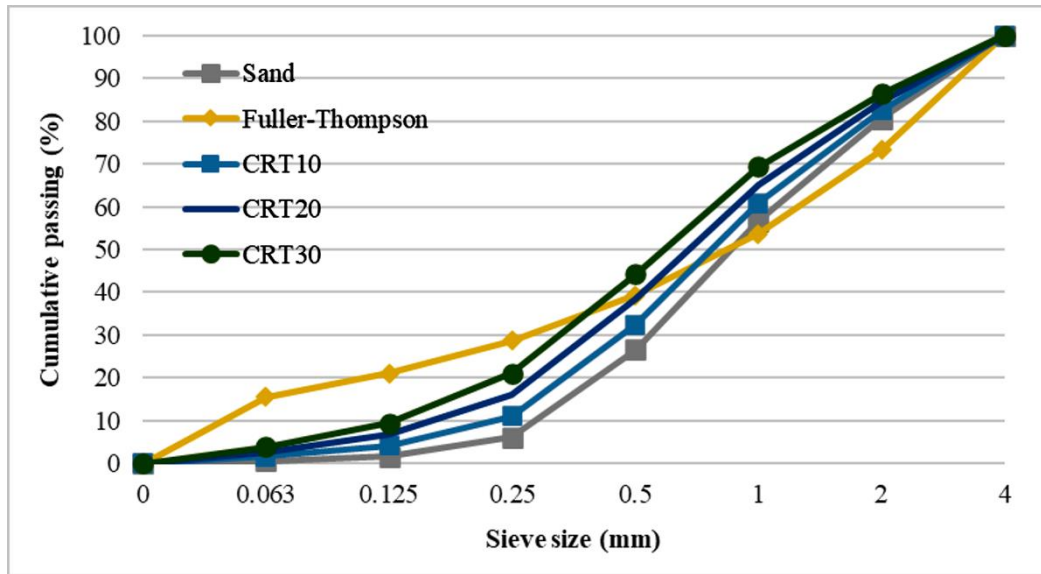
Figure 2. Particle size distributions of sand, CRT10, CRT20 and CRT30.

Table 2. Mortar mix designs.

Materials	Type of the mortars (kg/m^3)							
Compound	R	2.5CW	CRT10	CRT20	CRT30	2.5CW/CRT10	2.5CW/CRT20	2.5CW/CRT30
CEM I 42.5	350	341.3	350	350	350	341.3	341.3	341.3
CW	0	8.75	0	0	0	8.75	8.75	8.75
Sand	1050	1050	945	840	735	945	840	735
CRT	0	0	105	210	315	105	210	315
Water	175	175	175	175	175	175	175	175

to a constant weight for at least 24 hours in the oven. Dry unit weights were calculated by proportioning the sample weights to their volumes, and water absorption rates were calculated from the difference (%) between the two weighings [25]. The other 3 samples of 40x40x160 mm were subjected to a 3-point flexural test according to EN 196-1 and their FS were found. Again according to the same standard, the CS of the samples was found by breaking the 40x40 mm part into a cubic shape [26]. Samples with dimensions of 71x71x71 mm were subjected to the Böhme abrasion test according to EN 13892 [27]. The samples were subjected to abrasive action on the horizontal rotating disk, 16 times each time, and 22 rotations each time. Volumetric material losses from the surface of the samples were determined.

3. Experimental Results

3.1. Workability (Flow)

As it is seen in Figure 3, the flow of all samples containing admixtures is higher than that of the reference sample. The 2.50% replacement of cement with CW provides a 5.33% increase in flow with an increase of 8 mm [3], and an increase of up to 20% has been achieved by providing an increase of approximately 40 mm in the use of CRT [10]. The use of both colemanite and CRT increased slightly, reaching a difference of approximately 50 mm compared to the reference sample. Using the amount of CRT at the level of 30% reduces the flow compared to the levels of 10% and 20%.
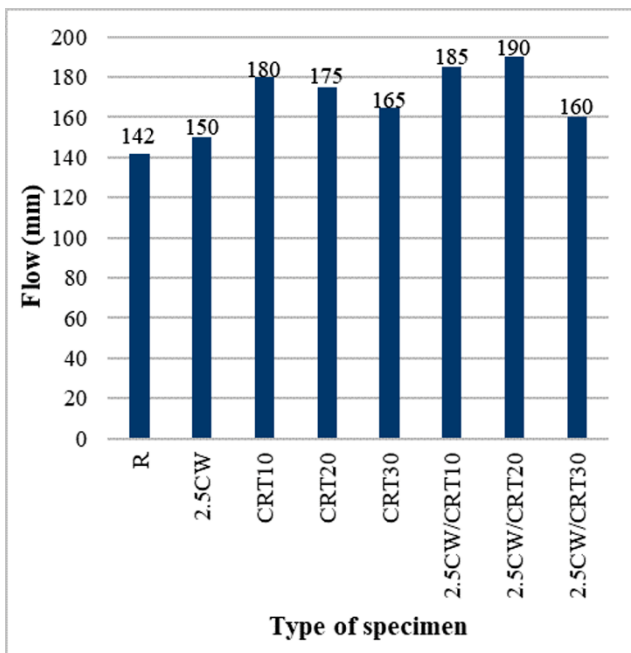

Figure 3. Flow value of the mortar samples.

3.2. Dry Unit Weight and Water Absorption

As can be seen in Figure 4, the addition of CW caused a unit weight increase of about 0.50% while reducing the water absorption by about 3% [3]. While the increase in the amount of CRT, the water absorption increased by about 11% and the unit weights increased by about 0.50%. In addition, water absorption decreased by about 20% compared to the reference sample by making a very serious decrease with the use of both CW and CRT [10]. On the other hand, the unit weight increased by 1.50% on average. Here, using CW and CRT together gave the best results.
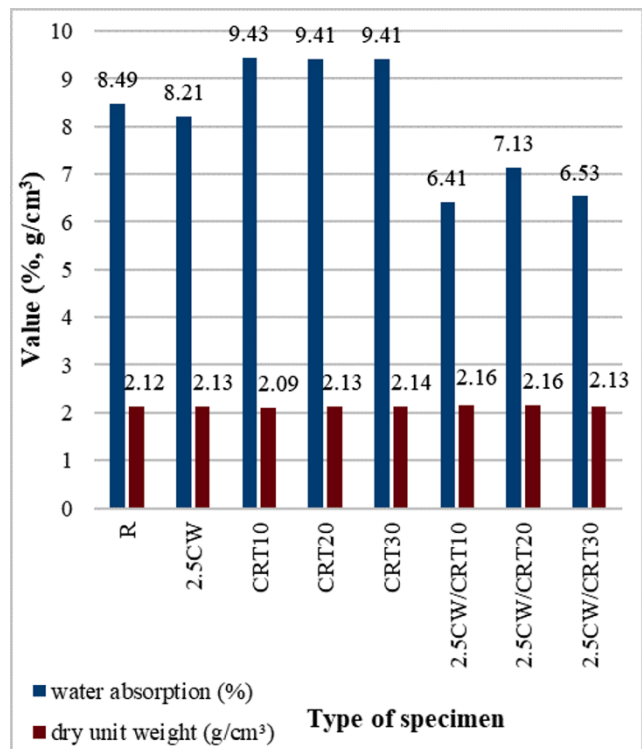
Figure 4. Dry unit weight and water absorption values of the mortar samples.

3.3. Compressive Strength (CS) and Flexural Strength (FS)

In Figure 5, it is seen that the CS and FS of the mortar reduce with the increase in the amount of additive. The addition of CW provided a very small increase in mortar strength compared to the reference sample [1, 3]. However, the use of CW and CRT together in mortar caused reductions of up to 30% in FS and up to 40% in CS [11, 20]. The replacement of up to 20% of sand with CRT resulted in a CS reduction of close to 5 MPa and a FS reduction of 0.17 MPa by remaining in more acceptable ranges [13].

Figure 5. CS and FS of the mortar samples.

3.4. Abrasion Resistance

Figure 6. Volume loss in mortar samples as a result of abrasion.

In Figure 6, it is seen that the lowest volume loss as a result of abrasion occurred in the reference sample with 7.16 cm^3. On the other hand, the CRT20 sample showed the highest volume loss value of 13.7 cm^3, with an increase of 47.6%. Yildirim [9] found that the addition of WG reduces the abrasion loss of concrete. Acc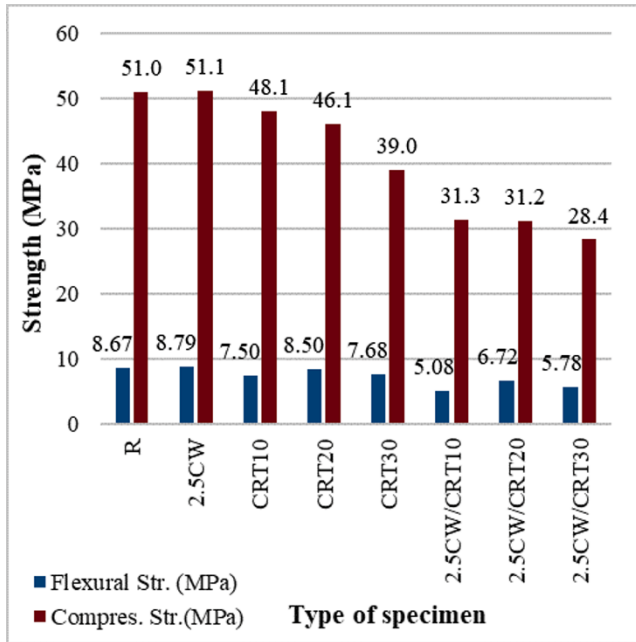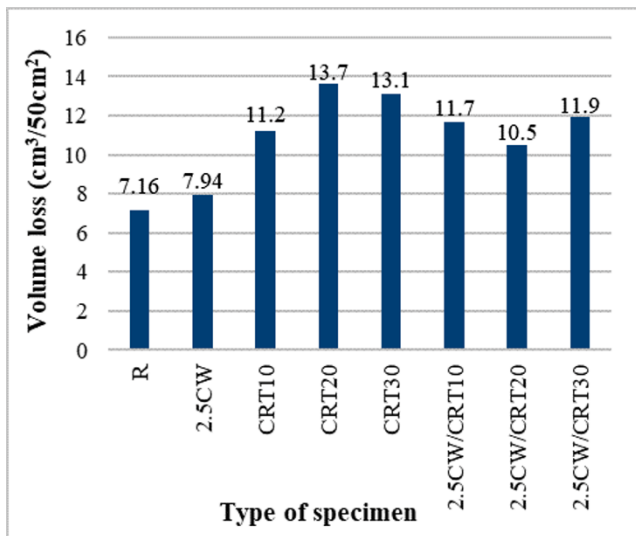ording to this; the contribution of the coarse aggregate used to the abrasion resistance can also be taken into consideration. Although the volume loss values of the CRT-added mortars were higher than the reference sample when CRT was used together with CW, it gave approximately 35% higher values on average

compared to the reference sample by reducing volume loss slightly. The volume loss of the mortar sample containing only CW showed a closer value to that of the reference sample, with 7.94 cm^3.

4. Discussion

In Table 3, the literature findings of the studies on concrete/mortar produced with WG or CW are shown and compared with the results of this study. Considering the percentage of replacement, type of substitute, and type of waste, the effect of these parameters on the relevant experiment is shown. The expression "+" means that the relevant value has increased, the expression "-" means that the relevant value has decreased, and the expression "No change" means that the relevant value has not changed or has not changed significantly. The abbreviations F.A, C.A, P.C and LCD define fine aggregate, coarse aggregate, Portland cement and liquid crystal display, respectively. The abbreviations "vol. %" and "wt. %" refer to the percent replacement by volume and mass of the waste material, respectively.

As can be seen from Table 3, different types of WG and their use in different proportions had different effects on the workability value of concrete/mortar. In the literature studies, WG was mostly replaced with fine aggregate and used in concrete/mortar. The use of CRT as WG in concrete/mortar generally increased the slump value of the concrete/mortar [28, 29, 38, 41-45]. These findings support the results of this study. It was stated that the low water absorption, high density, and smooth surface of the WG may have increased the slump of concrete [41]. However, in some studies, it has been stated that the use of CRT causes a decrease in the slump of concrete [40]. In some studies [46], the addition of CW to concrete/mortar had a positive influence on workability, while in some studies [3] it had a negative effect. It was also reported that the addition of CW didn't have a remarkable effect on workability [47].

MP such as FS, CS, and splitting tensile strength of concretes containing WG varied according to the type of WG, percentage of replacement, smoothness of WG, and its adherence to cement paste. The addition of WG caused an increase in FS, splitting tensile strength and CS for studies [6, 28, 29, 31, 33-36, 38, 40, 41, 43, 44] but caused a decrease for studies [21, 32, 37, 39, 42, 45]. The 50% and 100% replacement of fine aggregate by volume with CRT caused a 21% and 32% reduction in CS of the concrete, respectively. FS of concrete samples with 50% CRT and 100% CRT decreased by 9% and 14%, respectively, compared to the reference concrete [28]. Ali and Al-Tersawy [34] replaced fine aggregate with WG at 10%, 20%, 30%, 40%, and 50% by volume. For 10%,

Table 3. Literature findings on the PP and MP of concretes/mortars containing WG and CW.

Ref.	Source	Replacement (%)	Type of Sub.	Slump/Flow	Compressive strength	Tensile strength	Flexural strength	Density	Water absorption	Abrasion resistance
This study	CRT	10, 20 &30 (wt. %)	F.A	+	-		-	No change	+	-
[28]	CRT	50 & 100 (vol. %)	F.A	+	-		-		-	
[29]	CRT	25, 50, 75 & 100 (vol. %)	F.A	+	-		-	+	+	
[30]	Waste glass	20, 50 & 100 (vol. %)	F.A	No change	+/-		+	-	+	
[31]	Soda-lime silicate glass	10, 20, 30, 40 & 50 (wt. %)	F.A	+/-	-		-	-	-	
[21]	Waste glass	5, 10, 15 & 20 (vol. %)	F.A	-	+	No change		+	-	
[6]	LCD	20, 40, 60 & 80 (vol. %)	F.A	-	-	+/-	-			
[32]	Waste glass	25, 50, 75 & 100 (wt. %)	F.A	+	+	No change	No change			
[33]	Waste glass	10, 20 & 30 (vol. %)	C.A	-	-			-		
[34]	Waste glass	10, 20, 30, 40 & 50 (vol. %)	F.A	+	-	-	-			
[35]	Waste glass	15, 30, 45 & 60 (wt. %)	F.A	+	-	-	-	-	-	
[36]	Green waste glass	30, 50 & 70 (wt. %)	F.A	-	-	-	-			
[37]	Waste E-glass	10, 20, 30, 40 & 50 (wt. %)	F.A	-	+					
[38]	CRT	100 (wt. %)	C.A	+	-	-	-			
[39]	CRT	80 & 100 (wt. %)	F.A		+		+			
[40]	CRT	5, 15 & 25 (vol. %)	F.A	-	-		+/-	+		
[41]	CRT	25, 50 & 75 (vol. %)	F.A	+	-		-			
[42]	CRT	100 (wt. %)	F.A	+	+		+			
[43]	CRT	25, 50, 75 & 100 (vol. %)	F.A	+	-		-	+	-	
[44]	CRT	30, 60 & 100 (vol. %)	F.A	+	-			+	-	
[45]	CRT	25, 50 & 75 (wt. %)	F.A	+	+		+			
[46]	CW	2, 4, 6, 8, 10 & 12 (wt. %)	P.C	+	-			-		
[47]	CW	1, 3 & 5 (wt. %)	P.C	No change	+/-	+/-				
[48]	CW	1, 3, 5 & 7 (wt. %)	P.C	Fix	-				+	
[3]	CW	10, 20, 30, 40 & 50 (vol. %)	F.A and C.A	-	-	-		-		

20%, 30%, 40% and 50% WG replacement percentages, CS of the concretes reduced by 5%, 15%, 18%, 23% and 24% compared to the reference concrete, respectively. For 10%, 20%, 30%, 40%, and 50% WG replacement percentages, 9%, 15%, 16%, 24%, and 28% reductions occurred in splitting tensile strength of concrete, respectively. In addition, 3%, 11%, 12%, 23%, and 24% reductions in FS occurred for 10%, 20%, 30%, 40%, and 50% WG replacement percentages [34]. These literature findings are in agreement with the results of this study. Nevertheless, in some studies [30, 6, 40], the addition of WG caused both an increase and a decrease in MP of concrete. The addition of CW to concrete generally resulted in reductions in FS, CS and splitting tensile strength of concrete [3, 46-48].

The increment in the density of concrete containing WG is attributed to the greater specific gravity of WG than that of natural aggregate (fine aggregate) [29, 40, 43, 44]. On the other hand, if the specific gravity of WG is lower than that of natural aggregate, the density of concrete containing WG decreases [21, 30, 31, 33, 35]. Therefore, the specific gravity of WG on the density of concrete with WG is of great importance. The reason why there was no remarkable change in the density of concrete in this study was because of the closeness of the specific gravity of sand and WG. Because the specific gravity of CW is lower than that of Portland cement, the replacement of Portland cement with CW generally reduced the density of the concrete [3, 46].

Factors such as type of WG and water absorption of WG and the particle size of WG affected the water absorption of the concrete [28-31, 35, 43, 44]. In addition, it was stated that the pore space among the particles influences the water absorption of the concrete [29]. There are very few studies on the water absorption of concrete containing CW.

Literature studies on the abrasion resistance of concrete containing WG and CW are scarce. Therefore, more experimental studies are needed on the abrasion resistance of concrete with WG and CW.

5. Conclusion

The following results were obtained in this study:

1) The use of both CW and CRT increased the flow value of the mortar. The increase in flow value reached approximately 50 mm when CW was used with CRT together.

2) The use of CW and CRT caused very low increases in unit weights. While the use of CW reduced the water absorption rate by increasing the fullness of the mortar, the use of CRT increased the water absorption rate.

3) CS and FS showed a very low increase with the use

of CW, it showed serious decreases around 20 MPa with the use of both CW and CRT. The use of CRT up to 20% is a more acceptable rate in terms of strength and this rate caused a reduction in strength up to 5 MPa in comparison to the reference sample.

4) The addition of CW to the mortar increased the amount of abrasion of the mortar. The volume loss of the mortar sample containing 20% CRT is 9.1% higher than that of the reference sample. The combined use of CW and CRT caused a slight decrease in the volume loss compared to CRT.

5) In particular, the use of CW in mortar had a positive effect on FS, CS, workability, unit weight and water absorption while it had a negative effect on abrasion resistance. While the addition of CRT to the mortar caused a negative effect in general, it gave more acceptable values in terms of all properties when used up to 10%.

It is expected that the findings found in this study will benefit scientific studies in the future in terms of environmental protection and economic advantages. There is also a large amount of colemanite waste and WG in Turkey. It is also noteworthy that there is still very little literature research on colemanite. It will be beneficial to both to recycle it and to increase research on this waste. It is also noteworthy that the abrasion resistance of mortars with colemanite and glass aggregates has hardly been studied. Therefore, more work is needed on this subject.

Declaration of Ethical Standards

The authors of this article declare that the materials and methods used in this study do not require an ethical committee permission, and legal-special permission.

Conflict of Interest

The authors declare that they have no known competing financial interests or personal relationships that could have appeared to influence the work reported in this paper.

Acknowledgments

References

[1] Sevim U.K., 2011. Colemanite ore waste concrete with low shrinkage and high split tensile strength. Materials and Structures, **44**(1), pp. 187-193.

[2] Mushurov M., Canpolat O., Uysal M., Mukhallad M., Aygörmez Y., 2018. Investigation of waste products of boron and metakaolin utilizes. Journal of Sustainable Construction Materials and Technologies, **3**(2), pp. 212-220.

[3] Gencel O., Brostow W., Ozel C., 2010. An investigation on the concrete properties containing colemanite. International Journal of Physical Sciences, **5**(3), pp. 216-225.

[4] Jin W., Meyer C., Baxter S., 2000. "Glascrete"- Concrete with glass aggregate. ACI Materials Journal, **97**(2), pp. 208-213.

[5] Meyer C., 2009. The greening of the concrete industry. Cement and Concrete Composites, **31**(8), pp. 601-605.

[6] Wang H.Y., 2009. A study of the effects of LCD glass sand on the properties of concrete. Waste Management, **29**(1), pp. 335-341.

[7] Hreglich S., Falcone R., Vallotto M., 2001. The recycling of end of life panel glass from TV sets in glass fibres and ceramic productions. In Recycling and Reuse of Glass Cullet, Thomas Telford Publishing, London, UK, pp. 123-134.

[8] Iniaghe P.O., Adie G.U., 2015. Management practices for end-of-life cathode ray tube glass: Review of advances in recycling and best available technologies. Waste Management & Research, **33**(11), pp. 947-961.

[9] Yildirim S.T., 2018. Research on strength, alkali-silica reaction and abrasion resistance of concrete with cathode ray tube glass sand. Sustainable Buildings—Interaction Between a Holistic Conceptual Act and Materials Properties, IntechOpen, London, UK, pp. 131-149.

[10] Meyer C., 2003. Glass concrete. Concrete International, **25**(6), pp. 55-58.

[11] Kou S.C., Poon C.S., 2009. Properties of self-compacting concrete prepared with recycled glass aggregate. Cement and Concrete Composites, **31**(2), pp. 107-113.

[12] Ismail Z.Z., Al-Hashmi E.A., 2009. Recycling of waste glass as a partial replacement for fine aggregate in concrete. Waste Management, **29**(2), pp. 655-659.

[13] Kavas T., Çelik M.Y., Evcin A., 2004. Cam atıklarının çimento üretiminde katkı maddesi olarak kullanılabilirliğinin araştırılması. 5. Endüstriyel Hammaddeler Sempozyumu, İzmir, Türkiye, 13-14 Mayıs, pp. 114-119.

[14] Topçu İ.B., Boğa A.R., Bilir T., 2008. Alkali–silica reactions of mortars produced by using waste glass as fine aggregate and admixtures such as fly ash and Li2CO3. Waste Management, **28**(5), pp. 878-884.

[15] Özkan Ö., 2007. Properties of mortars containing waste bottle glass and blast furnace slag. Journal of the Faculty of Engineering and Architecture of Gazi University, **22**(1), pp. 87-94.

[16] Saha A.K., Khan M.N.N., Sarker P.K., Shaikh F.A., Pramanik A., 2018. The ASR mechanism of reactive aggregates in concrete and its mitigation by fly ash: A critical review. Construction and Building Materials, **171**, pp. 743-758.

[17] ASTM C1260, 2014. Standard Test Method for Potential Alkali Reactivity of Aggregates (Mortar-Bar Method). ASTM International, West Conshohocken, PA, USA.

[18] Shayan A., Xu A., 2004. Value-added utilisation of waste glass in concrete. Cement and Concrete Research, **34**(1), pp. 81-89.

[19] Shi C., Zheng K., 2007. A review on the use of waste glasses in the production of cement and concrete. Resources, Conservation and Recycling, **52**(2), pp. 234-247.

[20] Siddiqui A.M., Choudhury A.H., Merchant I.J., 2004. Acoustic emission monitoring of the fracture behaviour of concrete containing various size and shape of glass aggregates. Paper presented at 26th European Conference on Acoustic Emission Testing, Berlin, Germany, 15-17 September, pp. 115-130.

[21] Batayneh M., Marie I., Asi I., 2007. Use of selected waste materials in concrete mixes. Waste Management, **27**(12), pp. 1870-1876.

[22] TS EN 197-1, 2012. Cement- Part 1: Compositions and conformity criteria for common cements. Turkish Standarts Institution, Ankara.

[23] Fuller W.B., Thompson S.E., 1907. The laws of proportioning concrete. Transactions of the American Society of Civil Engineers, **59**(2), pp. 67-143.

[24] ASTM C 1437-07, 2008. Standard test method for flow of hydraulic cement mortar. ASTM International, West Conshohocken, PA, USA.

[25] ASTM C642-13, 2013. Standard test method for density, absorption, and voids in hardened concrete. ASTM International, West Conshohocken, PA, USA.

[26] EN 196-1, 2002. Methods of testing cement – Part 1: Determination of strength. Turkish Standarts Institution, Ankara.

[27] BS EN 13892-3, 2014. Methods of test for screed materials: Determination of wear resistance-Bohme. British Standards Institution, London, UK.

[28] Kim I.S., Choi S.Y., Yang E.I., 2018. Evaluation of durability of concrete substituted heavyweight waste glass as fine aggregate. Construction and Building Materials, **184**, pp. 269-277.

[29] Liu T., Wei H., Zou D., Zhou A., Jian H., 2020. Utilization of waste cathode ray tube funnel glass for ultra-high performance concrete. Journal of Cleaner Production, **249**, pp. 119333.

[30] Penacho P., de Brito J., Veiga M.R., 2014. Physico-mechanical and performance characterization of mortars incorporating fine glass waste aggregate. Cement and Concrete Composites, **50**, pp. 47-59.

[31] Tuaum A., Shitote S., Oyawa W., 2018. Experimental study of self-compacting mortar incorporating recycled glass aggregate. Buildings, **8**(2), pp. 15.

[32] Jiao Y., Zhang Y., Guo M., Zhang L., Ning H., Liu S., 2020. Mechanical and fracture properties of ultra-high performance concrete (UHPC) containing waste glass sand as partial replacement material. Journal of Cleaner Production, **277**, pp. 123501.

[33] Rashid K., Hameed R., Ahmad H.A., Razzaq A., Ahmad M., Mahmood A., 2018. Analytical framework for value added utilization of glass waste in concrete: Mechanical and environmental performance. Waste Management, **79**, pp. 312-323.

[34] Ali E.E., Al-Tersawy S.H., 2012. Recycled glass as a partial replacement for fine aggregate in self compacting concrete. Construction and Building Materials, **35**, pp. 785-791.

[35] Mardani-Aghabaglou A., Tuyan M., Ramyar K., 2015. Mechanical and durability performance of concrete incorporating fine recycled concrete and glass aggregates. Materials and Structures, **48**(8), pp. 2629-2640.

[36] Park S.B., Lee B.C., Kim J.H., 2004. Studies on mechanical properties of concrete containing waste glass aggregate. Cement and Concrete Research, **34**(12), pp. 2181-2189.

[37] Chen C.H., Huang R., Wu J.K., Yang C.C., 2006. Waste E-glass particles used in cementitious mixtures. Cement and Concrete Research, **36**(3), pp. 449-456.

[38] Pauzi N.N.M., Jamil M., Hamid R., Abdin A.Z., Zain M.F.M., 2019. Influence of spherical and crushed waste Cathode-Ray Tube (CRT) glass on lead (Pb) leaching and mechanical properties of concrete. Journal of Building Engineering, **21**, pp. 421-428.

[39] Walczak P., Małolepszy J., Reben M., Rzepa K., 2015. Mechanical properties of concrete mortar based on mixture of CRT glass cullet and fluidized fly ash. Procedia Engineering, **108**, pp. 453-458.

[40] Wang J., Guo S., Dai Q., Si R., Ma Y., 2019. Evaluation of cathode ray tube (CRT) glass concrete with/without surface treatment. Journal of Cleaner Production, **226**, pp. 85-95.

[41] Zhao H., Poon C.S., Ling T.C., 2013. Utilizing recycled cathode ray tube funnel glass sand as river sand replacement in the high-density concrete. Journal of Cleaner Production, **51**, pp. 184-190.

[42] Hui Z., Sun W., 2011. Study of properties of mortar containing cathode ray tubes (CRT) glass as replacement for river sand fine aggregate. Construction and Building Materials, **25**(10), pp. 4059-4064.

[43] Ling T.C., Poon C.S., 2011. Utilization of recycled glass derived from cathode ray tube glass as fine aggregate in cement mortar. Journal of Hazardous Materials, **192**(2), pp. 451-456.

[44] Liu T., Qin S., Zou D., Song W., 2018. Experimental investigation on the durability performances of concrete using cathode ray tube glass as fine aggregate under chloride ion penetration or sulfate attack. Construction and Building Materials, **163**, pp. 634-642.

[45] Hui Z., Poon C.S., Ling T.C., 2013. Properties of mortar prepared with recycled cathode ray tube funnel glass sand at different mineral admixture. Construction and Building Materials, **40**, pp. 951-960.

[46] Erdogmus E., 2014. Combined effect of waste colemanite and silica fume on properties of cement mortar. Science and Engineering of Composite Materials, **21**(3), pp. 369-375.

[47] Durgun M.Y., Sevinc A.H., 2019. High temperature resistance of concretes with GGBFS, waste glass powder, and colemanite ore wastes after different cooling conditions. Construction and Building Materials, **196**, pp. 66-81.

[48] Durgun M.Y., Özen S., Karakuzu K., Kobya V., Bayqra S.H., Mardani-Aghabaglou A., 2022. Effect of high temperature on polypropylene fiber-reinforced mortars containing colemanite wastes. Construction and Building Materials, **316**, pp. 125827.

Kocaeli University

Kocaeli Journal of Science and Engineering

http://dergipark.org.tr/kojose

Investigation of Mycotoxins In Packed Gluten Free Foods

Zeynep DEĞİRMEN [1] (iD) , Seda KARAYÜNLÜ BOZBAŞ [2, *] (iD)

[1] Department of Mycotoxin, Kocaeli Food Control Laboratory Directorate, Kocaeli, 41200, Turkey, **ORCID: 0000-0002-6773-7678**
[2] Department of Chemistry, Kocaeli University, Kocaeli, 41380, Turkey, **ORCID: 0000-0002-5177-3826**

Abstract

The number of people with celiac disease and gluten intolerance is increasing day by day. This increases the variety, number and consumption of gluten-free products. However, this study was the first in our country to determine whether the packaged gluten-free products contain mycotoxins. Aflatoxin (AF), ochratoxin (OTA), zearalenone (ZON), and deoxynivalenol (DON) were analyzed in 95 imported and domestic packaged gluten-free foods of different types and brands. Analyses were made with HPLC with fluorescent detector and HPLC with diode array detector. In addition, validation studies were completed with the addition of blank samples. OTA was detected in 9 food samples. In the OTA analysis, toxins were detected in 1 buckwheat flour, 3 pasta, 3 crackers or biscuits, 2 corn flours, but these values are below the values determined by the Turkish Food Codex (TFC). DON was found to be suitable for TFC in 7 types of pasta, 1 type of bread, and 3 types of crackers or biscuits.

1. Introduction

Mycotoxins are toxic metabolic products produced by some types of molds. These mycotoxins are low molecular- weight natural toxins with a wide range of chemical structures [1,2]. Today, it is known that more than 350 mold species produce mycotoxins. Molds that produce mycotoxins can be found everywhere and are carried by wind and air currents. Many kinds of molds need certain conditions for growth, development, and mycotoxin production. These conditions; can be summarized as humidity, temperature, substrate type, nutritional factors, oxygen and carbon dioxide levels in the atmosphere, the presence of other mold species, geographical location, and genetic conditions [3,4]. The most important molds that produce mycotoxins are Aspergillus, Penicillium, Fusarium, Alternaria species [1]. These molds produce mycotoxins, that affect humans and animals seriously, such as aflatoxin, ochratoxin A, deoxynivalenol, zearalenone, and fumonisin.

The year 1960 was a turning point in understanding

mycotoxins. Until that time, the molding of agricultural products was only an economic problem, and it was the center of attention due to the diseases it caused in living creatures after 1960. The cause of the disease, which resulted in the death of many poultry in England in 1960, was found to be the toxin in Brazilian peanuts used in animal feed. Since aflatoxin was first detected in Aspergillus flavus on this date, the first letters of these molds were used, and this mycotoxin was called aflatoxin [5, 6].

Molds can grow on countless food items, such as cereals, dried fruits, nuts, and spices, that can produce mycotoxins. Diseases caused by mycotoxins are called "mycotoxicoses" [7]. When mycotoxins are ingested, inhaled, or absorbed through the skin, they can cause many diseases or even death in human beings [8].

People with celiac disease and gluten intolerance have to consume gluten-free foods for their health. Especially celiac patients should definitely consume gluten-free products. Gluten is a high-molecular-weight, the main storage protein in cereals. It is a composite protein composed of glutenin and prolamines [9, 10]. Gluten is the substance that gives dough resilience and flexibility, which is why it is a common component of

* Corresponding Author: sedak@kocaeli.edu.tr

many food products.

The gluten-free product diet is characterized by more corn, rice, and other gluten-free grain consumption [11, 12]. In the past decade, some reports have focused on corn-based products, with some cases showing severe mycotoxin contamination. More recently, specific research on mycotoxin contamination of gluten-free diet products has been published with conflicting results [13–15].

Foods that mainly contribute to mycotoxin intake through a gluten-free diet are cereals such as rice, corn, buckwheat, etc., and leguminosae such as quinoa, soybean [11,12]. The increase in corn-based product consumption is the riskiest commodity due to the potential coexistence of more than one mycotoxin. This may be of particular concern for the vulnerable population group, such as celiac patients. To summarize briefly, mycotoxins are toxic compounds produced by certain fungal species that can contaminate food crops. Gluten-free foods, typically made from alternative grains such as rice, corn, and quinoa, can also be contaminated with mycotoxins. There are several types of research found in literature based on analyzed the mycotoxins in gluten-free foods [13-18]. Corn-based gluten-free products are a major essential ingredient for celiac patients. These products contain high levels of corn mold toxin. This poses a problem for those trying to improve their health after years of gluten-induced damage. A study on the presence of different mycotoxins in gluten-free products collected from the Italian market showed that FB and ZON were present in all product categories considered except pasta. Specifically, 29% of analyzed samples had FBs and 11% ZON, while few samples had low DON levels [18].

Positive values were obtained for DON in corn-based gluten-free products collected from the markets in Valencia [16]. However, urine biomarkers of mycotoxin exposure were monitored in the urine analyses of a group of celiac patients and individuals from the healthy control group with deoxynivalenol (DON), zearalenone (ZON), and fumonisin B1 (FB B1) [17]. Brera et al. (2014) detected the zearalenone contamination of gluten-free products. It has been evaluated whether those celiac patients were exposed to fumonisins (FB) and zearalenone (ZON) [15]. In the literature, the presence of mycotoxins in packaged gluten-free foods produced in Turkey was absent. It is estimated that between 250 and 750 thousand people in Turkey have celiac disease [19]. There is a group of people without celiac disease who also consume gluten-free foods because they find them healthier. Of course, they all carry the risk of consuming products containing mycotoxins. In this context, it is of great importance to investigate and report the presence of mycotoxin in gluten-free packaged foods. In this study, the presence of aflatoxin (AF), ochratoxin A (OTA), deoxynivalenol (DON), and zearalenone (ZON) was determined in 95 different products, and verification studies have been carried out. These products have been purchased from 2019 until 2021: pasta (16 packages), noodles (6 packages), corn flakes (6 packages), tarhana (4 packages), rice flour (5 packages), cornflour (8 packages), biscuit and cracker varieties (20 packages), bread (7 packages), cake mix (6 packages), buckwheat flour (3 packages), white mulberry flour (3 packages), carob flour (3 packages), chickpea flour (2 packages), chestnut flour (3 packages), and coconut flour (3 packages), which were collected from the Turkish hypermarkets and internet stores. Bought with the expiration date in mind.

2. Materials and Methods

2.1. Chemicals

The chemicals and reagents used during the studies were of analytical reagent grade and suitable for HPLC devices. The deionized water was obtained from the Millipore Q purification system (Millipore, Merck, Darmstadt, Germany). Methanol (CH_3OH) and acetonitrile (C_2H_3N) (both HPLC grade) were purchased from Merck (Darmstadt, Germany). Nitric acid (HNO_3), sodium chloride (NaCl), potassium bromide (KBr), acetic acid (CH_3COOH), disodium phosphate (Na_2HPO_4), potassium dihydrogen phosphate (KH_2PO_4) potassium chloride (KCl) were all analytical reagent bought from Merck (Darmstadt, Germany). Aflatoxin mix standards were obtained from Supelco, Ochratoxin, Zearalenone, and Deoxynivalenol Standards were obtained from Trilogy Analytical Laboratory (Washington, MO, USA). The immunoaffinity columns (IACs), AFTest® (product code: 12022), OchraTest™ (product code:13012), Deoksinivalenol TEST-P, Zeralenon TEST-P were from R Biopharm Rhône Ltd (Darmstadt, Germany). GF/A glass microfiber filters (125 mm) were from Sartorius (Göttingen, Germany).

2.2. Instruments

In weighing, analytical balances (Sartorius CP 3202S, Goettingen, Germany) were used for all experiments. Blender (Waring, USA) and grinder (Yazıcılar G2, Turkey) were used to grind and homogenize samples. Mobile phase degassed in an ultrasonic cleaner (Intersonic, Istanbul, Turkey)

Chromatographic analyses for ochratoxin A (OTA), deoxynivalenol (DON), and zearalenone (ZON) were carried out using an Agilent 1260 Infinity LC (Agilent Technologies, CA, USA). This HPLC is equipped with a binary pump, an online degasser, an autosampler, two

detectors (DAD and FLD), and a column thermostat. An Agilent HPLC 1100 (Agilent Technologies, CA, USA) device, which was equipped with an FLD detector (Agilent, Santa Clara, CA, USA), was used for aflatoxin analysis. A Kobra-cell-celld post-column derivative electrochemical cell was used for the complete separation of aflatoxins (B1, B2, G1, and G2) in the analytical column and to strengthen the fluorescence intensity of aflatoxin B1 and aflatoxin G1. The signals obtained as a result of the separations in the analytical column were calculated automatically by Chem Stations software (Agilent, Santa Clara, CA, USA). The data obtained during the analyses were stored on the hard disk of the computer. A centrifuge, Hettich 32A (Hettich Zentrifugen, Tuttlingen, Germany), a nitrogen generator (Parker Balston Nitro, NY, USA), and a vortex, DLAB MX-S (DLAB Scientific Inc., China), were also used during analysis.

2.3. Sample Preparation

95 different brands and types of gluten-free packaged food samples (such as biscuits, crackers, cakes, pasta, etc.) were purchased randomly from internet stores and health food departments of hypermarkets in Turkey. Some of those samples were imported from other countries. The samples were collected in Izmit (Turkey) during 2019. The duration of product collection is 2 years. During this time, the expiration dates of the products were monitored, and the products were kept in their original packaging at room temperature until they were analyzed. Blender and grinder were used to grind and homogenize samples. Homogenized samples were kept in appropriate conditions until analysis. In parallel with 95 samples and each sample, AF, OTA, DON, and ZON analyses were performed on products.

2.4. Homogenization

Mycotoxins have an irregular (not homogeneous) distribution in food and feed. Therefore, homogenization is very important in mycotoxin analysis. During this process, samples must be taken from different points to represent the lot. It is very important to homogenize the aggregate sample so that the analysis result from the laboratory is accurate and reproducible. Homogenization is a principle that reduces particle size and ensures a uniform distribution of contaminated particles in the crushed sample. For this, 10 analyses were made in parallel with the 8-numbered corn flour sample [20], and the graphic of homogenization of corn flour was obtained in Fig. 1. The blue and red colors in Fig. 1 show the results of parallel samples. They are not results before or after

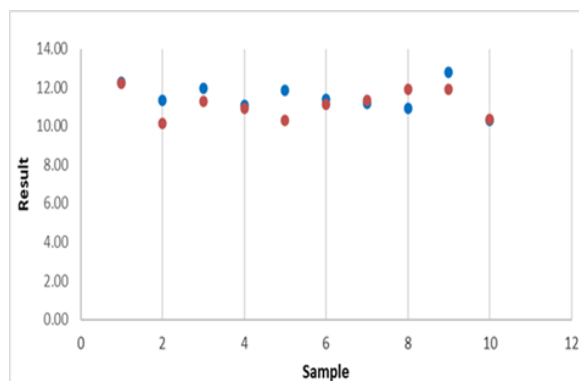homogenization. And the products were homogenized and analyzed after that.

Figure 1. Homogenization of corn flour.

2.5. Analytical Methods for Mycotoxins

After all samples were homogenized by grinding, aflatoxin (AF), ochratoxin A (OTA), deoxynivalenol (DON), and zearalenone (ZON) analyses were performed. Aflatoxin and ochratoxin analyses were done according to AOAC Official Methods 991.31 [21] and 2000.03 [22], respectively. Zearalenone analysis was done as mentioned in the literature [23]. Deoxynivalenol analysis was done with DONPREP, which was supplied from R-Biopharm Rhône Ltd., and deoxynivalenol analysis in cereal was done using water extraction. AF was extracted with $CH_3OH:H_2O$ (70:30), DON with 200 mL of ultrapure water, ZON with $CH_3OH:H_2O$ (80:20), and OTA with $AcCN:H_2O$ (60:40). The extracts were filtered through Whatman No. 4 filter paper. AF and ZON were filtered through microfiber filter paper once and passed through the IAK column. Reading was done on HPLC. LOD/LOQ, repeatability/reproducibility, recovery/accuracy, and linear measurement range (linearity) studies of all methods were performed with appropriate matrices. For this, a spike was applied to the blind sample. Measurements of aflatoxin, zeralenone, and ochratoxin were done with an HPLC/FLD device; HPLC/DAD was used for deoxynivalenol.

Aflatoxin analysis was carried out using an Agilent HPLC (1100) device equipped with an FLD detector. In the HPLC determination of aflatoxins B1, B2, G1, and G2, using fluorescence detection, excitation and emission wavelengths were set at 360 nm and 430 nm, respectively. Chromatographic separations were conducted on a column (ACE 5 C18–250 mm x 4.6 mm (Aberdeen, Scotland)), and the column temperature was 25 °C. The flow rate was 1.0 mL/min, and the injection volume was 100 µL. Isocratic mobile phase composition was 545 mL H_2O (ultrapure water), 182 mL AcCN, 273 mL CH_3OH, 120 mg KBr, and 350 µL 4M HNO_3. A post-column derivative electrochemical cell was used for the complete separation

of aflatoxins (B1, B2, G1, and G2) in the analytical column.

Ochratoxin analysis was carried out using an Agilent HPLC (1260) device. In the HPLC determination of ochratoxin by using fluorescence (FLD) detection, excitation and emission wavelengths were set at 330 nm and 460 nm, respectively. Chromatographic separations were conducted on a column (ACE 5 C18-250 mm x 4.6 mm / ODS-1 C18 5 μm 250 x 4.6 mm), and the column temperature was 40 °C. The flow rate was 1.0 mL/min, and the injection volume was 100 μL. The isocratic mobile phase composition was ultrapure water, AcCN-CH_3COOH (51:48:1) (v/v/v). Zearalenone analysis was carried out using an Agilent HPLC (1260) device. In the HPLC determination of ZON by using fluorescence (FLD) detection, excitation and emission wavelengths were set at 232 nm and 440 nm, respectively. Chromatographic separations were conducted on a column (ACE 5 C18-250 mm x 4.6 mm), and the column temperature was 40 °C. The flow rate was 1.0 mL/min, and the injection volume was 100 μL. The isocratic mobile phase composition was ultrapure water, AcCN (1/1 V/V).

Deoxynivalenol analysis was carried out using an Agilent HPLC (1260) device. In the HPLC determination of DON by using diode array (DAD) detection. The wavelength was set at 218 nm. Chromatographic separations were conducted on a column (ODS-EP 150 mm x 4.6 mm), and the column temperature was 40 °C. The flow rate was 1.0 mL/min, and the injection volume was 100 μL. The isocratic mobile phase composition was ultrapure water: AcCN-CH_3OH (94/3/3%).

2.6. Verification Studies

For method verification, detection (LOD) and quantification (LOQ) limits, precision, and reality parameters were studied. Analyses were performed by adding mycotoxin standards to homogenized samples for LOD/LOQ, precision (repeatability, reproducibility),) and reality (recovery) studies. Measurements were performed using spiked AF, OTA, DON, and ZON standards at the concentrations given in Table 1. For LOD/LOQ, 20 parallel studies were performed at the following concentrations: These concentrations in Table 1 for repeatability, recovery, and reproducibility were spiked. Six parallel studies on the same day for repeatability and recovery analysis were done. Six parallel studies were done on different days for reproducibility as well [24, 25].

Table 1. Spike concentrations of method verification.

	LOD/LOQ (μg/kg)	Repeatability/Recovery (μg/kg)	Reproducibility (μg/kg)
AF B_1	1.00	1.00 / 5.00	1.00 / 5.00
AF B_2	0.30	0.30/1.50	0.30/1.50
AF G_1	1.00	1.00 / 5.00	1.00 / 5.00
AF G_2	0.30	0.30/1.50	0.30/1.50
OTA	0.50	0.50/2.00/5.00	0.50/2.00/5.00
DON	250.00	250.00/1000.00	250.00/1000.00
ZON	10.00	10.00/50.00	10.00/50.00

LOD: limit of detection, LOQ: limit of quantification.

3. Results and Discussion

Celiac patients must eat gluten-free foods. For this reason, they cannot consume gluten-containing foods such as wheat, barley, and rye. Rice and corn or natural gluten-free products such as buckwheat, carob flour, and chickpea flour are mostly used in the products of patients with celiac disease.

Celiac disease is both a genetic disease and a lifelong food allergy. It is accepted as the most common genetic disease in men today. According to data obtained from the Health Information System, the number of diagnoses of celiac disease in Turkey is 68123 as of May 2019 [19]. Gluten-related diseases are primarily celiac disease, non-celiac gluten sensitivity, wheat allergy, and gluten ataxia [26]. The increase in celiac disease in the last 20 years may be related to, apart from changes in eating habits, the increase in awareness of the disease, the easy application of antibody screening tests, and the recognition of atypical or silent cases [19]. This situation rapidly increases the gluten-free product market in parallel with the increasing

demand for gluten-free products. The global market for gluten-free products has reached high numbers [27–30]. Today, foods that do not contain more than 20 mg of gluten per kilogram are considered gluten-free foods [31]. Therefore, it is important to determine the possible amounts of mycotoxins that may be exposed to people who eat gluten-free foods. Verification of analytical methods is found in Table 1.

3.1. Validation of analytical methods

As seen in Table 1, the concentrations in the table were spiked into the blank solution for validation studies. According to the obtained results, the study was subjected to appropriate statistical tests. For each method, measurement uncertainty parameters, which are included with the measurement result, characterize the distribution of values corresponding to the measured size, and show the quality of the measurement result, were calculated [24, 25]. The calculated results are given in Table 2.

Table 2. Validation results of methods for mycotoxins

	LOD (µg/kg)	LOQ (µg/kg)	Mean (µg/kg)	STD	Recovery %	*measurement uncertainty*
Total AF	0.40	1.32	2.47	0.75	93.47	X ± 0.13X
AF B₁	0.21	0.69	0.97	0.07	96.47	X ± 0.17X
OTA	0.09	0.29	0.24	0.02	92.01	X ± 0.14X
ZON	2.25	7.5	9.63	0.75	92.10	X ± 0.18X
DON	40.45	134.83	200.46	6.19	91.85	X ± 0.18X

According to Table 2 recovery is over 90% for all methods, and it has been found suitable according to the TFC.

After the validation processes of the methods were completed in the laboratory, 95 gluten-free foods purchased randomly were homogenized, and AF, OTA, ZON, and DON analyses were performed. Gluten-free foods with detectable levels of mycotoxins are given in Table 3 below.

In the DON analysis, results were obtained for 11 out of 95 products. The lineer range of DON analysis was 20–2000 µg/kg. The maximum limit allowed for pasta in TFC [32] is 750 µg/kg. The results were below and appropriate to this value, but the pasta5 and pasta7 results were found to be close to this value. It is thought that attention should be paid to the consumption of these products. It has been determined that these products were made from corn, which was very quickly contaminated. The maximum limit for bread is 500 µg/kg. 420 µg/kg was found to be suitable for bread. The maximum value for a biscuit or cracker is 500 µg/kg. Results were found below 500 µg/kg and are

suitable. According to Tolosa J. et al. (2021), FB1, ZON, and DON had the highest incidence rates, with total incidences of 90.5%, 71.4%, and 66.7%, respectively. On the other hand, in terms of mycotoxin levels, DON > NIV > FB1 > FB2 > ZON > HT-2 were in the top five. The substance with the highest content was DON (377.4 g/kg) [33]. Despite the significant amounts of mycotoxin found, particularly for DON, NIV, and FBs, none of the samples exceeded the maximum values (MLs) stipulated by the European Regulation [34].

Table 3. Mycotoxins detected in gluten-free products

Gluten-free food samples	*OTA (µg/kg)*	*DON (µg/kg)*
Buckwheat flour[3]	1.99	
Pasta[1]	2.52	
Pasta[3]	1.36	
Pasta[5]	1.41	725
Pasta[2]		480
Pasta[7]		740
Pasta[9]		650
Pasta[11]		550
Pasta[12]		386
Pasta[13]		410
Bread[5]		420
Crackers /biscuits[4]	2.34	
Crackers /biscuits[8]	1.14	
Crackers /biscuits[10]		480
Crackers /biscuits[11]	1.33	
Crackers /biscuits[18]		430
Crackers/biscuits[19]		495
Cornflakes[4]	1.94	
Cornflakes[6]	2.48	

Superscript numbers are shown the different brand of products

As a result of the mycotoxin analysis, OTA results were found in 9 of the 95 different packaged products studied. The maximum allowable limit for processed grains and grain products (offered for direct human consumption) in the Turkish Food Codex Contaminants Regulation (TFC) [32] is 3 µg/kg. Since the results found in the studied products are below 3 µg/kg, the results are appropriate.

In the study of Giannioti Z et al. (2023, a total of 28 organic whole grain oat flours, conventional whole grain oat flour, organic rice flour, and conventional rice flour were used for the detection of three mycotoxins (DON,

ZEN, and AFB1) occurring in gluten-free flours analyzed. They used the approved extraction method, LC-MS/MS, for analysis. They stated that there was multiple mycotoxin contamination in all flour types, especially in traditional whole-grain oat flour. In rice flour, one sample was found to contain zearalenone at a concentration of 83.2 µg/kg, higher than the level set by the European Commission for cereal flours [35].

According to the data in Table 3, the population most exposed to mycotoxins found in corn and rice foodstuffs (GF products) corresponds to those with celiac disease and gluten intolerance, and the highest exposure level among these groups is children.

When we look at the table, it is thought that the gluten-free foods in separate stands in the markets prevent the contamination of mycotoxins, and the storage conditions are better than for other products. It can be said that these foods are more reliable for consumers based on the findings and the interpretation of significant data. When we look at the table, it is thought that the gluten-free foods in separate stands in the markets prevent the contamination of mycotoxins, and the storage conditions are better than for other products. It can be said that these foods are more reliable for consumers based on the findings and the interpretation of significant data.

4. Conclusions

Four mycotoxins were analyzed for 95 different brands and types of gluten-free packaged foods. The results showed that the analytical procedure performed was accurate (recovery range of 90% to 97% for the majority of analytes), precise (RSDs < 18%), and sensitive (LODs 0.09 to 40.5 µg/kg). Many of these methods fall short of the limit that can be determined. The mycotoxin values in a few of them were determined according to the Turkish food codex, but the values found do not exceed the upper limit. The values of OTA and DON mycotoxins in gluten-free food samples were found in the range of 1.14–2.52 µg/kg for OTA and 38–740 µg/kg for DON. Both mycotoxin values were found in only one pasta sample of all samples. As a result of all analysis and validation studies, it is concluded that the consumption of gluten-free foods is not harmful in terms of mycotoxins in those products. It has been determined that 95 different gluten-free products are safe in terms of mycotoxins. This shows that the products analyzed are produced, stored, and transferred to the consumer under appropriate conditions.

Declaration of Ethical Standards

The authors of this article declare that the materials and methods used in this study do not require ethical committee permission and/or legal-special permission.

Conflict of Interest

The authors declare that they have no known competing financial interests or personal relationships that could have appeared to influence the work reported in this paper.

Acknowledgements

References

[1] Anfossi L., Giovannoli C. and Baggiani C. 2016. Mycotoxin detection. Current Opinion in Biotechnology **37**, pp. 120–126.

[2] Steyn P.S., Stander M.A., 1999. Mycotoxins with Special Reference to the Carcinogenic Mycotoxins: Aflatoxins, Ochratoxins and Fumonisins, 2nd ed. General and Applied Toxicology.

[3] Concon J.M., 1988. Mold and Mycotoxin Contamination of Food Products. In: Food Toxicology Part B: Contaminants and Additives. New York: Marcel Dekker Inc, 677-770.

[4] Ünüsan N., 2019 Systematic review of mycotoxins in food and feeds in Turkey. Food Control; **97**, pp. 1–14.

[5] Pons W.A. & Goldblatt L.A., 1965. The determination of aflatoxins in cottonseed products. J Am Oil Chem Soc. **42**(6), pp. 471-475.

[6] Miller K., 1987. Toksicological Aspacts of Food. The British Industrial Biological Research Association, El Sevier Applied Science, London and Newyork, pp. 164-171.

[7] Cardona T.D., Noomhorm A., Ilangantileke S.G., Guzman J.D., 1992. A small-scale chemical applicator to prevent aflatoxin contamination in maize cobs. Postharvest Biol Tec. **1**(4), pp. 327-342.

[8] Pitt J.I., 2013. Foodborne Infections and Intoxications: Chapter 30. Mycotoxins. Fourth ed. Elsevier Inc. Chapters, USA.

[9] Diez-Sampedro A., Olenick M., Maltseva T., Flowers M., 2019. A Gluten-Free Diet, Not an Appropriate Choice without a Medical Diagnosis. J Nutr Metab. 2438934, pp. 5.

[10] Bergamo P., Maurano F., Mazzarella G., Iaquinto G., Vocca I., Rivelli A.R., Rossi M. 2011. Immunological evaluation of the alcohol-soluble protein fraction from gluten-free grains in relation to celiac disease. Mol Nutr Food Res. **55**(8), pp. 1266-1270.

[11] Foschia M., Horstmann S., Arendt E.K., Zannini E. 2016. Nutritional therapy–Facing the gap between coeliac disease and gluten-free food. Int. J Food Microbiol. **239**, pp. 113-124.

[12] Volta U., Caio G., Tovoli F., De Giorgio R. 2013. Non-celiac gluten sensitivity: questions still to be answered despite increasing awareness. Cell Mol Immunol. **10**(5), pp. 383-392.

[13] Caldas E.D., Silva A.C. 2007. Mycotoxins in corn-based food products consumed in Brazil: an exposure assessment for fumonisins. J Agr Food Chem. **55**(19), pp. 7974-7980.

[14] Valitutti F., De Santis B., Trovato C.M., Montuori M., Gatti S., Oliva S., .. Catassi C. 2018. Assessment of mycotoxin exposure in breastfeeding mothers with celiac disease.Nutrients,**10**(3), pp.336.

[15] Brera C., Debegnach F., De Santis B., Di Ianni S., Gregori E., Neuhold S., Valitutti F. 2014. Exposure assessment to mycotoxins in gluten-free diet for celiac patients. Food Chem Toxicol. **69**, pp.13-17.

[16] Castillo M.Á., Montes R., Navarro A., Segarra R., Cuesta G., Hernández E. 2008. Occurrence of deoxynivalenol and nivalenol in Spanish corn-based food products. J Food Compost Anal. **21**(5), pp. 423-427.

[17] Cirlini M., Mazzeo T., Roncoroni L., Lombardo V., Elli L., Bardella M.T., ... & Pellegrini N. 2017. Are treated celiac patients at risk for mycotoxins? An Italian case-study. Toxins. **9**(1), pp. 11.

[18] Cano-Sancho G., Ramos A.J., Marín S., Sanchis V. 2012. Presence and co-occurrence of aflatoxins, deoxynivalenol, fumonisins and zearalenone in gluten-free and ethnic foods. Food Control **26**, pp. 282-286.

[19] Ministry of Health, General Directorate of Public Health (HSGM), (2020). Metabolism and Celiac, Celiac and its Incidence, https://hsgm.saglik.gov.tr/tr/metabolizma-ve-colyak/çölyak-ve-görülme-sıklığı.html. (Accessed date 05.02.2020)

[20] Thompson M., Ellison S.L., Wood R. 2006. The International Harmonized Protocol for the proficiency testing of analytical chemistry laboratories (IUPAC Technical Report). Pure Appl Chem;**78**(1), pp.145-196.

[21] Jr Dr George W. Latimer, 2016. Official Methods of Analysis of AOAC INTERNATIONAL, 20th Edition, 1-volume, 49.2.18, AOAC Official Method 991.31 Final Action 1994, Ch 49, pp.21, AOAC Offcial Methods of Analysis 2016, ISBN-10: 0935584870.

[22] Jr Dr George W. Latimer, 2016. Official Methods of Analysis of AOAC INTERNATIONAL, 20th Edition, 2-volume, 49.6.04, AOAC Official Method 2000.03 Ochratoxin, Immunoaffinity Column HPLC Final Action 2000, Ch 49, pp. 74 ISBN-13: 978-0935584875.

[23] Fazekas B., Tar A. 2001. Determination of zearalenone content in cereals and feedstuffs by immunoaffinity column coupled with liquid chromatography. J AOAC Int.;**84**(5), pp.1453-1459.

[24] General Directorate of Food and Control. (2021). Measurement uncertainty guide in chemical and physical analysis https://www.tarimorman.gov.tr/GKGM/Belgeler/DB_Gida_Kont/Kimyasal_Fiziksel_OB_Rehberi.pdf. (Accessed date 12.01.2021)

[25] General Directorate of Food and Control (2021). Method validation/verification guide in chemical and physical analysis. April 2018 https://www.tarimorman.gov.tr/GKGM/Belgeler/DB_Gida_Kont/Kimyasal_Fiziksel_Val_Ver_Rehberi.pdf. (Accessed date 12.01.2021).

[26] Ontiveros N., Rodríguez-Bellegarrigue C.I., GaliciaRodríguez G., Vergara-Jiménez M.J., Zepeda-Gómez E.M., Arámburo-Galvez J.G., et al. 2018. Prevalence of self-reported gluten-related disorders and adherence to a gluten-free diet in Salvadoran adult population. Int J Environ Res Public Health. **15**(4), pp. 786-97.

[27] Amil Dias J. 2017. Celiac Disease: What do we know in 2017? GE Port J Gastroenterol. **24**(6), pp. 275-78

[28] Ulusoy H.G., Rakıcıoğlu N. 2019. Bes Diy Derg **47**(2):87-92 DERLEME REVIEW Glutensiz Diyetin Sağlık Üzerine Etkileri, The Effects of Gluten-free Diet on Health. DOI: 10.33076/2019.BDD.1026

[29] Carroccio A., Giambalvo O., Blasca F., Iacobucci R., D'Alcamo A., Mansueto P. 2017. Self-Reported Non-Celiac Wheat Sensitivity in High School Students: Demographic and Clinical Characteristics. Nutrients **9**, pp. 771.

[30] Kutlu T. 2019. Gluten-free diet: is it really always beneficial ? Turk Pediatri Ars. **54**(2), pp.73–5.

[31] Balcı E. 2018. Çölyak Hastalığının Tedavisi Nasıldır? Gıda Bilgi Medya Bilişim Teknoloji A.Ş. https://www.gidabilgi.com/Makale/Detay/colyak-hastaliginin-tedavisi-nasildir--680615 11.04.2018 (Accessed date 12.05.2021).

[32] Turkish Food Codex Contaminants Regulation (2023) https://www.tarimorman.gov.tr/GKGM/Duyuru/495/Mevzuat-Taslagi-Tgk-Bulasanlar-Yonetmeligi (Accessed date 12.01.2023).

[33] Tolosa, J., Rodríguez-Carrasco, Y., Graziani, G., Gaspari, A., Ferrer, E., Mañes, J., & Ritieni, A. 2021. Mycotoxin Occurrence and Risk Assessment in Gluten-Free Pasta through UHPLC-Q-Exactive Orbitrap MS. Toxins, **13**(5), pp. 305.

[34] European Commission 2006. Commission Regulation (EC) No. 1881/2006 setting maximum levels for certain contaminants in foodstuffs. Off. J. Eur. Union 2006, L364, pp. 5–24.

[35] Giannioti Z., Albero B., Hernando M.D., Bontempo L., Pérez R.A. 2023. Determination of Regulated and Emerging Mycotoxins in Organic and Conventional Gluten-Free Flours by LC-MS/MS. Toxins.; **15**(2), pp.155.